Quark-mass dependence of pion scattering amplitudes

Dissertation

zur
Erlangung des Doktorgrades (Dr. rer. nat.)
der
Mathematisch-Naturwissenschaftlichen Fakultät
der
Rheinischen Friedrich-Wilhelms-Universität Bonn

vorgelegt von
Malwin Leonard Berengar Niehus
aus
Oldenburg (Oldb)

Bonn, 24. Februar 2022

Angefertigt mit Genehmigung
der Mathematisch-Naturwissenschaftlichen Fakultät
der Rheinischen Friedrich-Wilhelms-Universität Bonn

Promotionskommission

Erstgutachter:	PD Dr. Bastian Kubis
Zweitgutachter:	Prof. Dr. Carsten Urbach
Fachnahes Mitglied:	Prof. Dr. Bernhard Ketzer
Fachfremdes Mitglied:	Prof. Dr. Barbara Niethammer

Tag der mündlichen Prüfung: 10.06.2022
Erscheinungsjahr: 2022

Thus, we do not accept theories in which quarks are real, observable particles; [...].
[...]
The simplest and most obvious advantage [...] *is that the gluons are now just as fictitious as the quarks.*

Advantages of the Color Octet Gluon Picture [1]
Harald Fritzsch, Murray Gell-Mann, Heinrich Leutwyler

Scared to face the world, complacent career student
Some people graduate, but be [sic] *still stupid*

Good Morning [2]
Kanye West

Abstract

We analyze lattice-QCD data of the $\pi\pi \to \pi\pi$ P wave obtained at unphysical-high pion masses with the inverse-amplitude method at next-to-leading order and at next-to-next-to-leading order. We then extrapolate to the physical pion mass and determine the properties of the ρ resonance from its pole in the complex plane. By comparing both orders, we estimate the systematic error associated with the truncation. Subsequently, we use the inverse-amplitude method as input to Khuri–Treiman equations for $\gamma^{(*)}\pi \to \pi\pi$. The resulting dispersive framework is fit to lattice-QCD data at unphysical pion masses and then again extrapolated to the physical mass, where we determine the radiative coupling of the ρ, the lineshape, and the chiral anomaly of the process. Lastly, we develop a method to assess the statistics needed in experiments to be sensitive to higher-order pion rescattering in decays of a single particle into three pions and illustrate the approach for simple cases.

The main results of Part II of this thesis have been published in

M. Niehus, M. Hoferichter, B. Kubis, and J. Ruiz de Elvira,
Two-Loop Analysis of the Pion Mass Dependence of the ρ Meson,
Phys. Rev. Lett. **126**, 102002 (2021), arXiv:2009.04479 [hep-ph].

This paper provided the basis for

G. Colangelo, M. Hoferichter, B. Kubis, M. Niehus, and J. Ruiz de Elvira,
Chiral extrapolation of hadronic vacuum polarization,
Phys. Lett. B **825**, 136852 (2022), arXiv:2110.05493 [hep-ph].

Part III of this thesis is an expanded version of

M. Niehus, M. Hoferichter, and B. Kubis,
The $\gamma\pi \to \pi\pi$ anomaly from lattice QCD and dispersion relations,
JHEP **12**, 038 (2021), arXiv:2110.11372 [hep-ph].

The employed framework has been outlined partly before in

M. Niehus, M. Hoferichter, and B. Kubis,
Quark mass dependence of $\gamma^*\pi \to \pi\pi$,
PoS **CD2018**, 076 (2019), arXiv:1902.10150 [hep-ph]

and

M. Niehus,
Quark mass dependence of $\gamma\pi \to \pi\pi$,
Master's thesis, Bonn University (2017).

Contents

Chapter 1

Introduction

Arguably, the standard model (SM) of particle physics is a rather reductionist affair. According to it, matter consists of a large number of tiny particles interacting via the exchange of other tiny particles, with altogether only 17 different particle species in action.[1] There are three fundamental forces mediated via particle exchange in the SM: the electromagnetic interaction, the weak one, and the strong one, with the former two unified into the electroweak interaction [3–9]. The other known force, gravity, is not incorporated into the SM and instead described by the theory of general relativity [10]. It remains one of the major open problems in theoretical physics how to unify the former and the latter. However, gravity can be safely ignored under various circumstances. In this context, the SM is extremely successful, i.e., allows for precise predictions that have been confirmed by experiment over and over again. Even if extensions are needed—e.g., to explain the observed neutrino oscillations [9], or if new particles were discovered in an experiment—these would not at all enforce a change of the conceptual underpinning of the SM, namely quantum field theory (QFT), but merely require the addition of new terms to the Lagrangian of the SM. In fact, it has been argued that QFT is a necessity arising from the combination of special relativity and quantum physics that is needed to describe processes at the energy scales of relevance to particle physics [11]. There even exists a paradigm stating that the quantum theory of gravity might ultimately be a QFT [12], although loop quantum gravity [13] and string theory remain popular alternatives.

In itself, QFT is a highly complicated framework. Consider the strong interaction, which is described by a subset of the SM known as quantum chromodynamics (QCD). QCD is a gauge theory with gauge group $SU(3)$ [1] and, as such, it is a special case of a Yang–Mills theory. Establishing the existence and key properties of Yang–Mills theory is currently an unsolved problem in mathematical physics [14]; however, the theory can be successfully used to make predictions at the level of rigor of theoretical physics. Here, the main challenge lies in the non-perturbative nature of QCD at low energies, i.e., at the typical energy scales of nuclear physics. It is conjectured that the rise of the interaction strength with decreasing energy scale confines the fundamental degrees of freedom of QCD, the quarks and gluons, to bound states known as hadrons, with hundreds of hadrons observed experimentally [9], thereby giving rise to the field of hadron physics.

QCD describes a wide spectrum of physical phenomena, not only the confinement of quarks in hadrons, but also their asymptotic freedom at high energies. Moreover, it shows an interesting phase diagram that contains the quark gluon plasma [15]. There are further fascinating effects, namely anomalies, instantons, and the θ term, as well as a spontaneous symmetry breaking of a chiraly symmetry [8].

[1] Here we do not count antiparticles separately.

The rich physics paired with the difficulty to make predictions—caused by the failure of plain perturbation theory in the low-energy regime—motivates the development of different methods to compute observables. Three of those are of relevance to the work presented in this thesis. First, there is lattice QCD, a numerical approach based on a rotation from Minkowski spacetime to a Euclidean one and a subsequent discretization of a finite spacetime volume [16–18]. Second, there is chiral perturbation theory (ChPT), an effective field theory (EFT) that allows for a perturbative expansion by changing the degrees of freedom to pions, the pseudo-Goldstone bosons associated with the aforementioned spontaneous breakdown of the approximate chiral $SU(2)_\mathrm{L} \times SU(2)_\mathrm{R}$[2] symmetry [8, 20–22]. Third, there are dispersion relations, integral equations based on the properties of scattering amplitudes when studied as functions of complex variables [11, 23–28].

Of the aforementioned tools, lattice QCD is the only one that allows for computations directly based on the degrees of freedom of plain QCD, namely quarks and gluons. Hence, predictions can be made as soon as the fundamental parameters of QCD, the quark masses and the coupling strength, are fixed. This makes lattice QCD an extremely predictive tool. However, this power comes at a price. Lattice calculations are computationally very demanding and require strong hardware as well as sophisticated software [29–31]. Often, the computational cost is partially reduced by setting the quark masses to unphysically high values, which has the obvious drawback that results obtained in this way cannot be directly compared with experimental observations that are necessarily restricted to physical quark masses. Instead, such lattice results need to be extrapolated to physical quark masses, the so-called physical point. This extrapolation requires the use of tools beyond lattice QCD. Although computations at the physical point have become feasible, see Refs. [32–35] for examples, there are still computations performed at unphysical quark masses, e.g., the ones presented in Refs. [36, 37]. Additionally, the information on scattering of hadrons that can be gathered directly on the lattice is strongly limited, since the lattice is a finite volume in Euclidean spacetime, while scattering observables are defined in infinite-volume Minkowski space [38]. This apparent shortcoming can be circumvented via the Lüscher framework and extensions thereof, which translate finite-volume quantities to scattering observables [39]. For certain scattering processes, this translation requires continuous parametrizations of scattering amplitudes [40], which again cannot be provided by lattice QCD on its own. Indeed, lattice computations are intrinsically constrained to yield a finite number of data points. In passing, we note that alternatives to the Lüscher formalism have been developed [41, 42].

Contrarily to lattice QCD, ChPT is a perturbative tool that enables to compute observables analytically. Again, this goes hand in hand with drawbacks. ChPT contains free parameters beyond those of QCD, so-called low-energy constants (LECs). The higher the order of the perturbative expansion, the more LECs appear. In $SU(2)$ ChPT at leading order (LO) there are two LECs, at next-to-leading order (NLO) seven [21], at next-to-next-to-leading order (NNLO) 53 [43], and at next-to-next-to-next-to-leading order (NNNLO) 452 [44].[3] Of course, not all LECs contribute to a given process. Nevertheless, the drastic increase of the number of free parameters clearly points towards the practical limitations of ChPT. More severely, ChPT is limited to the onset of the low-energy region and fails quickly as soon as the energy is increased. Despite these issues, ChPT is a potent tool in the energy region where it converges well [22]. Naturally, the idea arises to fix the LECs via lattice QCD [47] and even use ChPT to extrapolate lattice results obtained at unphysical quark

[2]ChPT can be extended to $SU(3)_\mathrm{L} \times SU(3)_\mathrm{R}$ [19]; however, the explicit symmetry breaking by the quark masses is stronger than in the $SU(2)$ scenario. In this thesis we use $SU(2)$ ChPT.

[3]Here we do not include contact terms (i.e., those that contain only external fields) and consider the even-parity sector only. The numbers increase further if the odd-parity sector is included [45, 46].

masses towards the physical point [48]. In fact, ChPT can be extended to incorporate discretization artifacts associated with the lattice to allow for an improved analysis of lattice data [49].

As opposed to lattice QCD and ChPT, dispersion relations on their own do not enable to compute a wide range of observables, mainly, because they do not incorporate much information about the dynamics of the strong interaction. Instead, they put strong constraints on scattering amplitudes, based on analyticity, i.e., the requirement that such amplitudes are holomorphic functions of the kinematical variables except for singularities encoding the presence of physical states, probability conservation in the form of unitarity of the S matrix, and crossing symmetry. The constraints show their true power when combined with input data, which are often taken from experiments, see, e.g., Refs. [50–54]. In addition, these constraints can be combined with ChPT to extend the range of validity of the latter via the inverse-amplitude method (IAM) [55–58]. This combination can be used to extrapolate lattice data that are inaccessible to plain ChPT [59].

In this work, we study scattering processes and decays of hadrons as well as their electromagnetic interaction with an external photon. To be specific, we discuss $\pi\pi \to \pi\pi$ scattering of a pion π by its own kind, $\gamma^{(*)}\pi \to \pi\pi$ scattering of a pion with a photon γ that might be virtual as indicated by the superscript asterisk, and decays of a hadron into three pions.

Among these processes, $\pi\pi \to \pi\pi$ is clearly the prime example of hadronic scattering. Due to their pseudo-Goldstone nature the pions are the lightest hadrons, and hence stable within QCD. Thus, the charged pions are sufficiently long-lived to be controlled experimentally rather well.[4] In addition, the pions are the only states that can go on-shell in the region directly above the $\pi\pi$ threshold. Hence, they dominate the dynamics in this region, making it possible to restrict the attention to a single channel. Moreover, as a two-to-two particle process involving four scalars of equal mass[5] the kinematics of $\pi\pi \to \pi\pi$ are as simple as it gets. For this reasons it serves as a major testing ground in the development of dispersion relations,[6] another one being $\pi N \to \pi N$, the scattering of a pion by a nucleon N [62, 63]. In fact, dispersion relations quickly get out of hand if the number of external particles is increased, as illustrated by the absence of rigorous dispersive analyses of such multi-particle scattering in the current literature. On top of this, $\pi\pi \to \pi\pi$ is a major battle ground of ChPT [21, 64, 65], precisely because the latter is phrased in terms of pions. Furthermore, as the lightest member of the QCD spectrum pions often dominate the dynamics of hadronic processes at low energies. More precisely, via unitarity of the S matrix $\pi\pi \to \pi\pi$ is coupled to a plethora of scattering processes and decays, and thus providing key input to theoretical descriptions of these [51, 52, 66–72].

The process $\pi\pi \to \pi\pi$ is also intrinsically interesting due to the appearance of resonances. These short-lived phenomena show up as intermediate states in scattering processes. Specifically, in the $\pi\pi \to \pi\pi$ S wave there is the $f_0(500)$ resonance, which is of particular interest because it is the lightest known resonance in the spectrum of the strong interaction and it does not seem to be an ordinary quark-antiquark meson [73], as opposed to, e.g., the ρ resonance. The latter shows up in the P wave as the dominant physical effect at energies below 1 GeV. Often it saturates electromagnetic interactions of hadrons, in this way being a key player in the phenomenological approach known as vector meson dominance (VMD) [74]. ChPT fails to describe resonances, which

[4] While the charged pions decay via the weak interaction, the main decay channel of the neutral pion, $\pi^0 \to \gamma\gamma$, is driven by the electromagnetic interaction. Thus, the lifetime of the π^0 is nine orders of magnitude smaller than the one of its charged cousins [9].

[5] Of course, in reality the π^0 is slightly lighter than the $\pi^\pm$ [9]. However, throughout this thesis we work in the isospin limit and set the mass of all pions to the one of the charged pions.

[6] It must be stated that dispersion theory on its own, i.e., S-matrix theory, failed to describe $\pi\pi \to \pi\pi$ [60]. However, it provides strong and powerful constraints in the form of Roy equations [61] and modifications thereof [50].

arise due to the non-perturbative nature of low-energy QCD. Clearly, any understanding of the strong interaction in terms of QCD is incomplete as long as the properties of resonances cannot be computed accurately via the latter.

The apparent simplicity of the $\pi\pi \to \pi\pi$ P wave as well as the interesting physics associated with the ρ resonance make the P wave a prime candidate for investigations on the lattice via Lüscher's method, highlighted by the huge amount of computations of this kind, see Refs. [34, 36, 75–88]. The data have reached a formidable quality, with recent computations covering a wide range of quark masses [36], sometimes even extending to the physical point [34]. Although computations at the physical point do not require an extrapolation in the mass, analytical models are still needed to extract resonance properties. These are encoded as parameters of poles in the complex plane outside the direct reach of the lattice, and thus models that allow for an analytical continuation need to be fit to the data before the resonance characteristics can be properly determined. The quality of the data calls for high-quality models. One such model is the aforementioned IAM, which has been used to study the quark-mass dependence of both the S wave and the P wave for the first time in Ref. [89]. The IAM can be employed at different orders of ChPT, the higher the order, the more accurate the model. While lattice-QCD data have been analyzed with the IAM at NLO several times [59, 90–93], there is only one previous analysis at NNLO [94, 95], which was carried out a decade ago. At that time the lattice data were not nearly as good as they are nowadays. Hence, fits to the data alone were not stable. To obtain stable fits, additional constraints were put in by hand. Moreover, some data points required ad hoc shifts. This motivates a confrontation of the NNLO IAM with state-of-the-art lattice computations as presented in Part II. Again, note that an alternative to Lüscher's formalism has also been used to study the ρ [96].

One process connected via unitarity to the $\pi\pi \to \pi\pi$ P wave is $\gamma^{(*)}\pi \to \pi\pi$. Again the ρ appears; therefore $\gamma^{(*)}\pi \to \pi\pi$ gives access to the radiative coupling of the ρ and its sibling [97]. At low energies, the Wess–Zumino–Witten anomaly [98, 99] gives rise to a prediction for the scattering amplitude in terms of known physical constants [100–102]. While a similar prediction for $\pi^0 \to \gamma\gamma$, which is driven by an anomaly, too, is experimentally tested at the sub-percent level [103], the one for $\gamma\pi \to \pi\pi$ has been put to test at the 10 % level only, once via the corresponding Primakoff reaction [104] and once via an analysis of pion-electron scattering data [105]. This motivated the development of a dispersive framework [66], which in combination with modern experimental data that could become accessible in the future [106] would allow for a more stringent test of the anomaly prediction. In the meantime, the process has been computed on the lattice twice [107, 108], both times at quark masses significantly above the physical point. To extract the characteristics of the ρ and, most importantly, to test the anomaly prediction, we analyze these data with a dispersive framework in Part III, building upon previous work in Ref. [109]. This dispersive framework is a special case of the so-called Khuri–Treiman (KT) equations [110].

Via crossing symmetry $\gamma^{(*)}\pi \to \pi\pi$ is connected to $\gamma^* \to \pi\pi\pi$, i.e., the decay of a virtual photon into three pions. The associated decay amplitude is of exactly the same form as the one for $\omega(782) \to \pi\pi\pi$ and $\phi(1020) \to \pi\pi\pi$, that is, decays of the ω and ϕ resonances. More generally speaking, all these are special cases of a decay of a particle with $I^G(J^{PC}) = 0^-(1^{--})$ quantum numbers into three pions, where I denotes isospin, G the G parity, J angular momentum, P parity, and C charge conjugation. Indeed the KT equations that we use to analyze the lattice data allow for a description of the decay region, too. This points towards an interesting future perspective. Originally, the Lüscher formalism was restricted to two-to-two scattering, and afterwards extended to simple one-to-two decays [111]. In recent years, the formalism was generalized to include three-to-three scattering and decays into three particles, see Refs. [112–114] for reviews of the progress

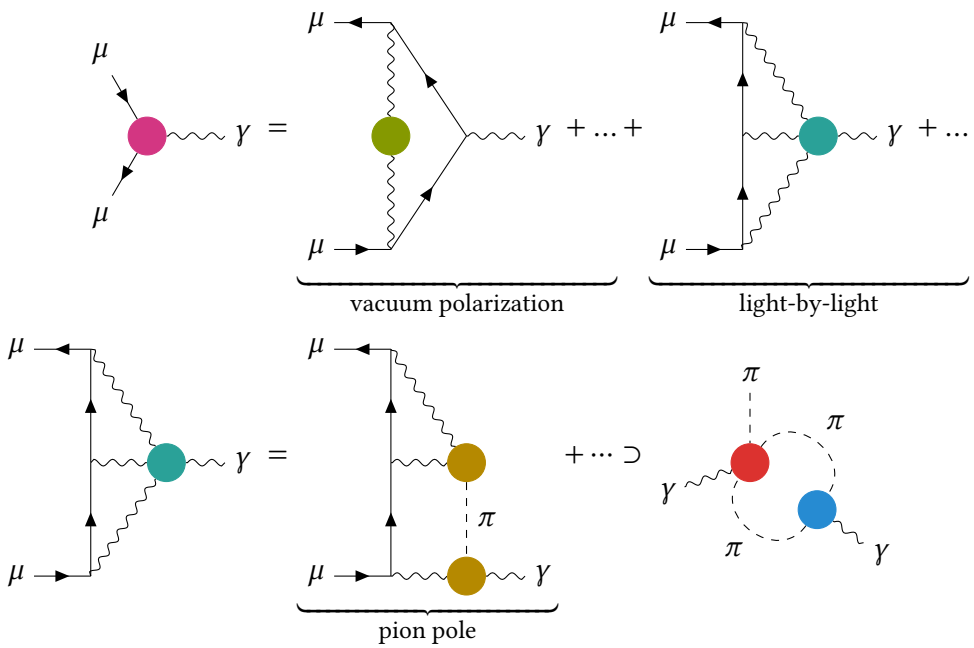

Figure 1.1: Hadronic contributions to the anomalous magnetic moment of the muon. The magnetic moment is extracted from the coupling of a muon to a photon. Hadrons contribute in two different ways to this coupling: via vacuum polarization and light-by-light scattering. Only the leading diagrams of both are depicted. A prominent contribution to the latter is the pion-pole term, which contains the pion transition form factor. The most important intermediate states in the transition form factor are $\pi\pi$ states. This allows for a decomposition of the transition form factor into the pion vector form factor and the $\gamma^{(*)}\pi \to \pi\pi$ amplitude [117, 118]. Both these objects, in turn, are related to $\pi\pi \to \pi\pi$, as we will see explicitly for $\gamma^{(*)}\pi \to \pi\pi$ in Part III. Accordingly, both pion–pion and photon–pion scattering are building blocks for a data-driven determination of the anomalous magnetic moment of the muon [119].

in this direction. By now, first lattice analyses of $\pi^+\pi^+\pi^+ \to \pi^+\pi^+\pi^+$ [35, 37, 115] and the formalism for decays like $\gamma^* \to \pi\pi\pi$ are available [116]. In the future these developments will open up new perspectives for dispersive frameworks like the one discussed in this thesis in the analysis of lattice data.

There is another interesting aspect of both $\pi\pi \to \pi\pi$ and $\gamma^{(*)}\pi \to \pi\pi$ that deserves attention. Both processes contribute to the anomalous magnetic moment of the muon [119], as illustrated in Fig. 1.1. This quantity shows a long-standing discrepancy between the SM prediction and the experimentally observed value, see Refs. [120, 121] for a historical perspective as well as an overview, Ref. [53] for the current theoretical prediction, and Ref. [122] for a recent experimental result. There is a lattice-QCD computation [123] that yields a theoretical prediction in agreement with the experimentally observed value and in contradiction to the prediction made in Ref. [53], but such a shift in the prediction would have consequences for other observables, thereby shifting the tension from one place to another [124]. The anomalous magnetic moment of the muon thus remains an interesting place of potential failure of the SM. If such a failure was manifested, this would point clearly to physics beyond the SM, that is, extensions of the SM [125]. These are a topic of hot debate, for the SM on its own fails to describe neutrino oscillations and dark matter.

Both the IAM used in the analysis of $\pi\pi \to \pi\pi$ and the KT equations used to analyze $\gamma^{(*)}\pi \to \pi\pi$ describe similar physics, namely the rescattering of pions, in other words, the repeated interaction of pions with themselves. Just like other physical systems, e.g., mechanical oscillations [126, Ch. 5] and electrical circuits [127, Vol. 2, Ch. 6], the rescattering can show resonant behavior. This manifests itself in the appearance of the aforementioned resonances, e.g., the ρ resonance in rescattering of two pions at an energy of roughly 760 MeV or the ω resonance in the rescattering of three pions at roughly 780 MeV.

In decays of a particle into three pions, there are different kinds of rescattering. First, there is $\pi\pi$ rescattering of a fixed pair of pions, with the other pion acting as a spectator. If the pions are in a P wave, this is completely dominated by the ρ resonance below 1 GeV. Second, there is rescattering where all pions participate but interact only pairwise, e.g., the first pion might rescatter with the second, and subsequently the second with the third. In the following, we refer to this as mixed rescattering. Third, there is genuine three pion rescattering, i.e., all pions interact with each other at one point in the FOURIER-transformed spacetime. KT equations might be considered as a black box that takes as input information on $\pi\pi$ scattering (including the resonances) and generates as output a decay or scattering amplitude that contains both the first and the second kind of rescattering. The third one needs to be built in manually. Usually, the first kind of rescattering dominates the second one. Hence, the question arises, if mixed rescattering can be observed experimentally. In Ref. [51] it was shown that the $\phi \to \pi\pi\pi$ data of Ref. [128] indeed point towards the existence of this kind of rescattering. Contrarily, in Ref. [129] the authors argued that no such effects are visible in their $\omega \to \pi\pi\pi$ data, which motivated a re-analysis of the same data in Ref. [130], this time taking into account information on $\omega \to \pi^0\gamma^*$, too. While the analysis confirmed the absence of statistically significant mixed rescattering in the decay into three pions, the authors claimed that mixed rescattering was necessary to simultaneously describe $\omega \to \pi^0\gamma^*$. In the light of these developments we introduce in Part IV a method to estimate the quality of experimental data that is necessary to probe mixed rescattering in decays into three pions, focusing on a simple system.

Having established the motivation of our research, we give a brief overview of this thesis. In Part I we introduce the core concepts of two-to-two particle scattering in the continuum and on the lattice that are of key relevance for the subsequent discussions. Equipped with this knowledge, we are ready to introduce the IAM and present our analysis of $\pi\pi \to \pi\pi$ lattice data in Part II. Subsequently, in Part III we confront $\gamma^{(*)}\pi \to \pi\pi$ lattice data with KT equations, building up on the foregoing analysis of $\pi\pi$ data. Then, in Part IV we discuss pion-rescattering effects in KT equations. Lastly, we sum up or results and draw conclusions in Part V.

Part I

Foundations

Chapter 2

Scattering of two particles in the continuum

Throughout this thesis, we will be confronted with scattering of two particles both in the initial and final state, i.e., processes of the form $\mathscr{P}_1(p_1) + \mathscr{P}_2(p_2) \to \mathscr{P}_3(p_3) + \mathscr{P}_4(p_4)$, with p_i the four-momentum of particle $\mathscr{P}_i$, $i = 1, \dots, 4$. Kinematically, such scattering is described by the four four-momenta, hence 16 real numbers. Since all frameworks that we are going to employ are in accordance with the laws of special relativity, we can make use of Poincaré invariance. This allows us to reduce the number of kinematical parameters to six, for the Poincaré group is ten-dimensional. In addition, if all particles are on-shell, i.e., p_i^2 is fixed for all $i = 1, \dots, 4$, there are only two remaining free parameters.

Denoting the free-particle state associated with a particle $\mathscr{P}$of momentum $\boldsymbol{p}$ as $|\mathscr{P}, \boldsymbol{p}\rangle$ (omitting further quantum numbers for the sake of notational simplicity), the scattering amplitude $\mathscr{M}$ of interest can be inferred from the S matrix $S = 1 + iT$ via the T matrix T according to

$$\begin{aligned}
&\langle \mathscr{P}_3\mathscr{P}_4, \boldsymbol{p}_3, \boldsymbol{p}_4 \,|S|\, \mathscr{P}_1\mathscr{P}_2, \boldsymbol{p}_1, \boldsymbol{p}_2\rangle \\
&= \langle \mathscr{P}_3\mathscr{P}_4, \boldsymbol{p}_3, \boldsymbol{p}_4 \,|\, \mathscr{P}_1\mathscr{P}_2, \boldsymbol{p}_1, \boldsymbol{p}_2\rangle + i\,\langle \mathscr{P}_3\mathscr{P}_4, \boldsymbol{p}_3, \boldsymbol{p}_4 \,|T|\, \mathscr{P}_1\mathscr{P}_2, \boldsymbol{p}_1, \boldsymbol{p}_2\rangle \\
&= \langle \mathscr{P}_3\mathscr{P}_4, \boldsymbol{p}_3, \boldsymbol{p}_4 \,|\, \mathscr{P}_1\mathscr{P}_2, \boldsymbol{p}_1, \boldsymbol{p}_2\rangle + i\,(2\pi)^4\,\delta^{(4)}(P - P')\,\mathscr{M}\left(\mathscr{P}_1(p_1)\mathscr{P}_2(p_2) \to \mathscr{P}_3(p_3)\mathscr{P}_4(p_4)\right).
\end{aligned} \tag{2.1}$$

Here $P := p_1 + p_2$, $P' := p_3 + p_4$, and $|\mathscr{P}_i\mathscr{P}_j, \boldsymbol{p}_i, \boldsymbol{p}_j\rangle := |\mathscr{P}_i, \boldsymbol{p}_i\rangle \otimes |\mathscr{P}_j, \boldsymbol{p}_j\rangle$.

It is convenient to introduce Lorentz invariant Mandelstam variables as

$$\begin{aligned}
s &:= (p_1 + p_2)^2 = (p_3 + p_4)^2\,, \\
t &:= (p_1 - p_3)^2 = (p_2 - p_4)^2\,, \\
u &:= (p_1 - p_4)^2 = (p_2 - p_3)^2\,,
\end{aligned} \tag{2.2}$$

where we made use of four-momentum conservation: $p_1 + p_2 = p_3 + p_4$. They obey the constraint $s + t + u = \sum_{i=1}^4 p_i^2$. Thus, if the particles are on-shell, only two Mandelstam variables are independent, in agreement with the parameter counting. In the center-of-mass (CM) frame, $s = (E^\star)^2$ holds, with $E^\star$ the total energy. Throughout this thesis, all quantities in the CM frame are denoted by a star as a superscript, if they are not Lorentz invariants.[1]

Instead of using two Mandelstam variables, e.g., s and t, to parametrize on-shell scattering, it is sometimes useful to use one Mandelstam variable, e.g., s, and one scattering angle, e.g., $\theta^\star :=$

[1] This is to be distinguished from complex conjugation: $a^\star$ denotes a quantity in the CM frame, while a^* denotes complex conjugation.

$\measuredangle(\boldsymbol{p}_1^\star, \boldsymbol{p}_3^\star)$, especially when discussing some consequences of rotational invariance. This invariance allows to expand a scattering amplitude into partial waves, that is, contributions to the scattering of fixed total angular momentum, as discussed pedagogically, e.g., in Ref. [131]. If the involved particles carry spin, the partial-wave expansion can become a delicate affair. One way to tackle the issues associated with spin is described in Ref. [132]. However, if the particles $\mathscr{P}_i$, $i = 1, \dots, 4$, are scalars, the partial-wave expansion of the associated scattering amplitude $\mathscr{M}$ simply reads

$$\mathscr{M}(s, z^\star) = 32\pi \sum_{l=0}^{\infty} (2l+1)\, t_l(s)\, P_l(z^\star)\,. \tag{2.3}$$

Here $z^\star \coloneqq \cos(\theta^\star)$ takes into account the dependence on the scattering angle, P_l denotes the l-th Legendre polynomial, and t_l is the partial wave of angular momentum l. Both the factors 32π as well as $2l+1$ are purely conventional, the former is the canonical choice for identical particles, the latter is introduced to make the use of the orthogonality relation of the Legendre polynomials,

$$\int_{-1}^{1} P_a(x)\, P_b(x)\, \mathrm{d}x = \frac{2}{2a+1}\delta_{ab}, \tag{2.4}$$

more convenient. Via this orthogonality relation, from Eq. (2.3)

$$t_l(s) = \frac{1}{64\pi} \int_{-1}^{1} P_l(z^\star)\, \mathscr{M}(s, z^\star)\, \mathrm{d}z^\star \tag{2.5}$$

follows.

Up to now, both $\mathscr{M}$ and t_l are $\mathbb{C}$-valued functions. In reality, for fixed particle species in the initial state, often there are several different two-particle combinations in the final state, which each might be produced with a certain probability. In general, the higher the energies, the more states are accessible. To describe multiple channels conveniently, $\mathscr{M}$ is rendered into a matrix-valued function. Each of its components is associated with a different combination of initial- and final-state particles. Accordingly, the partial waves t_l become matrix-valued functions, too. Since the subsequent discussion applies to arbitrary angular momenta, we drop the subscript and write T instead of t_l. Explicitly, we then have

$$\begin{aligned} T \,:\, \mathbb{C} &\to \mathrm{mat}_{\mathbb{C}}(n, n), \\ s &\mapsto T(s)\,. \end{aligned} \tag{2.6}$$

Here $n \in \mathbb{N}$ is the number of different channels under consideration, each entry $T_{fi}(s)$ corresponds to a specific particle content in the initial state i and final state f, and s denotes the usual Mandelstam variable.

Such an amplitude T has several interesting properties. First, it can be analytically continued to general complex values of s, in fact, it is holomorphic in s except for branch points, all of which are associated with thresholds of multi-particle intermediate states, and poles, associated with bound states. Such thresholds in the s channel lead to branch points on the positive real axis in the s plane, to which we attach branch cuts extending along this axis towards infinity, so called right-hand cuts. The impact of thresholds in the t and u channel on the analytic structure is convoluted due to the partial-wave projection. Often, the associated branch points are located at real values below the

lowest s-channel threshold, the associated cuts are located in the left half of the complex s plane, and thus they are known as left-hand cuts. The poles—if there are any—lie on the positive real axis below the lowest s-channel threshold. The function can be continued onto other RIEMANN sheets, as explicitly shown in Sec. 2.2. On these sheets there might be poles, which correspond to resonances. It should be stressed that these poles are the sole universal approach to extract resonance properties. Other methods, e.g., reading off properties from the cross section via a BREIT–WIGNER parametrization, yield results that often depend on the process in which the resonance appears, moreover, as soon as two or more resonances are nearby, or if there is a threshold in the neighborhood of the resonance, or the resonance pole is deep in the complex plane, such approaches fail completely [9].

Furthermore, T fulfills the SCHWARZ reflection principle,

$$T(s^*) = T(s)^* \tag{2.7}$$

for all values of s except those lying on branch cuts, in addition, it obeys a unitarity relation of the form

$$\mathrm{Im}\,(T) = T\sigma T^* \tag{2.8}$$

for values of s along the right-hand cut(s). Here the phase space σ is a function $\mathbb{C} \to \mathrm{mat}_{\mathbb{C}}(n,n)$, too. Equation (2.8) is a direct consequence of the unitarity of the S matrix.

In Sec. 2.1 the constraints put on the scattering amplitude by unitarity are made explicit via the K matrix. Subsequently, in Sec. 2.2 the analytic continuation to other RIEMANN sheets is discussed. Later, building on top of the K matrix, in Sec. 4.2 we introduce the IAM.

2.1 K matrix

Multiplying Eq. (2.8) from the left by T^{-1} and from the right by $(T^*)^{-1}$ yields

$$\begin{aligned}
\sigma &= T^{-1}\mathrm{Im}\,(T)\,(T^*)^{-1} \\
&= T^{-1}\frac{1}{2i}\left[T - T^*\right](T^*)^{-1} \\
&= \frac{1}{2i}\left[(T^*)^{-1} - T^{-1}\right] \\
&= \frac{1}{2i}\left[\left(T^{-1}\right)^* - T^{-1}\right] \\
&= -\mathrm{Im}\left(T^{-1}\right).
\end{aligned} \tag{2.9}$$

Hence,

$$\begin{aligned}
T^{-1} &= \mathrm{Re}\left(T^{-1}\right) + i\,\mathrm{Im}\left(T^{-1}\right) \\
&= \mathrm{Re}\left(T^{-1}\right) - i\sigma.
\end{aligned} \tag{2.10}$$

That is,

$$T = \left[K - i\sigma\right]^{-1}, \qquad K \coloneqq \mathrm{Re}\left(T^{-1}\right). \tag{2.11}$$

This is the general K-matrix[2] representation of T [133]. Along the right-hand cut(s), where Eq. (2.8) is valid, Eq. (2.11) holds. That is, all parametrizations for T that fulfill unitarity need to be of the form (2.11) (along the right-hand cut(s)).

[2]Often, in the literature, what we denote as K is called K^{-1}, see, for example, Eq. (5) in Ref. [39] (Eq. (6) in the `arXiv` version).

On the other hand, given a specific K-matrix parametrization along the right-hand cut(s), if the given parametrization of K is in fact holomorphic in some domain, it is possible to analytically continue this parametrization to the complex plane simply by promoting s to a complex instead of a real variable. In this case, the Schwarz reflection principle constrains K and σ. Namely, equating

$$T(s)^* = \left[K(s)^* + i\sigma(s)^*\right]^{-1} \tag{2.12}$$

with

$$T(s^*) = \left[K(s^*) - i\sigma(s^*)\right]^{-1} \tag{2.13}$$

yields

$$K(s)^* + i\sigma(s)^* = K(s^*) - i\sigma(s^*)\,, \tag{2.14}$$

which is fulfilled if

$$K(s^*) = K(s)^*\,, \qquad \sigma(s^*) = -\sigma(s)^*\,. \tag{2.15}$$

In the derivation of Eq. (2.27) it is shown that this constraint on σ is also required such that the analytic continuation of T to other Riemann sheets fulfills the Schwarz reflection principle.

As a special case, restrict the kinematics, such that only one channel is accessible. In this scenario, the unitarity relation (2.8) reads

$$\mathrm{Im}\,(T) = \sigma |T|^2 \tag{2.16}$$

and the K-matrix representation (2.11) boils down to

$$T = \frac{1}{K - i\sigma}. \tag{2.17}$$

In this case, the K matrix can be expressed via the argument (i.e., the phase) of T, using:

$$\begin{aligned} \cot\left[\arg\left(T\right)\right] &= \cot\left[-\arg\left(\frac{1}{T}\right)\right] \\ &= -\cot\left[\arg\left(\frac{1}{T}\right)\right] \\ &= -\frac{\mathrm{Re}\left(T^{-1}\right)}{\mathrm{Im}\left(T^{-1}\right)} \\ &= \frac{K}{\sigma}. \end{aligned} \tag{2.18}$$

That is, $K = \sigma\cot(\delta)$ with $\delta := \arg(T)$, and therefore

$$T = \frac{1}{\sigma}\frac{1}{\cot\left(\delta\right) - i} = \frac{1}{\sigma}\sin\left(\delta\right)e^{i\delta}. \tag{2.19}$$

If a given expression for $\cot(\delta)$ allows for a continuation into the complex plane simply by making s complex, according to Eq. (2.15) it needs to fulfill $\cot[\delta(s^*)] = -\cot[\delta(s)]^*$.

Often, the Chew–Mandelstam phase space [134] $I(s)$ with $\mathrm{Im}(I) = -\sigma$ along the right-hand cut is used in connection with the K-matrix representation. That is,

$$T = \frac{1}{\widetilde{K} + I} = \frac{1}{K - i\sigma}, \qquad \widetilde{K} := K - \mathrm{Re}\left(I\right). \tag{2.20}$$

2.2 Riemann sheets and resonance poles

To continue the matrix-valued amplitude T to other Riemann sheets (to search for resonance poles), the Schwarz reflection principle (2.7) comes in handy. Consider two Riemann sheets A and B that are connected along a cut along (a subset of) the positive real axis. To be precise, the amplitude T^A on sheet A and the amplitude T^B on sheet B are related via $T^A(s_+) = T^B(s_-)$. Here $s_\pm := s \pm i\epsilon$ with s a real number along the cut, $\epsilon > 0$, and a limit $\epsilon \searrow 0$ is implicit. Choose now $A = \mathrm{I}$, i.e., A is the physical sheet. Here unitarity in the form of Eq. (2.8) holds along the positive real axis if approached from above, i.e.,

$$T^{\mathrm{I}}(s_+)\,\sigma(s_+)\left[T^{\mathrm{I}}(s_+)\right]^* = \mathrm{Im}\left[T^{\mathrm{I}}(s_+)\right] = \frac{1}{2i}\left[T^{\mathrm{I}}(s_+) - T^{\mathrm{I}}(s_-)\right]. \tag{2.21}$$

That is,

$$T^B(s_-) - T^{\mathrm{I}}(s_-) = 2iT^B(s_-)\,\sigma(s_+)\,T^{\mathrm{I}}(s_-), \tag{2.22}$$

yielding

$$T^B(s_-) = T^{\mathrm{I}}(s_-)\left[1 - 2i\sigma(s_+)\,T^{\mathrm{I}}(s_-)\right]^{-1}. \tag{2.23}$$

It is crucial to note that in the derivation of Eq. (2.23) $T^{\mathrm{I}}(s_+) = T^B(s_-)$ was used, for the naive opposite relation $T^{\mathrm{I}}(s_-) = T^B(s_+)$ holds for arbitrary B only if there is only one branch point, i.e., in the single-channel case. To make full use of Eq. (2.23), it needs to be analytically continued into the complex plane, where resonance poles are located. To that end it is first necessary to continue $\sigma(s_+)$ above the cut to obtain its value at s_-. This continuation depends on the nearest branch point under consideration. For example, if σ is given along the postive real axis on the physical sheet as

$$\sigma(s) = \begin{pmatrix} \theta\left(s-4m^2\right)\sqrt{1-\frac{4m^2}{s}} & 0 \\ 0 & \theta\left(s-4M^2\right)\sqrt{1-\frac{4M^2}{s}} \end{pmatrix} \tag{2.24}$$

with $M > m > 0$, there are four sheets. For instance, the one connected to the physical sheet along the real axis between $4m^2$ and $4M^2$ is reached by considering only

$$\sigma^{\mathrm{II}}(s) = \begin{pmatrix} \sqrt{1-\frac{4m^2}{s}} & 0 \\ 0 & 0 \end{pmatrix}. \tag{2.25}$$

In either case, the continuation is performed such that $\sigma(s^*) = -\sigma(s)^*$, for in this way the Schwarz reflection principle holds also on the other sheets. Thus,

$$T^B(s_-) = T^{\mathrm{I}}(s_-)\left[1 + 2i\sigma^B(s_-)\,T^{\mathrm{I}}(s_-)\right]^{-1}. \tag{2.26}$$

Since the right hand side of Eq. (2.26) is holomorphic in s, via uniqueness of analytic continuation

$$T^B(s) = T^{\mathrm{I}}(s)\left[1 + 2i\sigma^B(s)\,T^{\mathrm{I}}(s)\right]^{-1}. \tag{2.27}$$

is obtained.

If instead the amplitude on the first sheet is reconstructed from the one on sheet B, Eq. (2.27) can be rearranged into

$$T^{\mathrm{I}}(s) = \left[1 - 2iT^B(s)\,\sigma^B(s)\right]^{-1} T^B(s). \tag{2.28}$$

To make the impact of the constraint $\sigma(s^*) = -\sigma(s)^*$ more explicit, consider the simple case of single-channel $\pi\pi$ scattering with phase space

$$\sigma(s) = \sqrt{1 - \frac{4M_\pi^2}{s}}, \tag{2.29}$$

M_π being the pion mass. For this to fulfill the aforementioned constraint, the branch cut of the square root needs to be aligned with the positive real axis. This can be achieved by replacing $\sqrt{\cdot}$ by $\text{sign}(\text{Im}(\cdot))\sqrt{\cdot}$, with $\sqrt{\cdot}$ having the cut along the negative real axis, as in many programming languages.[3]

A resonance is a pole on an unphysical Riemann sheet B off the real axis, that is, it corresponds to a value s_{pole} such that $|T^B|$ approaches infinity at s_{pole}. The real and imaginary part of s_{pole} determine the mass M and width Γ of the resonance via

$$s_{\text{pole}} =: \left(M \pm \frac{i}{2}\Gamma\right)^2. \tag{2.30}$$

Note that due to the Schwarz reflection principle such poles appear as complex-conjugated pairs, as indicated by the two signs in front of the width. Furthermore, the couplings are defined via the residue at the pole according to

$$g_a g_b := -16\pi \frac{2J+1}{\left(2p\left(s_{\text{pole}}\right)\right)^{2J}} \operatorname{res}\left(T^B_{ab}, s_{\text{pole}}\right). \tag{2.31}$$

Here J is the angular momentum quantum number of the partial wave T under consideration (which in turn defines the angular momentum of the resonance), p is the momentum in the CM system, and a (b) labels the row (column) of T^B, which correspond to multi-particle channels. Hence, g_a is the coupling of the resonance to channel a, while g_b is the one to channel b.

In general, according to Eq. (2.27) the poles of T^B are given as solutions of

$$0 = \det\left[1 + 2i\sigma^B(s)\, T^{\text{I}}(s)\right]. \tag{2.32}$$

This condition implies that the inverse in Eq. (2.27) does not exist at the poles, in addition, it implies $0 \neq T^{\text{I}}(s)$, in this way assuring that there is no cancellation due to a simultaneous zero in the numerator of T^B.

If there is only one channel of interest (i.e., one combination of in- and out-states), Eq. (2.31) collapses to

$$g^2 = -16\pi \frac{2J+1}{\left(2p\left(s_{\text{pole}}\right)\right)^{2J}} \operatorname{res}\left(T^{\text{II}}, s_{\text{pole}}\right) \tag{2.33}$$

and Eq. (2.32) simplifies to

$$0 = 1 + 2i\sigma(s)\, T^{\text{I}}(s). \tag{2.34}$$

Using this, an easy way to calculate the residue and the coupling g can be derived: abbreviating the denominator of T^{II} as

$$d(s) := 1 + 2i\sigma(s)\, T^{\text{I}}(s) \tag{2.35}$$

[3]Note that due to the presence of the cut $\sigma(s^*) = -\sigma(s)^*$ does not imply $\text{Re}[\sigma(s)] = 0$ if $s \in [4M_\pi^2, \infty)$.

and expanding it around s_{pole} yields[4]

$$\begin{aligned}
\operatorname{res}\left(T^{\text{II}}, s_{\text{pole}}\right) &= \lim_{s\to s_{\text{pole}}} \left(s - s_{\text{pole}}\right) T^{\text{II}}(s) \\
&= \lim_{s\to s_{\text{pole}}} \left(s - s_{\text{pole}}\right) \frac{T^{\text{I}}(s)}{d(s)} \\
&= \lim_{s\to s_{\text{pole}}} \left(s - s_{\text{pole}}\right) \frac{T^{\text{I}}(s)}{d\left(s_{\text{pole}}\right) + d'\left(s_{\text{pole}}\right)\left(s - s_{\text{pole}}\right) + O\left(\left(s - s_{\text{pole}}\right)^2\right)} \\
&= \lim_{s\to s_{\text{pole}}} \frac{T^{\text{I}}(s)}{d'\left(s_{\text{pole}}\right) + O\left(s - s_{\text{pole}}\right)} \\
&= \frac{T^{\text{I}}\left(s_{\text{pole}}\right)}{d'\left(s_{\text{pole}}\right)},
\end{aligned} \tag{2.36}$$

where $d'(s) = \mathrm{d}\, d(s)/\mathrm{d}s$.

[4]Here we assume that the pole is of single order. While this assumption holds true for all scenarios of relevance to this work, there exists the possibility of higher-order resonance poles. The possibility of such poles is discussed in some detail in Ref. [135].

Chapter 3

Scattering of two particles on the lattice

The computation of scattering via lattice QCD is a challenging problem. From a conceptual point of view, the challenge lies in the fact that there is no direct way to simulate a scattering process on the lattice, because the Euclidean spacetime and finite volume do not match the scenario of continuum scattering theory, namely a Minkowski spacetime of infinite extent. Instead, one has to resort to indirect methods, which turn a supposed weakness of the lattice—the finite volume—into a tool, by carefully investigating the impact of the finite volume on observables. In Sec. 3.1 we give a very superfical reminder of the basic aspects of lattice QCD that are relevant to understand the subsequent discussion of the indirect approach towards scattering, whose derivation is presented in detail in Sec. 3.2. This discussion allows us to understand why the computations are often carried out at unphysically high quark masses, see Sec. 3.3. There we also clarify the relation between the pion mass and quark masses and explain, why we often use the terms pion-mass dependence and quark-mass dependence interchangeably. We conclude with a brief discussion of rotational symmetry on the lattice in Sec. 3.4.

3.1 Correlation functions in lattice QCD

In QCD—as in any QFT—the relevant information is contained in correlation functions, which are of the form

$$\begin{aligned}&\langle 0|\mathcal{T}\left\{O_1\left(A,\overline{\psi},\psi\right)O_2\left(A,\overline{\psi},\psi\right)\cdots O_N\left(A,\overline{\psi},\psi\right)\right\}|0\rangle\\&\quad=\frac{\int \mathrm{D}A\,\mathrm{D}\overline{\psi}\mathrm{D}\psi O_1\left(A,\overline{\psi},\psi\right)O_2\left(A,\overline{\psi},\psi\right)\cdots O_N\left(A,\overline{\psi},\psi\right)\exp\left[iS\left[A,\overline{\psi},\psi\right]\right]}{\int \mathrm{D}A\,\mathrm{D}\overline{\psi}\mathrm{D}\psi\exp\left[iS\left[A,\overline{\psi},\psi\right]\right]}.\end{aligned}\tag{3.1}$$

Here $\mathcal{T}$ denotes the time-ordered product, $|0\rangle$ the vacuum, A the gluon fields, ψ and $\overline{\psi}$ the quark fields, and S the action. In addition, $O_1,\ldots,O_N$ are operators depending on the fundamental fields. In lattice QCD, Eq. (3.1) is analytically continued into Euclidean spacetime, as a result $\exp(iS)$ is replaced by $\exp(-S^{\text{Euclid}})$, with S^{Euclid} the Euclidean action. Subsequently, the theory is put into a finite volume and discretized [17, 18].

To be precise, we introduce the lattice with volume $T\times L^3$. Here $T=aT^{\text{lat}}$ is the temporal extent of the lattice, with $T^{\text{lat}}\in\mathbb{N}$ the number of sites along the temporal direction and a the lattice spacing, i.e., the temporal distance between two adjacent lattice sites. The spatial extent L is defined analogously, that is, $L=a_{\text{s}}L^{\text{lat}}$ with $L^{\text{lat}}\in\mathbb{N}$ and a_{s} the distance in one spatial direction between two adjacent sites. The latter is related to the lattice spacing via the anisotropy $\xi:=a_{\text{s}}/a$,

i.e., $a_s = \xi a$. Accordingly, the lattice contains $T^{\text{lat}} \times (L^{\text{lat}})^3$ sites. It is this lattice that replaces the infinite volume EUCLIDean spacetime.

Since S^{EUCLID} is real, $\exp(-S^{\text{lat}})$ can be interpreted as a (non-normalized) probability density. Accordingly, the path integral can be computed by Monte-Carlo techniques. To that end, samples corresponding to different values of the gluonic fields are drawn from a probability distribution that is derived from $\exp(-S^{\text{lat}})$, these samples are called gauge configurations. Correlation functions of a given set of operators can subsequently be computed by evaluating the operators on all different gauge configurations and averaging the result.

The computation of a correlation function in this way is in general costly from a numerical perspective. Hence, to assess the statistical error associated with the finiteness of the number of gauge configurations, it is not feasible to perform the computation again and again. Instead, the gauge configurations are computed once only, subsequently, bootstrap (or jackknife) samples are generated from the configurations. The operators under consideration can then be re-evaluated on each bootstrap sample, yielding multiple different values of the correlation function at hand. Using the resulting set of values, statistical quantities, e.g., variances, can be estimate in the standard way [136].

On the lattice all quantities are expressed in terms of lattice units. To that end, each quantity is multiplied with the appropriate power of the lattice spacing to render it dimensionless, e.g., $M_\pi^{\text{lat}} = aM_\pi$. The exception is the spatial lattice length L^{lat} that is given in terms of a_s, as described above. Throughout this thesis, all powers of a and a_s are displayed explicitly and quantities determined on the lattice are often indicated via a superscript $^{\text{lat}}$.

3.2 LÜSCHER formalism and extensions

The indirect approach to scattering is based on the following observation: what one can compute on the lattice in an at least conceptually straightforward manner are energy levels corresponding to single- and multi-particle states. These energy levels are shifted with respect to their continuum counterparts due to the finite spatial extent of the lattice. There are two different kinds of shifts. First, those that scale like $\exp(-M_\pi L)$, which are undesirable but fortunately exponentially suppressed. Hence, via working with lattices that yield large values of $M_\pi L$, these shifts can be rendered small. Second, those that scale like polynomials of $1/L$. As shown explicitly first by LÜSCHER in Refs. [137, 138] in a field theoretic context, these polynomial shifts of two-particle energy levels are related to scattering length and phases via certain quantization conditions. A few years later he extended the quantization conditions in Ref. [139]. While the core part of his derivation presented ibidem—albeit being technically challenging—rests solely on non-relativistic quantum mechanics, nowadays it is more custom to derive the quantization conditions via the methods of EFT [140], a derivation that is in its gist similar to the original one in Ref. [138]. This is because the field theoretic approach allows for an extension of the quantization conditions in different contexts: different kinematic settings [140], coupled channels [141], external currents [40], and more particles [142]. For a review of this formalism in the context of two-particle scattering, see Ref. [39].

Here, we pedagogically discuss the detailed field-theoretic derivation of the quantization conditions for both $\pi\pi \to \pi\pi$ and $\gamma^{(*)}\pi \to \pi\pi$. To that end, we work in continuous (i.e., non-discretized) MINKOWSKI space with a finite spatial, but infinite temporal extent. This differs considerably from the scenario encountered in lattice-QCD computations as discussed in Sec. 3.1. Nevertheless, the results obtained in the finite-volume MINKOWSKI space can be carried over to the lattice, for it is precisely the effect of the finite volume that is at the heart of LÜSCHER's method. The discretiza-

tion yields artifacts that need to be treated separately, while the finite temporal extent amounts to a finite temperature, again a different effect than the one we are interested in. Moreover, the final results, Eq. (3.73) and Eq. (3.112), require as input only quantities that can be computed in EUCLIDean spacetime, namely energy levels and the matrix element on the left-hand side of Eq. (3.112). Alternatively, in the following we could replace the correlation functions in MINKOWSKI spacetime by the appropriate analytically continued EUCLIDean correlation functions, which would however render the notation less convenient.

3.2.1 Kinematics

In the following, we consider the scattering process $\pi\pi \to \pi\pi$. First, consider an arbitrary frame (called the lab frame), in which the total momentum of the two pions is $\boldsymbol{P}$, which is also called the boost momentum. That is, one pion has four-momentum $k = (\omega_k, \boldsymbol{k})$, with $\omega_k = \sqrt{|\boldsymbol{k}|^2 + M_\pi^2}$ its energy, while the other has four-momentum $k' = (\omega_{P-k}, \boldsymbol{P}-\boldsymbol{k})$, with energy $\omega_{P-k} = \sqrt{|\boldsymbol{P}-\boldsymbol{k}|^2 + M_\pi^2}$. Hence, the total energy is $E = \omega_k + \omega_{P-k}$ and the total four-momentum reads $P = (E, \boldsymbol{P})$. We might pick a cartesian coordinate system of $\mathbb{R}^3$ such that the first basis vector points into the direction of $\boldsymbol{P}$, i.e., it is given as $\boldsymbol{P}/|\boldsymbol{P}| =: \boldsymbol{e}_P$. In this basis, an arbitrary vector $\boldsymbol{v}$ looks like $\boldsymbol{v} = (v_\parallel, \tilde{v}_\perp)$ with $v_\parallel \in \mathbb{R}$ the component in the direction of $\boldsymbol{P}$ and $\tilde{v}_\perp$ the remaining components. More precisely, these are defined via

$$v_\parallel = \boldsymbol{v} \cdot \boldsymbol{e}_P, \qquad \boldsymbol{v}_\perp = \begin{pmatrix} 0 \\ \tilde{v}_\perp \end{pmatrix} = \boldsymbol{v} - v_\parallel \boldsymbol{e}_P. \tag{3.2}$$

Accordingly, in this basis the total momentum $\boldsymbol{P}$ reads $\boldsymbol{P} = (|\boldsymbol{P}|, \tilde{0})$. Hence, $\tilde{k}_\perp + \tilde{k}'_\perp = \tilde{0}$ and $k_\parallel + k'_\parallel = |\boldsymbol{P}|$.

Now consider the CM frame. As before, all quantities in this frame are denoted by a star as a superscript. By definition, $\boldsymbol{P}^\star = 0$. We want to find a LORENTZ transformation Λ that connects the two frames, i.e., $P^\star = \Lambda P$ or, more verbose,

$$\begin{pmatrix} E^\star \\ \boldsymbol{0} \end{pmatrix} = \Lambda \begin{pmatrix} E \\ |\boldsymbol{P}| \\ \tilde{0} \end{pmatrix}. \tag{3.3}$$

Clearly, it is sufficient to focus on the subspace corresponding to the first two components, that is, $\Lambda = \Lambda_2 \oplus \mathbb{1}_2$. Inserting the general form of a LORENTZ boost with rapidity ζ for Λ_2 results in

$$\begin{pmatrix} E^\star \\ 0 \end{pmatrix} = \begin{pmatrix} \cosh\zeta & -\sinh\zeta \\ -\sinh\zeta & \cosh\zeta \end{pmatrix} \begin{pmatrix} E \\ |\boldsymbol{P}| \end{pmatrix} = \gamma \begin{pmatrix} 1 & -\beta \\ -\beta & 1 \end{pmatrix} \begin{pmatrix} E \\ |\boldsymbol{P}| \end{pmatrix} \tag{3.4}$$

with the LORENTZ factor $\gamma = \cosh\zeta$ as well as $\beta = \tanh\zeta$. Multiplying this out yields

$$\beta = \frac{|\boldsymbol{P}|}{E}, \qquad \gamma = \frac{E}{E^\star}, \qquad (E^\star)^2 = E^2 - |\boldsymbol{P}|^2. \tag{3.5}$$

More generally, applying Λ to an arbitrary four-vector $v = (v^0, v_\parallel, \tilde{v}_\perp)$ we obtain $v^\star = \Lambda v$ with components

$$v^{\star 0} = \gamma\left(v^0 - \beta v_\parallel\right), \qquad v_\parallel^\star = \gamma\left(v_\parallel - \beta v^0\right), \qquad \tilde{v}_\perp^\star = \tilde{v}_\perp. \tag{3.6}$$

Using Eq. (3.6) $\boldsymbol{k}^\star + \boldsymbol{k}'^\star = 0$ follows, as expected. This implies $\omega_k^\star = \omega_{P-k}^\star$, since $k^2 = (k')^2 = M_\pi^2$ and Λ is an isometry of the MINKOWSKI product. From Eq. (3.4) it follows that the inverse of Λ_2 can be obtained by replacing β by $-\beta$, and thus the inverse of Eq. (3.6) reads

$$v^0 = \gamma\left(v^{\star 0} + \beta v_\parallel^\star\right), \qquad v_\parallel = \gamma\left(v_\parallel^\star + \beta v^{\star 0}\right), \qquad \tilde{v}_\perp = \tilde{v}_\perp^\star, \tag{3.7}$$

as can be easily verified explicitly by using $\gamma^{-2} = 1 - \beta^2$. It is customary to use the LORENTZ invariant MANDELSTAM variable $s = (k + k')^2 = (k^\star + k'^\star)^2 = (E^\star)^2$, see Ch. 2, as well as $q^\star = |\boldsymbol{k}^\star|$ such that $E^\star = 2\sqrt{M_\pi^2 + q^{\star 2}}$.

3.2.2 Angular-momentum basis

Consider a function $f : \mathbb{R}^3 \to \mathbb{C}$. In spherical polar coordinates, i.e., $\boldsymbol{r} = (|\boldsymbol{r}|, \theta, \phi)$, f can be decomposed using the spherical harmonics Y_{lm} according to

$$f(\boldsymbol{r}) = \sum_{l=0}^{\infty} \sum_{m=-l}^{l} f_{lm}(|\boldsymbol{r}|) \sqrt{4\pi} Y_{lm}(\theta, \phi). \tag{3.8}$$

Since the spherical harmonics are orthogonal, that is,

$$\int \mathrm{d}\Omega\, Y_{lm}^*(\theta, \phi)\, Y_{l'm'}(\theta, \phi) = \delta_{ll'}\delta_{mm'}, \tag{3.9}$$

the coefficients f_{lm} are given as

$$f_{lm}(|\boldsymbol{r}|) = \frac{1}{\sqrt{4\pi}} \int \mathrm{d}\Omega\, Y_{lm}^*(\theta, \phi)\, f(\boldsymbol{r}). \tag{3.10}$$

This decomposition is possible because the spherical harmonics constitute a basis for all smooth, $\mathbb{C}$-valued functions defined on of a two-dimensional sphere. So do their complex conjugates, so that an alternative decomposition reads

$$\begin{aligned} f(\boldsymbol{r}) &= \sum_{l=0}^{\infty} \sum_{m=-l}^{l} \tilde{f}_{lm}(|\boldsymbol{r}|) \sqrt{4\pi} Y_{lm}^*(\theta, \phi), \\ \tilde{f}_{lm}(|\boldsymbol{r}|) &= \frac{1}{\sqrt{4\pi}} \int \mathrm{d}\Omega\, Y_{lm}(\theta, \phi)\, f(\boldsymbol{r}). \end{aligned} \tag{3.11}$$

We stress that the factor $\sqrt{4\pi}$ in Eq. (3.8) is purely conventional (in fact, it can be replaced by an arbitrary function of $|\boldsymbol{r}|$, resulting merely in a re-definition of f_{lm}). It is chosen such that $\sqrt{4\pi} Y_{00}(\theta, \phi) = 1$.

These statements can be generalized to functions of several variables. Let $h : \mathbb{R}^3 \times \mathbb{R}^3 \to \mathbb{C}$ be a smooth function. Applying Eq. (3.8) to the first argument and Eq. (3.11) to the second yields

$$\begin{aligned} h(\boldsymbol{r}, \boldsymbol{r}') &= 4\pi Y_{lm}(\theta, \phi)\, h_{lml'm'}\left(|\boldsymbol{r}|, |\boldsymbol{r}|'\right) Y_{l'm'}^*(\theta', \phi'), \\ h_{lml'm'}\left(|\boldsymbol{r}|, |\boldsymbol{r}|'\right) &= \frac{1}{4\pi} \int \mathrm{d}\Omega \int \mathrm{d}\Omega'\, Y_{lm}^*(\theta, \phi)\, Y_{l'm'}(\theta', \phi')\, h(\boldsymbol{r}, \boldsymbol{r}'), \end{aligned} \tag{3.12}$$

with a summation about repeated indices implicit.

It is instructive to apply this decomposition to the $\pi\pi \to \pi\pi$ scattering amplitude $\mathscr{M}$ for fixed total isospin. In the CM frame, according to Eq. (2.3) its decomposition into partial waves t_l reads

$$\mathscr{M}(s, \cos\theta^\star) = 32\pi \sum_{l=0}^{\infty} t_l(s)\,(2l+1)\,P_l(\cos\theta^\star)\,. \tag{3.13}$$

Here P_l denotes the l-th Legendre polynomial and $\theta^\star$ the scattering angle, i.e., $|\boldsymbol{k}^\star|\,|\boldsymbol{k}'^\star|\cos\theta^\star = \boldsymbol{k}^\star \cdot \boldsymbol{k}'^\star$ with $\boldsymbol{k}^\star$ the momentum of an ingoing pion and $\boldsymbol{k}'^\star$ the momentum of an outgoing pion. Using

$$P_l\!\left(\frac{\boldsymbol{k}^\star}{|\boldsymbol{k}^\star|}\cdot\frac{\boldsymbol{k}'^\star}{|\boldsymbol{k}'^\star|}\right) = \frac{4\pi}{2l+1}\sum_{m=-l}^{m=l} Y_{lm}\left(\Omega_k^\star\right) Y_{lm}^*\left(\Omega_{k'}^\star\right), \tag{3.14}$$

with $\Omega_r = (\theta_r, \phi_r)$ the angular components of the vector $\boldsymbol{r}$, we obtain

$$\begin{aligned}
\mathscr{M}(s, \cos\theta^\star) &= 4\pi \sum_{l=0}^{\infty}\sum_{m=-l}^{m=l} 32\pi\, t_l(s)\, Y_{lm}\left(\Omega_k^\star\right) Y_{lm}^*\left(\Omega_{k'}^\star\right) \\
&= 4\pi\, Y_{lm}\left(\Omega_k^\star\right) \mathscr{M}_{lml'm'}(s)\, Y_{l'm'}^*\left(\Omega_{k'}^\star\right), \\
\mathscr{M}_{lml'm'}(s) &= 32\pi\,\delta_{ll'}\delta_{mm'} t_l(s)\,,
\end{aligned} \tag{3.15}$$

which is the decomposition (3.12) applied in this specific context.

For future use, it is convenient to define homogeneous polynomials $\mathscr{Y}_{lm}$ via

$$\mathscr{Y}_{lm}(\boldsymbol{r}) \coloneqq |\boldsymbol{r}|^l\, Y_{lm}(\Omega_r)\,. \tag{3.16}$$

3.2.3 Finite-volume Minkowski space

In the following we will work in finite-volume four-dimensional Minkowski space denoted by $\mathbb{M}_L$. To be precise, we consider a Minkowski space of infinite time extent, but confined to a spatial box of volume L^3. That is, $x^i \in [0, L]$ for $i = 1, 2, 3$. Hence, $\mathbb{M}_L$ can be decomposed into $\mathbb{M}_L = \mathbb{R} \times \mathbb{L}$ with $\mathbb{L} \coloneqq [0, L]^3$. Furthermore, we require periodic boundary conditions, i.e., we identify $x^i = L$ with $x^i = 0$. Thus $\mathbb{L}$, the spatial part of $\mathbb{M}_L$, is in fact a three-dimensional torus. Given that the spatial part of the eigenfunctions of the momentum operator reads $e^{i\boldsymbol{x}\cdot\boldsymbol{p}}$, this enforces $\boldsymbol{p} \in \mathbb{Z}_L^3$ with $\mathbb{Z}_L \coloneqq \{n2\pi/L : n \in \mathbb{Z}\}$: the components of all momenta are integer multiples of $2\pi/L$. Accordingly, momentum integrals are replaced by sums,

$$\int \frac{\mathrm{d}^3 p}{(2\pi)^3} \to \frac{1}{L^3}\sum_{\boldsymbol{p}\in\mathbb{Z}_L^3}. \tag{3.17}$$

The Poisson summation formula, given in Eq. (3.31) and discussed in detail in Sec. 3.2.4, shows that the sum on the right-hand side of Eq. (3.17) is indeed equal to the integral on the left-hand side if the limit $L \to \infty$ is performed (and the integrand is non-singular).

We denote integer vectors using Fraktur. In this way, we can write each momentum $\boldsymbol{p}$ as

$$\boldsymbol{p} = \frac{2\pi}{L}\mathfrak{p} \tag{3.18}$$

with $\mathfrak{p} \in \mathbb{Z}^3$. This motivates us to introduce

$$\delta_{\boldsymbol{pq}} \equiv \delta_{\mathfrak{pq}} \coloneqq \prod_{j=1}^{3}\delta_{\mathfrak{p}^j\mathfrak{q}^j} = \frac{1}{L^3}\int_{\mathbb{L}} \mathrm{d}^3x\, e^{i\boldsymbol{x}\cdot(\boldsymbol{p}-\boldsymbol{q})}, \tag{3.19}$$

where the last equality can be proven by directly computing the integral. This definition is naturally accompanied by

$$\delta_L^{(3)}(\boldsymbol{x}) \coloneqq \frac{1}{L^3} \sum_{\boldsymbol{p} \in \mathbb{Z}_L^3} e^{i\boldsymbol{p}\cdot\boldsymbol{x}} = \sum_{\mathfrak{n} \in \mathbb{Z}^3} \delta^{(3)}(\boldsymbol{x} - L\mathfrak{n}) \,. \tag{3.20}$$

Here the last equality arises from the use of the Poisson summation formula, compare Eq. (3.28). If we restrict our attention to $0 \leq x^i < L$, $i = 1, 2, 3$, only the $\mathfrak{n} = 0$ term on the right-hand side of Eq. (3.20) is of relevance, resulting in $\delta_L^{(3)}(\boldsymbol{x}) = \delta^{(3)}(\boldsymbol{x})$. Consider now a function $f : \mathbb{L} \to \mathbb{C}$. We define its Fourier transform as

$$\mathscr{F}[f](\boldsymbol{p}) \coloneqq \int_{\mathbb{L}} \mathrm{d}^3 x \, e^{-i\boldsymbol{p}\cdot\boldsymbol{x}} f(\boldsymbol{x}) \,. \tag{3.21}$$

Conversely, let $g : \mathbb{Z}_L^3 \to \mathbb{C}$ be a function defined in momentum space. Its Fourier transform reads

$$\mathscr{F}^{-1}[g](\boldsymbol{x}) \coloneqq \frac{1}{L^3} \sum_{\boldsymbol{p} \in \mathbb{Z}_L^3} e^{i\boldsymbol{p}\cdot\boldsymbol{x}} g(\boldsymbol{p}) \,. \tag{3.22}$$

One may use Eq. (3.19) and Eq. (3.20) to check that Eq. (3.21) and Eq. (3.22) are indeed mutually inverse.

Lastly, consider the spectrum of the Hamilton operator in the finite volume. Since momenta are discretized, the spectrum is discrete, too. We denote the eigenstates of the Hamiltonian by $|E_n, \boldsymbol{p}; L\rangle$ with E_n the corresponding energy (that might depend on both L and $\boldsymbol{p}$). Those states are normalized according to

$$\langle E_n, \boldsymbol{p}; L \,|\, E_m, \boldsymbol{q}; L\rangle = \delta_{nm}\delta_{\boldsymbol{pq}}, \tag{3.23}$$

with $\delta_{\boldsymbol{pq}}$ given by Eq. (3.19).

3.2.4 Loops in finite volume

In the following[1], we relate a loop integral in infinite volume to the one in finite volume. This relation is of great importance in the subsequent derivation of the quantization conditions. Consider a one-loop integral in infinite-volume Minkowski space, namely

$$I_{\mathrm{IV}}(P) \coloneqq \int \frac{\mathrm{d}^4 k}{(2\pi)^4} \frac{f(k)}{\left[k^2 - M_\pi^2 + i\epsilon\right]\left[(P-k)^2 - M_\pi^2 + i\epsilon\right]}, \tag{3.24}$$

with f a non-singular, but otherwise almost arbitrary complex-valued function, except for the requirement that its asymptotic behaviour is such that the integral converges. Now consider the same theory, but with the ordinary Minkowski space replaced by $\mathbb{M}_L$. Accordingly, Eq. (3.24) is replaced by

$$I_{\mathrm{FV}}(P, L) \coloneqq \frac{1}{L^3} \sum_{\boldsymbol{k} \in \mathbb{Z}_L^3} \int \frac{\mathrm{d}k^0}{2\pi} \frac{f(k)}{\left[k^2 - M_\pi^2 + i\epsilon\right]\left[(P-k)^2 - M_\pi^2 + i\epsilon\right]}. \tag{3.25}$$

It is important to realize that the sum runs over momenta in the lab frame, i.e., the frame that does not move with respect to the spatial cube, for only in this frame the components of the three-momenta are constrained in such an simple way. The goal of this section is to derive an expression for $D \coloneqq I_{\mathrm{FV}} - I_{\mathrm{IV}}$.

[1] The discussion in this section closely follows Ref. [140].

Since f is non-singular, the only poles in the integrand of I_{FV} arise from its denominator. To render those poles more explicit, we decompose the denominator to obtain

$$I_{\mathrm{FV}}(P,L) = \frac{1}{L^3}\sum_{\boldsymbol{k}\in\mathbb{Z}_L^3}\int\frac{\mathrm{d}k^0}{2\pi}\frac{f(k)}{\left(k^0-\omega_k+i\epsilon\right)\left(k^0+\omega_k-i\epsilon\right)\left(k^0-E-\omega_{P-k}+i\epsilon\right)\left(k^0-E+\omega_{P-k}-i\epsilon\right)}. \tag{3.26}$$

That is, there are four singularities in k^0, located at $\pm\omega_k \mp i\epsilon$ and $E \pm \omega_{P-k} \mp i\epsilon$. We close the k^0 contour of integration in the lower half plane and use the residue theorem to obtain

$$I_{\mathrm{FV}}(P,L) = -\frac{i}{L^3}\sum_{\boldsymbol{k}\in\mathbb{Z}_L^3}\left(\frac{f(\omega_k,\boldsymbol{k})}{2\omega_k\left[(E-\omega_k)^2-\omega_{P-k}^2+i\epsilon\right]}+\frac{f(E+\omega_{P-k},\boldsymbol{k})}{2\omega_{P-k}\left[(E+\omega_{P-k})^2-\omega_k^2\right]}\right). \tag{3.27}$$

Here we kept the $i\epsilon$ in the only place were it is going to be of relevance in the following.

To make further progress, we need another tool, namely the Poisson summation formula, which states that [143]

$$\sum_{\mathfrak{n}\in\mathbb{Z}^3} h(\mathfrak{n}) = \sum_{\mathfrak{l}\in\mathbb{Z}^3}\mathcal{F}[h](\mathfrak{l}), \tag{3.28}$$

with $h : \mathbb{R}^3 \to \mathbb{C}$ a function and $\mathcal{F}[h]$ its Fourier transform, defined as

$$\mathcal{F}[h](\boldsymbol{x}) = \int \mathrm{d}^3y \exp\left[-2\pi i\boldsymbol{x}\cdot\boldsymbol{y}\right]h(\boldsymbol{y}). \tag{3.29}$$

Also, we made use of our convention to denote integer vectors using Fraktur. Applying the Poisson summation formula to $h(\boldsymbol{x}) = g(2\pi\boldsymbol{x}/L)$, renaming $\mathfrak{l} \to -\mathfrak{l}$ in the sum on the right-hand side of Eq. (3.28), and performing the change of variables $\boldsymbol{k} = 2\pi\boldsymbol{y}/L$ in the integral on the right hand side of Eq. (3.29) results in

$$\frac{1}{L^3}\sum_{\boldsymbol{k}\in\mathbb{Z}_L^3} g(\boldsymbol{k}) = \sum_{\mathfrak{l}\in\mathbb{Z}^3}\int\frac{\mathrm{d}^3k}{(2\pi)^3}\exp\left[iL\mathfrak{l}\cdot\boldsymbol{k}\right]g(\boldsymbol{k}), \tag{3.30}$$

which holds true for arbitrary functions g. It is instructive to separate the $\mathfrak{l} = 0$ term from the sum, obtaining

$$\frac{1}{L^3}\sum_{\boldsymbol{k}\in\mathbb{Z}_L^3} g(\boldsymbol{k}) = \int\frac{\mathrm{d}^3k}{(2\pi)^3}g(\boldsymbol{k}) + \sum_{\mathfrak{l}\in\mathbb{Z}^3\setminus\{0\}}\int\frac{\mathrm{d}^3k}{(2\pi)^3}\exp\left[iL\mathfrak{l}\cdot\boldsymbol{k}\right]g(\boldsymbol{k}). \tag{3.31}$$

If the function g is non-singular and falls of quickly for large arguments, the terms with $\mathfrak{l} \neq 0$ are exponentially suppressed for large L (in accordance with the Riemann–Lebesgue lemma), i.e.,

$$\frac{1}{L^3}\sum_{\boldsymbol{k}\in\mathbb{Z}_L^3} g(\boldsymbol{k}) = \int\frac{\mathrm{d}^3k}{(2\pi)^3}g(\boldsymbol{k}) \tag{3.32}$$

ignoring exponentially suppressed corrections. That is, for non-singular functions there is effectively no difference between the finite volume and the infinite volume. All important differences between finite and infinite volume arise from singularities.

Equipped with this knowledge, the canonical next step is to investigate the singularities of Eq. (3.27). From here on, we restrict the analysis to energies between the two-pion threshold and

the four-pion one, i.e., $4M_\pi^2 < {E^\star}^2 < 16M_\pi^2$. Inside this kinematical range, the second term on the right-hand side of Eq. (3.27) has no singularities, and thus according to Eq. (3.32) the sum over it can be replaced by an integral. Moreover, I_{IV} can also be brought into the form of Eq. (3.27), with the only difference that the sum in Eq. (3.27) is to be replaced by an integral (since to arive at Eq. (3.27) only the k^0 integral has been performed, which is the same in both the finite-volume expression (3.25) and the infinite-volume one (3.24)). Putting all this together, we obtain

$$\begin{aligned} D(P,L) &= I_{\mathrm{FV}}(P,L) - I_{\mathrm{IV}}(P) \\ &= -i \sum\!\!\!\!\!\!\int_{\boldsymbol{k}} \frac{f(\omega_k, \boldsymbol{k})}{2\omega_k \left[(E-\omega_k)^2 - \omega_{P-k}^2 + i\epsilon \right]}, \end{aligned} \tag{3.33}$$

with

$$\sum\!\!\!\!\!\!\int_{\boldsymbol{k}} \coloneqq \left[\frac{1}{L^3} \sum_{\boldsymbol{k} \in \mathbb{Z}_L^3} - \int \frac{\mathrm{d}^3 k}{(2\pi)^3} \right]. \tag{3.34}$$

In principle, we could now use Eq. (3.31) to rewrite this expression as a sum over $\mathbb{Z}^3 \setminus \{0\}$, however, it is beneficial to spend some effort to further manipulate it.

To do so, we rewrite it in terms of CM-frame variables. Using Eqs. (3.5) and (3.6) we obtain

$$(E-\omega_k)^2 - \omega_{P-k}^2 = E^\star \left(E^\star - 2\omega_k^\star \right). \tag{3.35}$$

Furthermore, we have

$$\frac{1}{E^\star - 2\omega_k^\star} = \frac{E^\star + 2\omega_k^\star}{4\left({q^\star}^2 - |\boldsymbol{k}^\star|^2 \right)} \tag{3.36}$$

and introduce a function $f^\star$ defined via

$$f^\star(\boldsymbol{k}^\star) \coloneqq f(\omega_k, \boldsymbol{k}) \tag{3.37}$$

(we suppress the argument $\omega_k^\star$, for it is fixed via $\boldsymbol{k}^\star$) resulting in[2]

$$D(P,L) = -i \sum\!\!\!\!\!\!\int_{\boldsymbol{k}} \frac{f^\star(\boldsymbol{k}^\star)\left(E^\star + 2\omega_k^\star \right)}{8\omega_k E^\star \left({q^\star}^2 - |\boldsymbol{k}^\star|^2 + i\epsilon \right)}. \tag{3.38}$$

To simplify this even further, we make use of Eq. (3.8) to decompose $f^\star$:

$$D(P,L) = -\frac{i}{2E^\star} \sum_{l,m} \sum\!\!\!\!\!\!\int_{\boldsymbol{k}} \frac{f_{lm}^\star(|\boldsymbol{k}^\star|)\sqrt{4\pi} Y_{lm}\left(\Omega_k^\star\right)\left(E^\star + 2\omega_k^\star \right)}{4\omega_k \left({q^\star}^2 - |\boldsymbol{k}^\star|^2 + i\epsilon \right)}. \tag{3.39}$$

With the abbreviation

$$g_{lm}(E^\star, |\boldsymbol{k}^\star|) \coloneqq \frac{f_{lm}^\star(|\boldsymbol{k}^\star|)}{|\boldsymbol{k}^\star|^l} \frac{E^\star + 2\omega_k^\star}{4\omega_k^\star}, \tag{3.40}$$

[2]It is crucial to note that $q^\star = \sqrt{{E^\star}^2/4 - M_\pi^2}$ is here an external parameter that can be varied freely, while $\boldsymbol{k}^\star$ is the loop momentum. In particular, $q^\star$ is not fixed to equal $|\boldsymbol{k}^\star|$.

we arrive at

$$\begin{aligned} & D(P,L) \\ &= -\frac{i}{2E^\star}\sum_{l,m}\sum\!\!\!\!\!\!\int_{\boldsymbol{k}}\frac{\omega_k^\star}{\omega_k}\frac{g_{lm}(E^\star,|\boldsymbol{k}^\star|)\sqrt{4\pi}\mathcal{Y}_{lm}(\boldsymbol{k}^\star)}{q^{\star 2}-|\boldsymbol{k}^\star|^2+i\epsilon} \\ &= -\frac{i}{2E^\star}\sum_{l,m}\sum\!\!\!\!\!\!\int_{\boldsymbol{k}}\frac{\omega_k^\star}{\omega_k}\left\{\frac{g_{lm}(E^\star,|\boldsymbol{k}^\star|)-g_{lm}(E^\star,q^\star)\,e^{\alpha\left(q^{\star 2}-|\boldsymbol{k}^\star|^2\right)}}{q^{\star 2}-|\boldsymbol{k}^\star|^2+i\epsilon}\right\}\sqrt{4\pi}\mathcal{Y}_{lm}(\boldsymbol{k}^\star) \\ &\quad -\frac{i}{2E^\star}\sum_{l,m}\sum\!\!\!\!\!\!\int_{\boldsymbol{k}}\frac{\omega_k^\star}{\omega_k}\frac{g_{lm}(E^\star,q^\star)\,e^{\alpha\left(q^{\star 2}-|\boldsymbol{k}^\star|^2\right)}}{q^{\star 2}-|\boldsymbol{k}^\star|^2+i\epsilon}\sqrt{4\pi}\mathcal{Y}_{lm}(\boldsymbol{k}^\star)\,. \end{aligned} \tag{3.41}$$

Here $\alpha > 0$ is an arbitrary positive real number and $\mathcal{Y}_{lm}$ is defined in Eq. (3.16). The term inside the curly brackets has no singularity, and therefore according to Eq. (3.32) its contribution vanishes. Using

$$g_{lm}(E^\star,q^\star) = \frac{f_{lm}^\star(q^\star)}{q^{\star l}} \tag{3.42}$$

we are left with

$$D(P,L) = -\frac{i}{2E^\star}\sum_{l,m}\sum\!\!\!\!\!\!\int_{\boldsymbol{k}}\frac{\omega_k^\star}{\omega_k}\frac{f_{lm}^\star(q^\star)\,e^{\alpha\left(q^{\star 2}-|\boldsymbol{k}^\star|^2\right)}}{q^{\star 2}-|\boldsymbol{k}^\star|^2+i\epsilon}\frac{1}{q^{\star l}}\sqrt{4\pi}\mathcal{Y}_{lm}(\boldsymbol{k}^\star)\,. \tag{3.43}$$

Again employing Eq. (3.6),

$$\frac{\partial k_\parallel^\star}{\partial k_\parallel} = \frac{\omega_k^\star}{\omega_k} \tag{3.44}$$

follows, resulting in

$$\int \mathrm{d}^3k = \int \mathrm{d}^2k_\perp \mathrm{d}k_\parallel = \int \mathrm{d}^2k_\perp^\star \mathrm{d}k_\parallel^\star \frac{\omega_k}{\omega_k^\star} = \int \mathrm{d}^3k^\star \frac{\omega_k}{\omega_k^\star}. \tag{3.45}$$

Thus,

$$D(P,L) = -\frac{i}{2E^\star}\sum_{l,m}\left[\frac{1}{L^3}\sum_{\boldsymbol{k}\in\mathbb{Z}_L^3}\frac{\omega_k^\star}{\omega_k} - \int\frac{\mathrm{d}^3k^\star}{(2\pi)^3}\right]\frac{f_{lm}^\star(q^\star)\,e^{\alpha\left(q^{\star 2}-|\boldsymbol{k}^\star|^2\right)}}{q^{\star 2}-|\boldsymbol{k}^\star|^2+i\epsilon}\frac{1}{q^{\star l}}\sqrt{4\pi}\mathcal{Y}_{lm}(\boldsymbol{k}^\star)\,. \tag{3.46}$$

Focus on the integral first. As a special case of Eq. (3.9) we deduce

$$\int \mathrm{d}\Omega_k^\star Y_{lm}\left(\Omega_k^\star\right) = \sqrt{4\pi}\int \mathrm{d}\Omega_k^\star Y_{00}^*\left(\Omega_k^\star\right)Y_{lm}\left(\Omega_k^\star\right) = \sqrt{4\pi}\delta_{l0}\delta_{m0} = \sqrt{4\pi}\delta_{l0}, \tag{3.47}$$

where we used that $l = 0$ requires $m = 0$ automatically. Therefore,

$$\begin{aligned}
&\frac{i}{2E^\star}\sum_{l,m}\int\frac{\mathrm{d}^3k^\star}{(2\pi)^3}\frac{f^\star_{lm}(q^\star)\,e^{\alpha\left(q^{\star 2}-|\boldsymbol{k}^\star|^2\right)}}{q^{\star 2}-|\boldsymbol{k}^\star|^2+i\epsilon}\frac{1}{q^{\star l}}\sqrt{4\pi}\mathcal{Y}_{lm}(\boldsymbol{k}^\star)\\
=&\frac{i}{2E^\star}\sum_{l,m}\int_0^\infty\frac{\mathrm{d}\,|\boldsymbol{k}^\star|\,|\boldsymbol{k}^\star|^2}{(2\pi)^3}\frac{f^\star_{lm}(q^\star)\,e^{\alpha\left(q^{\star 2}-|\boldsymbol{k}^\star|^2\right)}}{q^{\star 2}-|\boldsymbol{k}^\star|^2+i\epsilon}\frac{|\boldsymbol{k}^\star|^l}{q^{\star l}}\sqrt{4\pi}\int\mathrm{d}\Omega^\star_k Y_{lm}\left(\Omega^\star_k\right)\\
=&\frac{if^\star_{00}(q^\star)}{4E^\star\pi^2}\int_0^\infty\mathrm{d}\,|\boldsymbol{k}^\star|\,\frac{|\boldsymbol{k}^\star|^2\,e^{\alpha\left(q^{\star 2}-|\boldsymbol{k}^\star|^2\right)}}{(q^\star-|\boldsymbol{k}^\star|+i\epsilon)(q^\star+|\boldsymbol{k}^\star|+i\epsilon)}\\
=&\frac{f^\star_{00}(q^\star)\,q^\star}{8\pi E^\star}+\frac{if^\star_{00}(q^\star)}{4E^\star\pi^2}\fint\mathrm{d}\,|\boldsymbol{k}^\star|\,\frac{|\boldsymbol{k}^\star|^2\,e^{\alpha\left(q^{\star 2}-|\boldsymbol{k}^\star|^2\right)}}{q^{\star 2}-|\boldsymbol{k}^\star|^2}
\end{aligned}\tag{3.48}$$

where in the last line the Cauchy principal value is applied. Inserting this back into Eq. (3.46) finally yields [140]

$$D(P,L)=\frac{f^\star_{00}(q^\star)\,q^\star}{8\pi E^\star}-\frac{i}{2E^\star}\sum_{l,m}\frac{f^\star_{lm}(q^\star)}{q^{\star l}}c^P_{lm}\left(q^{\star 2},L\right),\tag{3.49}$$

with

$$c^P_{lm}\left(q^{\star 2},L\right):=\frac{1}{L^3}\sum_{\boldsymbol{k}\in\mathbb{Z}^3_L}\frac{\omega^\star_k}{\omega_k}\frac{e^{\alpha\left(q^{\star 2}-|\boldsymbol{k}^\star|^2\right)}}{q^{\star 2}-|\boldsymbol{k}^\star|^2}\sqrt{4\pi}\mathcal{Y}_{lm}(\boldsymbol{k}^\star)-\delta_{l0}\fint\frac{\mathrm{d}^3k^\star}{(2\pi)^3}\frac{e^{\alpha\left(q^{\star 2}-|\boldsymbol{k}^\star|^2\right)}}{q^{\star 2}-|\boldsymbol{k}^\star|^2}.\tag{3.50}$$

Since the choice of the precise value of α in the derivation is arbitrary, the coefficients c^P_{lm} are in fact independent of α. Often they are replaced by the generalized zeta functions $Z^{\mathfrak{P}}_{lm}$ that are defined as

$$c^P_{lm}\left(q^{\star 2},L\right)=:-\frac{1}{2L\pi^{3/2}}\left(\frac{2\pi}{L}\right)^l Z^{\mathfrak{P}}_{lm}\left(1,\left(\frac{q^\star L}{2\pi}\right)^2\right).\tag{3.51}$$

There is one striking aspect of Eq. (3.49), namely that all quantities are evaluated at $q^\star$, which is determined via

$$q^\star=\sqrt{\frac{E^{\star 2}}{4}-M_\pi^2}=\sqrt{\frac{P^2}{4}-M_\pi^2}.\tag{3.52}$$

In particular, recall that according to Eq. (3.37) $f^\star_{lm}(q^\star)=f_{lm}(\omega_{q^\star},q^\star)$, that is, f is evaluated on-shell. Furthermore, while $\boldsymbol{P}$ is constrained to take on values in $\mathbb{Z}^3_L$, i.e., is discretized, $P^0=E$ is a priori arbitrary (except for the constraint $2M_\pi<E^\star<4M_\pi$), and thus $q^\star$ can take on any value out of a continuous range of real values.

3.2.5 Correlation functions in finite volume

In this section[3] we want to study correlation functions in Minkowski space of infinite time extent, again confined to a spatial box of size L^3 with periodic boundary conditions. To be precise, the

[3]The derivation in this section has been presented multiple times in the literature, here we orient ourselves closely by Refs. [39, 40, 140, 141].

object of interest is

$$C(P,L) \coloneqq \int_L \mathrm{d}^4x\, e^{iPx} \left\langle 0 \left| T\left\{ \mathcal{O}_1(x)\, \mathcal{O}_2^\dagger(0) \right\} \right| 0 \right\rangle, \tag{3.53}$$

with P an arbitrary four-momentum and T the time-ordered product. Here we introduced the shorthand notation

$$\int_L \mathrm{d}^4x \coloneqq \int_{-\infty}^{\infty} \mathrm{d}x^0 \int_{\mathbb{L}} \mathrm{d}^3x. \tag{3.54}$$

In addition, $\mathcal{O}_2^\dagger$ denotes an operator with the appropriate quantum numbers to create a pair of pions, and $\mathcal{O}_1$ one that annihilates such a pair (these do not need to be Hermitian conjugates of each other and they do not need to be local). That is, C is the correlation function relevant for $\pi\pi \to \pi\pi$ scattering.

We restrict our attention to energies below a cutoff that is high enough such that all physical phenomena we are interested in occur at energies well below this cutoff. In principle it is possible to construct an EFT that describes the interactions among pions at energies below this cutoff by integrating out all higher-energetic degrees of freedom from QCD. Of course in practice this might not be feasible except for at very low energies, where ChPT is valid, but since we do not need to use at all any specific characteristics of this EFT (like interaction vertices etc.), all we need to rely upon is that such an EFT exists. Furthermore, we assume that G parity is a good quantum number, i.e., that interactions between an odd number of pions are forbidden.

In this EFT the perturbative expansion of C to all orders is depicted in Fig. 3.1. It is given in terms of the fully dressed one-pion propagator (denoted in the following by Δ) and the so called Bethe–Salpeter kernel B. The latter is defined as the sum of all diagrams that are two-particle-irreducible (2PI) in the s channel. In particular, it contains all t and u channel loops to all orders as well as all contributions from higher-energetic intermediate states (e.g., four-pion states). Note that this expansion is—if summed to all orders, which we will do in the following—exact.

From here on, we restrict our attention to CM energies above the two-pion threshold and below the four-pion one, i.e., $2M_\pi < E^\star < 4M_\pi$. Since we operate in finite volume, all loop integrals are in fact of the form

$$\frac{1}{L^3} \sum_{\boldsymbol{p} \in \mathbb{Z}_L^3} \int \frac{\mathrm{d}p^0}{2\pi}, \tag{3.55}$$

where p is the loop momentum. They can be decomposed as

$$\frac{1}{L^3} \sum_{\boldsymbol{p} \in \mathbb{Z}_L^3} \int \frac{\mathrm{d}p^0}{2\pi} = \int \frac{\mathrm{d}^4p}{(2\pi)^4} + \int \frac{\mathrm{d}p^0}{2\pi} \sum\!\!\!\!\!\!\int_{\boldsymbol{p}}, \tag{3.56}$$

with the shorthand notation defined in Eq. (3.34). According to the discussion in Sec. 3.2.4, the important differences between finite volume and infinite volume arise from singularities, all other differences are exponentially suppressed. Intermediate propagators exhibit poles only if the corresponding particle can go on-shell. However, in the kinematic range of interest the multi-particle contributions in the s channel contained in the Bethe–Salpeter kernel cannot go on-shell. The same holds true for the t- and u-channel loops, for we consider the region of s-channel scattering. Hence, there are no relevant singularities in the Bethe–Salpeter kernel, such that the sum in all internal loops of B can be replaced by integrals, effectively replacing B by its infinite-volume

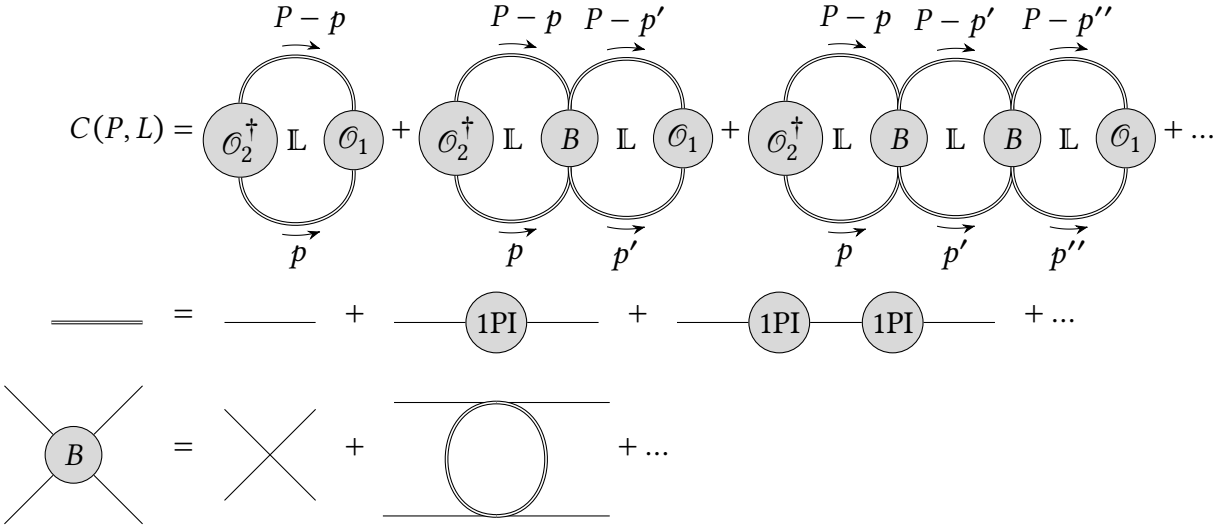

Figure 3.1: The perturbative expansion of the correlation function C in a general EFT. Ordinary internal lines denote LO single-pion propagators, while the fully dressed single-pion propagator Δ is denoted by double lines. It is given as a geometric series of one-particle-irreducible (1PI) terms. p, p', and p'' denote loop momenta. An $\mathbb{L}$ inside a loop indicates that Eq. (3.55) is used instead of an ordinary integral [39].

counterpart. Since the finite-volume expression of B is not needed in the following, all subsequent mentions of B refer to the infinite-volume Bethe–Salpeter kernel.[4] In addition, the intermediate states of lowest energy in the 1PI terms in the dressed propagator are two-pion states. Hence, for intermediate states in the 1PI terms of both dressed propagators in an s-channel loop to go on-shell simultaneously, the overall energy needs to exceed the four-pion threshold. Thus, the only singularities of interest arise if both pions in an s-channel loop go on-shell, i.e., precisely the singularities studied in Sec. 3.2.4.

Applying the decomposition (3.56) to all s-channel two-particle loops depicted in the top row of Fig. 3.1 and rearranging the terms leads to the decomposition

$$C(P, L) = C_\infty(P) + C_{\text{cut}}(P, L). \tag{3.57}$$

Here C_∞ is the infinite-volume correlation function and the perturbative expansions of C_∞ and C_{cut} are shown in Fig. 3.2. The cuts indicate that in the corresponding loop

$$\int \frac{\mathrm{d}p^0}{2\pi} \sum\!\!\!\!\!\!\int_{\boldsymbol{p}} \tag{3.58}$$

is used instead of an ordinary loop integral. According to the discussion in Sec. 3.2.4, only the singularities are of relevance; hence, in the cut loops the fully dressed propagators can effectively be replaced by the ordinary ones. For this to work smoothly, we pick renormalization conditions such that:

$$\Delta(p) \xrightarrow[p^2 \to M_\pi^2]{} \frac{i}{p^2 - M_\pi^2 + i\epsilon}. \tag{3.59}$$

[4] This is why there is no $\mathbb{L}$ inside the loop in the last row of Fig. 3.1.

Therefore, the internal propagators in the first row of Fig. 3.2 are denoted by simple lines instead of double ones.

At this stage it is useful to decompose all quantities via spherical harmonics, as explained in Sec. 3.2.2, that is,

$$\begin{aligned}
\mathscr{M}\left(p^\star, p'^\star\right) &= 4\pi Y_{l_1m_1}\left(\Omega_p^\star\right) \mathscr{M}_{l_1m_1l_2m_2}\left(p^{\star\,0}, |\boldsymbol{p}^\star|, p'^{\star\,0}, |\boldsymbol{p}'^\star|\right) Y^*_{l_2m_2}\left(\Omega_{p'}^\star\right), \\
\mathcal{Q}_1\left(p^\star\right) &= \sqrt{4\pi}\mathcal{Q}_{1lm}\left(p^{\star\,0}, |\boldsymbol{p}^\star|\right) Y_{lm}\left(\Omega_p^\star\right), \\
\mathcal{Q}_2\left(p^\star\right) &= \sqrt{4\pi}\mathcal{Q}_{2lm}\left(p^{\star\,0}, |\boldsymbol{p}^\star|\right) Y^*_{lm}\left(\Omega_p^\star\right),
\end{aligned} \tag{3.60}$$

with sums over repeated indices implied. Here we are allowing for off-shell momenta (i.e., $p^{\star\,0} \neq \omega_p^\star$) and all functions are defined with respect to CM momenta.

Denote the first diagram in the second row of Fig. 3.2 as $C_{\text{cut}}^{\text{LO}}$. Expressed as a formula it reads

$$C_{\text{cut}}^{\text{LO}}(P,L) = i^2\eta \int \frac{\mathrm{d}p^0}{2\pi} \sum\!\!\!\!\!\!\int_{\boldsymbol{p}} \frac{\mathcal{Q}_2\left(p^\star\right)\mathcal{Q}_1\left(p^\star\right)}{\left[p^2 - M_\pi^2 + i\epsilon\right]\left[(P-p)^2 - M_\pi^2 + i\epsilon\right]}, \tag{3.61}$$

where the factor i^2 arises from the numerators of the two propagators, $\eta = 1/2$ if the pions in the loop are considered to be identical, and $\eta = 1$ otherwise. This is just a special case of the expression D studied in Sec. 3.2.4 with (see Eq. (3.37))

$$f^\star\left(p^\star\right) = \mathcal{Q}_2\left(p^\star\right)\mathcal{Q}_1\left(p^\star\right). \tag{3.62}$$

Since all momenta are evaluated on-shell, we can suppress $p^{\star\,0}$ in the following. We use Eq. (3.10) to obtain (with $|\boldsymbol{q}^\star| = q^\star$)

$$\begin{aligned}
f^\star_{lm}\left(q^\star\right) &= \frac{1}{\sqrt{4\pi}} \int \mathrm{d}\Omega_q^\star Y^*_{lm}\left(\Omega_q^\star\right) f(\boldsymbol{q}^\star) \\
&= \sqrt{4\pi}\mathcal{Q}_{2l_2m_2}\left(q^\star\right)\mathcal{Q}_{1l_1m_1}\left(q^\star\right) \int \mathrm{d}\Omega_q^\star Y^*_{lm}\left(\Omega_q^\star\right) Y^*_{l_2m_2}\left(\Omega_q^\star\right) Y_{l_1m_1}\left(\Omega_q^\star\right).
\end{aligned} \tag{3.63}$$

In particular, Eq. (3.9) implies

$$f^\star_{00}\left(q^\star\right) = \mathcal{Q}_{2l_2m_2}\left(q^\star\right)\mathcal{Q}_{1l_1m_1}\left(q^\star\right)\delta_{l_1l_2}\delta_{m_1m_2} = \mathcal{Q}_{2lm}\left(q^\star\right)\mathcal{Q}_{1lm}\left(q^\star\right). \tag{3.64}$$

By virtue of Eq. (3.49),

$$C_{\text{cut}}^{\text{LO}}(P,L) = -\eta\mathcal{Q}_{2l_2m_2}\mathcal{F}_{l_2m_2l_1m_1}\mathcal{Q}_{1l_1m_1}, \tag{3.65}$$

with

$$\begin{aligned}
\mathcal{F}_{l_2m_2l_1m_1} =& \frac{q^\star}{8\pi E^\star}\delta_{l_2l_1}\delta_{m_2m_1} \\
&- \frac{i}{2E^\star}\frac{\sqrt{4\pi}}{q^{\star l}} c^P_{lm}\left(q^{\star\,2}, L\right) \int \mathrm{d}\Omega_q^\star Y^*_{lm}\left(\Omega_q^\star\right) Y^*_{l_2m_2}\left(\Omega_q^\star\right) Y_{l_1m_1}\left(\Omega_q^\star\right).
\end{aligned} \tag{3.66}$$

Here again a sum over l and m is implicit.

The higher-order terms in the expansion of C_{cut} can be manipulated in exactly the same way. Before writing down the result, it is convenient to introduce a notation for matrices and vectors

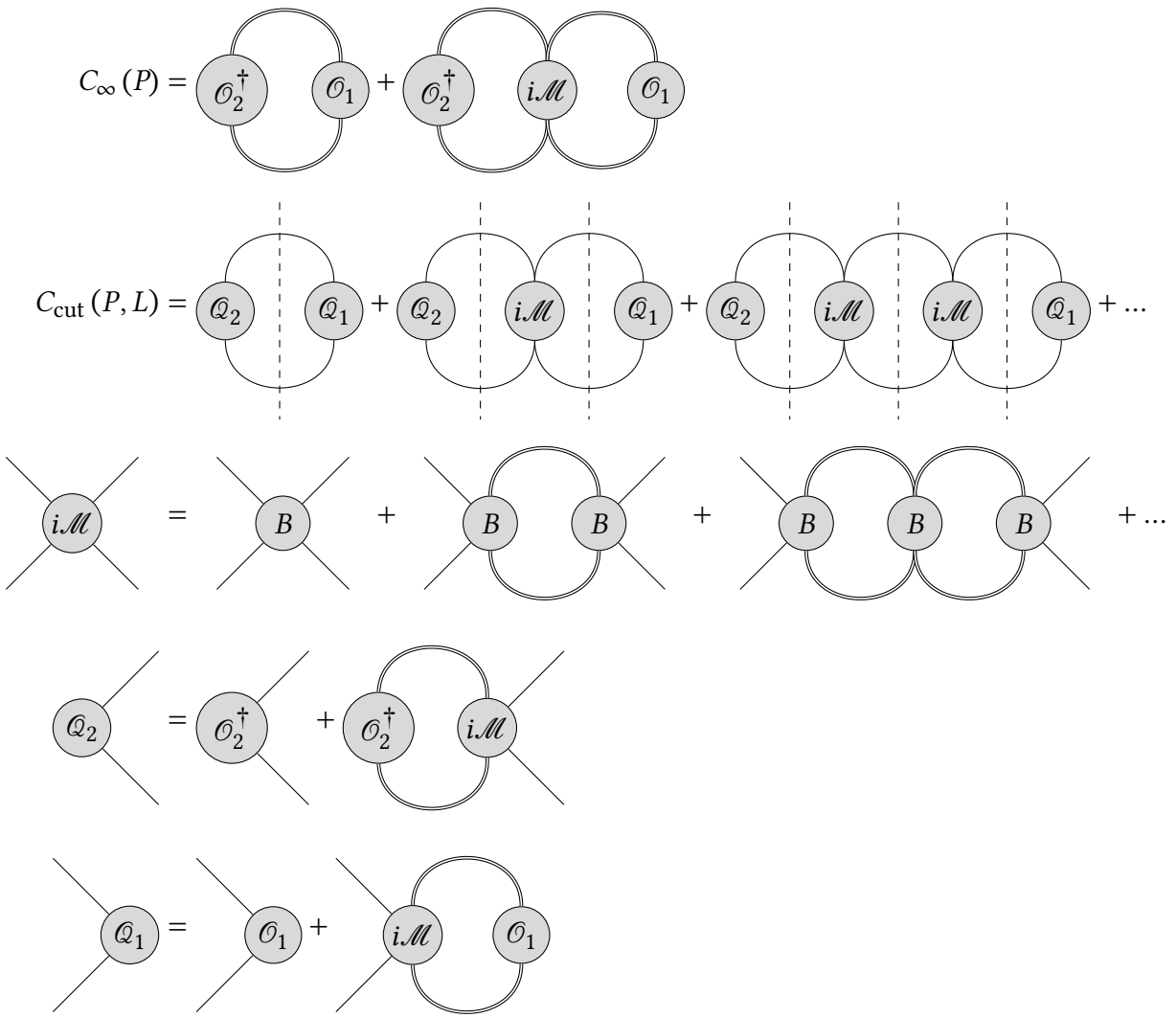

Figure 3.2: The correlation function C expressed in terms of the infinite-volume scattering amplitude $\mathscr{M}$ [39, 141]. The cuts (i.e., vertical dashed lines) in the first row indicate that Eq. (3.58) is used to compute the loop integrals. This notation is motivated by the fact that this amounts to evaluating the intermediate quantities on-shell, see Eq. (3.49).

in angular-momentum space, namely to denote by $\mathcal{M}$ the matrix with components $\mathscr{M}_{l_1 m_1 l_2 m_2}$, by $\mathcal{Q}_1$ the column vector with components $\mathcal{Q}_{1lm}$, and by $\mathcal{Q}_2$ the row vector with components $\mathcal{Q}_{2lm}$.

Equation (3.65) now reads $C_{\text{cut}}^{\text{LO}} = -\eta \mathcal{Q}_2 \mathcal{F} \mathcal{Q}_1$. Application to all orders results in

$$\begin{aligned} & C_{\text{cut}}(P,L) \\ &= \mathcal{Q}_2 (-\eta\mathcal{F}) \mathcal{Q}_1 + \mathcal{Q}_2 (-\eta\mathcal{F}) i\mathcal{M} (-\eta\mathcal{F}) \mathcal{Q}_1 + \mathcal{Q}_2 (-\eta\mathcal{F}) i\mathcal{M} (-\eta\mathcal{F}) i\mathcal{M} (-\eta\mathcal{F}) \mathcal{Q}_1 + \dots \\ &= \mathcal{Q}_2 (-\eta\mathcal{F}) \sum_{j=0}^{\infty} [-i\eta\mathcal{M}\mathcal{F}]^j \mathcal{Q}_1 \\ &= \mathcal{Q}_2 (-\eta\mathcal{F}) [\mathbb{1} + i\eta\mathcal{M}\mathcal{F}]^{-1} \mathcal{Q}_1 \\ &= -\mathcal{Q}_2 \left[(\eta\mathcal{F})^{-1} + i\mathcal{M}\right]^{-1} \mathcal{Q}_1. \end{aligned} \tag{3.67}$$

Inserting this into Eq. (3.57) finally yields

$$C(P,L) = C_\infty(P) - \mathcal{Q}_2 \left[(\eta\mathcal{F})^{-1} + i\mathcal{M}\right]^{-1} \mathcal{Q}_1. \tag{3.68}$$

To complete our analysis, we consider the Fourier transform of C with respect to energy, i.e.,

$$\mathscr{C}(x^0, \boldsymbol{P}, L) := \int \frac{\mathrm{d}P^0}{2\pi} e^{-ix^0P^0} C(P,L). \tag{3.69}$$

Inserting Eq. (3.53) results in

$$\mathscr{C}(x^0, \boldsymbol{P}, L) = \int_{\mathbb{L}} \mathrm{d}^3x\, e^{-i\boldsymbol{P}\cdot\boldsymbol{x}} \left\langle 0 \left| T\left\{\mathcal{O}_1(x)\, \mathcal{O}_2^\dagger(0)\right\}\right| 0 \right\rangle. \tag{3.70}$$

In the following, choose $x^0 > 0$, such that the time-ordered product can be dropped. Inserting a complete set of eigenstates of the Hamiltonian yields

$$\begin{aligned} \mathscr{C}(x^0, \boldsymbol{P}, L) &= \sum_{n,\boldsymbol{p}_n} \int_{\mathbb{L}} \mathrm{d}^3x\, e^{-i\boldsymbol{P}\cdot\boldsymbol{x}} \langle 0 | \mathcal{O}_1(x) | E_n, \boldsymbol{p}_n; L\rangle \left\langle E_n, \boldsymbol{p}_n; L \left| \mathcal{O}_2^\dagger(0)\right| 0\right\rangle \\ &= \sum_{n,\boldsymbol{p}_n} e^{-ix^0E_n} \int_{\mathbb{L}} \mathrm{d}^3x\, e^{-i\boldsymbol{x}\cdot(\boldsymbol{P}-\boldsymbol{p}_n)} \langle 0 | \mathcal{O}_1(0) | E_n, \boldsymbol{p}_n; L\rangle \left\langle E_n, \boldsymbol{p}_n; L \left| \mathcal{O}_2^\dagger(0)\right| 0\right\rangle \\ &= L^3 \sum_n e^{-ix^0E_n} \langle 0 | \mathcal{O}_1(0) | E_n, \boldsymbol{P}; L\rangle \left\langle E_n, \boldsymbol{P}; L \left| \mathcal{O}_2^\dagger(0)\right| 0\right\rangle, \end{aligned} \tag{3.71}$$

where in the last step Eq. (3.19) is used. A different representation of $\mathscr{C}$ can be obtained by inserting Eq. (3.68) into Eq. (3.69):

$$\mathscr{C}(x^0, \boldsymbol{P}, L) = \mathscr{C}_\infty(x^0, \boldsymbol{P}) - \int \frac{\mathrm{d}P^0}{2\pi} e^{-ix^0P^0} \mathcal{Q}_2 \left[(\eta\mathcal{F})^{-1} + i\mathcal{M}\right]^{-1} \mathcal{Q}_1. \tag{3.72}$$

Here $\mathscr{C}_\infty$ denotes the Fourier transform of C_∞ with respect to energy.

As a function of energy, $C_\infty(P)$ is free of singularities in the kinematical region of interest, $2M_\pi < E^\star < 4M_\pi$. Contrary to C_∞, $C(P,L)$ has poles as a function of energy, since the continuum of two-pion states is replaced by a discrete spectrum in finite volume, as explained in Sec. 3.2.3. Hence, according to Eq. (3.57), these poles need to be located in $C_{\text{cut}}(P,L)$. Moreover, the pole positions must depend on L, for the allowed values of momenta depend on L. As Eq. (3.68) shows,

the only L-dependent term in C_{cut} is $\mathcal{F}$, and thus the poles arise solely due to $[(\eta\mathcal{F})^{-1}+i\mathcal{M}]^{-1}$. This expression has poles at energies where the inverse does not exist, that is [39, 140]

$$0 = \det\left[(\eta\mathcal{F})^{-1} + i\mathcal{M}\right]. \tag{3.73}$$

Here the determinant acts in angular-momentum space. Equation (3.73) is called Lüscher's quantization condition.

The factor $e^{-ix^0P^0}$ in Eq. (3.72) allows for closing the integration contour with a semicircle in the lower half complex P^0 plane, for we consider $x^0 > 0$. Thus, we can compute the integral by summing up all residues at the poles. Comparison with Eq. (3.71) reveals that the poles, i.e., solutions of Eq. (3.73), are indeed located at E_n, furthermore, this comparison yields

$$\begin{aligned} &i\operatorname{res}\left(\mathcal{Q}_2\left[(\eta\mathcal{F})^{-1}+i\mathcal{M}\right]^{-1}\mathcal{Q}_1, E_n\right) \\ &= i\mathcal{Q}_2(E_n)\lim_{P^0\to E_n}\left(P^0-E_n\right)\left[(\eta\mathcal{F})^{-1}+i\mathcal{M}\right]^{-1}\mathcal{Q}_1(E_n) \\ &= L^3\left\langle 0\left|\mathcal{O}_1(0)\right|E_n,\boldsymbol{P};L\right\rangle\left\langle E_n,\boldsymbol{P};L\left|\mathcal{O}_2^\dagger(0)\right|0\right\rangle. \end{aligned} \tag{3.74}$$

Note that this relation holds only for the poles between $2M_\pi$ and $4M_\pi$, for outside this range Eq. (3.68) does not hold, that is, it does not need to reproduce Eq. (3.71) correctly. For future use, we define [39]

$$\mathcal{R}_n := i\lim_{P^0\to E_n}\left(P^0-E_n\right)\left[(\eta\mathcal{F})^{-1}+i\mathcal{M}\right]^{-1}. \tag{3.75}$$

Now let $\mathcal{O}_1 = \mathcal{O}_2$. Note that this implies $\mathcal{Q}_2 = \mathcal{Q}_1^\dagger$ (the transpose is meant to act in angular-momentum space). Via Eq. (3.74) we obtain

$$\mathcal{Q}_1^\dagger\mathcal{R}_n\mathcal{Q}_1 = L^3\left|\langle 0\left|\mathcal{O}_1(0)\right|E_n,\boldsymbol{P};L\rangle\right|^2. \tag{3.76}$$

Since the right-hand side of Eq. (3.76) is real, $\mathcal{Q}_1^\dagger\mathcal{R}_n\mathcal{Q}_1 = \mathcal{Q}_1^\dagger\mathcal{R}_n^\dagger\mathcal{Q}_1$. This relation needs to hold for arbitrary choices of $\mathcal{Q}_1$, the only requirement being that $\mathcal{Q}_1$ is indeed associated with an operator that annihilates two pions. Nevertheless, on its own it is insufficient to deduce that $\mathcal{R}_n$ is Hermitian. However, it can be shown that as soon as the residual rotational symmetry in the finite volume—see Sec. 3.4—is taken into account, $\mathcal{R}_n$ can be reduced to a Hermitian matrix [40], and thus in the following, in particular in the derivation of the Lellouch–Lüscher formula (3.112), we treat $\mathcal{R}_n$ effectively as Hermitian.

3.2.6 Quantization condition via K matrix

It is illuminating to rewrite Eq. (3.73) using the K matrix [39, 40]. For simplicity, pick $\eta = 1/2$, i.e., treat the pions in the loops as identical particles. Since Eq. (2.29) implies $q^\star/E^\star = \sigma(s)/2$, according to Eq. (3.66) $\mathcal{F}$ decomposes into

$$\begin{aligned} i\eta\mathcal{F} &= \frac{i\sigma}{32\pi}\mathbb{1} + \mathcal{F}_{\mathrm{r}}, \\ \left(\mathcal{F}_{\mathrm{r}}\right)_{l_2m_2l_1m_1} &:= \frac{1}{4E^\star}\frac{\sqrt{4\pi}}{q^{\star l}}c_{lm}^P\left(q^{\star 2},L\right)\int \mathrm{d}\Omega_q^\star Y_{lm}^*\left(\Omega_q^\star\right)Y_{l_2m_2}^*\left(\Omega_q^\star\right)Y_{l_1m_1}\left(\Omega_q^\star\right). \end{aligned} \tag{3.77}$$

Furthermore, the individual partial waves appearing in $\mathcal{M}$ can be expressed via the K matrix, see Eq. (2.17), combined with Eq. (3.15) this yields

$$\mathcal{M}_{l_1 m_1 l_2 m_2} = \delta_{l_1 l_2}\delta_{m_1 m_2} 32\pi \left(K_{l_1} - i\sigma\right)^{-1} \tag{3.78}$$

or equivalently

$$\mathcal{M}^{-1} = \frac{1}{32\pi}\left(\mathcal{K} - i\sigma\mathbb{1}\right), \qquad \mathcal{K}_{l_1 m_1 l_2 m_2} \coloneqq \delta_{l_1 l_2}\delta_{m_1 m_2} K_{l_1}. \tag{3.79}$$

Here $\mathcal{K}$ denotes the K matrix in angular-momentum space. Since in the s-channel scattering region the scattering amplitude does not have poles, its inverse exists, i.e., $\det[\mathcal{M}^{-1}] = 1/\det[\mathcal{M}] \neq 0$. Thus, Eq. (3.73) is equivalent to

$$\begin{aligned} 0 &= \det\left[\eta\mathcal{F}\right] \det\left[\left(\eta\mathcal{F}\right)^{-1} + i\mathcal{M}\right] \det\left[\mathcal{M}^{-1}\right] \\ &= \det\left[\mathcal{M}^{-1} + i\eta\mathcal{F}\right]. \end{aligned} \tag{3.80}$$

Plugging in Eq. (3.79) and Eq. (3.77) shows that this is in turn equivalent to [39, 40]

$$0 = \det\left[\frac{1}{32\pi}\mathcal{K} + \mathcal{F}_\mathrm{r}\right]. \tag{3.81}$$

Since we work to all orders in perturbation theory, the scattering amplitude satisfies the constraints imposed by unitarity, in particular, the K matrix is real. Via Eq. (3.81) this implies that $\mathcal{F}_\mathrm{r}$ is real, comparison with Eq. (3.77) shows $\mathcal{F}_\mathrm{r} = \mathrm{Re}(i\eta\mathcal{F})$.

3.2.7 Constraints on angular momentum

Lüscher's quantization condition, either in the form of Eq. (3.73) or Eq. (3.81), requires to compute a determinant of an infinite-dimensional matrix in angular-momentum space. As such, it is useless for practical applications. To simplify it, we need to ignore angular momenta exceeding a certain maximal angular momentum l_max, i.e., we ignore all higher partial waves: $t_l = 0$ for all $l > l_\mathrm{max}$. This implies that $\mathcal{M}$ decomposes into $\mathcal{M} = \mathcal{M}^\mathrm{low} \oplus 0$, with $\mathcal{M}_\mathrm{low}$ a diagonal matrix in the subspace with $l \leq l_\mathrm{max}$. Note that contrary to $\mathcal{M}$, $\mathcal{F}$ is not diagonal. To proceed, we follow the approach of Ref. [140], namely we use projection operators. To be specific, the projection operators read

$$\begin{aligned} \mathcal{P}^\mathrm{low}_{l_1 m_1 l_2 m_2} &\coloneqq \Theta\left(l_\mathrm{max} - l\right)\delta_{l_1 l_2}\delta_{m_1 m_2}, \\ \mathcal{P}^\mathrm{high}_{l_1 m_1 l_2 m_2} &\coloneqq \Theta\left(l - l_\mathrm{max} - 1\right)\delta_{l_1 l_2}\delta_{m_1 m_2}, \end{aligned} \tag{3.82}$$

with

$$\Theta(x) \coloneqq \begin{cases} 1 & \text{if } x \geq 0, \\ 0 & \text{if } x < 0 \end{cases} \tag{3.83}$$

the Heaviside step function. Clearly, $\mathcal{M} = \mathcal{M}\mathcal{P}^\mathrm{low} = \mathcal{P}^\mathrm{low}\mathcal{M}$. Tracing back the manipulations performed in Eq. (3.67), we have

$$\begin{aligned} \left[\left(\eta\mathcal{F}\right)^{-1} + i\mathcal{M}\right]^{-1} &= \eta\mathcal{F} + \eta\mathcal{F}\left(-i\mathcal{M}\right)\eta\mathcal{F} + \eta\mathcal{F}\left(-i\mathcal{M}\right)\eta\mathcal{F}\left(-i\mathcal{M}\right)\eta\mathcal{F} + \ldots \\ &= \eta\mathcal{F} + \eta\mathcal{F}\left(-i\mathcal{M}\right)\eta\mathcal{F} + \eta\mathcal{F}\left(-i\mathcal{M}\right)\mathcal{P}^\mathrm{low}\eta\mathcal{F}\mathcal{P}^\mathrm{low}\left(-i\mathcal{M}\right)\eta\mathcal{F} + \ldots \\ &= \eta\mathcal{F} + \eta\mathcal{F}\sum_{j=0}^{\infty}\left(-i\eta\mathcal{M}\mathcal{P}^\mathrm{low}\mathcal{F}\mathcal{P}^\mathrm{low}\right)^j\left(-i\mathcal{M}\right)\eta\mathcal{F} \\ &= \eta\mathcal{F} + \eta\mathcal{F}\left[\mathbb{1} + i\eta\mathcal{M}\mathcal{P}^\mathrm{low}\mathcal{F}\mathcal{P}^\mathrm{low}\right]^{-1}\left(-i\mathcal{M}\right)\eta\mathcal{F}. \end{aligned} \tag{3.84}$$

That is, the quantization condition reads

$$\begin{aligned} 0 &= \det\left[\mathbb{1} + i\eta\mathcal{M}\mathcal{P}^{\text{low}}\mathcal{F}\mathcal{P}^{\text{low}}\right] \\ &= \det\left[\mathbb{1} + i\eta\mathcal{M}^{\text{low}}\mathcal{F}^{\text{low}}\right], \end{aligned} \tag{3.85}$$

with $\mathcal{P}^{\text{low}}\mathcal{F}\mathcal{P}^{\text{low}} =: \mathcal{F}^{\text{low}} \oplus 0$, i.e., $\mathcal{F}^{\text{low}}$ is $\mathcal{F}$ constrained to the subspace with $l \leq l_{\text{max}}$. Multiplying Eq. (3.85) from the right with $\det[(\eta\mathcal{F}^{\text{low}})^{-1}]$ finally yields

$$0 = \det\left[\left(\eta\mathcal{F}^{\text{low}}\right)^{-1} + i\mathcal{M}^{\text{low}}\right], \tag{3.86}$$

which in turn can be expressed as

$$0 = \det\left[\frac{1}{32\pi}\mathcal{K}^{\text{low}} + \mathcal{F}_{\text{r}}^{\text{low}}\right]. \tag{3.87}$$

Despite the fact that $\mathcal{F}$ is not diagonal, the quantization condition in the form of Eq. (3.73) or Eq. (3.81) is replaced by Eq. (3.86) or Eq. (3.87), respectively, if partial waves of angular momenta larger than l_{max} are ignored. The matrices of interest are now finite-dimensional, thereby making the quantization condition a tool of practical use.

There is another problem, namely that the matrix elements of $\mathcal{F}$ contain an infinite sum over angular momenta, see Eq. (3.66). To tackle this problem, we express the product of two spherical harmonics as [144, App. IV]

$$\begin{aligned} &Y_{l_1 m_1}(\Omega)\, Y_{l_2 m_2}(\Omega) \\ &= \sqrt{\frac{(2l_1+1)(2l_2+1)}{4\pi}} \sum_{l,m} (-1)^m \sqrt{2l+1} \begin{pmatrix} l_1 & l_2 & l \\ m_1 & m_2 & -m \end{pmatrix} \begin{pmatrix} l_1 & l_2 & l \\ 0 & 0 & 0 \end{pmatrix} Y_{lm}(\Omega)\,. \end{aligned} \tag{3.88}$$

Here the Wigner 3-j symbols are defined via Clebsch–Gordan coefficients,

$$\begin{pmatrix} l_1 & l_2 & l_3 \\ m_1 & m_2 & m_3 \end{pmatrix} := \frac{(-1)^{l_1 - l_2 - m_3}}{\sqrt{2l_3+1}} \langle l_1 m_1 l_2 m_2 \,|\, l_3, -m_3 \rangle\,, \tag{3.89}$$

and we follow the usual convention to keep the Clebsch–Gordan coefficients real. Combining Eq. (3.88) with Eq. (3.9) shows that

$$\begin{aligned} \mathcal{Y}^{lm}_{l_2 m_2 l_1 m_1} &:= \int \mathrm{d}\Omega_q^\star Y^*_{lm}\left(\Omega_q^\star\right) Y^*_{l_2 m_2}\left(\Omega_q^\star\right) Y_{l_1 m_1}\left(\Omega_q^\star\right) \\ &= \sqrt{\frac{(2l_1+1)(2l_2+1)}{4\pi(2l_1+1)}} \langle l m l_2 m_2 \,|\, l_1 m_1 \rangle \langle l 0 l_2 0 \,|\, l_1 0 \rangle\,. \end{aligned} \tag{3.90}$$

According to the basic rules of angular momentum addition, $|l - l_2| \leq l_1 \leq |l + l_2|$ needs to hold, such that the Clebsch–Gordan coefficients appearing in $\mathcal{Y}^{lm}$ are non-vanishing. Consider $l \geq l_2$. Consequently, $l - l_2 \leq l_1$, which is in turn equivalent to $l \leq l_1 + l_2$. Inserting this into Eq. (3.66) results in [39]

$$\mathcal{F}_{l_2 m_2 l_1 m_1} = \frac{q^\star}{8\pi E^\star}\mathbb{1}_{l_2 m_2 l_1 m_1} - \frac{i}{2E^\star} \sum_{l=0}^{l_1+l_2} \sum_m \frac{\sqrt{4\pi}}{q^{\star l}} c_{lm}^P\left(q^{\star 2}, L\right) \mathcal{Y}^{lm}_{l_2 m_2 l_1 m_1}. \tag{3.91}$$

Since we consider only $l_i \leq l_{\text{max}}$, $i = 1, 2$, the sum appearing in $\mathcal{F}$ is in fact finite.

3.2.8 Lellouch–Lüscher formalism

Next we want to study $\gamma^{(*)}\pi \to \pi\pi$ scattering in the finite volume.[5] Before we do so, it is expedient to study the fully dressed propagator in slightly more detail. That is, we focus on

$$\Delta(P,L) = \int_L \mathrm{d}^4x\, e^{iPx} \left\langle 0 \left| T\left\{\phi(x)\,\phi^\dagger(0)\right\}\right| 0\right\rangle, \tag{3.92}$$

with ϕ an operator that annihilates a single pion. Its Fourier transform with respect to energy reads

$$\tilde{\Delta}\left(x^0, \boldsymbol{P}, L\right) \coloneqq \int \frac{\mathrm{d}P^0}{2\pi} e^{-iP^0x^0} \Delta(P,L)\,. \tag{3.93}$$

Let us choose $x^0 > 0$, such that the factor $e^{-iP^0x^0}$ allows for closing the contour of integration in the lower half complex plane. We can perform the integral via the residue theorem, picking up the contribution of the pole that is fixed via the renormalization conditions stated in Eq. (3.59), to obtain

$$\tilde{\Delta}\left(x^0, \boldsymbol{P}, L\right) = \frac{1}{2\omega_P} e^{-iE_\pi x^0} + \dots \tag{3.94}$$

Here $E_\pi \coloneqq \sqrt{M_\pi^2 + |\boldsymbol{P}|^2}$ is the energy at the pole. The dots denote contributions arising from poles at higher energies (i.e., when intermediate propagators in the loop contributions to the 1PI terms depicted in Fig. 3.1 go on-shell). Alternatively, we can insert a complete set of eigenstates of the Hamiltonian to obtain in complete analogy to Eq. (3.71)

$$\begin{aligned}\tilde{\Delta}\left(x^0, \boldsymbol{P}, L\right) &= L^3 \sum_n e^{-ix^0E_n} \left|\left\langle E_n, \boldsymbol{P}; L \left|\phi^\dagger(0)\right| 0\right\rangle\right|^2 \\ &= L^3 e^{-ix^0E_\pi} \left|\left\langle E_\pi, \boldsymbol{P}; L \left|\phi^\dagger(0)\right| 0\right\rangle\right|^2 + \dots,\end{aligned} \tag{3.95}$$

where $\langle E_\pi, \boldsymbol{P}; L|$ is the lowest-lying state that has overlap with $\phi^\dagger(0)\,|0\rangle$. Since $\phi^\dagger$ has the appropriate quantum numbers to create a single pion, this state is precisely a single pion state with energy E_π. Comparing Eq. (3.94) with Eq. (3.95), we deduce

$$L^3 \left|\left\langle E_\pi, \boldsymbol{P}; L \left|\phi^\dagger(0)\right| 0\right\rangle\right|^2 = \frac{1}{2\omega_P}. \tag{3.96}$$

Now we are ready to tackle the process $\gamma^{(*)}\pi \to \pi\pi$. That is, the object of interest is the correlation function

$$G(P_\mathrm{i}, P_\mathrm{f}, L) \coloneqq \int_L \mathrm{d}^4x \int_L \mathrm{d}^4y\, e^{i(P_\mathrm{f}x - P_\mathrm{i}y)} \left\langle 0 \left| T\left\{\mathcal{O}_1(x)\, J(0)\, \phi^\dagger(y)\right\}\right| 0\right\rangle. \tag{3.97}$$

Here $\phi^\dagger$ creates a single pion, while $\mathcal{O}_1$ is the same operator as the one appearing in Eq. (3.53), that is, it annihilates two pions. Although we are later interested in the electromagnetic current, at this stage J is an arbitrary current that couples the incoming pion of momentum P_i to the outgoing two-pion state with momentum P_f. Hence, the four-momentum injected by the current is $Q = P_\mathrm{f} - P_\mathrm{i}$.

[5] The main reference for this section is Ref. [40], see also Ref. [39].

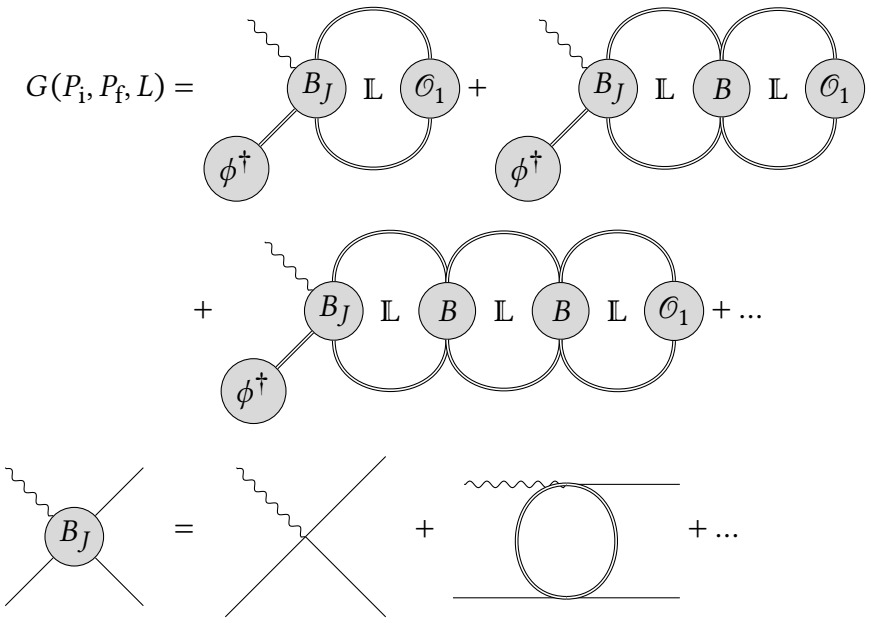

Figure 3.3: The perturbative expansion of the correlation function G in a general EFT [39, 40]. This is to be compared with Fig. 3.1.

To relate finite-volume quantities to infinite-volume ones, we proceed in analogy to Sec. 3.2.5. First, we consider the Fourier transform with respect to energy of G:

$$\mathscr{G}\left(x^0, y^0, \boldsymbol{P}_\mathrm{i}, \boldsymbol{P}_\mathrm{f}, L\right) \coloneqq \int \frac{\mathrm{d}P_\mathrm{i}^0}{2\pi} \int \frac{\mathrm{d}P_\mathrm{f}^0}{2\pi} e^{-i\left(x^0 P_\mathrm{f}^0 - y^0 P_\mathrm{i}^0\right)} G(P_\mathrm{i}, P_\mathrm{f}, L)\,. \tag{3.98}$$

Let $x^0 > 0 > y^0$. Accordingly,

$$\mathscr{G}\left(x^0, y^0, \boldsymbol{P}_\mathrm{i}, \boldsymbol{P}_\mathrm{f}, L\right) = \int_{\mathbb{L}^3} \mathrm{d}^3 x \int_{\mathbb{L}^3} \mathrm{d}^3 y e^{-i(\boldsymbol{P}_\mathrm{f}\cdot\boldsymbol{x} - \boldsymbol{P}_\mathrm{i}\cdot\boldsymbol{y})} \left\langle 0 \left| \mathscr{O}_1(x) J(0) \phi^\dagger(y) \right| 0 \right\rangle. \tag{3.99}$$

We insert a complete set of eigenstates of the Hamiltonian on each side of J. Since $\phi^\dagger(y)$ creates a single pion, it has non-vanishing overlap with the lowest-lying single-particle state, whose energy we denote by E_π. Compared to this, the overlap of $\phi^\dagger(y)$ with all other states in the spectrum is exponentially suppressed, and thus we keep only the leading term arising from $|E_\pi, \boldsymbol{p}; L\rangle$. Using Eq. (3.19) we arrive at

$$\begin{aligned} &\mathscr{G}\left(x^0, y^0, \boldsymbol{P}_\mathrm{i}, \boldsymbol{P}_\mathrm{f}, L\right) \\ &= L^6 e^{iE_\pi y^0} \sum_n e^{-iE_n x^0} \left\langle 0 \left| \mathscr{O}_1(0) \right| E_n, \boldsymbol{P}_\mathrm{f}; L \right\rangle \left\langle E_n, \boldsymbol{P}_\mathrm{f}; L \left| J(0) \right| E_\pi, \boldsymbol{P}_\mathrm{i}; L \right\rangle \left\langle E_\pi, \boldsymbol{P}_\mathrm{i}; L \left| \phi^\dagger(0) \right| 0 \right\rangle. \end{aligned} \tag{3.100}$$

Alternatively, we can compute G to all orders in perturbation theory by extending our abstract EFT to incorporate insertions of the current J. The expansion is depicted in Fig. 3.3. Here B_J is the analogue of the Bethe–Salpeter kernel B, i.e., it sums up all diagrams that are 2PI in the s channel. In addition, $\mathscr{Q}$ denotes the contributions arising from $\phi^\dagger$. Decomposing the loops again via Eq. (3.56)

yields Fig. 3.4, with H the infinite-volume amplitude corresponding to $\pi \to \pi\pi$ with an insertion of the current J. Next, we decompose H with respect to spherical harmonics, $H = \sqrt{4\pi} H_{lm} Y^*_{lm}$, and define $\mathcal{H}^\dagger$ as the row vector in angular-momentum space with components H_{lm}. In complete analogy to Eqs. (3.67) and (3.68) we obtain

$$G(P_\mathrm{i}, P_\mathrm{f}, L) = G_\infty(P_\mathrm{i}, P_\mathrm{f}) + G_\mathrm{cut}(P_\mathrm{i}, P_\mathrm{f}, L), \tag{3.101}$$

with

$$G_\mathrm{cut}(P_\mathrm{i}, P_\mathrm{f}, L) = -\mathcal{Q}\Delta(P_\mathrm{i})\mathcal{H}^\dagger\left[(\eta\mathcal{F})^{-1} + i\mathcal{M}\right]^{-1}\mathcal{Q}_1, \tag{3.102}$$

where Δ denotes the fully dressed single-pion propagator. Inserting this into Eq. (3.98) results in

$$\mathcal{G}\left(x^0, y^0, \boldsymbol{P}_\mathrm{i}, \boldsymbol{P}_\mathrm{f}, L\right) = \mathcal{G}_\infty\left(x^0, y^0, \boldsymbol{P}_\mathrm{i}, \boldsymbol{P}_\mathrm{f}\right) + \mathcal{G}_\mathrm{cut}\left(x^0, y^0, \boldsymbol{P}_\mathrm{i}, \boldsymbol{P}_\mathrm{f}, L\right), \tag{3.103}$$

with

$$\mathcal{G}_\mathrm{cut}\left(x^0, y^0, \boldsymbol{P}_\mathrm{i}, \boldsymbol{P}_\mathrm{f}, L\right) = -\int\frac{\mathrm{d}P^0_\mathrm{i}}{2\pi}\int\frac{\mathrm{d}P^0_\mathrm{f}}{2\pi}e^{-i\left(x^0P^0_\mathrm{f} - y^0P^0_\mathrm{i}\right)}\mathcal{Q}\Delta(P_\mathrm{i})\mathcal{H}^\dagger\left[(\eta\mathcal{F})^{-1} + i\mathcal{M}\right]^{-1}\mathcal{Q}_1. \tag{3.104}$$

First, we perform the integral over P^0_i. Since $y^0 < 0$, the presence of the term $e^{iy^0P^0_\mathrm{i}}$ ensures that we can close the contour of integration with a semicircle in the lower complex plane, picking up the pole of $\Delta(P_\mathrm{i})$ at $P^2_\mathrm{i} = M^2_\pi$, see Eq. (3.59). Accordingly,

$$\mathcal{G}_\mathrm{cut}\left(x^0, y^0, \boldsymbol{P}_\mathrm{i}, \boldsymbol{P}_\mathrm{f}, L\right) = -\frac{1}{2\omega_{P_\mathrm{i}}}e^{iy^0P^0_\mathrm{i}}\int\frac{\mathrm{d}P^0_\mathrm{f}}{2\pi}e^{-ix^0P^0_\mathrm{f}}\mathcal{Q}\mathcal{H}^\dagger\left[(\eta\mathcal{F})^{-1} + i\mathcal{M}\right]^{-1}\mathcal{Q}_1, \tag{3.105}$$

where now $P^0_\mathrm{i} = \sqrt{M^2_\pi + |\boldsymbol{P}_\mathrm{i}|^2} = E_\pi$. Since $x^0 > 0$, the P^0_f integral can be evaluated by closing the contour of integration with a semicircle in the lower half plane, too. Picking up the poles of $[(\eta\mathcal{F})^{-1} + i\mathcal{M}]^{-1}$ leads to

$$\mathcal{G}_\mathrm{cut}\left(x^0, y^0, \boldsymbol{P}_\mathrm{i}, \boldsymbol{P}_\mathrm{f}, L\right) = \frac{1}{2\omega_{P_\mathrm{i}}}e^{iy^0E_\pi}\sum_n e^{-ix^0E_n}\mathcal{Q}\mathcal{H}^\dagger\mathcal{R}_n\mathcal{Q}_1 + \ldots \tag{3.106}$$

Here the sum runs over all poles that lie above the two-pion threshold, but below higher multi-particle thresholds, since only here Eq. (3.102) is valid, the dots include all remaining terms. Furthermore, $\mathcal{R}_n$ is defined in Eq. (3.75).

Inserting Eq. (3.106) into Eq. (3.103) and comparing with Eq. (3.100) reveals

$$L^6\left\langle 0\left|\mathcal{O}_1(0)\right|E_n, \boldsymbol{P}_\mathrm{f}; L\right\rangle\left\langle E_n, \boldsymbol{P}_\mathrm{f}; L\left|J(0)\right|E_\pi, \boldsymbol{P}_\mathrm{i}; L\right\rangle\left\langle E_\pi, \boldsymbol{P}_\mathrm{i}; L\left|\phi^\dagger(0)\right|0\right\rangle = \frac{1}{2\omega_{P_\mathrm{i}}}\mathcal{Q}\mathcal{H}^\dagger\mathcal{R}_n\mathcal{Q}_1 \tag{3.107}$$

for all E_n below higher multi-particle thresholds. Since $\mathcal{Q}$ just equals the contribution arising from an external scalar, $\mathcal{Q} = 1$. Computing the absolute value squared on both sides and expressing the matrix element of $\mathcal{O}_1$ via Eq. (3.76) and the one of $\phi^\dagger$ via Eq. (3.96) yields

$$\left|\left\langle E_n, \boldsymbol{P}_\mathrm{f}; L\left|J(0)\right|E_\pi, \boldsymbol{P}_\mathrm{i}; L\right\rangle\right|^2 = \frac{1}{L^6}\frac{1}{2\omega_{P_\mathrm{i}}}\frac{\mathcal{H}^\dagger\mathcal{R}_n\mathcal{Q}_1\mathcal{Q}_1^\dagger\mathcal{R}_n\mathcal{H}}{\mathcal{Q}_1^\dagger\mathcal{R}_n\mathcal{Q}_1}, \tag{3.108}$$

where we used the fact that $\mathcal{R}_n$ can be effectively treated as Hermitian, as discussed below Eq. (3.76).

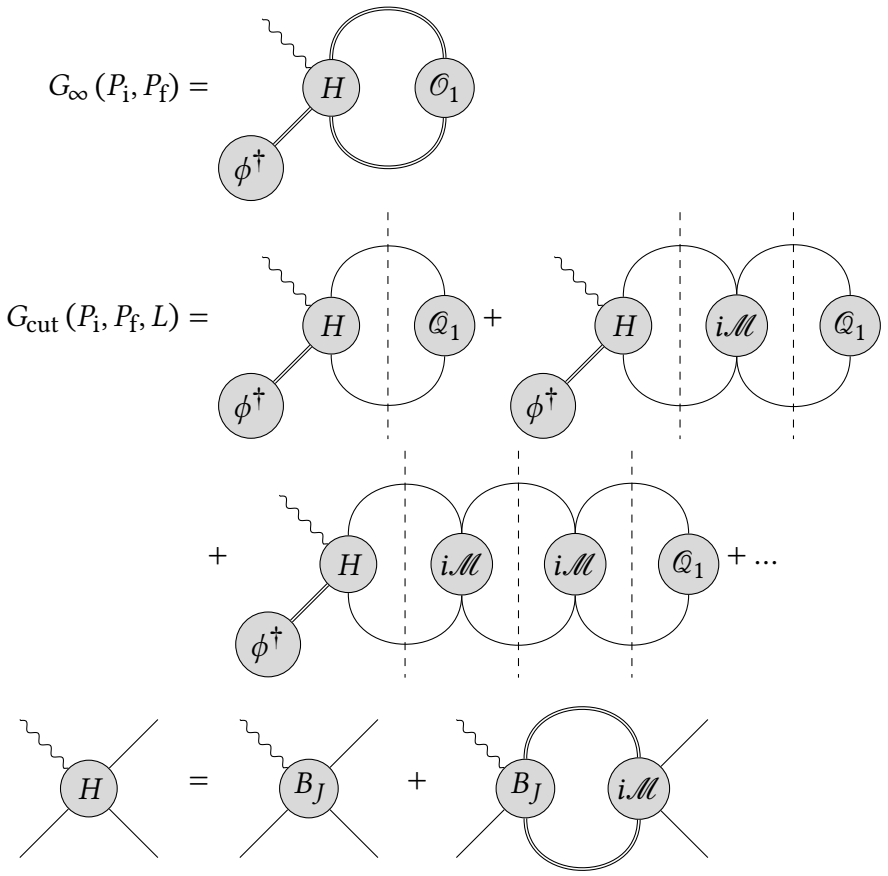

Figure 3.4: The analogue of Fig. 3.2 for the correlation function G.

Introducing $\mathcal{L} \coloneqq (\eta\mathcal{F})^{-1} + i\mathcal{M}$, we can rewrite Eq. (3.75) as

$$\mathcal{R}_n = i \lim_{P^0 \to E_n} \left(P^0 - E_n\right) \mathcal{L}^{-1}. \tag{3.109}$$

Denote the eigenvalues of $\mathcal{L}$ by λ_k, such that

$$\det\left[\mathcal{L}\right] = \prod_k \lambda_k, \qquad \det\left[\mathcal{L}^{-1}\right] = \prod_k \frac{1}{\lambda_k}. \tag{3.110}$$

Thus, $\det[\mathcal{R}_n] = \prod_k r_k$, with

$$r_k \coloneqq i \lim_{P^0 \to E_n} \frac{\left(P^0 - E_n\right)}{\lambda_k\left(P^0\right)} \tag{3.111}$$

the k-th eigenvalue of $\mathcal{R}_n$ and we have made the dependence of λ_k on the energy explicit. Let us now make the additional assumption that there is no degeneracy, that is, for each energy E_n there is only one state in the spectrum.[6] According to the discussion surrounding Eq. (3.73), at this energy $\det[\mathcal{L}] = 0$; therefore, at least one of the eigenvalues $\{\lambda_k\}$ vanishes. If there is indeed no degeneracy,

[6] As explained in Ref. [40, p. 18] (p. 19 in the `arXiv` version), indeed there is no degeneracy as soon as Eq. (3.108) is projected onto a given irreducible representation of the symmetry group of the lattice, see also Sec. 3.4.

only a single eigenvalue vanishes, without loss of generality we say that λ_0 is this eigenvalue. Then Eq. (3.111) enforces $r_k = 0$ for all $k \neq 0$. Since $\mathcal{R}_n$ is effectively Hermitian, we have $r_k \in \mathbb{R}$, and there exists an associated set of orthonormal eigenvectors $\mathcal{V}_k$ of $\mathcal{R}_n$ that constitutes a basis. Accordingly, $\mathcal{R}_n = r_0 \mathcal{V}_0 \mathcal{V}_0^\dagger$, furthermore, we can express $\mathcal{Q}_1$ in this basis: $\mathcal{Q}_1 = \sum_k q_k \mathcal{V}_k$, $q_k \in \mathbb{C}$. Inserting these expressions into Eq. (3.108) and making use of $\mathcal{V}_k^\dagger \mathcal{V}_j = \delta_{kj}$ we arrive at

$$|\langle E_n, \boldsymbol{P}_\mathrm{f}; L \,|J(0)|\, E_\pi, \boldsymbol{P}_\mathrm{i}; L\rangle|^2 = \frac{1}{L^6} \frac{1}{2\omega_{P_\mathrm{i}}} \mathcal{H}^\dagger \mathcal{R}_n \mathcal{H}. \tag{3.112}$$

This is the generalized Lellouch–Lüscher formula, derived in this way for the first time in Ref. [40], stated in a form resembling the expression given in Eq. (33) of Ref. [39] (Eq. (34) in the `arXiv` version).

The key feature of Eq. (3.112) is that the left-hand side can be computed in the finite volume, since it is a matrix element of the operator J between finite-volume states, while the right-hand side contains the infinite-volume scattering amplitude H (more precisely, the corresponding vector $\mathcal{H}$ in angular-momentum space). So it allows for extracting the infinite-volume scattering amplitude from a finite-volume matrix element. However, note that the right-hand side involves the $\pi\pi \to \pi\pi$ scattering amplitude $\mathcal{M}$ (contained in $\mathcal{R}_n$). Thus, an explicit parametrization of $\mathcal{M}$ is needed before $\mathcal{H}$ can be determined. The free parameters of this parametrization are to be fixed via Eq. (3.73).

3.3 Role of the pion mass

Now that we are acquainted with the Lüscher formalism, we can understand the reasons behind the common use of values of the quark masses that exceed the physical ones in lattice-QCD computations.

First, the Gell-Mann–Oakes–Renner relation states that [145]

$$M_\pi^2 = (m_u + m_d) \left| \frac{\langle 0 \,|\overline{u}u|\, 0\rangle}{F_\pi^2} \right|_{m_u, m_d \to 0} + \ldots \tag{3.113}$$

Here m_u is the mass of the up quark, m_d the one of the down quark, u the field associated with the former, F_π the pion decay constant, and the dots denote higher orders in the quark masses. That is, the square of the pion mass is proportional to the masses of the light quarks. This relation is incorporated into LO ChPT, with the corrections being of higher order in ChPT. To be precise, denoting the LO pion mass as M, to NLO

$$M_\pi^2 = M^2 \left\{ 1 + \frac{M^2}{F^2} \left[2l_3^r + \frac{1}{32\pi^2} \ln\left(\frac{M^2}{\mu^2}\right) \right] \right\} \tag{3.114}$$

holds [21]. Here l_3^r is a renormalized LEC, F the pion decay constant in the chiral limit, and μ the renormalization scale. Since the ChPT expansion of the pion mass converges well, independent of their sign the higher-order terms do not alter the core result: the pion mass increases with increasing quark masses. Hence, we might speak about pion-mass dependence instead of quark-mass dependence. Since the models we are going to employ in the analysis of lattice data are phrased in terms of M_π, indeed for the remainder of this thesis we will mostly speak of pion-mass dependence.

Accordingly, low pion masses require low values of the quark masses. These masses show up in the QCD action, and thus in the correlation functions, see Sec. 3.1. To be precise, they are a part of the DIRAC operator, $i\not{D}-m$, with D the covariant derivative and $m = \mathrm{diag}(m_u, m_d, \dots)$ the quark mass matrix. For technical reasons, (a modified and properly discretized version of) this operator needs to be inverted repeatedly in the computation of correlation functions. Traditionally, this inversion gets numerically more costly the lower the smallest eigenvalue of the DIRAC operator, which scales roughly like m_u. That is, the lower the quark masses, the more expensive the computation, making calculations at the physical pion mass challenging. However, algorithmic advances have alleviated this problem [9].

Second, throughout the derivation of LÜSCHER's method, we ignored exponentially suppressed terms, i.e., terms that scale at most like $\exp(-M_\pi L)$. In a numerical computation it needs to be ensured that these corrections are indeed small, that is, $M_\pi L$ needs to be sufficiently large. Hence, the lower the pion mass, the larger the required values of L. At the same time, it is not desirable to increase the lattice spacing a_s too much, because otherwise discretization artifacts become huge. Thus, to obtain large values of $L = a_\mathrm{s} L^\mathrm{lat}$, the number of lattice sites in one spatial direction, L^lat, needs to be large. That is why a lower value of the pion mass requires a higher number of lattice sites, $T^\mathrm{lat} \times (L^\mathrm{lat})^3$, making the computation again more costly.

Third, the derivation of the LÜSCHER formalism presented in Sec. 3.2 takes into account only the lowest-lying intermediate multi-particle states, namely $\pi\pi$ states. There are a lot of additional multi-particle states that increase in relevance the higher the energy. As we discuss in Part II, the mass of the ρ resonance changes only slightly with varying pion mass. On the other hand, the value of the threshold of, e.g., a four-pion state changes drastically. At physical pion masses, the ρ is well above the four-pion threshold and not too far away from the six-pion threshold. Admittedly, phenomenology indicates that the ρ couples almost exclusively to two pions [9]. However, in the energy region above 1 GeV inelastic effects show up that seem to be dominated by four-pion states instead of $K\overline{K}$ states [51].[7] Hence, the current limitations of the LÜSCHER formalism to states with less than four particles put a serious constraint on computations at the physical point [34]. As a workaround, one can resort to computations at pion masses high enough such that the ρ resonance region is at least partly or even completely below the four-pion threshold, which works due to the aforementioned very mild pion-mass dependence of the ρ mass.

3.4 Rotational symmetry and the lattice

Another specific of the lattice requires attention. As discussed in Sec. 3.1, the spatial part of the lattice is a cube with edge length L and spacing a_s. Thus, contrary to the continuum three-dimensional EUCLIDean space of infinite extent, the lattice is not invariant under $O(3)$. Instead, rotational invariance is reduced to those rotations that leave the cube invariant, i.e., the octahedral group including parity. Accordingly, $\pi\pi$ states on the lattice cannot be directly classified via angular momentum, which arises as a quantum number of the irreducible representations (irreps) of $SO(3)$ (more precisely, its double cover $SU(2)$). These irreps are to be replaced by the ones of the symmetry group of the cube. For a given continuum angular momentum J, there are several irreps that can contribute.

As soon as the total momentum $\boldsymbol{P} = (2\pi/L)\mathfrak{P}$ of the two pions is non-vanishing, the situation gets more complicated. To be precise, the lab frame introduced in Sec. 3.2.1 is the rest frame of the

[7] Note that the situation is reversed for the S wave due to the presence of the $f(980)$ resonance at the $K\overline{K}$ threshold. Here, four-pion states become relevant at much higher energies only [146].

$\lvert\mathfrak{P}\rvert^2$	$\mathfrak{P}$
0	$(0,0,0)$
1	$(0,0,1)$
2	$(1,1,0)$
3	$(1,1,1)$
4	$(0,0,2)$

Table 3.1: The bijective relation between $\mathfrak{P}$ and its absolute value squared.

lattice, hence the name boost momentum for $\boldsymbol{P}$ and its integer counterpart $\mathfrak{P} \in \mathbb{Z}^3$. Since the CM frame of the two pions moves with constant velocity with respect to the lattice, relativistic length contraction sets in. From the point of view of the CM the lattice is distorted, thereby reducing the number of symmetries. For an accessible discussion see Ref. [147], the important point for this work is that each $\pi\pi$ level on the lattice corresponds to a state belonging to a certain irrep[8] of the discrete symmetry group under consideration.

Since the lattice is cubic, $\mathfrak{P} = (n,0,0)$, $\mathfrak{P} = (0,n,0)$, and $\mathfrak{P} = (0,0,n)$ with $n \in \mathbb{N}$ are related by rotations that leave the lattice invariant, and in addition, $\mathfrak{P}$ and $-\mathfrak{P}$ are related by parity, which is also a symmetry of the cube. Thus, these apparently different boost vectors describe the same physics, so it is sufficient to consider only one of them (for each n); here the choice to single out the z axis is made. By similar symmetry arguments, $(0,1,1)$, $(1,0,1)$, and $(1,1,0)$ describe the same physics. Accordingly, for low values of $|\mathfrak{P}|^2$, $|\mathfrak{P}|^2$ and $\mathfrak{P}$ are related bijectively, see Table 3.1. This bijective relation breaks down for high values of $|\mathfrak{P}|^2$, e.g., both $\mathfrak{P} = (2,2,1)$ and $\mathfrak{P} = (0,0,3)$ map to $|\mathfrak{P}|^2 = 9$.

[8] In the literature, different naming conventions for the irreps exist. What we will call $B1$ in the following is called B_2 in Ref. [148] and $B2$ is called B_1. Similarly, $A1$ is called A_1 and $E2$ simply E. Compare also Table 5.2 below with Table XVI in Ref. [148].

Part II

Pion-mass dependence of $\pi\pi \to \pi\pi$

The main results of this part have been published in Ref. [149].

Chapter 4

Continuum scattering amplitude

Here we specialize the general form of two-to-two scattering amplitudes discussed in Ch. 2 to $\pi\pi \to \pi\pi$ focusing on the P wave. First, in Sec. 4.1 we express the P wave via ChPT. The resulting expressions are unitarized in Sec. 4.2 via the IAM to allow for a description of the ρ resonance. Lastly, we investigate effects associated with the mass of the strange quark in Sec. 4.3.

4.1 Chiral perturbation theory

Denote the partial wave of $\pi\pi \to \pi\pi$ scattering with isospin I and angular momentum J as t^{IJ}. In $SU(2)$ ChPT it can be expanded according to

$$t^{IJ} = t_2^{IJ} + t_4^{IJ} + t_6^{IJ} + \mathcal{O}\left(\frac{p^8}{\Lambda_\chi^8}\right). \tag{4.1}$$

Here t_k^{IJ} denotes terms of order p^k/Λ_χ^k, pion momenta and masses are collectively denoted by p, and Λ_χ is the breakdown scale of ChPT. In the following, we focus on the P wave, i.e., $I = J = 1$. The explicit expressions of the other partial waves are given in Ref. [149]. The LO terms t_2^{IJ} have been calculated as early as in Ref. [150], the P wave reads

$$t_2^{11}(s) = \frac{s - 4M_\pi^2}{96\pi F^2}. \tag{4.2}$$

The NLO scattering amplitude is given in Ref. [21]; performing the partial-wave projection via Eq. (2.5) yields

$$F^4 \mathrm{Re}\left[t_4^{IJ}(s)\right] = \sum_{i=0}^{2} b_i^{IJ}(s)\,[L(s)]^i + \sum_{i=1}^{3} b_{l_i^r}^{IJ}(s) l_i^r \tag{4.3}$$

for $s \geq 4M_\pi^2$. Here F denotes the pion decay constant in the chiral limit, l_i^r are ordinary renormalized LECs that correspond to terms in the NLO ChPT Lagrangian, and

$$L(s) = \ln\left[\frac{1+\sigma(s)}{1-\sigma(s)}\right], \tag{4.4}$$

with σ the phase space as given in Eq. (2.29). The coefficients b_i^{IJ} and $b_{l_i^r}^{IJ}$ are functions of Mandelstam s and the pion mass only. They are displayed explicitly in App. A. It is possible to bring $\mathrm{Re}[t_4^{11}]$ into a slightly more compact form as compared to Eq. (4.3), see Ref. [151].

The NNLO part of the scattering amplitude has been computed in Ref. [64]. Again, it can be partial-wave projected using Eq. (2.5). However, this time it is significantly more challenging to obtain a result in closed analytic form. The detailed procedure is described in Ref. [149], the result reads

$$\begin{aligned} F^6 \mathrm{Re}\left[t_6^{IJ}(s)\right] = &\sum_{i=0}^{4} c_i^{IJ}(s)\,[L(s)]^i + \sum_{i=1}^{3} c_{l_i^r}^{IJ}(s) l_i^r + c_{l_3^{r2}}^{IJ}(s)\left(l_3^r\right)^2 \\ &+ d^{IJ}(s)\Big[\mathrm{Li}_3\big(\sigma_+(s)\big) + \mathrm{Li}_3\big(\sigma_-(s)\big) - L(s)\,\mathrm{Li}_2\big(\sigma_-(s)\big)\Big] + P^{IJ}(s), \end{aligned} \tag{4.5}$$

again for $s \geq 4M_\pi^2$. Here

$$\sigma_\pm(s) := \frac{2\sigma(s)}{\sigma(s) \pm 1}. \tag{4.6}$$

Moreover, polylogarithms show up, whose explicit form reads

$$\mathrm{Li}_n(x) := \frac{(-1)^{n-1}}{(n-2)!} \int_0^1 \frac{\ln^{n-2}(t)\ln(1-xt)}{t} \mathrm{d}t = \sum_{k=1}^{\infty} \frac{x^k}{k^n}. \tag{4.7}$$

The coefficients c_i^{IJ}, $c_{l_i^r}^{IJ}$, and $c_{l_3^{r2}}^{IJ}$ depend not only on s and the pion mass but also on the renormalization scale μ, which appears via chiral logarithms; the explicit expressions are given in App. A. In addition, three further LECs show up via the polynomial

$$P^{11}(s) := \frac{s-4M_\pi^2}{\pi}\left(r_a M_\pi^4 + r_b s M_\pi^2 + r_c s^2\right). \tag{4.8}$$

More specifically, the three LECs can be written in terms of the renormalized conventional NNLO LECs r_{2-6}^r, r_F^r as defined in Refs. [65, 152] according to

$$\begin{aligned} r_a &:= \frac{r_2^r}{96} + \frac{r_3^r}{24} - \frac{r_4^r}{24} + \frac{3r_5^r}{20} - \frac{r_6^r}{60} - \frac{r_F^r}{12288\pi^4}, \\ r_b &:= -\frac{r_3^r}{96} + \frac{r_4^r}{32} - \frac{3r_5^r}{40} + \frac{r_6^r}{120}, \\ r_c &:= \frac{3}{320}(r_5^r + r_6^r). \end{aligned} \tag{4.9}$$

Up to now, we have discussed only the real parts of the partial waves. To obtain the imaginary parts, we insert the expansion (4.1) into the unitarity condition (2.16) and equate the terms of different chiral order on both sides, resulting in

$$\begin{aligned} &\mathrm{Im}\left(t_2^{IJ}\right) = 0, \\ &\mathrm{Im}\left(t_4^{IJ}\right) = \sigma\left|t_2^{IJ}\right|^2 = \sigma\mathrm{Re}\left(t_2^{IJ}\right)^2, \\ &\mathrm{Im}\left(t_6^{IJ}\right) = 2\sigma\mathrm{Re}\left(t_2^{IJ}\left(t_4^{IJ}\right)^*\right) = 2\sigma t_2^{IJ}\mathrm{Re}\left(t_4^{IJ}\right), \end{aligned} \tag{4.10}$$

where we made use of the fact that for $s \in \mathbb{R}$ the LO contributions are purely real, see also Eq. (4.2). That is, the ChPT expansion (4.1) does not satisfy unitarity exactly, but only perturbatively. This failure is associated with the fact that ChPT on its own does not allow for a description of resonances. However, it allows us to easily compute the imaginary parts of the partial waves, given only the real parts, i.e., Eqs. (4.2), (4.3), and (4.5).

So far we focused on real values of MANDELSTAM s above the scattering threshold. Noting that the expressions of the partial waves are holomorphic, we can, via the uniqueness of analytic continuation, obtain the partial waves for arbitrary $s \in \mathbb{C}$ simply by promoting s to be complex. It is worth noting that Eq. (4.3) and Eq. (4.5) develop non-vanishing imaginary parts for general complex s. Furthermore, Eq. (4.10) breaks down as soon as one leaves the scattering region, neither of which is a problem.

Finally, we turn our attention to the pion decay constant in the chiral limit. It can be related to the physical pion decay constant F_π via ChPT, to NLO this relation is given in Ref. [21], while the NNLO result is discussed in Ref. [65], see Ref. [153] for a slightly more convenient expression. Both results are given in terms of M, the pion mass to LO in ChPT. Using ChPT to replace M by M_π, we obtain

$$F_\pi = F\left[1 + F_4\frac{M_\pi^2}{16\pi^2F^2} + F_6\left(\frac{M_\pi^2}{16\pi^2F^2}\right)^2\right], \tag{4.11}$$

with

$$\begin{aligned} F_4 &:= 16\pi^2 l_4^r - \ln\left(\frac{M_\pi^2}{\mu^2}\right), \\ F_6 &:= \left(16\pi^2\right)^2 r_F^r - 16\pi^2\left(l_2^r + \frac{1}{2}l_1^r + 32\pi^2 l_3^r l_4^r\right) - \frac{13}{192} \\ &\quad + \left(16\pi^2\left(7l_1^r + 4l_2^r - l_4^r\right) + \frac{29}{12}\right)\ln\left(\frac{M_\pi^2}{\mu^2}\right) - \frac{3}{4}\ln^2\left(\frac{M_\pi^2}{\mu^2}\right) \end{aligned} \tag{4.12}$$

the NLO and NNLO coefficient, respectively. Here μ is the renormalization scale, and throughout this work we stick to the common choice $\mu = 770\,\text{MeV}$.

4.2 Inverse-amplitude method

As alluded to in the discussion of perturbative unitarity in the form of Eq. (4.10), ChPT alone does not allow for a description of resonances. To improve on this, the K matrix as given in Eq. (2.11) is matched to ChPT, i.e., Eq. (4.1), at low energies, taking perturbative unitarity into account:[1]

$$\begin{aligned} K &= T^{-1} + i\sigma \\ &= \frac{1}{t_2 + t_4} + i\frac{\text{Im}\,(t_4)}{t_2^2}. \end{aligned} \tag{4.13}$$

This expression for K is not real, thereby violating unitarity. However, expanding this to NLO in ChPT results in

$$\begin{aligned} K &= \frac{1}{t_2} - \frac{t_4}{t_2^2} + i\frac{\text{Im}\,(t_4)}{t_2^2} \\ &= \frac{t_2 - \text{Re}\,(t_4)}{t_2^2}, \end{aligned} \tag{4.14}$$

with K indeed purely real. That is,

$$T = \frac{t_2^2}{t_2 - t_4}. \tag{4.15}$$

[1] From here on, we drop the superscript IJ for notational convenience. To avoid confusion with MANDELSTAM t, we write T instead of t^{IJ}. The only explicit expressions of relevance in this work are the ones for the $\pi\pi$ P wave, but note that the IAM itself is not restricted to the P wave; in fact, it is not even restricted to $\pi\pi$ scattering.

This expression is precisely the so-called IAM for a single channel at NLO [55–58] (for the coupled channel calculation, see Ref. [133]). This derivation makes it clear that the IAM is obtained by matching the general K-matrix representation with ChPT. There is one subtle point: Eq. (4.15) can be obtained by solely expanding $T^{-1} = 1/(t_2 + t_4)$, bypassing the K matrix and perturbative unitarity. However, in this way it is not a priori clear that the resulting expression (4.15) satisfies unitarity as given in Eq. (2.8), while the derivation presented here makes this obvious. Moreover, the K matrix turns out to be real only due to perturbative unitarity, which is therefore a mandatory ingredient to obtain an amplitude that fulfills unitarity. Another subtle point is that, according to the derivation presented here, Eq. (4.15) is a priori valid only along the real axis above threshold, where unitarity applies. However, t_2 is an entire function and t_4 a holomorphic function except for branch points at threshold and at zero (the latter corresponding to the left-hand cut). Thus, Eq. (4.15) can be analytically continued into the entire complex plane apart from those branch points and possible zeros of the denominator. Furthermore, since at low energies Eq. (4.15) agrees with the ChPT expansion, the former inherits a left-hand cut from ChPT, which agrees with the ChPT left-hand cut to NLO. Even more important, when continued to the second Riemann sheet via Eq. (2.27), the IAM exhibits poles associated with resonances. In particular, the two poles (one in the upper and one in the lower half plane) associated with the ρ resonance show up in the P wave.

The same construction can be carried out to higher orders, e.g., NNLO:

$$\begin{aligned} K &= T^{-1} + i\sigma \\ &= \frac{1}{t_2 + t_4 + t_6} + i\sigma \\ &= \frac{1}{t_2}\frac{1}{1 + \frac{t_4+t_6}{t_2}} + i\sigma \\ &= \frac{1}{t_2}\left[1 - \frac{t_4 + t_6}{t_2} + \frac{t_4^2}{t_2^2}\right] + i\sigma. \end{aligned} \tag{4.16}$$

To show that this expression is indeed real, perturbative unitarity, i.e., Eq. (4.10), can be used again:

$$\begin{aligned} \mathrm{Im}\,(K) &= \frac{1}{t_2^3}\left[\mathrm{Im}\left(t_4^2\right) - t_2\left(\mathrm{Im}\,(t_4) + \mathrm{Im}\,(t_6)\right)\right] + \sigma \\ &= \frac{1}{t_2^3}\left[2\mathrm{Re}\,(t_4)\,\mathrm{Im}\,(t_4) - t_2\left(\mathrm{Im}\,(t_4) + \mathrm{Im}\,(t_6)\right)\right] + \sigma \\ &= \frac{1}{t_2^3}\left[2\mathrm{Re}\,(t_4)\,\sigma t_2^2 - t_2\left(\sigma t_2^2 + 2\sigma t_2 \mathrm{Re}\,(t_4)\right)\right] + \sigma \\ &= -\sigma + \sigma \\ &= 0. \end{aligned} \tag{4.17}$$

That is,

$$K = \frac{1}{t_2^3}\left[t_2^2 - t_2\mathrm{Re}\,(t_4 + t_6) + \mathrm{Re}\,(t_4)^2 - \mathrm{Im}\,(t_4)^2\right] \tag{4.18}$$

and [154, 155]

$$T = \left\{\frac{1}{t_2}\left[1 - \frac{t_4 + t_6}{t_2} + \frac{t_4^2}{t_2^2}\right]\right\}^{-1} = \frac{t_2^2}{t_2 - t_4 - t_6 + \frac{t_4^2}{t_2}}. \tag{4.19}$$

There is an additional subtlety in the derivation of Eqs. (4.15) and (4.19), namely, it proceeds via inverting the partial wave T. It is not guaranteed that T is invertible for all values of s under consideration. Indeed, as a consequence of chiral symmetry, some partial waves vanish at certain s values below threshold, the ADLER zeros [156]. Hence, these partial waves are not invertible at those positions. Since the ADLER zeros do not interfere with the right-hand cut, the derivation of Eqs. (4.15) and (4.19) goes through, but problems might arise in the analytic continuation of these expressions away from the right-hand cut, especially to the sub-threshold region. This is where an alternative derivation by means of dispersion relations comes in handy. It was carried out in Ref. [58] for the NLO IAM and adapted in Ref. [154] for the NNLO IAM. The advantage of a dispersive derivation is that the poles in T^{-1} and its ChPT expansion associated with the ADLER zeros can be taken care of via the residue theorem, as shown at NLO in Ref. [157] and NNLO in Ref. [94], yielding the so-called modified IAM. However, the $\pi\pi \to \pi\pi$ P wave of interest is free of ADLER zeros, so that we stick to the ordinary IAM.

When searching for resonance poles on the second RIEMANN sheet of the NNLO P wave IAM, a problem arises: on top of the pair of poles associated with the ρ resonance an additional pair of poles shows up, for the denominator of Eq. (4.19) includes higher powers of MANDELSTAM s than the one of Eq. (4.15). This pair is not associated with any physical resonance. At sensible values of the LECs the additional poles are very deep in the complex plane and do not affect the physical region sizably. Nevertheless, a numerical search for poles needs to be guided such that it converges towards the correct pole.

In passing we stress that the IAM is far from perfect. It fulfills elastic unitarity in the s channel exactly. Physically, the unitarization of the ChPT expansion corresponds to taking into account iterated $\pi\pi$ rescattering, as explored in more detail in Ch. 10. However, this rescattering is not incorporated into the t channel and u channel, and thus the IAM is not crossing symmetric. Stated differently, while the IAM improves the ChPT description of $\pi\pi \to \pi\pi$ along the right-hand cut, it does nothing to improve the left-hand cut. Nevertheless, since ChPT is crossing symmetric, and the IAM resembles ChPT at low energies, the IAM describes the left-hand cut correctly to the employed order of ChPT [154].

4.2.1 Perturbative expansion of the pole trajectory

The derivation of the IAM in Sec. 4.2 makes it clear that the IAM resembles ChPT at low energies, while it improves on it in the resonance region. However, a priori this improvement focuses on the energy dependence only. Concerning the pion-mass dependence, the situation is less clear. Of course, if both the energy and the pion mass are small, ChPT is recovered, but if the energy is in the resonance region, i.e., beyond the breakdown scale of plain ChPT, with the pion mass still being small, it is not guaranteed that the results are in agreement with constraints stemming from chiral symmetry.

To be precise, according to chiral symmetry the expansion of the mass m of a mesonic resonance and its width Γ in terms of M, the pion mass to LO ChPT, reads [158]:

$$\begin{aligned} m &= a_0 + a_2 M^2 + a_3 M^3 + O(M^4), \\ \Gamma &= b_0 + b_2 M^2 + b_3 M^3 + O(M^4). \end{aligned} \tag{4.20}$$

Here a_k and b_k, $k \in \{0, 2, 3\}$, are constants. Equation (4.20) has a few striking features. First, note that according to Eq. (3.113) $M^2 \propto m_q$, with m_q the mass of the light quarks (i.e., the up and down

quark). Hence, odd powers of M have a branch point at $m_q = 0$, rendering the expansion non-analytical if rewritten in terms of m_q. While there is no term linear in M in Eq. (4.20), such non-analytic contributions arise if a_3 or b_3 do not vanish. This can happen only if there is an interaction coupling the resonance to a pion and another resonance of the same mass m. In the case of interest, the ρ resonance, this happens if the ω resonance is taken into account and assumed to be mass-degenerate with the former. In that case, the coefficients a_3 and b_3 scale with $g_{\omega\rho\pi}$, the coupling of the $\omega \to \rho\pi$ interaction [159]. Based on this, in Ref. [87] the coupling $g_{\omega\rho\pi}$ was extracted from an analysis of $\pi\pi \to \pi\pi$ lattice data. However, the IAM is based on plain ChPT without any explicitly added resonances, and therefore a term of order M^3 is not expected to show up in the case of interest. Thus, if not explicitly stated otherwise, we will set $a_3 = b_3 = 0$ from here on. Second, note that terms of order $M^n \ln[M^2/\mu^2]$, with $n \geq 0$, are in general not forbidden by chiral symmetry, again yielding branch points at vanishing mass. The non-trivial constraint stated in Eq. (4.20) is that such logarithms show up at order M^4 earliest. In particular, there is no term proportional to $M^2 \ln[M^2/\mu^2]$. This constraint is not fulfilled by several unitarization methods, as explained in Ref. [158]. Thus, it is worthwhile to check explicitly if the NNLO IAM is in accordance with Eq. (4.20) (the NLO IAM was already tested in Ref. [158]). To do so, we follow the procedure suggested ibidem.

For an explicit check, it is beneficial to rewrite Eq. (4.20) via the pole position s_{pole}, see Eq. (2.30), as

$$\begin{aligned} s_{\text{pole}} &= \left(m - \frac{i}{2}\Gamma\right)^2 \\ &= \left(a_0 - \frac{i}{2}b_0\right)^2 + 2\left(a_0 - \frac{i}{2}b_0\right)\left(a_2 - \frac{i}{2}b_2\right)M^2 + O\left(M^4\right). \end{aligned} \tag{4.21}$$

We aim to determine the pole position from the IAM as an expansion in the pion mass and check if it agrees with Eq. (4.21). Since we computed the ChPT amplitudes in terms of M_π instead of M, we work with the former. That is, we expand the pole as

$$s_{\text{pole}} = s_0 + \sum_{k=1}^{\infty}\left(s_k + s_k^L \ln\left[\frac{M_\pi^2}{\mu^2}\right]\right)M_\pi^k, \tag{4.22}$$

with s_0, s_k, and s_k^L being constants. Expressing M_π in terms of M via ChPT this expansion can be rewritten in terms of M. In particular, in this way we see that Eq. (4.21) is equivalent to $s_{\text{pole}} = s_0 + s_2 M_\pi^2 + O(M_\pi^4)$. Inserting Eq. (4.15) and Eq. (4.19) into Eq. (2.34) yields

$$0 = t_2 - t_4 + 2i\sigma t_2^2 \tag{4.23}$$

at NLO and

$$0 = t_2 - t_4 + 2i\sigma t_2^2 + \frac{t_4^2}{t_2} - t_6 \tag{4.24}$$

at NNLO at s_{pole}. The expansion (4.22) is inserted into these two conditions and the result is expanded around $M_\pi = 0$. In addition to the logarithms in Eq. (4.22), there are polylogarithms in the ChPT amplitudes. Hence, in fact, we deal with an expansion in terms of $M_\pi^k \ln[M_\pi^2/\mu^2]^j$, $k, j \in \mathbb{N}_0$. Since Eqs. (4.23) and (4.24) need to hold for all values of M_π, each of the coefficients in the expansion needs to vanish separately. Thereby, we obtain a set of equations for the unknowns s_0, s_k, and s_k^L. Keeping all terms below order M_π^4, at NLO the equations can be solved analytically, resulting in

$$s_{\text{pole}}^{\text{NLO}} = \frac{288F^2\pi^2 + (45 - 18i\pi)M_\pi^2}{2 - 3i\pi + 288\pi^2\left(l_2^r - 2l_1^r\right)} + O\left(M_\pi^4\right). \tag{4.25}$$

So the NLO IAM is indeed in accordance with the constraints imposed by chiral symmetry on the pole position, as already stated in Ref. [158] without giving an explicit form of the coefficients. Note that there is another solution at threshold, $s_{\text{pole}} = 4M_\pi^2$, which is, however, spurious, since at threshold the zero in the numerator and denominator of the NLO IAM cancel.

At NNLO, the truncated system of equations cannot be solved analytically in a straightforward manner, so we rely on a numerical solution. To that end, we replace the LECs by their numerical values as obtained in the fits to lattice data, which are described in Ch. 6. Since the NNLO IAM has two genuine poles, we need to guide the numerical routine towards the correct one, the ρ pole. Using `Mathematica`, it is sufficient to constrain $\text{Re}(s_0)$ to lie within reasonable bounds, e.g., $0.4\,\text{GeV}^2 < \text{Re}(s_0) < 0.8\,\text{GeV}^2$. We then repeat this procedure for several different sets of values of the LECs. In all cases, all coefficients below order M_π^4 are (within the error stemming from machine precision) zero, except for s_0 and s_2, confirming that the NNLO IAM is in agreement with the chiral constraints, too.

4.3 Kaon-mass dependence

Up to now, we have worked with $SU(2)$ ChPT, i.e., we took only up and down quarks into account. Equivalently speaking, we focused on the role of pions, which is motivated by their dominant role in ρ physics. In addition, the lattice computations whose results we are analyzing in this work are carried out with degenerate up and down quarks, that is, they are explicitly isospin symmetric. Moreover, the extension of the IAM to coupled channels suffers from conceptual problems, most dominantly issues in its construction that are related to left-hand cuts, see Ref. [93] and references therein. For these reasons we work with the isospin symmetric $SU(2)$ IAM.

Nevertheless, the lattice datasets are obtained at different values of m_s, so one might wonder how to take this into account. Fortunately, in Refs. [160, 161] $SU(2)$ ChPT has been matched to $SU(3)$ ChPT to determine the kaon-mass dependence of the $SU(2)$ LECs. Focusing on the constants that are of relevance for the $SU(2)$ IAM, the results obtained ibidem can be recast into

$$\begin{aligned} F^{\text{matched}}\left(M_{K\pi}^2\right) &= F\left[1 + f\left(M_{K\pi}^2\right) - f\left(\overline{M}_{K\pi}^2\right)\right], \\ f\left(M_{K\pi}^2\right) &\coloneqq \frac{M_{K\pi}^2}{F^2}\left[8L_4^r - \frac{1}{32\pi^2}\ln\left(\frac{M_{K\pi}^2}{\mu^2}\right)\right], \end{aligned} \tag{4.26}$$

as well as

$$l_i^{r,\text{matched}}\left(M_{K\pi}^2\right) = l_i^r - \frac{a_i}{768\pi^2}\ln\left(\frac{M_{K\pi}^2}{\overline{M}_{K\pi}^2}\right), \tag{4.27}$$

with $a_1 = 1$, $a_2 = 2$, $a_3 = 4/3$. Here

$$M_{K\pi}^2 \coloneqq \left(M_K^2 - \frac{1}{2}M_\pi^2\right), \qquad \overline{M}_{K\pi}^2 \coloneqq \left(\overline{M}_K^2 - \frac{1}{2}\overline{M}_\pi^2\right), \tag{4.28}$$

where the values of the masses at the physical point are indicated with bars and L_4^r is an $SU(3)$ LEC. The formulae as shown here incorporate only NLO contributions. It is not feasible to take NNLO effects into account, for then additional LECs show up, whose values are known only poorly, if at all.

To estimate the impact of the kaon-mass dependence, we need to fix L_4^r. While the determination of this LEC from phenomenology is tricky and accompanied with large uncertainties [162], the

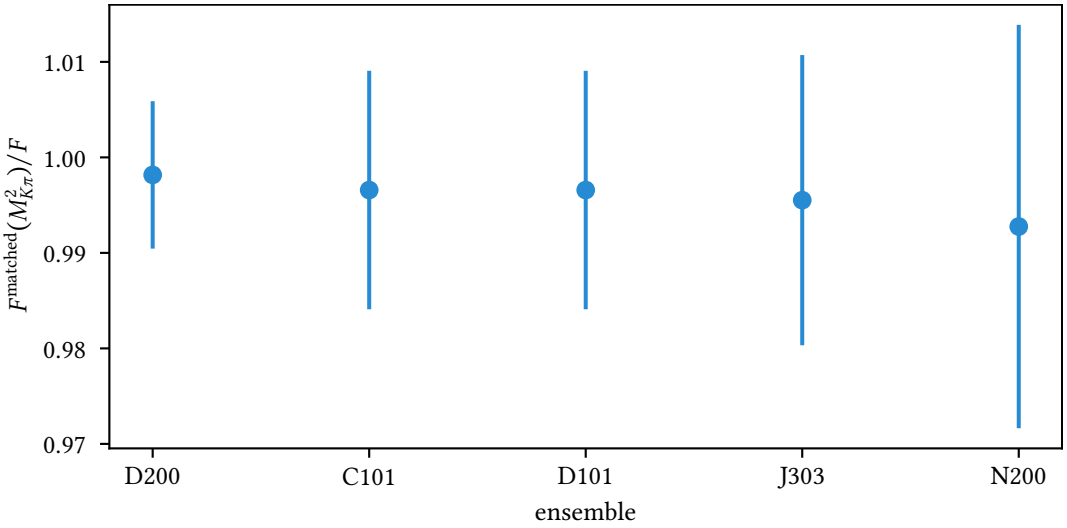

Figure 4.1: The pion decay constant as a function of M_π and M_K for the CLS data. The datasets are sorted in order of increasing pion mass from left to right.

Flavour Lattice Averaging Group (FLAG) provides an $N_\text{f} = 2+1+1$ value $L_4^r = 0.09(34)\times 10^{-3}$ [47, 163] that we use as an estimate. In Fig. 4.1 we display the pion decay constant at the masses of the different datasets of the Coordinated Lattice Simulations (CLS) collaboration that are introduced in more detail in Table 5.1. The error bars incorporate the sizable error of L_4^r. The central value deviates less than 1 % from the physical one in all cases. Even when the errors are taken into account, the deviation is at most 3 % in case of the N200 dataset and smaller in all other cases. In addition, note that the errors are correlated, i.e., the data points in Fig. 4.1 are shifted in sync either all upwards or all downwards if L_4^r is varied. Similarly, the kaon-mass dependence of the l_i^r turns out to be mild. As will become clear in Ch. 6 these effects are too small to be of great significance in our analysis, so we treat F and the LECs as kaon-mass independent in the following.

Chapter 5

Lattice data

Building up on the general discussion of scattering on the lattice in Ch. 3, in this chapter we discuss the specifics of $\pi\pi$ scattering on the lattice and take a close look at several available datasets. To this end, we explicitly display some finite volume energy levels in Sec. 5.1 and investigate Lüscher's quantization condition for the special case of the $\pi\pi$ P wave in Sec. 5.2.

5.1 Energy levels

Consider the CM energy $E^\star = 2\sqrt{(q^\star)^2 + M_\pi^2}$ of the two pions and their energy E in the lab frame (the rest frame of the lattice) as introduced in Sec. 3.2.1. Translating the former into lattice units by multiplying with the appropriate power of the lattice spacing a yields

$$a^2(E^\star)^2 = 4\left(a^2(q^\star)^2 + a^2M_\pi^2\right) = 4\left(\Xi^2(\mathfrak{q}^\star)^2 + a^2M_\pi^2\right), \qquad \Xi \coloneqq \frac{2\pi}{L^{\text{lat}}\xi}. \tag{5.1}$$

Here we have introduced $q^\star =: 2\pi\mathfrak{q}^\star/L$.[1] Similarly, translating the lab frame energy E into lattice units results in

$$(aE)^2 = \left(\sqrt{\Xi^2\left|\mathfrak{P}\right|^2 + (aM_\pi)^2} + \sqrt{\Xi^2\left|\mathfrak{P} - \mathfrak{k}\right|^2 + (aM_\pi)^2}\right)^2, \tag{5.2}$$

with $\mathfrak{P}, \mathfrak{k}$ the integer triplets corresponding to the boost momentum P and the momentum k of a single pion, respectively, see Eq. (3.18). Combining this with Eq. (3.5) gives an expression for all allowed free CM energy levels for a fixed lattice geometry:

$$a^2(E^\star)^2 = \left(\sqrt{\Xi^2\left|\mathfrak{P}\right|^2 + (aM_\pi)^2} + \sqrt{\Xi^2\left|\mathfrak{P} - \mathfrak{k}\right|^2 + (aM_\pi)^2}\right)^2 - \Xi^2\mathfrak{P}^2, \quad \mathfrak{P}, \mathfrak{k} \in \mathbb{Z}^3. \tag{5.3}$$

Using Eq. (5.1), this can be translated into the corresponding values of $(\mathfrak{q}^\star)^2$ [164]. Furthermore, Eqs. (3.5) and (5.1) allow for an expression of the Lorentz factor $\gamma = E/E^\star$ solely in terms of lattice quantities:

$$4\left(\gamma^2 - 1\right) = \frac{\left|\mathfrak{P}\right|^2}{(\mathfrak{q}^\star)^2 + \left(\frac{aM_\pi}{\Xi}\right)^2}. \tag{5.4}$$

[1] Note that $\mathfrak{q}^\star$ is a real number, not necessarily an integer.

collaboration	name	M_π/MeV	M_K/MeV	L^{lat}	$a \times 10^4$/MeV	ξ
CLS	N401	284	–	48	3.9	1
	N200	283	465	48	3.2	1
	J303	258	474	64	2.5	1
	C101	223	474	48	4.4	1
	D101	223	474	64	4.4	1
	D200	200	482	64	3.2	1
HadSpec	840_20	391	550	20	1.8	3.4
	840_24	391	550	24	1.8	3.4
	860_32	236	500	32	1.7	3.5

Table 5.1: An overview of the lattice ensembles analyzed in this work. The values of the masses, the spacings a, and the anisotropies ξ are only approximate.

As discussed in Sec. 3.4, the pions on the lattice are classified via finite-volume irreps. For a fixed irrep, the number of allowed free energy levels is reduced, i.e., only a subset of Eq. (5.3) constitutes the spectrum; this subset is given by the poles of Lüscher's quantization condition, see Sec. 5.2.

Energy levels of a pair of interacting pions have been computed by many different collaborations. Here, we focus on the levels of Ref. [36], which have been computed on gauge configurations provided by the CLS collaboration, as well as the ones by the Hadron Spectrum (HadSpec) collaboration presented in Refs. [82, 165]. Each collaboration has computed the energy levels corresponding to different pion masses and lattice spacings. Table 5.1 gives an overview over the different datasets, called ensembles in the following. Exemplarily, both the lowest-lying free energy levels as well as the interacting ones of the CLS ensemble D101 are shown in Fig. 5.1. Clearly, the levels as obtained in the computation are shifted with respect to the free ones. It is precisely this shift that allows for an extraction of scattering information via Lüscher's method.

In addition to the $\pi\pi$ energy levels, CLS computed the values of the pion decay constant on all ensembles except for N401 [166], which is thus excluded from our analysis.

5.2 The quantization condition

Ignoring contributions from partial waves with $l \geq 3$, performing the projection onto finite volume irreps, and using the fact that S and P waves decouple, Lüscher's quantization condition in the form of Eq. (3.87) can be reduced to a simple quantization condition for the P wave that reads [148]:

$$\cot\left[\delta\left(\mathfrak{q}^{\star 2}\right)\right] = \frac{1}{\mathfrak{q}^\star \gamma \pi^{3/2}} \left\{ Z_{00}^{\mathfrak{P}}\left(1, \mathfrak{q}^{\star 2}\right) + \frac{1}{\mathfrak{q}^{\star 2}} \left[\alpha_{20}^{\mathfrak{P},\Lambda} Z_{20}^{\mathfrak{P}}\left(1, \mathfrak{q}^{\star 2}\right) + \alpha_{22}^{\mathfrak{P},\Lambda} Z_{22}^{\mathfrak{P}}\left(1, \mathfrak{q}^{\star 2}\right) \right] \right\}, \tag{5.5}$$

which will be abbreviated as

$$\cot\left[\delta\left(\mathfrak{q}^{\star 2}\right)\right] = \mathscr{Z}\left(\mathfrak{q}^{\star 2}\right). \tag{5.6}$$

In this form it depends not only on the lattice characteristics and the boost momentum $\mathfrak{P}$, but also on the irrep Λ the two pions live in. Here $\alpha_{lm}^{\mathfrak{P},\Lambda}$ are numerical coefficients, whose values are given

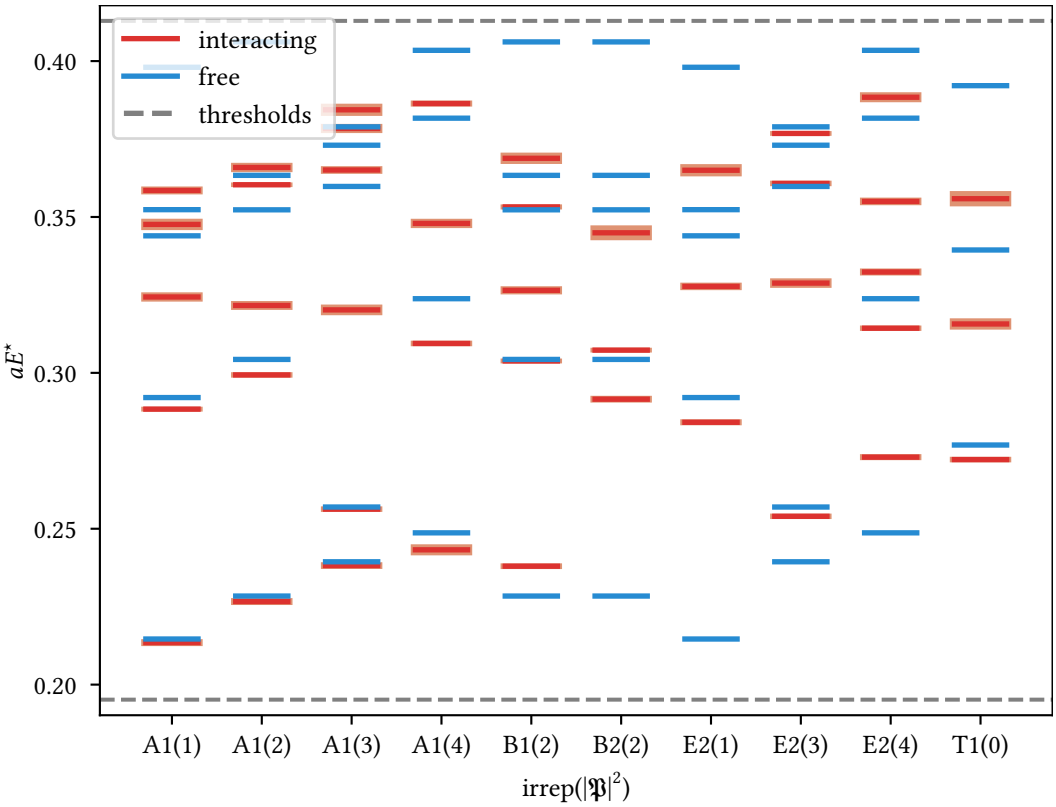

Figure 5.1: The lowest-lying free energies in the CM frame on a lattice with $L^{\text{lat}} = 64$ for different values of the irrep and boost, see also Table 3.1. In addition, the interacting energy levels of the ensemble D101 are shown, including their error bands. The lower-lying dashed line marks the $\pi\pi$ threshold, while the upper one corresponds to the $K\overline{K}$ threshold. Each free energy level is associated with a pole of $\mathscr{Z}$, see Sec. 5.2. The trivial free energies located at the $\pi\pi$ threshold are excluded from the plot.

Λ \ $\mathfrak{P}$	000	001 / 002	110	111
A1		2	$-1-\sqrt{6}i$	$-2\sqrt{6}i$
B1			$-1+\sqrt{6}i$	
B2			2	
E2		-1		$\sqrt{6}i$
T1				

Table 5.2: The values of the coefficients appearing in the quantization condition. Here Λ labels the irrep and $\mathfrak{P}$ the boost momentum. To obtain the correct values for $\alpha_{lm}^{\mathfrak{P},\Lambda}$, divide the values given in the table by $\sqrt{5}$. Then, the real part yields the value of $\alpha_{20}^{\mathfrak{P},\Lambda}$, while the imaginary part times i is the value of $\alpha_{22}^{\mathfrak{P},\Lambda}$. Empty entries correspond to vanishing coefficients.

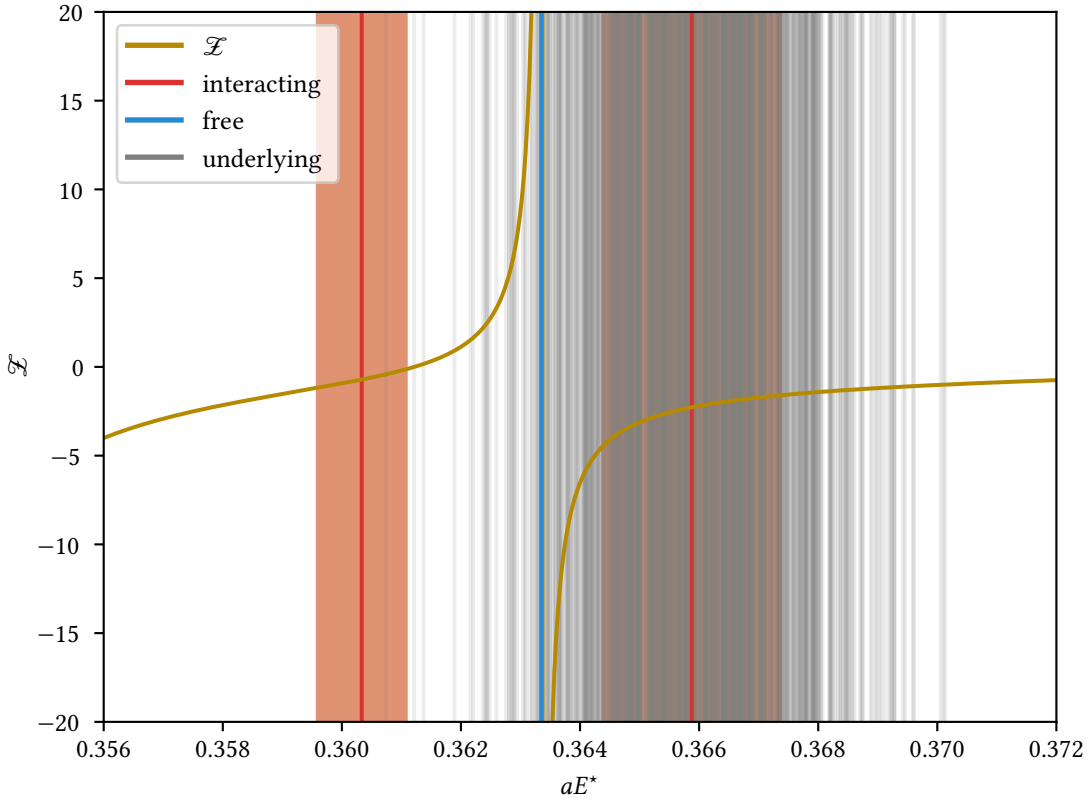

Figure 5.2: The right-hand side of the quantization condition (5.6) as a function of the energy with $L^{\text{lat}} = 64$, $\mathfrak{P} = (1,1,0)$, and $\Lambda = \text{A1}$. Shown is the region around one pole, which corresponds to a free energy level. Also shown are the two energy levels of the ensemble D101 that are closest to the pole, including their error bands. In addition, for the higher of these two interacting energy levels all the resampled energy values underlying the estimation of the error band are depicted in gray. This figure corresponds to the second column of Fig. 5.1, namely it shows the two highest interacting energy levels of that column.

in Table 5.2, $\delta = \arg(T)$ is the phase of the $\pi\pi \to \pi\pi$ P wave, see Eq. (2.19), and $Z_{lm}^{\mathfrak{P}}$ are generalized zeta functions as defined in Eq. (3.51).

It is expedient to study the pole structure of Eq. (5.5). According to Eq. (3.51) the zeta functions have poles whenever the denominator in the sum in Eq. (3.50) vanishes, i.e., whenever $q^{\star 2} = |\boldsymbol{k}^\star|^2 = k_\parallel^{\star 2} + |\tilde{k}_\perp^\star|^2$. That is, the poles overlap with the free energy levels. To check this explicitly, note that $k^{\star 0} = \omega_k^\star = E^\star/2$ holds, since at such a pole the pions are on-shell. Combining this with Eqs. (3.5) and (3.7) yields

$$k_\parallel^\star = k_\parallel^\star + \beta\left(\frac{E^\star}{2} - \frac{E^\star}{2}\right) = k_\parallel^\star + \beta\omega_k^\star - \beta\frac{E^\star}{2} = \frac{1}{\gamma}\left(k_\parallel - \frac{|\boldsymbol{P}|}{2}\right), \tag{5.7}$$

that is, singularities arise when [140, 148]

$$\mathfrak{q}^{\star 2} = \left[\frac{1}{\gamma}\left(\mathfrak{k}_\parallel - \frac{|\mathfrak{P}|^2}{2}\right)\right]^2 + \left|\tilde{\mathfrak{k}}_\perp\right|^2, \quad \mathfrak{k} \in \mathbb{Z}^3. \tag{5.8}$$

Note that the right-hand side of Eq. (5.8) depends on $\mathfrak{q}^{\star 2}$, for the Lorentz factor shows up, which

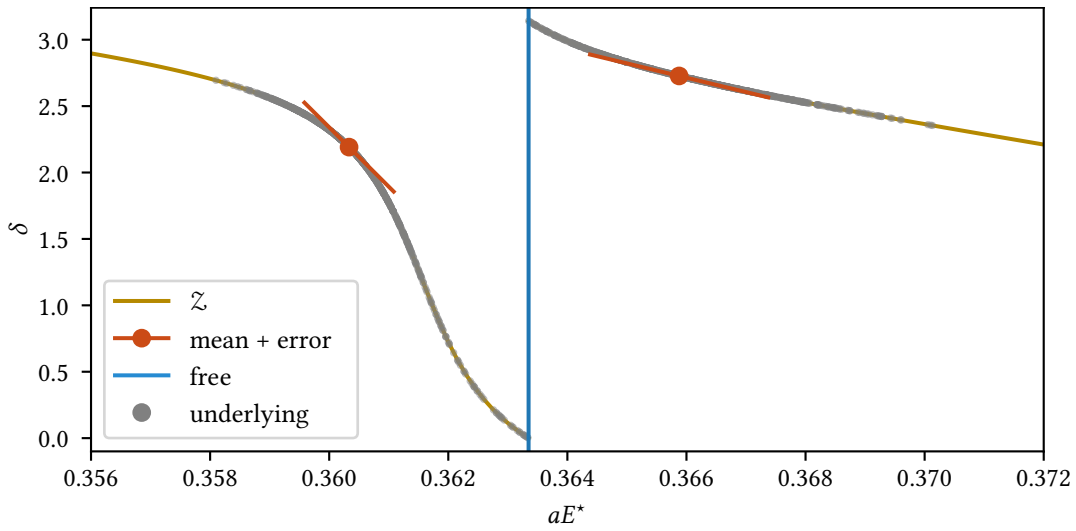

Figure 5.3: The analogue of Fig. 5.2 in the $(aE^\star, \delta)$ plane. The phases need to lie on the curve traced out by $\mathcal{Z}$, as defined in Eq. (6.1), that is, the energies and phases are correlated. For each of the two interacting energy levels all the underlying values are depicted in gray, i.e., each gray point associated with the higher energy level corresponds to one gray vertical line in Fig. 5.2. Also shown are the mean values and the linear approximations to the curve $\mathcal{Z}$ corresponding to one standard deviation as estimated from the underlying energies. As can be seen, this linear approximation works qualitatively rather well, so to keep the plots easily comprehensible in the following only the linearly approximated errors are shown without all the underlying data points. It is worth noting that the phases are not uniquely determined, for the cotangent is periodic with period π, and thus, in principle, each obtained phase can be shifted by integer multiples of π. In this plot all phases are chosen to lie within $[0, \pi)$. In particular, the data points with energies slightly below the free energy belong partly to the higher energy level, see the leftmost gray lines in Fig. 5.2.

depends on $\mathfrak{q}^{\star\,2}$ according to Eq. (5.4). Expressing the Lorentz factor in this way, Eq. (5.8) boils down to a quadratic equation in $\mathfrak{q}^{\star\,2}$, and thus it can be solved straightforwardly. The solutions coincide with the (corresponding values of $\mathfrak{q}^{\star\,2}$ of the) free energy levels as given in Eq. (5.3). This correspondence is intuitively clear: the pions are free if the interaction vanishes, that is, if $T = 0$, i.e., if $\delta = 0$, which, in turn, implies $\cot(\delta) = \infty$. Hence, according to Eq. (5.6) $\mathcal{Z}$ needs to have a pole, too. Depending on the precise values of $\alpha_{lm}^{\mathfrak{P},\Lambda}$, some of the poles of the zeta functions in the quantization condition cancel. It is the subset of Eq. (5.8) without such a cancellation that builds the allowed free energy levels.

To sum up, Eq. (5.5) relates the CM energies of $\pi\pi$ states on the lattice to the P-wave scattering phase shift δ at the corresponding energy (via taking a detour over $\mathfrak{q}^{\star\,2}$). This quantization condition is displayed for a fixed boost and irrep on a given lattice in Fig. 5.2 together with both interacting and free energy levels, illustrating the pole structure that is associated with the generalized zeta functions. Furthermore, for a single interacting energy level not only the central value and its error are shown, but also the energies as evaluated on the resampled gauge configurations, as discussed in Sec. 3.1. Inserting these energies into Eq. (5.5) yields the phases depicted in Fig. 5.3, which clearly shows the correlation between the phases and energies. In reality, the situation is slightly more complicated than indicated by these figures. Namely, the different samples drawn from the

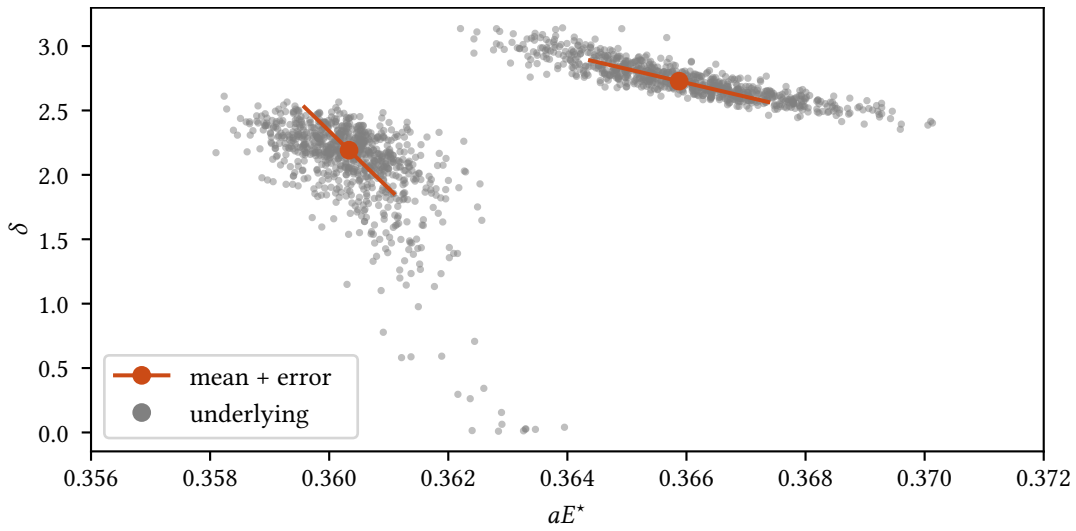

Figure 5.4: Same as Fig. 5.3, but this time the variation in the pion mass on the different samples is taken into account.

gauge configurations yield not only different $\pi\pi$ energy levels, but also different pion masses. Since Eq. (5.5) depends on the pion mass, too, each vertical gray line in Fig. 5.2 corresponds to a slightly shifted version of the curve traced out by $\mathscr{Z}$, and the same logic applies to Fig. 5.3. That is, the gray dots ibidem do not lie on a one-dimensional line, but instead constitute two-dimensional clouds sourrounding the mean values, as indicated in Fig. 5.4.

Chapter 6

Fit and results

Finally, we use the formalism introduced in Ch. 4 to analyze the lattice data described in Ch. 5. We start by explaining how to confront the continuum model with the lattice in Sec. 6.1 and Sec. 6.2, and subsequently discuss a naive way to incorporate discretization artifacts into the framework in Sec. 6.3. Building on top of the detailed discussion of the error computation in Sec. 6.4, we then present our results in Sec. 6.5.

6.1 Translating a continuum model to the lattice

As we have seen, given an energy, the quantization condition needs to be evaluated once to yield the corresponding phase. In principle, one can continue to fit a given model δ^{mod}, which specifies the phase as a function of the energy and model parameters, to the data points in the $(aE^\star, \delta)$ plane. However, one needs to be careful to take the correlations of the phases and energies into account. While this can be achieved via the introduction of auxiliary parameters [86], to avoid these complication we follow the reversed approach here (at the cost of other complications).

Given an expression for the phase as a function of the energy, it can be plugged into Eq. (5.5); subsequently, this equation can be solved numerically to determine $\mathfrak{q}^{\star\,2}$ for a given combination of boost momentum $\mathfrak{P}$ and irrep Λ. In this way, for fixed model parameters the continuum model δ^{mod} can be translated into discrete energy levels on the lattice, which then allows for a comparison of the model with a given lattice calculation. It is worth noting that for a fixed combination of boost and irrep, there are in general several solutions to the quantization condition. The one with the lowest energy is the ground state, while the higher-lying ones are exited states.

Unfortunately, the evaluation of the generalized zeta functions $Z_{lm}^{\mathfrak{P}}$ is computationally demanding, so that solving the quantization condition for a given model δ^{mod} can be quite time consuming. This is especially worrisome if the quantization condition needs to be solved repeatedly, e.g., in the context of a fit. Hence, it is desirable to speed up the evaluation of this condition. There are two, in principle, straightforward methods.

The first is to interpolate the generalized zeta functions. That is, for each needed boost and irrep, the three zeta functions appearing in Eq. (5.5) are interpolated as functions of $\mathfrak{q}^{\star\,2}$, carefully taking the poles into account. In practice, the functions are interpolated between the poles, going as close to the poles as numerical precision allows. This requires to use quite a few sites in the interpolation, for the zeta functions change rapidly close to the poles. As soon as the quantization condition is also needed for different values of the mass aM_π^{lat}, the interpolation gets more expensive. Since the Lorentz factor depends on this mass according to Eq. (5.4), so do the zeta functions.

Hence, in this case they are needed as functions of both the momentum $\mathfrak{q}^{\star 2}$ and the mass aM_π^{lat}, so they need to be interpolated on a two-dimensional grid, significantly decreasing the numerical benefits of interpolation.

As an alternative, second method, the quantization condition can be Taylor expanded, as shown in Ref. [92] for a fixed value of aM_π^{lat}. To that end, rewrite Eq. (5.6) as

$$\delta(aE^\star) = \operatorname{arccot}\left[\mathcal{Z}(aE^\star)\right] =: \mathcal{Z}(aE^\star), \tag{6.1}$$

where everything is now expressed in terms of the energy $aE^\star$ corresponding to the momentum $\mathfrak{q}^\star$. If a model δ^{mod} is plugged into the quantization condition, its numerical solution yields an energy $aE^{\star\text{mod}}$ such that

$$\delta^{\text{mod}}\left(aE^{\star\text{mod}}\right) = \mathcal{Z}\left(aE^{\star\text{mod}}\right). \tag{6.2}$$

Now, assume that the corresponding lattice calculation produced a value $aE^{\star\text{lat}}$ close by to $aE^{\star\text{mod}}$ (if the model is somehow capable of describing the lattice data, this should hold true). In this case it is justified to Taylor expand both sides of Eq. (6.2), yielding

$$\begin{aligned}&\delta^{\text{mod}}\left(aE^{\star\text{lat}}\right) + \frac{\mathrm{d}\delta^{\text{mod}}}{\mathrm{d}\left(aE^\star\right)}\left(aE^{\star\text{lat}}\right)\left[aE^{\star\text{mod}} - aE^{\star\text{lat}}\right]\\ =&\mathcal{Z}\left(aE^{\star\text{lat}}\right) + \frac{\mathrm{d}\mathcal{Z}}{\mathrm{d}\left(aE^\star\right)}\left(aE^{\star\text{lat}}\right)\left[aE^{\star\text{mod}} - aE^{\star\text{lat}}\right] + O\left(\left[aE^{\star\text{mod}} - aE^{\star\text{lat}}\right]^2\right).\end{aligned} \tag{6.3}$$

Neglecting the higher-order terms results in

$$aE^{\star\text{mod}} = aE^{\star\text{lat}} + \frac{\left[\mathcal{Z} - \delta^{\text{mod}}\right]\left(aE^{\star\text{lat}}\right)}{\frac{\mathrm{d}\left[\delta^{\text{mod}} - \mathcal{Z}\right]}{\mathrm{d}(aE^\star)}\left(aE^{\star\text{lat}}\right)}. \tag{6.4}$$

In this way, the calculation of the energies $aE^{\star\text{mod}}$ corresponding to the continuum model requires merely the evaluation of the quantization condition and its derivative at the given energy $aE^{\star\text{lat}}$, instead of a time-demanding numerical solution of Eq. (5.5). Note also that these two values are independent of the model δ^{mod}, and thus they stay unchanged during a fit, thereby drastically increasing performance.

To take into account the mass dependence, this second method needs to be modified slightly. In this case, instead of fixing the mass to equal aM_π^{lat}, the quantization condition is evaluated at a mass aM_π^{mod}, that is Eq. (6.2) is replaced by

$$\delta^{\text{mod}}\left(aE^{\star\text{mod}}, aM_\pi^{\text{mod}}\right) = \mathcal{Z}\left(aE^{\star\text{mod}}, aM_\pi^{\text{mod}}\right). \tag{6.5}$$

Assuming that aM_π^{mod} is close to aM_π^{lat} once again, this equation can be Taylor expanded in both variables up to second order, yielding, in complete analogy with the foregoing calculation,

$$aE^{\star\text{m}} = aE^{\star\text{l}} + \frac{\left[\mathcal{Z} - \delta^{\text{m}}\right]\left(aE^{\star\text{l}}, aM_\pi^{\text{l}}\right) + \left(aM_\pi^{\text{m}} - aM_\pi^{\text{l}}\right)\frac{\partial}{\partial(aM)}\left[\mathcal{Z} - \delta^{\text{m}}\right]\left(aE^{\star\text{l}}, aM_\pi^{\text{l}}\right)}{\frac{\partial}{\partial(aE^\star)}\left[\delta^{\text{m}} - \mathcal{Z}\right]\left(aE^{\star\text{l}}, aM_\pi^{\text{l}}\right)}, \tag{6.6}$$

where, for brevity, the superscripts mod and lat are abbreviated as m and l, respectively. The only difference between Eq. (6.4) and Eq. (6.6) is the additional term proportional to the mass difference

in the numerator of the latter, for the evaluation at M_π^{lat} of the right-hand side of Eq. (6.4) is implicit. The only additional information needed are the derivatives with respect to the mass.

Note again that Eqs. (6.4) and (6.6) are valid only if $|aE^{\star\text{mod}} - aE^{\star\text{lat}}| \ll 1$, i.e., if the model is somehow capable to describe the lattice data. Hence, in a practial application one should first work with the full quantization condition, use it to compute the energy levels $aE^{\star\text{mod}}$, and check if they are indeed close to the energy levels $aE^{\star\text{lat}}$. Only then it is justified to use the approximated versions of the quantization conditions in further work with the model.

6.2 Fitting the inverse-amplitude method

Having a look at the explicit ChPT expression as discussed in Sec. 4.1 shows that at NLO both the pion decay constant and the P wave depend on a single LEC each, namely $\mathbb{L}_1^{\text{NLO}} := \{l_4^r\}$ and $\mathbb{L}_2^{\text{NLO}} := \{l_2^r - 2l_1^r\}$, respectively, while at NNLO more LECs appear: $\mathbb{L}_1^{\text{NNLO}} := \{l_1^r, l_2^r, l_3^r, l_4^r, r_F^r\}$ and $\mathbb{L}_2^{\text{NNLO}} := \{l_1^r, l_2^r, l_3^r, r_a, r_b, r_c\}$. On top of these dimensionless LECs the ChPT expressions depend on the dimensionful quantities F and M_π. To work in lattice units, both these parameters are given in powers of the lattice spacing. Inserting the different orders of the ChPT P wave into Eq. (4.15) and Eq. (4.19) yields explicit expressions for the NLO and NNLO IAM T, respectively. The corresponding phase can be computed as $\delta^{\text{IAM}} = \arg(T)$, which, in turn, allows for a computation of associated energy levels $aE^{\star\text{IAM}}$ via Eq. (6.6). We label the different $\pi\pi$ energy levels of a given ensemble as $aE_k^{\star\text{lat}}$, $k = 1, \ldots, N$. Each such level corresponds to a boost vector as well as an irrep (and possibly an excitation). The associated IAM energy is denoted by $aE_k^{\star\text{IAM}}$. Altogether, the lattice data on a given ensemble constitute a vector v^{lat}, while the model at hand yields a vector v^{mod}, which are given explicitly as

$$v^{\text{lat}} := \begin{pmatrix} aF_\pi^{\text{lat}} \\ aM_\pi^{\text{lat}} \\ aE_1^{\star\text{lat}} \\ aE_2^{\star\text{lat}} \\ \vdots \\ aE_N^{\star\text{lat}} \end{pmatrix}, \qquad v^{\text{mod}} := \begin{pmatrix} aF_\pi^{\text{ChPT}}\,(aF, aM_\pi; \mathbb{L}_1) \\ aM_\pi^{\text{IAM}} \\ aE_1^{\star\text{IAM}}\,(aF, aM_\pi; \mathbb{L}_2) \\ aE_2^{\star\text{IAM}}\,(aF, aM_\pi; \mathbb{L}_2) \\ \vdots \\ aE_N^{\star\text{IAM}}\,(aF, aM_\pi; \mathbb{L}_2) \end{pmatrix}. \tag{6.7}$$

Here the pion mass is rendered a fit parameter to take into account the error of aM_π^{lat} [167], such that the set of fit parameters reads $\mathbb{F} := \{aF\} \cup \{aM_\pi\} \cup \mathbb{L}_1 \cup \mathbb{L}_2$. Building on this, the χ^2 on the given ensemble is defined as

$$\chi^2(\mathbb{F}) := \left(v^{\text{lat}} - v^{\text{mod}}\right)^T C^{-1} \left(v^{\text{lat}} - v^{\text{mod}}\right), \tag{6.8}$$

where C is the covariance matrix of the quantities computed on the lattice.

Since everything is defined in lattice units, the explicit value of the lattice spacing is nowhere needed, with one exception, namely, the renormalization scale μ that shows up in the pion decay constant at both NLO and NNLO as well as in the NNLO P wave. The value of this scale needs to be fixed to 770 MeV, both to allow for a comparison of the obtained LECs with literature values and to allow for fitting several ensembles simultaneously. Thus, the lattice spacing creeps in via $\mu \mapsto a\mu$.

If several ensembles are fitted simultaneously, the total χ^2 is the sum of terms of the form (6.8), each corresponding to a single ensemble.[1] Because there is a sole value of F in physical units, in case

[1] Since each ensemble has individual gauge configurations, there is no correlation between different ensembles.

multiple ensembles share the same value of a, they also share a single fit parameter aF, otherwise there is an individual fit parameter aF for each ensemble. That is, for each value of a there is one fit parameter aF. Similarly, there is one fit parameter aM_π for each different value of aM_π^{lat} (with two values considered equal if they agree numerically and are obtained at the same value of a). In such a global fit the set of fit parameters then reads $\mathbb{F} = \{aF_j\}_{j=1}^{A} \cup \{aM_{\pi,j}\}_{j=1}^{A'} \cup \mathbb{L}_1 \cup \mathbb{L}_2$ with A the number of lattice spacings and A' the number of different pion masses.

To fit the model to the data, the χ^2 is minimized with respect to the fit parameters $\mathbb{F}$. Especially at NNLO this minimization is non-trivial, for the number of fit parameters is relatively high and there is a significant number of local minima. To avoid getting trapped in those, we use the differential-evolution algorithm [168]. When appropriately tuned, this allows for a reliable global search in parameter space, while needing less computation time than a Monte-Carlo algorithm. The heuristic algorithm works roughly as follows: one starts with a population of trial solutions, i.e., vectors in parameter space. The number of trial solutions is known as the population size. Subsequently, the trial solutions are combined randomly into new candidates, which replace the old ones if they yield lower values of the χ^2. How strong the modifications are is controlled by a parameter known as the differential weight, while the crossover probability influences the number of vector components of the trial solutions that are modified. This procedure is iterated, and the process terminates if all trial solutions are close to each other, i.e., if the standard deviation of their χ^2s is as small as 1 ppb of the absolute value of the mean of those χ^2s. To further improve the convergence, dithering is employed, i.e., the differential weight is set anew between each iteration to a randomly chosen value within 0.5 and 1. The population size is set to $20\,|\mathbb{F}|$ in a global fit to the CLS ensembles, while it is set to $40\,|\mathbb{F}|$ in a fit to the HadSpec data. With the other parameters set in this way, the crossover probability can be fixed to unity, which reduces the computation time. The resulting fit parameters obtained in this way are fed in Powell's method [169] as initial guesses, which is used to refine the results, where we aim again for a tolerance at the 1 ppb level. We use the implementation in `SciPy` [170] for both algorithms. That this choice of algorithms indeed yields stable fits was confirmed by repeating the minimization 100 times with randomly drawn initial guesses. Indeed all 100 results are very close to each other, albeit there is a small spread. To improve on this, all fit results presented later were obtained by repeating the same fit several times and keeping the best result.[2] The precise choice of the parameters of the algorithms as outlined above is the result of some tuning, i.e., repeating a fit with different parameters and carefully observing the impact on the χ^2 and the stability.

While the use of Eq. (6.6) instead of the full quantization condition to compute the energies $aE_k^{\star\text{IAM}}$ speeds up the fit drastically, care needs to be taken before one draws conclusions from the resulting minimal value of the χ^2. Namely, usually the χ^2 turns out to be (at most) a few percent larger than the one obtained using the full quantization condition. To understand this effect, note that the LECs $\mathbb{L}_2$ enter the χ^2 via the energies $aE_k^{\star\text{IAM}}$ only. Ignoring the other fit parameters (for the time being) we write symbolically $\chi^2(\{aE_k^{\star\text{IAM}}(\mathbb{L}_2)\})$. A fit with the full quantization condition yields values of $aE_k^{\star\text{IAM}}(\mathbb{L}_2)$ such that this χ^2 is at a global minimum; Taylor expanding the quantization condition means that these energies are approximated, and since we are at a minimum, this can only increase the value of χ^2.[3] To take this effect into account, we perform the fits with the

[2] To be able to obtain the same point in parameter space with high accuracy when repeating the same fit is particularly important in the case of jackknife resampling, see Sec. 6.4, for two jackknife samples differ only very slightly, and thus result in almost identical points in parameter space.

[3] This argument applies as long as the increase in χ^2 cannot be compensated for by a change of the fit parameters in a Taylored fit as compared to the ones resulting from a fit using the full quantization condition.

approximated quantization condition and subsequently use the resulting fit parameters to evaluate the full χ^2; the resulting values are the ones we quote in the following. Furthermore, to ensure that the use of the approximated quantization is justified in the first place, a few individual fits are performed both with and without the approximation, where indeed the resulting values of the fit parameters turn out to be compatible.

6.3 Discretization artifacts

While the quantization condition is built upon finite-volume effects, it is derived in the continuum, that is, discretization effects due to non-zero lattice spacing a are neglected. But the lattice calculations are carried out at non-vanishing lattice spacing, and thus it is likely that they are polluted by artifacts due to the discretization. To take such artifacts into account, the quantization condition needs to be modified. For the data at hand, the discretization procedure is tuned in a way that the artifacts are of order a^2 and higher; hence, there is no need to take terms linear in a into account. A naive ansatz is then to modify Eq. (6.1) according to

$$\delta(aE^\star) + ga^2 = \mathcal{Z}(aE^\star)\,, \tag{6.9}$$

such that in the limit $a \searrow 0$ the original quantization condition is reproduced. Here $g \in \mathbb{R}$ is another free parameter that needs to be adjusted by the fit. This model is insofar crude as it ignores a possible energy dependence of g, in addition, effects of higher orders in a are not taken into account.

Note that a has mass dimension -1, so that g is a dimensionful parameter. It is convenient to render it dimensionless by introducing a quantity with mass dimension 1, for example the pion decay constant in the chiral limit, F (this choice is in principle arbitrary, but well-suited for our fits that already incorporate aF as a fit parameter):

$$ga^2 = \frac{g}{F^2}(aF)^2 =: g(aF)^2\,, \tag{6.10}$$

where g was redefined to absorb the factor F^{-2}, thereby obtaining

$$\delta(aE^\star) + g(aF)^2 = \mathcal{Z}(aE^\star)\,. \tag{6.11}$$

Now both g and aF are dimensionless.[4]

Based on Eq. (6.11) it is straightforward to generalize Eq. (6.4). To this end, Eq. (6.2) needs to be replaced by

$$\delta^{\text{mod}}\left(aE^{\star\text{mod}}\right) + g(aF)^2 = \mathcal{Z}\left(aE^{\star\text{mod}}\right). \tag{6.12}$$

Taylor expanding both sides around $aE^{\star\text{lat}}$ yields

$$aE^{\star\text{mod}} = aE^{\star\text{lat}} + \frac{\left[\mathcal{Z} - \delta^{\text{mod}}\right]\left(aE^{\star\text{lat}}\right) - g(aF)^2}{\frac{\mathrm{d}\left[\delta^{\text{mod}} - \mathcal{Z}\right]}{\mathrm{d}(aE^\star)}\left(aE^{\star\text{lat}}\right)}. \tag{6.13}$$

[4] Usually, $aF = O(10^{-2})$, so as long as it is not multiplied by a large number, it is always possible to Taylor expand any relation involving aF around $aF = 0$. When the energy dependence of the coefficient multiplying $(aF)^2$ in such an expansion is neglected, Eq. (6.11) is reobtained in this way even if initially the lattice artifacts are modelled in a different way, e.g., as $\cot[\delta(aE^\star)] + ga^2 = \mathcal{Z}(aE^\star)$, by merely redefining g.

Now the coefficient in front of $(aF)^2$ depends on the energy $E^{\star\mathrm{lat}}$. Since the energy dependence of this coefficient was ignored anyway in the inital ansatz (6.9), it might as well be ignored here, resulting in

$$aE^{\star\mathrm{mod}} = aE^{\star\mathrm{lat}} + \frac{\left[\mathcal{Z} - \delta^{\mathrm{mod}}\right]\left(aE^{\star\mathrm{lat}}\right)}{\frac{\mathrm{d}\left[\delta^{\mathrm{mod}} - \mathcal{Z}\right]}{\mathrm{d}(aE^{\star})}\left(aE^{\star\mathrm{lat}}\right)} + g\,(aF)^2\,, \tag{6.14}$$

where, again, g was redefined. Equation (6.6) might be modified in the exact same way.

By the same logic, we can try to model lattice artifacts in the pion decay constant by adding a term to Eq. (4.11), resulting in

$$aF_\pi = aF\left[1 + F_4\frac{(aM_\pi)^2}{16\pi^2\,(aF)^2} + F_6\left(\frac{(aM_\pi)^2}{16\pi^2\,(aF)^2}\right)^2\right] + g_F(aF)^2\,, \tag{6.15}$$

with g_F another new dimensionless fit parameter.

6.4 Error analysis

Altogether there are four different sources of errors: the statistical one stemming from the data, the error of the lattice spacing a, the error of the literature value of F (that is needed in the fit to the HadSpec data), and the error due to the truncation of the chiral expansion. In the following, we address these kinds of errors one by one.

6.4.1 Statistical error of the data

To determine the statistical error stemming from the lattice data, jackknife samples are drawn from the data and the fit is repeated on all those samples. If several ensembles with a different number of underlying bootstrap samples are fitted at once, the data first need to be resampled via a parametric jackknife, such that each ensemble has the same number of samples.

To be precise, first focus on a single ensemble. It contains N two-particle energy levels $aE_k^{\star\mathrm{lat}}$, $k = 1, \ldots, N$, compare Eq. (6.7). In fact, as illustrated in Fig. 5.2 each of these energy levels consists of $G \in \mathbb{N}$ values, where each value corresponds to a bootstrap sample of the underlying gauge configurations: $\mathbb{E}_k := \left\{aE_k^{\star 1}, \ldots, aE_k^{\star G}\right\}$, with $aE_k^{\star\mathrm{lat}} = \sum_{b=1}^{G} aE_k^{\star b}/G$ the mean of those values. The corresponding entries of the covariance matrix C appearing in Eq. (6.8) are computed using the standard estimator

$$C_{ij} = \frac{1}{G-1}\sum_{b=1}^{G}\left(aE_i^{\star b} - aE_i^{\star\mathrm{lat}}\right)\left(aE_j^{\star b} - aE_j^{\star\mathrm{lat}}\right). \tag{6.16}$$

To discuss the error analysis in detail, it is expedient to focus on one two-particle energy level and abstract away the details. That is, instead of $\mathbb{E}_k$, consider for the time being a set $\mathbb{X} := \{X_1, \ldots, X_G\}$ containing G outcomes of a random variable X. Usually, to attempt an error analysis the bootstrap is applied. That is, $B \in \mathbb{N}$ bootstrap samples $\mathbb{X}^b := \left\{X_1^b, \ldots X_G^b\right\}$, $b = 1, \ldots, B$ are generated, where each X_g^b is drawn randomly and uniformly with replacement from $\mathbb{X}$ (that is, the a priori probability that X_g^b equals X_k is $1/G$ for all $g, k \in 1, \ldots, G$, and $b \in 1 \ldots B$). On each bootstrap sample the mean $\overline{X}^b := \sum_{g=1}^{G} X_g^b/G$ is computed. The variance of the bootstrap means is an

estimator of the variance of the mean. That is, for sufficiently high B,

$$\frac{1}{B-1}\sum_{b=1}^{B}\left(\overline{X}^{b}-\frac{1}{B}\sum_{c=1}^{B}\overline{X}^{c}\right)^{2}\approx \mathrm{Var}\left[\overline{X}\right] \tag{6.17}$$

holds.

Coming back to the fit at hand, the aforementioned procedure would be applied to each energy level $\mathbb{E}_k$, yielding B outcomes $\{aE_1^{\star\mathrm{lat},b},\dots,aE_N^{\star\mathrm{lat},b}\}$, $b=1,\dots,B$. On each such outcome the fit can be repeated, each time resulting in different values of the fit parameters. Their errors can then be estimated via the covariance matrix of the B different sets of parameter values.

However, in the scenario at hand this approach fails. This is due to the fact that the values $aE_k^{\star\mathrm{lat}}$ are often very close to a pole of the quantization condition. The underlying set $\mathbb{E}_k$ might contain a significant number of values located on the other side of the nearby pole compared to the central value $aE_k^{\star\mathrm{lat}}$, see Fig. 5.2. Hence, some of the bootstrap samples will yield values $aE_k^{\star\mathrm{lat},b}$ that are separated from the true mean $aE_k^{\star\mathrm{lat}}$ by a pole, thereby being associated with completely different values of the scattering phase. In this way, the error would be drastically overestimated.

To circumvent this problem, the bootstrap is replaced by a jackknife. Consider the general random variable X investigated before. The G jackknife samples are generated via deleting single values X_k: $\mathbb{X}_j := \{X_1, X_2, \dots, X_{j-1}, X_{j+1}, X_{j+2}, \dots, X_G\}$. Again the means $\overline{X}_j$ are computed and used instead of the bootstrap means $\overline{X}^{b}$. The following results are readily established [167]: the mean of the means of the jackknife samples equals the mean of the original data,

$$\frac{1}{G}\sum_{j=1}^{G}\overline{X}_j=\overline{X}. \tag{6.18}$$

Furthermore,

$$\overline{X}_j-\overline{X}=\frac{1}{G-1}\left(\overline{X}-X_j\right) \tag{6.19}$$

holds, which can be used to compute the variance of the jackknife means, resulting in

$$\begin{aligned}\frac{1}{G-1}\sum_{j=1}^{G}\left(\overline{X}_j-\overline{X}\right)^{2}&=\frac{1}{(G-1)^{2}}\mathrm{Var}\left[X\right]\\&=\frac{G}{(G-1)^{2}}\mathrm{Var}\left[\overline{X}\right].\end{aligned} \tag{6.20}$$

Here $\mathrm{Var}[\overline{X}]=\mathrm{Var}[X]/G$ is used. Hence, to obtain the variance of the mean, the variance of the jackknife means needs to be multiplied by a factor $(G-1)^2/G =: \mathscr{G}$. Comparison with Eq. (6.17) shows that this is precisely the factor that relates the variance of the jackknife means with the variance of the bootstrap means.

Carrying this over to the fit at hand, the procedure reads as follows: instead of bootstrap samples, G jackknife samples of each energy level are drawn. That is, there are G outcomes $\{aE_{1,j}^{\star\mathrm{lat}},\dots,aE_{N,j}^{\star\mathrm{lat}}\}$, $j=1,\dots,G$, where $aE_{k,j}^{\star\mathrm{lat}}$ denotes the mean obtained using the j-th jackknife sample. Since the variance of these means is a factor $1/\mathscr{G}\approx 1/G$ smaller than the variance of the bootstrap means, the risk of jumping over poles in the quantization condition is drasticly reduced. The fit is repeated on all G different jackknife samples, the covariance matrix of the fit parameters

can then be computed in the standard way. However, according to the foregoing discussion the matrix obtained in this way needs to be multiplied by the factor $\mathscr{G}$.

In addition to the energy levels, the pion decay constants and masses are fitted, if available. Often, the individual values of these parameters on the G bootstrap samples of gauge configurations underlying the two-particle energy levels are not available. Instead, a central value with an error is given, e.g., $aF_\pi^{\text{lat}} \pm \Delta aF_\pi^{\text{lat}}$. To include this error in the analysis, for each jackknife sample j, a value $aF_{\pi,j}^{\text{lat}}$ is drawn from a normal distribution with mean aF_π^{lat} and standard deviation $\Delta aF_\pi^{\text{lat}}/\sqrt{\mathscr{G}}$. This value is subsequently used in the fit. That is, a parametric bootstrap is employed, but with the standard deviation downscaled to match the discrepancy between Eq. (6.20) and Eq. (6.17). This is dubbed parametric jackknife in the following. The same procedure is applied to the masses $aM_\pi^{\text{lat}} \pm \Delta aM_\pi^{\text{lat}}$.

In a simultaneous fit to several ensembles, the situation is slightly more complicated. This is due to the fact that the ensembles often differ in the number G of underlying bootstrap samples of gauge configurations. However, this number is hardwired into the jackknife, as the omnipresence of the factor $\mathscr{G}$ illustrates. To obtain the same factor on all ensembles, the strategy described in Ref. [87] is used: on each ensemble the covariance matrix C is computed via Eq. (6.16). Then, one fixes a number $J \in \mathbb{N}$ of desired jackknife samples. Subsequently, on each ensemble J samples $\{aE_{1,j}^{\star\text{lat}}, \dots, aE_{N,j}^{\star\text{lat}}\}$, $j = 1, \dots, J$ are drawn from a multivariate normal distribution with covariance matrix $C/\mathscr{J}/G$, with $\mathscr{J} := (J-1)^2/J$. That is, a parametric jackknife is applied again. The additional division by G is necessary, for the diagonal entries of C correspond (in the language developed previously in the discussion of the general random variable X) to $\text{Var}[X]$, but here we are interested in $\text{Var}[\overline{X}]$, see also Eq. (6.17). The fit is then repeated on all J samples and the results obtained in this way need to be rescaled by the appropriate power of $\mathscr{J}$.

6.4.2 Error of the lattice spacing

As already alluded to in Sec. 6.2, the numerical value of the lattice spacing a enters the fit only via the renormalization scale μ, if the pion decay constant is fitted. If the decay constant has not been computed on the lattice (as it is the case for the HadSpec data), the lattice spacing also enters in the translation of the literature value of F into lattice units.

Since in lattice-QCD computations everything is computed in powers of a, the determination of a, called scale setting, is a non-trivial task. As a matter of fact, a cannot be determined exactly, but carries an error on its own. This is why we have deliberately designed the fit in a way that the impact of the lattice spacing is as small as possible. There are several ways to set the scale. The CLS collaboration employs two different methods [166]. Strategy 1 uses the Wilson flow as suggested by Lüscher [171], while strategy 2 sets the scale via combinations of decay constants. The resulting values are incompatible within their errors, already hinting at how error-prone scale setting is. Strategy 1, the one preferred by the authors of Ref. [166], is based on a dimension two quantity t_0 evaluated at the symmetrical point $m_u = m_d = m_s$ (with m_s the mass of the strange quark). In Ref. [166] the reference value is determined as $T_0^{\text{ref}} := \sqrt{8t_0} = 0.413(5)(2)\,\text{fm}$, where the first error is statistical and the second systematical. In addition, for each lattice spacing, the value of t_0/a^2 is given, denoted in the following as $T_{0,k}^{\text{lat}}$, $k = 1, 2, 3$. These values are only weakly correlated, however, the correlations of the resulting values $a_k = T_0^{\text{ref}}/\sqrt{8T_{0,k}^{\text{lat}}}$ are significant, because the reference value is common to all of them. To take this correlation into account, we parametrically draw samples of the form $\{T_{0,j}^{\text{ref}}, T_{0,1j}^{\text{lat}}, T_{0,2j}^{\text{lat}}, T_{0,3j}^{\text{lat}}\}$ (where j indicates the sample), compute on each sample the three lattice spacings and estimate their covariance in the standard way. In doing so,

we draw the samples from a normal distribution, adding the statistical and systematical errors in quadrature. Contrarily, we approximate the covariance matrix of strategy 2 as diagonal, with the errors given in Ref. [166]. It is worth noting that strategy 1 requires a slight shift in both the pion masses and the decay constants. However, in the computation of the CLS $\pi\pi$ energy levels in Ref. [36] the shifts of the pion masses were not taken into account, and thus throughout our analysis of CLS data we use non-shifted values. Strategy 2 does not suffer from this problem.

HadSpec determines the two lattice spacings via the mass M_Ω of the Ω baryon. To that end, aM_Ω is computed on each ensemble [82, 172]; dividing by the experimental value [9] yields the value of the lattice spacing. Again both values are correlated due to the common experimental value, which we take into account by resampling, although the resulting off-diagonal entries of the covariance matrix are suppressed by an order of magnitude compared to the diagonal ones, for the error of the experimentally determined Ω mass is small.

To incorporate the error of the lattice spacings a_k, $k = 1, \dots, K$, a corresponding fit parameter a_k^{fit} is introduced for each lattice spacing. This fit parameter is used instead of the value obtained from the lattice to translate the renormalization scale into lattice units (and the literature value of F, if required). Furthermore, the term

$$\chi_a^2 := \sum_{j,k=1}^{K} \left(a_j - a_j^{\text{fit}}\right) \left(C_a^{-1}\right)_{jk} \left(a_k - a_k^{\text{fit}}\right) \tag{6.21}$$

is added to the χ^2, with C_a the covariance matrix of the lattice spacings on the different ensembles. That is, the replacement

$$\chi^2 \mapsto \chi^2\big|_{\boldsymbol{a}\mapsto\boldsymbol{a}^{\text{fit}}} + \chi_a^2 \tag{6.22}$$

is performed. Via a parametric boostrap several samples $\{a_{kj}\}_{k=1}^{K}$ (with j labeling the sample) are drawn from a multivariate normal distribution with covariance matrix C_a and the fit is repeated for each such sample. From the different fit results the errors can be obtained via the standard estimators.

6.4.3 Error of F

In the fit to the HadSpec data, F_π/F is set to the $N_\text{f} = 2 + 1$ FLAG average [47, 173–177], while F_π is fixed to its Particle Data Group (PDG) value [9] to obtain $F = 86.89(58)\,\text{MeV}$. To include this error in the fit, a fit parameter F^{fit} is introduced and the replacement

$$\chi^2 \mapsto \chi^2\big|_{F\mapsto F^{\text{fit}}} + \left(\frac{F - F^{\text{fit}}}{\Delta F}\right)^2 \tag{6.23}$$

is performed.

6.4.4 Truncation error

Lastly, we address the error arising due to the truncation of the chiral expansion at NLO or NNLO. To this end, we utilize the approach of Ref. [178]. Consider a perturbative expansion of some quantity X in powers of an expansion parameter $\alpha \ll 1$:

$$X = X_0 + X_1 + X_2 + \cdots = \sum_{k=0}^{\infty} X_k, \qquad X_k = O\left(\alpha^k\right). \tag{6.24}$$

In practice, the expansion often needs to be truncated. The question arises how to estimate the error ΔX_k associated with the truncation at order k without calculating terms of higher order. Noting that missing terms after a truncation are at least one order in α higher, the idea is to use the recursion

$$\Delta X_k = \max\{\alpha \Delta X_{k-1}, \alpha |X_k - X_{k-1}|\}, \quad k \geq 0, \tag{6.25}$$

with $\Delta X_{-1} \coloneqq 0$ and $X_{-1} \coloneqq 0$ for notational convenience. This recursion can be solved to obtain

$$\Delta X_k = \max \bigcup_{j=0}^{k} \left\{\alpha^{k-j+1} \left|X_j - X_{j-1}\right|\right\}. \tag{6.26}$$

That is, we compute all differences of two adjacent terms multiplied by the appropriate power of α and maximize, with the absolute values inserted to obtain positive quantities.

In the scenario at hand, the ChPT expansion of the P wave has two expansion parameters: $\alpha_1 \coloneqq M_\pi^2/M_\rho^2$ and $\alpha_2 \coloneqq s/M_\rho^2$. Here the breakdown scale is set to M_ρ, for the ρ is the lightest resonance in this partial wave and plain ChPT does not incorporate resonances. While the IAM improves the s dependence via unitarization and allows for a description of the ρ, it does nothing to improve the M_π dependence of the amplitude. Hence, we take only α_1 into account. Noting that the NLO IAM corresponds to the lowest order in our formalism and the NNLO IAM to the subsequent order, Eq. (6.26) yields

$$\begin{aligned} \Delta X_{\mathrm{NLO}} &= \alpha_1 \left|X_{\mathrm{NLO}}\right|, \\ \Delta X_{\mathrm{NNLO}} &= \max\left\{\alpha_1^2 X_{\mathrm{NLO}}, \alpha_1 \left|X_{\mathrm{NLO}} - X_{\mathrm{NNLO}}\right|\right\}, \end{aligned} \tag{6.27}$$

with $X_{(\mathrm{N})\mathrm{NLO}}$ the quantity as obtained from the (N)NLO IAM. This is an educated guess of the truncation error; in particular, due to the non-perturbative nature of the IAM an observable does not really decompose like $X = X_{\mathrm{NLO}} + X_{\mathrm{NNLO}} + \ldots$

6.5 Results

6.5.1 CLS

First, we discuss the fits to the CLS data. We fit all ensembles listed in Table 5.1 except for N401 simultaneously, once using the NLO IAM, once the NNLO one. A simultaneous fit to ensembles that differ in pion mass has the huge benefit that the data constrain not only the energy dependence, but also the dependence on the pion mass. At NLO only two LECs show up, one in the P wave and one in the decay constant, which can be fixed even if only data at a single pion mass are available. However, to fix the LECs at NNLO it is crucial to control the pion mass dependence, because some LECs are mainly sensitive to the mass, see, e.g., r_a in Eq. (4.8). For the time being we rely on strategy 1 to set the scale, see Sec. 6.4.2.

In the NNLO amplitude the LEC l_3^r shows up, which relates the pion mass to its value M in LO ChPT. Since no information about this value enters our analysis, NNLO fits with l_3^r as a completely free parameter are not stable. Accordingly, we constrain l_3^r to be close to its literature value $l_3^{r,\mathrm{lit}} = 0.8(3.8) \times 10^{-3}$ [162] by adding a term $[(l_3^r - l_3^{r,\mathrm{lit}})/\Delta l_3^{r,\mathrm{lit}}]^2$ to the χ^2, which indeed renders the fit stable. The resulting LECs are shown in Tables 6.1 and 6.2, while a comparison of the fit with the data of a single ensemble is depicted in Fig. 6.1. Moreover, in Fig. 6.2 the covariance matrix of

	fit	Ref. [162]	FLAG [47]
$(l_2^r - 2l_1^r) \times 10^3$	12.62(25)(0)	9.9(1.3)	19(17)
$l_4^r \times 10^3$	−2.6(1.1)(0.2)	6.2(1.3)	3.8(2.8)

Table 6.1: The LECs obtained from a global fit of the NLO IAM and the pion decay constant to the CLS ensembles. While the first error arises due to the statistical error of the lattice data as discussed in Sec. 6.4.1, the second corresponds to the error of the lattice spacing, see Sec. 6.4.2. These values are to be compared with the ones extracted from ChPT analyses as given in the second column and from $N_\mathrm{f} = 2 + 1$ lattice-QCD computations [47, 173–177] given in the third column.

	fit	Ref. [162]	Refs. [65, 153]
$l_1^r \times 10^3$	−6.1(1.8)(0.1)	−4.03(63)	
$l_2^r \times 10^3$	2.58(90)(7)	1.87(21)	
$l_3^r \times 10^3$	0.776(65)(4)	0.8(3.8)	
$l_4^r \times 10^3$	−33(13)(0)	6.2(1.3)	
$r_a \times 10^6$	28(12)(1)		13
$r_b \times 10^6$	−4.8(2.6)(0.2)		−9.0
$r_c \times 10^6$	2.1(1.3)(0.1)		1.1
$r_F^r \times 10^3$	2.7(1.2)(0)		0

Table 6.2: Same as Table 6.1, but with the NNLO IAM instead of the NLO one. Since the NNLO LECs are notoriously difficult to determine [162], in the absence of precise literature values we fall back to resonance saturation estimates [65, 153] that are shown in the last column. Note that these estimates are uncertain.

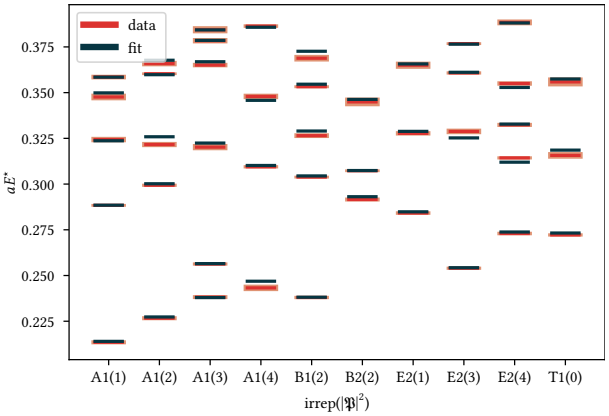

(a) The $\pi\pi$ energy levels. The axes labels are as in Fig. 5.1. For the data, central values are indicated in red and error bands in orange.

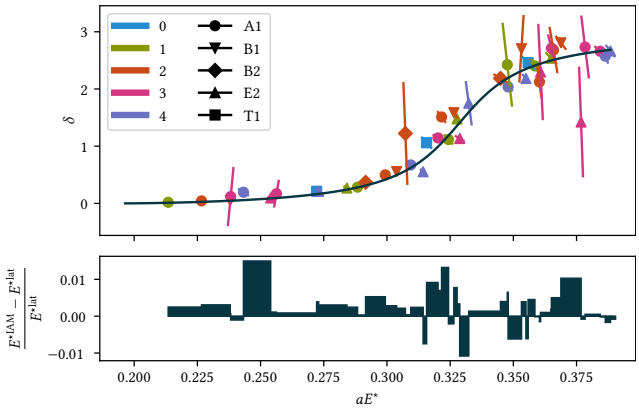

(b) The phases as extracted from the energies compared to the fit curve as well as the relative differences of the IAM and lattice energy levels. The colors encode $|\mathfrak{P}|^2$ and the markers the irrep.

Figure 6.1: The result of the simultaneous fit of the NNLO IAM to the different CLS ensembles compared to the data of the ensemble of lowest pion mass, D101.

the LECs obtained in the NNLO fit is visually presented. Clearly, several LECs are heavily (anti-) correlated, e.g., l_1^r and r_c.

Since the unitarization in the construction of the IAM amounts effectively to a resummation of iterated $\pi\pi$ scattering, the values of the LECs when used with the IAM are expected to differ from their values in plain ChPT, for the latter does not incorporate this rescattering [58, 154, 179, 180]. Hence, the small deviations of the values obtained in the fits from the literature values come at no surprise, with one exception: there is a huge discrepancy in l_4^r, which amounts to 5.1σ at NLO and 3σ at NNLO. On the other hand, the NNLO LECs agree qualitatively rather well with the rough estimates via resonance saturation.

To judge the quality of the fits, in Table 6.3 we do not only display the χ^2/dof but also the Bayesian information criterion (BIC) that is defined as

$$\mathrm{BIC} := \chi^2 + |\mathbb{F}| \ln(N), \tag{6.28}$$

with N the total number of data points fitted and $|\mathbb{F}|$ the number of fit parameters [181]. Neither at NLO nor NNLO the χ^2/dof is fully satisfactory. Nevertheless, it decreases significantly when increasing the order, and thus clearly favors the NNLO fit. Moreover, despite the factor $|\mathbb{F}|$ in Eq. (6.28) that punishes the introduction of additional fit parameters, the BIC decreases by 22 when going from NLO to NNLO, and therefore providing strong evidence in favor of the NNLO fit [181].

As described in Sec. 4.2, the IAM exhibits the ρ pole on the second Riemann sheet, whose position and residue can be determined numerically via Eq. (2.34) and Eq. (2.36) given the fit values of the LECs. The mass M_ρ, width Γ_ρ, and coupling $g_{\rho\pi\pi}$ of the ρ resonance can subsequently be extracted using Eq. (2.30) and Eq. (2.33). Here the subscript of the coupling $g_{\rho\pi\pi}$ indicates that this is the coupling of the ρ to two pions. The ρ characteristics computed in this way are shown in Table 6.3 at the physical point, which is defined by the PDG value of the pion mass here and the following. For comparison they are accompanied by the results of a thorough dispersive analysis of

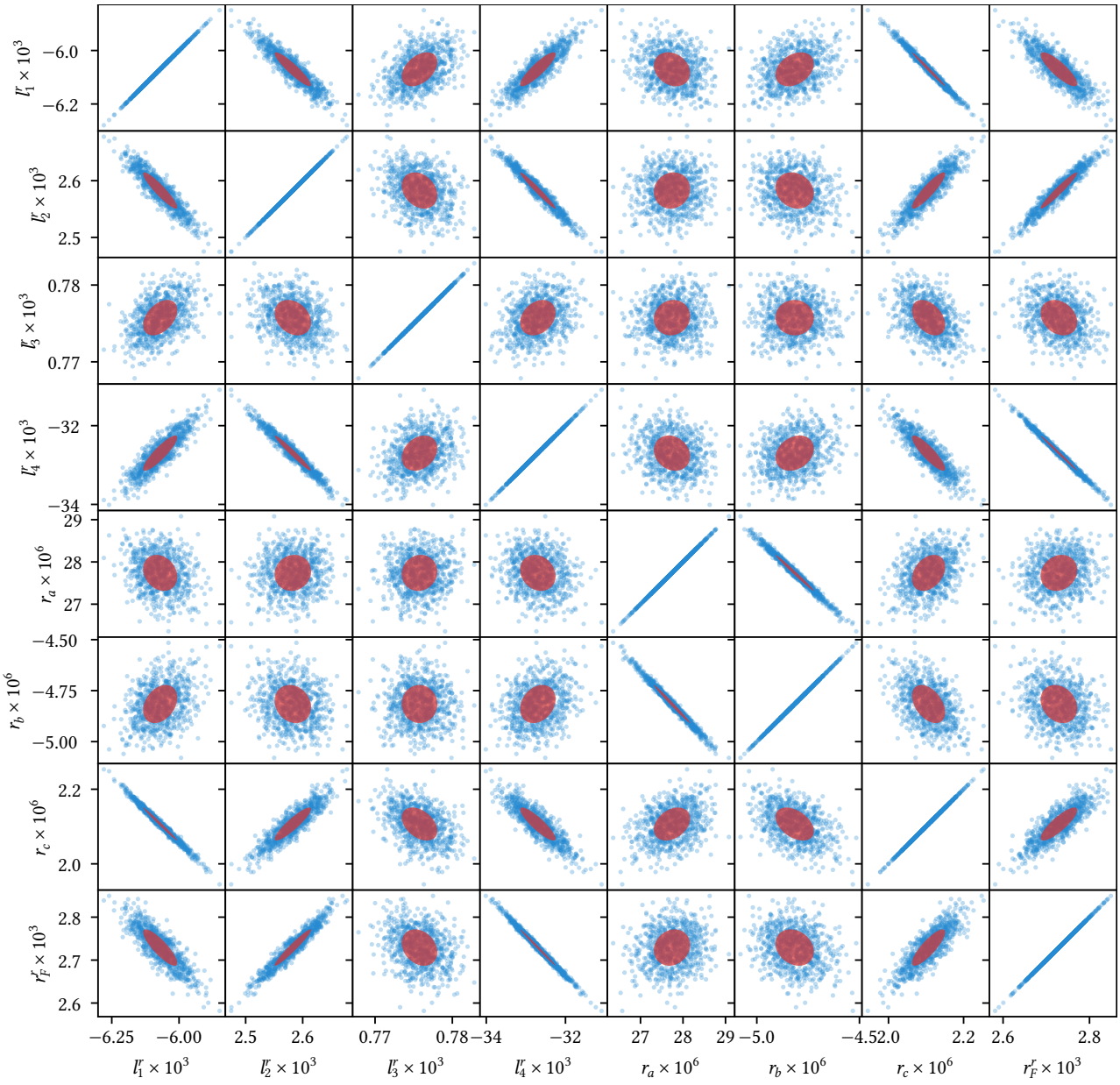

Figure 6.2: The covariance matrix of the LECs obtained in a global fit of the NNLO IAM and pion decay constant to the CLS ensembles. Each blue point is the value on one jackknife sample, in red the ellipses correspoinding to the 1σ confidence intervals are shown. To obtain the statistical errors given in Table 6.2, the scaling factor discussed in Sec. 6.4.1 needs to be taken into account.

	NLO	NNLO	Refs. [9, 47, 173–177, 182]
χ^2/dof	$216/(122-9) = 1.91$	$165/(123-15) = 1.53$	
BIC	259	237	
M_ρ/MeV	761.4(5.1)(0.3)(24.7)	749(12)(1)(1)	$763.7^{+1.7}_{-1.5}$
Γ_ρ/MeV	150.9(4.4)(0.1)(4.9)	129(12)(1)(1)	$146.4^{+2.0}_{-2.2}$
$\text{Re}(g_{\rho\pi\pi})$	5.994(54)(0)(194)	5.71(23)(2)(1)	$5.98^{+0.04}_{-0.07}$
$-\text{Im}(g_{\rho\pi\pi})$	0.731(21)(0)(24)	0.46(14)(2)(1)	$0.56^{+0.07}_{-0.10}$
F/MeV	88.27(0.23)(0.04)(2.86)	93.5(2.3)(0.1)(0.2)	86.89(58)

Table 6.3: A comparison of the NLO and NNLO fits to the CLS data. In addition to the quality of the fit, the ρ characteristics at the physical point as well as the obtained value of F are shown. The errors are as in Table 6.1, additionally, the third error is the one arising from the truncation as discussed in Sec. 6.4.4. For comparison, the ρ characteristics from a dispersive analysis [182] as well as the value of F as computed in Sec. 6.4.3 are listed in the last column.

experimental data [182] that makes use of Roy-like equations. The ρ properties are compatible with the literature values within their statistical error at both orders, the most significant discrepancies being the 2.2σ deviation of $\text{Im}(g_{\rho\pi\pi})$ at NLO and the 1.4σ one of the width at NNLO.

In addition, by inverting Eq. (4.11) we can compute F in physical units given the obtained values of the LECs as well as the PDG values of M_π and F_π [9]. The results and the literature value are shown in Table 6.3, too. This time the NLO result is compatible with the literature value only if the truncation error is taken into account. Contrarily, there is a 2.8σ discrepancy at NNLO.

In Fig. 6.3 we show the phase of both fits at the physical point in comparison with the one obtained in another dispersive analysis of experimental data [183]. Both results overlap within their error bands with the reference phase in almost the entire depicted energy range, with a very tiny deviation of the NNLO IAM towards the end of the resonance region and a modest deviation of the NLO result towards high energy values, which are anyway beyond the region of the ρ.

Finally, we can study the pion-mass dependence of the main observables at hand, namely the ρ properties as well as the pion decay constant, as depicted in Fig. 6.4. First, note that the error bands get significantly narrower at NNLO as compared to NLO, for the truncation error decreases, an effect that gets particularly enhanced at large pion masses due to the increase of the expansion parameter α_1 in Eq. (6.27) with growing pion mass. Second, the ρ gets only slightly heavier when the pion mass is increased, while the coupling stays almost constant. This directly explains the rapid decrease of the width with growing pion mass, for the decrease in available phase space is not at all compensated for by an increase of the coupling strength. These findings confirm the behavior that was conjectured in Ref. [89] based on the NLO IAM and subsequently observed in Ref. [94]. Third, there is a mild decrease of M_ρ at large pion masses at NNLO. This contradicts expectations from phenomenology: the Kawarabayashi–Suzuki–Fayyazuddin–Riazuddin (KSFR) relation states that [184, 185] (see also Ref. [186] for the form given here)

$$M_\rho^2 = 2g_{\rho\pi\pi}^2 F_\pi^2, \tag{6.29}$$

which is clearly violated by the observed pion-mass dependence of the NNLO amplitude at high energies. Moreover, the ρ can be described rather well as a quark-antiquark state, which also points towards an increase in M_ρ with increasing quark masses [187].

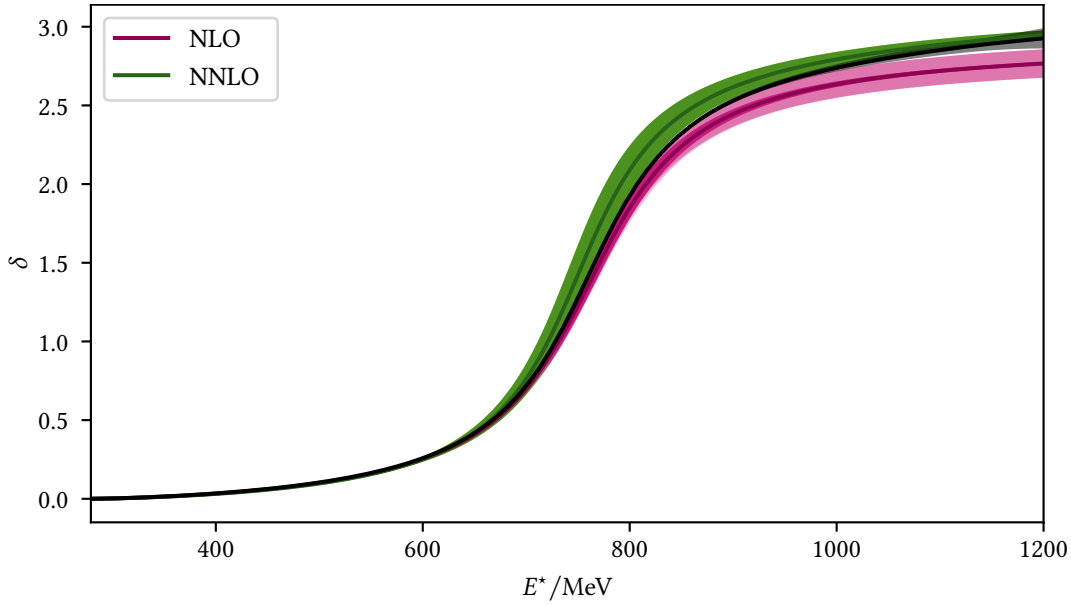

Figure 6.3: The phase obtained in global fits to the CLS ensembles extrapolated to the physical point. Both the result of the NLO and NNLO fit are shown including their error bars, whose color encoding is described in detail in Fig. 6.4. In addition, the result of a dispersive analysis [183] is depicted in black.

Altogether, there is a discrepancy in l_4^r both at NLO and NNLO, a tension in $\mathrm{Im}(g)$ at NLO and in Γ_ρ at NNLO, as well as deviations in both F and M_ρ at NNLO, the latter being visible at high pion masses. Moreover, the fit quality in terms of χ^2/dof is not satisfactory. To check if these issues might be related to the scale setting, we re-perform both the NLO and NNLO fit, but this time using strategy 2 to set the scale, see Sec. 6.4.2. At NLO we obtain $\chi^2/\mathrm{dof} = 213/(122-9) = 1.88$ and at NNLO $\chi^2/\mathrm{dof} = 165/(123-15) = 1.53$; comparison with Table 6.3 shows that there is a tiny improvement at NLO and none at NNLO. The resulting LECs are compared with the previously obtained ones in Table 6.4 and Table 6.5. Clearly, the value of l_4^r is still off, although the distance to the literature value decreases.

One might wonder if it is possible to enforce the literature value of l_4^r by adding a constraint $[(l_4^r \times 10^3 - 6.2)/1.3]^2$ to the χ^2 of strategy 2. However, this worsens the χ^2 at both orders, and, moreover, the improvement in l_4^r (0.4×10^{-3} at NLO and 5.4×10^{-3} at NNLO) is compensated for by a deterioriation of l_2^r, which equals -0.21×10^{-3} at NNLO, suddenly being in conflict with its literature value, a change that is in agreement with the correlation of $-98\,\%$ of both LECs in the strategy-1 fit, see Fig. 6.2. A similar trade-off can be observed at NNLO with respect to the observables. While the value of F is shifted from 90.8 MeV to 86.5 MeV closer to its literature value, the ρ pole at the physical point moves from $(755-64i)^2\,\mathrm{MeV}^2$ to $(807-77i)^2\,\mathrm{MeV}^2$, the mass of the latter being way too high. Hence, the inconsistency between scale setting via strategy 1 and the energy levels due to the omission of the pion mass shifts—see Sec. 6.4.2—alone does not explain the issues plaguing the strategy 1 fit results.

The observed trade-off between F and the ρ pole hints at a tension between the data on the pion decay constant and the $\pi\pi$ energy levels. To investigate this further, we use Eq. (4.11) in its inverted form—that is, F as a function of F_π and M_π—to fit the decay constant as a function of the pion mass. At NLO there are two fit parameters, namely F and l_4^r, while there are six at NNLO. This

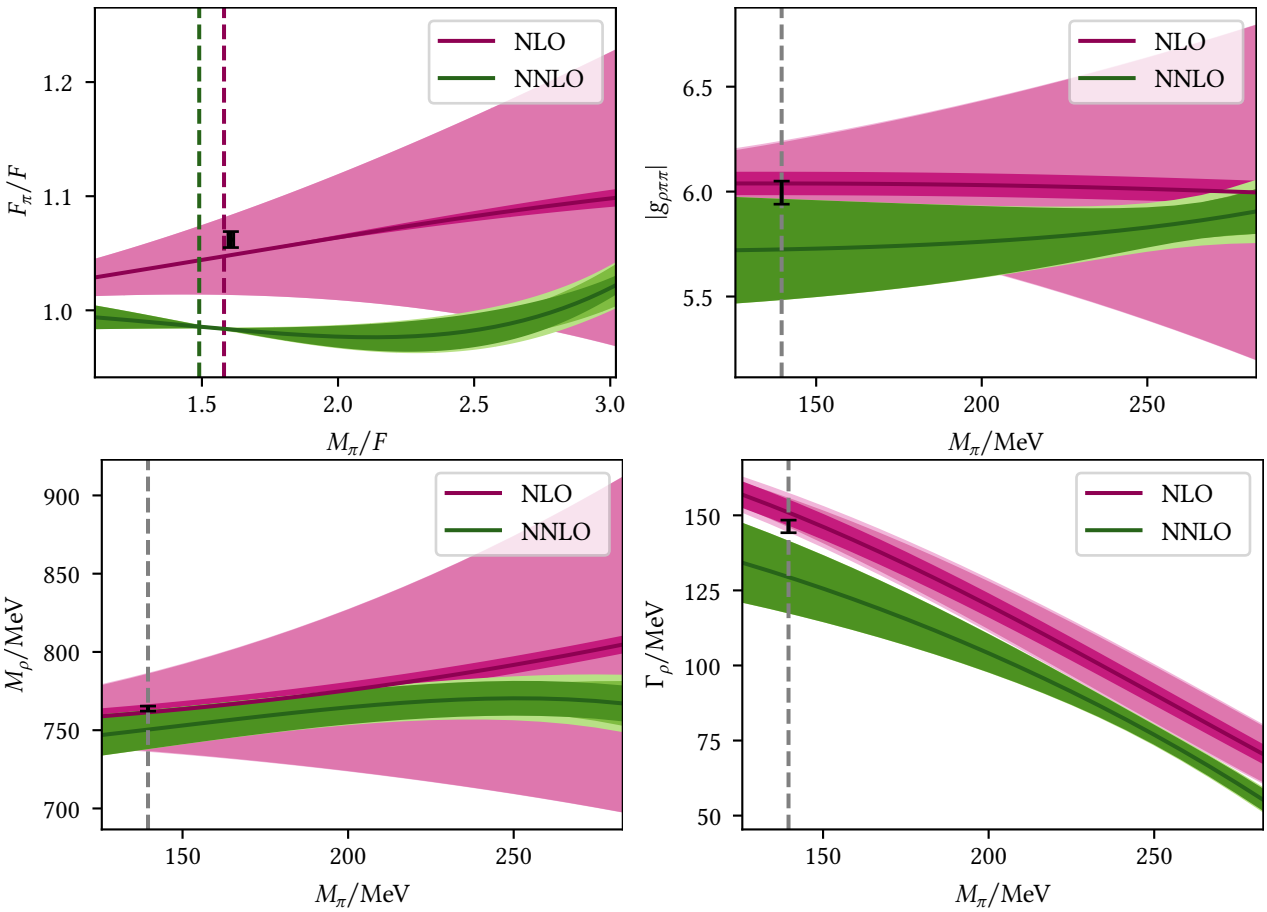

Figure 6.4: The pion-mass dependence of the pion decay constant as well as the properties of the ρ resonance as extracted from global fits to the CLS ensembles, both at NLO and NNLO. The physical point is indicated by dashed vertical lines. Since—in an attempt to diminish the effect of the scale setting—the pion decay constant is plotted in units of F and the value of this quantity at the physical point differs at NLO and NNLO, there are two such lines in the corresponding plot. In each plot, the error band of highest color saturation corresponds to the combined statistical error of the data and the one of the lattice spacing, the slightly less saturated one represents the truncation error, and the least saturated one the total error. For comparison the black ranges denote reference values at the physical point, namely the ρ properties taken from Ref. [182] and the pion decay constant as in Sec. 6.4.3.

	strategy 2	strategy 1	Ref. [162]	FLAG [47]
$(l_2^r - 2l_1^r) \times 10^3$	12.64(25)(1)	12.62(25)(0)	9.9(1.3)	19(17)
$l_4^r \times 10^3$	−2.0(1.1)(0.2)	−2.6(1.1)(0.2)	6.2(1.3)	3.8(2.8)

Table 6.4: The LECs obtained in a simultaneous fit to the CLS ensembles using the NLO IAM and strategy 2 to set the scale. These are to be compared with the ones of the strategy-1 fit. See Table 6.1 for further explanations concerning the errors and the literature values.

	strategy 2	strategy 1	Ref. [162]	Refs. [65, 153]
$l_1^r \times 10^3$	-2.5	$-6.1(1.8)(0.1)$	$-4.03(63)$	
$l_2^r \times 10^3$	1.48	2.58(90)(7)	1.87(21)	
$l_3^r \times 10^3$	0.822	0.776(65)(4)	0.8(3.8)	
$l_4^r \times 10^3$	-16	$-33(13)(0)$	6.2(1.3)	
$r_a \times 10^6$	17	28(12)(1)		13
$r_b \times 10^6$	-1.7	$-4.8(2.6)(0.2)$		-9.0
$r_c \times 10^6$	0.24	2.1(1.3)(0.1)		1.1
$r_F^r \times 10^3$	1.4	2.7(1.2)(0)		0

Table 6.5: Same as Table 6.4 but for NNLO fits. See also Table 6.2.

	strategy 2	strategy 1	strategy 1 (shifted)	reference
F/MeV	87.72(87)	82.51(84)	82.48(93)	86.89(58)
$l_4^r \times 10^3$	0.8(1.0)	1.3(1.0)	1.3(1.1)	3.8(2.8), 6.2(1.3)

Table 6.6: The results of fits to the CLS pion decay constants as a function of the pion mass. The obtained values of the LECs are displayed for the three different strategies to set the scale. Their errors incorporate the statistical error of both aF_π^{lat} and aM_π^{lat}. The reference value of F is as in Sec. 6.4.3, the first one of l_4^r is taken from the lattice [47, 173–177], and the second one of l_4^r from phenomenology [162].

makes NNLO fits impossible, for there are only four data points. Moreover, the values are obtained at three different lattice spacings, and thus we are forced to set the scale before we are able to fix the two parameters at NLO via a fit. We do this three times: once via strategy 2 and twice via strategy 1, both with and without the shifts of the pion masses and decay constants. The results are displayed in Table 6.6 and Fig. 6.5. Clearly, in case of strategy 1 it does not make a significant difference if the data are shifted or not. Independently of the strategy, the obtained value of l_4^r is in tension with the value from phenomenology, while it survives the confrontation with the lattice reference value, both because the central value of the latter is smaller than the one of Ref. [162] and because its error is larger. However, only strategy 2 yields a value of F that is compatible with the one from literature. Note that this analysis does not incorporate the error of the lattice spacings. The tension is likely to decrease somewhat if this error was included, for this would increase the error of the results.

Based on these observations we draw the following conclusions: on its own, the CLS pion decay constants seem to be compatible with NLO ChPT, for at least strategy 2 yields compatible outcomes. Nevertheless, there is some tension. Moreover, the differences between strategy 1 and strategy 2 hint at a non-negligible impact of the scale setting. However, as soon as the $\pi\pi$ energy levels are included, it becomes impossible with our model to simultaneously obtain results of F and the ρ pole at the physical point that agree with literature values. More specifically, a satisfactory ρ pole at NNLO enforces values of F that are too high. To achieve these large values of F the fit pushes l_4^r far away from its literature values. The problem seems to be, at least partly, with the $\pi\pi$ energy levels, for on its own the pion decay constants allow for values of l_4^r that are significantly

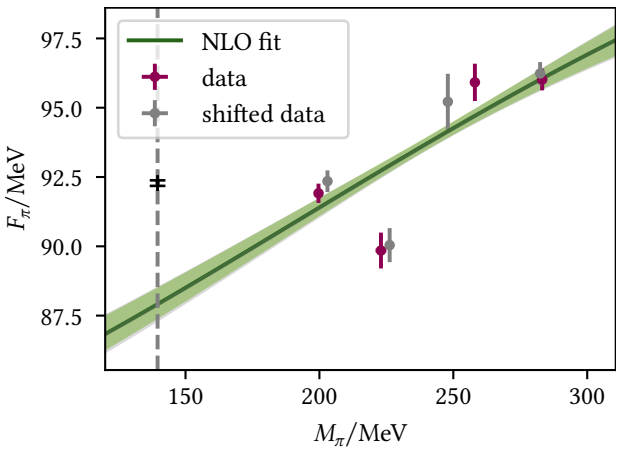

(a) Strategy 1. The green curve shows the result of a fit to the non-shifted data, while the outcome of a fit to the shifted data is shown as a gray overlay. Both results are almost indistinguishable.

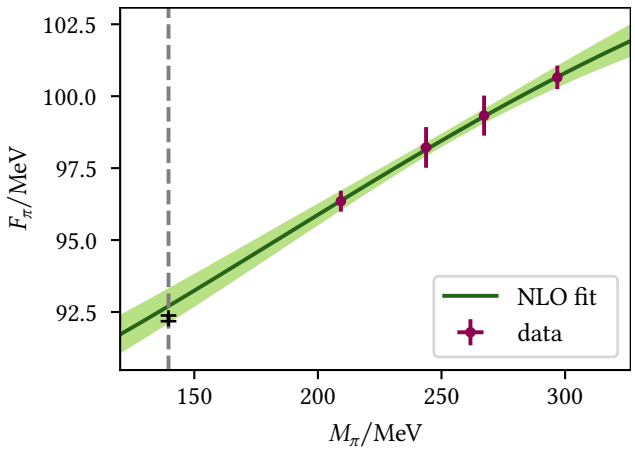

(b) Strategy 2. As in the strategy-1 fit, the error band is associated with the error of aF_π^{lat} and aM_π^{lat}.

Figure 6.5: The CLS pion decay constants compared to fit results. Again, the physical point is indicated by vertical gray lines; furthermore, the PDG value of F_π [9] is shown in black.

closer to the literature. This all points towards the influence of artifacts that are associated with the lattice computation, e.g., discretization artifacts.

Hence, we include two additional parameters g and g_F in the strategy-1 IAM fit to model discretization artifacts in the crude way described in Sec. 6.3. At NLO, this improves the fit quality considerably, reducing the χ^2 to $\chi^2/\text{dof} = 183/(122-11) = 1.65$, to be compared with Table 6.3. Even in the absence of lattice artifacts this would have come at no surprise, for the NLO fit is rather rigid, with initially only two LECs as fit parameters. Our modeling of the discretization artifacts effectively doubles the number of fit parameters and renders the fit much more flexible. Nevertheless, it is reassuring to observe that $l_4^r = 2.4 \times 10^{-4}$ gets pushed closer to its literature value, while $g_F = -2.0$ is sizable, and $F = 87.7\,\text{MeV}$ is even closer to its literature value than before. However, $g = 0.69$ comes out small and the ρ pole deteriorates, reading $(729-66i)^2\,\text{MeV}^2$ at the physical point, hinting at the fact that our modeling of the lattice artifacts—especially in the $\pi\pi$ energy levels—is too crude to improve the situation. At NNLO, the χ^2 does not change significantly, so that the additional fit parameters worsen the χ^2/dof to become $\chi^2/\text{dof} = 165/(123-17) = 1.56$. That is, the NNLO expressions do have sufficiently many free fit parameters to mimic the lattice artifacts, such that the unrefined parametrization of discretization artifacts does not yield an improvement. A more detailed understanding of the lattice artifacts would be necessary to completely settle this issue.

Coming back to the discussion in Sec. 4.3, we note that it is very likely that the discrepancies observed in the CLS fits are too large to arise solely from the use of an $SU(2)$ formalism that ignores the kaon. For example, the shift observed in Table 6.6 in F when switching from strategy 2 to 1 is at the 6 % level, and thus larger than the kaon-mass effects described in Sec. 4.3. Similarly, the discrepancy in F at NNLO shown in Table 6.3 is too large to plausibly hint merely at kaon-mass effects.

	fit	Ref. [162]	FLAG
$(l_2^r - 2l_1^r) \times 10^3$	12.908(59)(68)(99)	9.9(1.3)	19(17)

Table 6.7: The single LEC as fixed by a fit of the NLO IAM to the three ensembles by HadSpec. The first error is associated with the statistical error of the data and the second one with the error of the lattice spacing as in Table 6.1. On top of this the third error encompasses the error of the literature value of F. The reference values are as in Table 6.1, too.

	fit	Ref. [162]	Refs. [65, 153]
$l_1^r \times 10^3$	−4.17(85)(24)(32)	−4.03(63)	
$l_2^r \times 10^3$	1.44(25)(13)(18)	1.87(21)	
$r_a \times 10^6$	11.5(2.0)(0.4)(0.6)		13
$r_b \times 10^6$	−4.39(84)(25)(25)		−9.0
$r_c \times 10^6$	0.97(0.43)(0.12)(0.16)		1.1

Table 6.8: The LECs determined by fitting the NNLO IAM to the HadSpec ensembles. For an explanation of the errors see Table 6.7 and for the reference values consult Table 6.2.

6.5.2 HadSpec

Second, we discuss the fits to the data by HadSpec. While the CLS data cover five different pion masses, the older data by HadSpec are obtained at two different masses, thereby reducing the control of the pion-mass dependence, see Table 5.1. To obtain stable fits despite these limitations, the LEC l_3^r has to be fixed to its literature value, i.e., $l_3^r = 8.2 \times 10^{-4}$ [162]. In addition, the settings of the differential-evolution algorithm need to be more lavish as described in Sec. 6.2. Since the pion decay constant on the ensemble of lower pion mass is not available, we do not fit the pion decay constant at all, but treat F as outlined in Sec. 6.4.3. Note that if instead the ensemble of lower pion mass were to be excluded from the fit (as we did with the CLS ensemble N401), data at merely one pion mass would be left, thereby making it impossible to control the pion-mass dependence that is crucial to obtain stable fits at NNLO. Furthermore, since the literature value of F is given in MeV, it needs to be translated to lattice units via multiplication by the lattice spacing a. Thus, the impact of the error of the spacing a gets enhanced as compared to the CLS fits. The resulting LECs are listed in Table 6.7 and Table 6.8, the fit quality and ρ properties at the physical point in Table 6.9, and the phase at the physical point as well as the pion-mass dependence of the ρ characteristics are shown in Fig. 6.6. Clearly, for several quantities the largest source of uncertainty arises from the lattice spacing a in accordance with its more dominant role. While the LECs are fairly compatible with the literature, the ρ pole at the physical point at NNLO deviates considerably from its literature value. This goes hand in hand with the observation that the phase δ at the physical point is better at NLO than at NNLO. However, there is no decrease of M_ρ at high pion masses, contrarily to the results of the CLS fit.

It is worth comparing the results at NLO to the ones of Ref. [59]. There the authors fitted the NLO IAM to the lightest ensemble only, obtaining $\chi^2/\mathrm{dof} = 1.26$ and a ρ pole at the physical point corresponding to $M_\rho = 755(2)(1)^{+20}_{-2}$ MeV and $\Gamma_\rho = 129(3)(1)^{+7}_{-1}$ MeV. However, this analysis

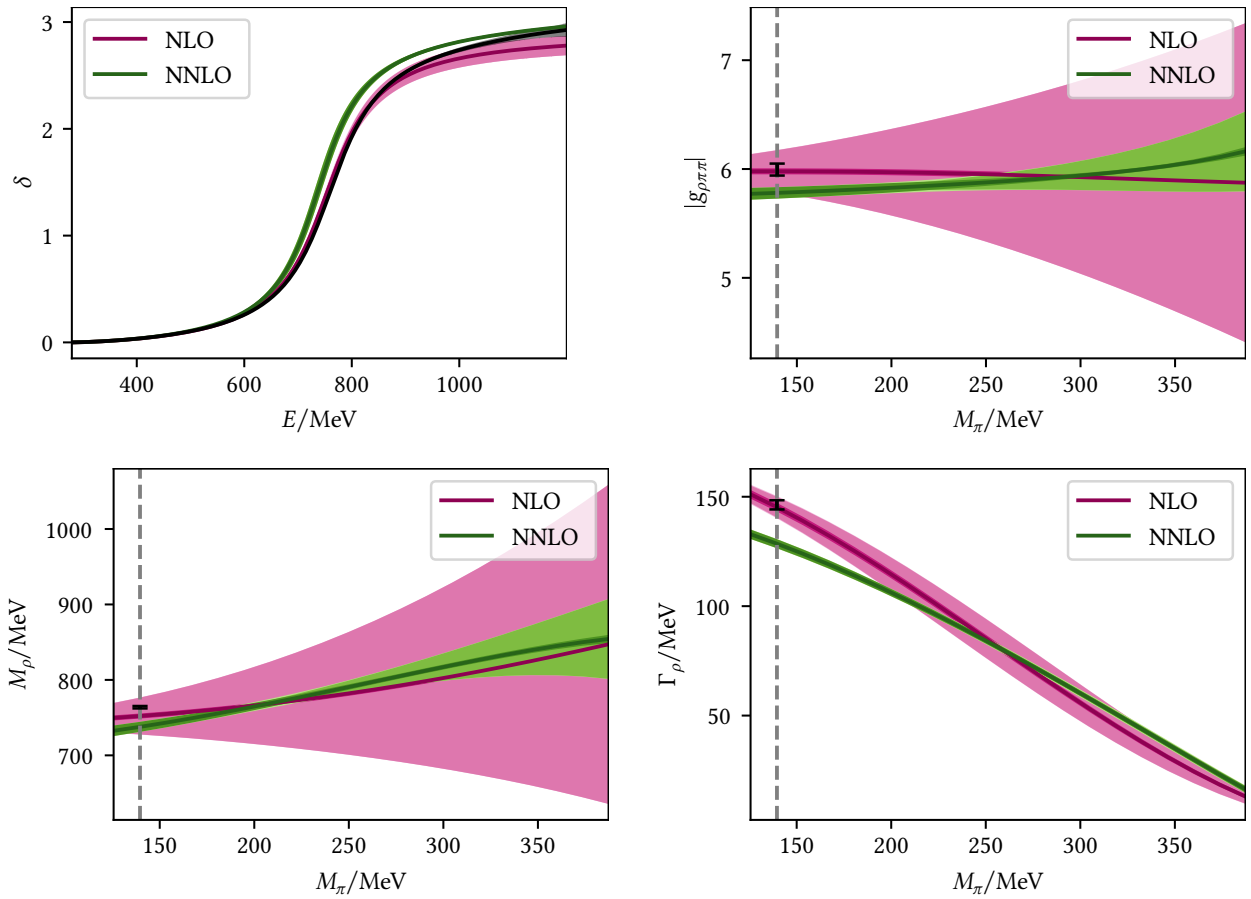

Figure 6.6: Same as Figs. 6.3 and 6.4 but for global fits to the ensembles by HadSpec. The error band corresponding to the statistical error of the data includes the impact of the error of the literature value of F.

	NLO	NNLO
χ^2/dof	$124/(52-4) = 2.58$	$75/(52-8) = 1.70$
BIC	140	106
M_ρ/MeV	752.1(2.0)(2.4)(1.2)(24.4)	737.8(3.8)(5.4)(0.6)(0.8)
Γ_ρ/MeV	145.2(1.2)(1.4)(0.7)(4.7)	128.5(0.9)(1.9)(0.1)(0.5)
$\text{Re}(g_{\rho\pi\pi})$	5.937(12)(14)(20)(192)	5.765(51)(17)(0)(6)
$-\text{Im}(g_{\rho\pi\pi})$	0.7089(44)(51)(74)(230)	0.426(12)(10)(7)(9)

Table 6.9: The quality of the fit as well as the ρ properties at the physical point for both the NLO and NNLO fit to the ensembles by HadSpec. The errors arise, in order of appearance, due to the statistical error of the data, the error of the lattice spacing, the error of the literature value of F, and the truncation error.

is flawed for the IAM was expressed in terms of F_π instead of F. To take into account the pion-mass dependence of the former, the LEC l_4^r appearing in Eq. (4.11) at NLO was kept as a free fit parameter, resulting in $l_4^r = -28(6)(3)^{+1}_{-11} \times 10^{-3}$. That is, the parameter l_4^r that is supposed to describe the physics associated with the decay constant was adjusted to parametrize the $\pi\pi$ P wave. This amounts at best to the inconsistent incorporation of a spurious higher-order effect into the IAM; note that l_4^r does show up in the P wave neither at NLO nor NNLO, see Sec. 4.1. In this way the number of fit parameters was doubled, and thus the fit became sufficiently flexible to describe the data of only a single ensemble rather well and yielded a comparatively low value of χ^2/dof. Unsurprisingly, the resulting values of both l_4^r and Γ_ρ are in conflict with literature. Perhaps coincidentally the shift in l_4^r shows the same tendency as the one observed in our fits to the CLS data.

Part III

Pion-mass dependence of $\gamma^{(*)}\pi \to \pi\pi$

This part is an expanded version of Ref. [188].

Chapter 7

Continuum scattering amplitude

Now that we are equipped with a potent description of the $\pi\pi \to \pi\pi$ P wave, namely the IAM, we are in a position to construct a continuum model of the $\gamma^{(*)}\pi \to \pi\pi$ amplitude, again focusing on the P wave. First, in Sec. 7.1 we define the amplitude in a precise manner, relate different representations of the amplitude, and introduce several observables. Second, in Sec. 7.2 we discuss the KT equation for this process. Lastly, in Sec. 7.3 we describe how to control the pion-mass dependence and extract the anomaly.

7.1 $\gamma^{(*)}\pi \to \pi\pi$ scattering amplitude

Before defining the $\gamma^{(*)}\pi \to \pi\pi$ scattering amplitude, we must be precise about the involved pion states. Single pion states $|\pi, \boldsymbol{k}\rangle$ are characterized by their momentum $\boldsymbol{k}$ and normalized in the standard manner [189], i.e.,

$$\langle \pi, \boldsymbol{k} \,|\, \pi, \boldsymbol{k'} \rangle = 2\omega_k (2\pi)^3 \, \delta^{(3)} (\boldsymbol{k} - \boldsymbol{k'}) \,. \tag{7.1}$$

Here the notation is as in Sec. 3.2.1. They are associated with an infinite-dimensional unitary representation U of the Poincaré group, which assigns to each element (Λ, a) of the latter the unitary operator $U(\Lambda, a)$, where $a \in \mathbb{R}^4$ represents a translation and Λ is a Lorentz transformation. This operator acts on the pion states as [11]

$$U(\Lambda, a) \, |\pi, \boldsymbol{k}\rangle = e^{-iak} \, |\pi, \boldsymbol{\Lambda k}\rangle \,. \tag{7.2}$$

Here $\boldsymbol{\Lambda k} = (\Lambda k)^j \boldsymbol{e}_j$, with $\boldsymbol{e}_j$, $j = 1, 2, 3$, the customary basis vectors of $\mathbb{R}^3$. For brevity, we write $U(\Lambda) \coloneqq U(\Lambda, 0)$. Consider now a scenario similar to the one outlined in Sec. 3.2.1, namely two pions with individual four-momenta k, k', and total four-momentum $P = k + k'$. They are described by the product state $|\pi\pi, \boldsymbol{k}, \boldsymbol{k'}\rangle \coloneqq |\pi, \boldsymbol{k}\rangle \otimes |\pi, \boldsymbol{k'}\rangle$, which is related to the state $|\pi, \boldsymbol{k}^\star\rangle \otimes |\pi, \boldsymbol{k'}^\star\rangle$ in the CM frame by a Lorentz transformation $\Lambda_R \Lambda_B$, where Λ_B is a Lorentz boost in the x^3 direction and Λ_R is a rotation, such that $P = \Lambda_R \Lambda_B P^\star$. That is,

$$\begin{aligned} |\pi, \boldsymbol{k}\rangle \otimes |\pi, \boldsymbol{k'}\rangle &= U(\Lambda_R \Lambda_B) \, |\pi, \boldsymbol{k}^\star\rangle \otimes U(\Lambda_R \Lambda_B) \, |\pi, \boldsymbol{k'}^\star\rangle \\ &= |\pi, \boldsymbol{\Lambda_R \Lambda_B k}^\star\rangle \otimes |\pi, \boldsymbol{\Lambda_R \Lambda_B k'}^\star\rangle \,, \end{aligned} \tag{7.3}$$

with $k'^\star = (\omega_k^\star, -\boldsymbol{k}^\star)$. Since both Λ_R and Λ_B are determined by P, we can choose P and $\Omega_k^\star$ instead of labeling the two pion states by the six quantum numbers $\boldsymbol{k}$ and $\boldsymbol{k'}$, with $\Omega_k^\star$ as defined in Sec. 3.2.2.

That is, we write $|\pi\pi, P, \Omega_k^\star\rangle \coloneqq |\pi, \boldsymbol{k}\rangle \otimes |\pi, \boldsymbol{k'}\rangle$. In full analogy to Eq. (3.11), we can decompose these states into a partial-wave basis[1]

$$\left|\pi\pi, P, \Omega_k^\star\right\rangle = \sum_{l=0}^{\infty} \sum_{m=-l}^{l} \sqrt{4\pi}\, Y_{lm}^*\left(\Omega_k^\star\right) |\pi\pi, P, l, m\rangle\,, \tag{7.4}$$

with the inverse given as

$$|\pi\pi, P, l, m\rangle = \frac{1}{\sqrt{4\pi}} \int \mathrm{d}\Omega_k^\star\, Y_{lm}\left(\Omega_k^\star\right) \left|\pi\pi, P, \Omega_k^\star\right\rangle. \tag{7.5}$$

Now we can study the scattering amplitude $\mathscr{M}$ of the process $\gamma^{(*)}(\lambda_\gamma, q)\pi^+(p) \to \pi^+(k)\pi^0(k')$, where λ_γ denotes the helicity of the up to now on-shell photon. With the T matrix as introduced in Ch. 2, we have

$$\left\langle \pi\pi, \boldsymbol{k}, \boldsymbol{k'} \left| iT \right| \gamma\pi, \lambda_\gamma, \boldsymbol{q}, \boldsymbol{p} \right\rangle = i\,(2\pi)^4\, \delta^{(4)}\left(q + p - k + k'\right) \mathscr{M}\left(s, t\right), \tag{7.6}$$

with $s = (k + k')^2$ and $t = (p - k)^2$. This amplitude can be inferred from the matrix element

$$\langle \pi\pi, \boldsymbol{k}, \boldsymbol{k'} \left| J^\mu(0) \right| \pi, \boldsymbol{p} \rangle \tag{7.7}$$

of the electromagnetic current

$$J^\mu \coloneqq \frac{2}{3} e\, \bar{u}\gamma^\mu u - \frac{1}{3} e\, \bar{d}\gamma^\mu d \tag{7.8}$$

in position space via [117]

$$\mathscr{M}\left(s, t, q^2\right) = \epsilon_\mu\left(\lambda_\gamma, q\right) \langle \pi\pi, \boldsymbol{k}, \boldsymbol{k'} \left| J^\mu(0) \right| \pi, \boldsymbol{p} \rangle\,. \tag{7.9}$$

Here e is the (positive) elementary charge, u and d are the fields associated with the up and down quark, respectively, and ϵ_μ is the polarization vector of the photon. Note that here we allow for off-shell photons, i.e., the virtuality q^2 can take on arbitrary real values, and we have $\mathscr{M}(s, t) = \mathscr{M}(s, t, q^2 = 0)$. The symmetries of the process allow for decomposing Eq. (7.7) as [51, 66]

$$\left\langle \pi\pi, \boldsymbol{k}, \boldsymbol{k'} \left| J_\mu(0) \right| \pi, \boldsymbol{p} \right\rangle = i\epsilon_{\mu\nu\alpha\beta} p^\nu k^\alpha k'^\beta \mathscr{F}\left(s, t, q^2\right), \tag{7.10}$$

with $\mathscr{F}$ being a complex-valued function, which in turn can be expressed via partial waves f_J of total angular momentum J via [51, 132] (see also Ref. [190, App. B])

$$\mathscr{F}\left(s, t, q^2\right) = \sum_{j=0}^{\infty} f_{2j+1}\left(s, q^2\right) P'_{2j+1}\left(z^\star\right). \tag{7.11}$$

An individual partial wave can be projected out via the relation

$$\frac{1}{2} \int_{-1}^{1} P'_n(x) \left[P_{m-1}(x) - P_{m+1}(x)\right] \mathrm{d}x = \delta_{nm}. \tag{7.12}$$

[1] This decomposition is chosen instead of Eq. (3.8) to be in accordance with the standard choice of polarization vectors, see the derivation of Eq. (7.21).

The non-vanishing spin of the photon is the reason for the appearance of derivatives of Legendre polynomials instead of ordinary ones as in Eq. (2.3).

Our goal is now to derive an alternative representation of the matrix element that is used in lattice-QCD computations. To that end, we build upon the discussion in Ref. [191, App. D], slightly modifying it. Decomposing the $\pi\pi$ state in Eq. (7.7) via Eq. (7.4) yields

$$\left\langle \pi\pi, \boldsymbol{k}, \boldsymbol{k'} \left| J_\mu(0) \right| \pi, \boldsymbol{p} \right\rangle = \sum_{l=0}^{\infty} \sum_{m=-l}^{l} \sqrt{4\pi} Y_{lm}\left(\Omega_k^\star\right) \left\langle \pi\pi, P, l, m \left| J_\mu(0) \right| \pi, \boldsymbol{p} \right\rangle . \tag{7.13}$$

According to Eq. (7.5) the P-wave component reads

$$\begin{aligned} &\left\langle \pi\pi, P, 1, m \left| J_\mu(0) \right| \pi, \boldsymbol{p} \right\rangle \\ &= \frac{1}{\sqrt{4\pi}} \int \mathrm{d}\Omega_k^\star Y_{1m}^*\left(\Omega_k^\star\right) \left\langle \pi\pi, \boldsymbol{k}, \boldsymbol{k'} \left| J_\mu(0) \right| \pi, \boldsymbol{p} \right\rangle \\ &= \frac{1}{\sqrt{4\pi}} \int \mathrm{d}\Omega_k^\star Y_{1m}^*\left(\Omega_k^\star\right) \left\langle \pi\pi, \boldsymbol{\Lambda_R \Lambda_B k^\star}, \boldsymbol{P} - \boldsymbol{\Lambda_R \Lambda_B k^\star} \left| J^\mu(0) \right| \pi, \boldsymbol{p} \right\rangle , \end{aligned} \tag{7.14}$$

where we made use of Eq. (7.3) and $k' = P - k$. Inserting Eq. (7.10) and exploiting the antisymmetry of the Levi-Civita symbol results in

$$\begin{aligned} &\left\langle \pi\pi, P, 1, m \left| J_\mu(0) \right| \pi, \boldsymbol{p} \right\rangle \\ &= \frac{i}{\sqrt{4\pi}} \int \mathrm{d}\Omega_k^\star Y_{1m}^*\left(\Omega_k^\star\right) \epsilon_{\mu\nu\alpha\beta} p^\nu \left(\Lambda_R \Lambda_B k^\star\right)^\alpha P^\beta \mathscr{F}\left(s, t, q^2\right) \\ &= \frac{i}{\sqrt{4\pi}} \sum_{j=0}^{\infty} f_{2j+1}\left(s, q^2\right) \epsilon_{\mu\nu\alpha\beta} p^\nu \left(\Lambda_R \Lambda_B\right)^\alpha{}_\rho P^\beta \int \mathrm{d}\Omega_k^\star Y_{1m}^*\left(\Omega_k^\star\right) k^{\star\rho} P'_{2j+1}\left(z^\star\right) , \end{aligned} \tag{7.15}$$

where we made use of the fact that Λ_R and Λ_B are independent of the direction of $\boldsymbol{k}^\star$.[2]

To make further progress, we need to compute the integral

$$\Xi_{mj}^\rho := \int \mathrm{d}\Omega_k^\star \, Y_{1m}^*\left(\Omega_k^\star\right) k^{\star\rho} P'_j\left(z^\star\right) . \tag{7.16}$$

Since the photon is allowed to be virtual, i.e., off-shell, all three polarizations $\lambda_\gamma \in \{\pm 1, 0\}$ are allowed. However, the case $\lambda_\gamma = 0$ is of no relevance due to the vanishing phase space [190, App. B]. Aligning the quantization axis of the angular momentum of the $\pi\pi$ system with the axis associated with the helicity of the photon (without loss of generality, we pick the x^3 axis), we can thus focus on $m = \pm 1$. From

$$Y_{1,\pm 1}\left(\Omega_k^\star\right) = \mp \frac{1}{2} \sqrt{\frac{3}{2\pi}} e^{\pm i\phi^\star} \sin\theta^\star \tag{7.17}$$

we can directly deduce that

$$\Xi_{\pm 1,j}^0 = \int \mathrm{d}\Omega_k^\star \, Y_{1m}^*\left(\Omega_k^\star\right) \omega_k^\star P'_j\left(z^\star\right) = 0, \tag{7.18}$$

[2] This is because rotating $\boldsymbol{k}^\star$ and $\boldsymbol{k'}^\star = -\boldsymbol{k}^\star$ does not change $P^\star$, and thus $P = \Lambda_R \Lambda_B P^\star$ remains unchanged for fixed $\Lambda_R \Lambda_B$, too, despite the fact that k and k' are affected.

because the integrand depends on $\phi^\star$ only via the phase $e^{\pm i\phi^\star}$, which yields zero when integrated over $[0, 2\pi]$. For the same reason, the third component of

$$\begin{aligned}\Xi_{\pm 1,j} &= \int \mathrm{d}\Omega_k^\star \, Y_{1m}^* \left(\Omega_k^\star\right) \boldsymbol{k}^\star P_j' \left(z^\star\right) \\ &= \mp \frac{|\boldsymbol{k}^\star|}{2} \sqrt{\frac{3}{2\pi}} \int \mathrm{d}\Omega_k^\star \, e^{\mp i\phi^\star} \sin\theta^\star \begin{pmatrix} \sin\theta^\star \cos\phi^\star \\ \sin\theta^\star \sin\phi^\star \\ \cos\theta^\star \end{pmatrix} P_j' \left(z^\star\right)\end{aligned} \tag{7.19}$$

also vanishes. As a special case of Eq. (7.12) we obtain

$$\delta_{n1} = \frac{3}{4} \int_{-1}^{1} P_n' \left(x\right) \left(1 - x^2\right) \mathrm{d}x, \tag{7.20}$$

and thus

$$\begin{aligned}\Xi_{\pm 1,j} &= \sqrt{\frac{2\pi}{3}} \, |\boldsymbol{k}^\star| \, \delta_{j1} \begin{pmatrix} 0, & \mp 1, & i, & 0 \end{pmatrix}^T \\ &= \mp \sqrt{\frac{4\pi}{3}} \, |\boldsymbol{k}^\star| \, \delta_{j1} \epsilon^* \left(\pm 1, P^\star\right),\end{aligned} \tag{7.21}$$

with $\epsilon(\lambda_{\pi\pi}, P^\star)^*$ being the polarization vector of the outgoing $\pi\pi$ state of helicity $\lambda_{\pi\pi}$. That is, indeed only the P wave contributes, as it is required by angular-momentum conservation.

Inserting Eq. (7.21) into Eq. (7.15) leads via $\Lambda_R \Lambda_B \epsilon(\lambda_{\pi\pi}, P^\star) = \epsilon(\lambda_{\pi\pi}, \Lambda_R \Lambda_B P^\star)$ [11] to

$$\left\langle \pi\pi, P, 1, \pm 1 \left| J_\mu(0) \right| \pi, \boldsymbol{p} \right\rangle = \mp \frac{i}{\sqrt{3}} \, |\boldsymbol{k}^\star| \, \epsilon_{\mu\nu\alpha\beta} p^\nu \epsilon^{*\alpha} \left(\pm 1, P\right) P^\beta f_1 \left(s, q^2\right). \tag{7.22}$$

Since we are also interested in matrix elements with off-shell photons, despite the vanishing phase space we also consider $m = 0$, focusing on the P wave. Explicitly, we have

$$\Xi_{01} = \sqrt{\frac{4\pi}{3}} \, |\boldsymbol{k}^\star| \left(0, 0, 0, 1\right)^T = \sqrt{\frac{4\pi}{3}} \, |\boldsymbol{k}^\star| \, \epsilon^*(0, P^\star). \tag{7.23}$$

Extending Eq. (7.22) to this case results in

$$\left\langle \pi\pi, P, 1, m \left| J_\mu(0) \right| \pi, \boldsymbol{p} \right\rangle = \eta\left(m\right) \frac{i}{\sqrt{3}} \, |\boldsymbol{k}^\star| \, \epsilon_{\mu\nu\alpha\beta} p^\nu \epsilon^{*\alpha} \left(m, P\right) P^\beta f_1 \left(s, q^2\right), \tag{7.24}$$

with $\eta(\pm 1) = \mp 1$, $\eta(0) = 1$ a pure phase. We rewrite this in terms of

$$\mathscr{A}\left(s, q^2\right) := \frac{M_\pi |\boldsymbol{k}^\star|}{2e\sqrt{3}} f_1 \left(s, q^2\right) \tag{7.25}$$

as

$$\left\langle \pi\pi, P, 1, m \left| J_\mu(0) \right| \pi, \boldsymbol{p} \right\rangle = \eta\left(m\right) e \frac{2i}{M_\pi} \epsilon_{\mu\nu\alpha\beta} p^\nu \epsilon^{*\alpha} \left(m, P\right) P^\beta \mathscr{A}\left(s, q^2\right), \tag{7.26}$$

which is precisely the decomposition used in lattice-QCD computations.

Equipped with the two decompositions of the matrix element we can turn our focus to the observables we are interested in. First, the cross section $\sigma_{\gamma\pi}$ for $q^2 = 0$ can be computed in a straightforward manner. In the CM frame

$$\frac{\mathrm{d}\sigma_{\gamma\pi}}{\mathrm{d}\Omega_k^\star} \left(s, \Omega_k^\star\right) = \frac{1}{64\pi^2 s} \frac{|\boldsymbol{k}^\star|}{|\boldsymbol{p}^\star|} \frac{1}{2} \sum_{\lambda_\gamma = \pm 1} \left|\mathscr{M}\left(s, t\right)\right|^2 \tag{7.27}$$

holds [189]. Inserting Eq. (7.9) and Eq. (7.10) results in [66]

$$\sigma_{\gamma\pi}(s) = \frac{\left(s-4M_\pi^2\right)^{3/2}\left(s-M_\pi^2\right)}{1024\pi\sqrt{s}} \int_{-1}^{1} \left(1-z^\star\right)^2 \left|\mathscr{F}(s,t,0)\right|^2 \mathrm{d}z^\star. \tag{7.28}$$

Truncating the expansion (7.11) after the P wave simplifies the cross section, yielding

$$\sigma_{\gamma\pi}(s) = \frac{\left(s-4M_\pi^2\right)^{3/2}\left(s-M_\pi^2\right)}{768\pi\sqrt{s}} \left|f_1(s,0)\right|^2. \tag{7.29}$$

Second, at vanishing energy, the anomalous nature of the process fixes the amplitude in terms of the pion decay constant $F_\pi = 92.28(10)\,\mathrm{MeV}$ [9] as $\mathscr{F}(0,0,0) =: eF_{3\pi}$ with [100]

$$F_{3\pi} = \frac{1}{4\pi^2 F_\pi^3} = 32.23(10)\,\mathrm{GeV}^{-3}. \tag{7.30}$$

Third, we want to determine the radiative coupling $g_{\rho\gamma\pi}$ of the ρ resonance to the $\gamma\pi$ state. To that end, we need to continue f_1 to its second Riemann sheet. To do so, we take a look at the unitarity relation of f_1. If only $\pi\pi$ intermediate states are taken into account, the right-hand cut of f_1 starts at $4M_\pi^2$ in the Mandelstam-s plane and extends along the positive real axis towards infinity. The unitarity relation of f_1 along this right-hand cut then reads [51]

$$\mathrm{Im}\left[f_1\left(s,q^2\right)\right] = f_1\left(s,q^2\right)\sin\left[\delta(s)\right]e^{-i\delta(s)}, \quad s\in[4M_\pi^2,\infty), \tag{7.31}$$

which is to be compared with the $\pi\pi \to \pi\pi$ unitarity relation (2.16). As before, δ denotes the $\pi\pi\to\pi\pi$ P-wave phase shift. In passing we note that Eq. (7.31) implies (modulo 2π)

$$\arg\left[f_1\left(s,q^2\right)\right] = \begin{cases}\delta(s), & \mathrm{Im}\left[f_1\left(s,q^2\right)\right]\geq 0\\ \delta(s)-\pi, & \mathrm{Im}\left[f_1\left(s,q^2\right)\right]<0\end{cases}, \tag{7.32}$$

which is a special case of Watson's theorem [192]. Now we can repeat the derivation of Eq. (2.27), but with Eq. (7.31) replacing Eq. (2.8), leading to

$$f_1^{\mathrm{II}}\left(s,q^2\right) = \frac{f_1\left(s,q^2\right)}{1+2i\sigma(s)\,T(s)}, \tag{7.33}$$

with T, as before, being the $\pi\pi$ P wave. Clearly, Eq. (7.33) has a pair of poles at the same position as T^{II}, namely at $s_\rho = (M_\rho - i\Gamma_\rho/2)^2$ and s_ρ^*. The radiative coupling $g_{\rho\gamma\pi}$ is defined via the residue at the pole as [97]

$$\mathrm{res}\left[f_1^{\mathrm{II}}, s_\rho\right] =: -2e g_{\rho\gamma\pi} g_{\rho\pi\pi}. \tag{7.34}$$

The prefactor differs from Eq. (2.31) to facilitate the comparison with VMD models.

7.2 Dispersive representation of $\gamma^{(*)}\pi \to \pi\pi$

Because the unitarity relation (7.31) does not take on the simple form (2.16), the $\gamma^{(*)}\pi\to\pi\pi$ P wave cannot be described by the single-channel IAM. Instead, in the following, a more complicated dispersive representation of the $\gamma^{(*)}\pi\to\pi\pi$ amplitude is described. It is based on the reconstruction theorem as introduced in Sec. 7.2.1, which allows for expressing $\mathscr{F}$ in terms of a function of a single Mandelstam variable. Using partial-wave unitarity in the form of Eq. (7.31) this function can be partially fixed via the $\pi\pi$ P wave, rendering it into a form suitable for numerical solution, as discussed in Sec. 7.2.2.

7.2.1 Reconstruction theorem

Here, we derive the reconstruction theorem for $\gamma^{(*)}\pi \to \pi\pi$. In the derivation, we follow a general pattern, that can also be applied in other two-to-two particle scattering processes, e.g., $\eta\pi \to \pi\pi$ [52], $\eta'\pi \to \eta\pi$ [70], $\gamma K \to K\pi$ [193], etc. However, due to the huge symmetry of the process $\gamma^{(*)}\pi \to \pi\pi$ as well as its simple partial-wave expansion the equations are particularly short in the case under consideration. Note that this simplicity is not essential to the argument, but merely renders the formulas more compact.

For the time being, we focus on the scattering region, i.e., we enforce $q^2 < (3M_\pi)^2$, such that the photon cannot decay. Moreover, we take into account only $\pi\pi$ intermediate states. We denote by $\Lambda_{q^2} \coloneqq \{(s,t,u) \in \mathbb{C}^3 | s+t+u = R\}$, with $R \coloneqq 3M_\pi^2 + q^2$, the set of on-shell MANDELSTAM variables and introduce $\digamma_{q^2} : \Lambda_{q^2} \mapsto \mathbb{C}$ via

$$\digamma_{q^2}(s,t,R-s-t) \coloneqq \mathscr{F}\left(s,t,q^2\right). \tag{7.35}$$

That is, $\digamma_{q^2}$ is nothing else than the scalar part of the scattering amplitude, but we stay flexible about which MANDELSTAM variables to use to parametrize it. For notational convenience, we drop the subscript q^2 in the following. Invariance under charge conjugation implies $\digamma(s,t,u) = \digamma(u,t,s)$, while isospin invariance yields $\digamma(s,t,u) = \digamma(t,s,u)$. Hence, $\digamma$ is completely symmetric. Since in the isospin limit the s, t, and u channel are the same, $\digamma$ has a right-hand cut starting at $s^{\text{thr}} = u^{\text{thr}} = t^{\text{thr}} = 4M_\pi^2$ and extending to infinity in all three MANDELSTAM variables. Thus, we can write down the fixed-t dispersion relation [194] (see, e.g., Ref. [109] for a pedagogical derivation)

$$\begin{aligned}\digamma_s^t(s) \coloneqq \digamma\left(s,t,u^t(s)\right)\big|_{t\text{ fixed}} = P_{n-1}^t(s) &+ \frac{1}{2\pi i}\int_{s^{\text{thr}}}^{\infty} \text{disc}_x\left[\digamma\left(x,t,u^t(x)\right)\right] \mathrm{D}_s^n x \\ &+ \frac{1}{2\pi i}\int_{u^{\text{thr}}}^{\infty} \text{disc}_x\left[\digamma\left(s^t(x),t,x\right)\right] \mathrm{D}_u^n x.\end{aligned} \tag{7.36}$$

Here $a^b(x) \coloneqq R - b - x$ for a, b MANDELSTAM variables, n denotes the number of subtractions, and P_{n-1}^t is the subtraction polynomial of degree $n-1$. In addition,

$$\mathrm{D}_a^n x \coloneqq \frac{Q_n(a)}{Q_n(x)}\frac{1}{x-a}\mathrm{d}x \tag{7.37}$$

is the combination of the integral measure, the CAUCHY kernel associated with the MANDELSTAM variable a, and Q_n, which is given in terms of the subtraction points $\{s_k\}_{k=1}^n$ as

$$Q_n(\zeta) \coloneqq \prod_{k=1}^{n}(\zeta - s_k). \tag{7.38}$$

Lastly,

$$\text{disc}_x[f(x)] \coloneqq \lim_{\epsilon \searrow 0}\left[f(x+i\epsilon) - f(x-i\epsilon)\right] \tag{7.39}$$

denotes the discontinuity of a function f with respect to the variable x. Of course, n needs to be chosen high enough such that the integrals converge.

In general, denote by $\digamma_b^a$, $a \neq b$ the dispersion relation for fixed a as a function of b (the other MANDELSTAM variable is expressed in terms of a and b). This dispersion relation is valid for $a \in \mathbb{R}$ if

$$a > R - b^{\text{thr}} - c^{\text{thr}}, \tag{7.40}$$

for otherwise the left- and right-hand cuts overlap. Naively, one expects six different dispersion relations, since in $\digamma_b^a$ there are three choices for a and (if a is fixed) there are two remaining choices for b, and thus overall $3 \times 2 = 6$ choices. However, the two fixed-u dispersion relations are interrelated in the following way:

$$\digamma_s^u\left(s^u(t)\right) = \digamma\left(s^u(t), t^u\left(s^u(t)\right), u\right) = \digamma\left(s^u(t), t, u\right) = \digamma_t^u(t). \tag{7.41}$$

Similarly, one derives $\digamma_t^u(t^u(s)) = \digamma_s^u(s)$. That is, the two fixed-u dispersion relations contain the same information. The same line of reasoning applies to the fixed-s and fixed-t dispersion relations; hence, there are three manifestly different dispersion relations, one fixed-s, one fixed-u and one fixed-t. The choice of the independent variable in each of these three relations is arbitrary. In the following, $\digamma_s^u$, $\digamma_s^t$ and $\digamma_t^s$ are chosen.

The derivation of the reconstruction theorem proceeds now as follows: first, all three dispersion relations are written down. Second, the partial-wave expansions of the appropriate channels are used to express the discontinuities in the dispersive integrals. Third, the dispersion relations are symmetrized. Finally, the symmetrized expression is analytically continued. The last step is nontrivial due to the restricted domain of validity of the dispersion relations, as will become clear below.

The first step yields, in addition to Eq. (7.36),

$$\begin{aligned}
\digamma_s^u(s) &= P_{n-1}^u(s) + \frac{1}{2\pi i}\int_{s^{\text{thr}}}^{\infty} \operatorname{disc}_x\left[\digamma\left(x, t^u(x), u\right)\right] \mathrm{D}_s^n x \\
&\quad + \frac{1}{2\pi i}\int_{t^{\text{thr}}}^{\infty} \operatorname{disc}_x\left[\digamma\left(s^u(x), x, u\right)\right] \mathrm{D}_t^n x, \\
\digamma_t^s(t) &= P_{n-1}^s(t) + \frac{1}{2\pi i}\int_{t^{\text{thr}}}^{\infty} \operatorname{disc}_x\left[\digamma\left(s, x, u^s(x)\right)\right] \mathrm{D}_t^n x \\
&\quad + \frac{1}{2\pi i}\int_{u^{\text{thr}}}^{\infty} \operatorname{disc}_x\left[\digamma\left(s, t^s(x), x\right)\right] \mathrm{D}_u^n x.
\end{aligned} \tag{7.42}$$

In the second step, the partial-wave expansion (7.11) is needed. The kinematic variable $z^\star$ can be expressed as a function of the MANDELSTAM variables according to (see Eq. (7.59))

$$z^\star(s,t,u) = \frac{t-u}{\sigma(s)\sqrt{\lambda\left(s, q^2, M_\pi^2\right)}}. \tag{7.43}$$

This dependence renders the derivation of the reconstruction theorem incorporating F waves and higher partial waves cumbersome. Here we will assume

$$\operatorname{disc}_x\left[f_J(x)\right] = 0, \qquad \forall J \geq 3. \tag{7.44}$$

This assumption might be justified by the empirical finding that at low energies the ρ resonance dominates the scattering process. Now the discontinuity in each dispersive integral in Eq. (7.36) and Eq. (7.42) is expressed in terms of partial waves. To that end it is crucial to realize that the partial-wave expansion is a priori defined in the physical scattering region only. Hence, in the integrals along the s-channel cut the s-channel partial-wave expansion is needed and similarly for the other channels. For $\gamma^{(*)}\pi \to \pi\pi$ due to the symmetry of $\digamma$ the partial-wave expansion in all channels has the same structure (i.e., incorporates the same functions f_J). Moreover, we need to

assure that the physical scattering region and the domain of validity of the dispersion relation at hand have non-empty overlap, which is the case if $q^2 < M_\pi^2$. Performing this manipulation results in

$$\begin{aligned}
\mathfrak{f}_s^t(s) &= P_{n-1}^t(s) + \frac{1}{2\pi i}\int_{4M_\pi^2}^\infty \mathrm{disc}_x\left[f_1(x)\right]\mathrm{D}_s^n x \\
&\quad + \frac{1}{2\pi i}\int_{4M_\pi^2}^\infty \mathrm{disc}_x\left[f_1(x)\right]\mathrm{D}_u^n x, \\
\mathfrak{f}_s^u(s) &= P_{n-1}^u(s) + \frac{1}{2\pi i}\int_{4M_\pi^2}^\infty \mathrm{disc}_x\left[f_1(x)\right]\mathrm{D}_s^n x \\
&\quad + \frac{1}{2\pi i}\int_{4M_\pi^2}^\infty \mathrm{disc}_x\left[f_1(x)\right]\mathrm{D}_t^n x, \\
\mathfrak{f}_t^s(t) &= P_{n-1}^s(t) + \frac{1}{2\pi i}\int_{4M_\pi^2}^\infty \mathrm{disc}_x\left[f_1(x)\right]\mathrm{D}_t^n x \\
&\quad + \frac{1}{2\pi i}\int_{4M_\pi^2}^\infty \mathrm{disc}_x\left[f_1(x)\right]\mathrm{D}_u^n x.
\end{aligned} \tag{7.45}$$

The domain of validity of the dispersion relations in Eq. (7.45) is no longer restricted by the domain of validity of the partial-wave expansion, since the partial wave f_1 is integrated only along the physical scattering regions.

For the next steps to cumulate in the desired result, it is crucial that the domains of definition of the three dispersion relations as restricted by Eq. (7.40) have non-vanishing overlap, i.e., that there exists a set $D \subseteq \Lambda$ that possesses an accumulation point with respect to a larger domain such that all three dispersion relations hold inside D. Combining the three constraints yields

$$D = \left\{(s,t,R-t-s) \,:\, s > q^2 - 5M_\pi^2, \quad t > q^2 - 5M_\pi^2, \quad s+t < 8M_\pi^2\right\}, \tag{7.46}$$

which is non-empty if $q^2 < 9M_\pi^2$.

Each dispersion relation in Eq. (7.45) misses exactly one dispersive integral that is present in the other dispersion relations. Consider, for instance, the $\mathfrak{f}_s^t$ dispersion relation. It misses the integral along the t-channel cut, which is present in the two other dispersion relations. If this missing integral is subtracted from P_{n-1}^t for fixed values of t the result is again a polynomial of degree $n-1$ in s, i.e.

$$P_{n-1}^t(s) - \frac{1}{2\pi i}\int_{4M_\pi^2}^\infty \mathrm{disc}_x\left[f_1(x)\right]\mathrm{D}_t^n x = \tilde{P}_{n-1}^t(s). \tag{7.47}$$

Hence, we can write

$$\begin{aligned}
\mathfrak{f}_s^t(s) &= \tilde{P}_{n-1}^t(s) + \frac{1}{2\pi i}\int_{4M_\pi^2}^\infty \mathrm{disc}_x\left[f_1(x)\right]\mathrm{D}_s^n x \\
&\quad + \frac{1}{2\pi i}\int_{4M_\pi^2}^\infty \mathrm{disc}_x\left[f_1(x)\right]\mathrm{D}_u^n x \\
&\quad + \frac{1}{2\pi i}\int_{4M_\pi^2}^\infty \mathrm{disc}_x\left[f_1(x)\right]\mathrm{D}_t^n x.
\end{aligned} \tag{7.48}$$

Analogously, for the other channels we obtain

$$\begin{aligned}
\mathcal{F}_s^u(s) &= \tilde{P}_{n-1}^u(s) + \frac{1}{2\pi i}\int_{4M_\pi^2}^\infty \mathrm{disc}_x\left[f_1(x)\right]\mathrm{D}_s^n x \\
&\quad + \frac{1}{2\pi i}\int_{4M_\pi^2}^\infty \mathrm{disc}_x\left[f_1(x)\right]\mathrm{D}_u^n x \\
&\quad + \frac{1}{2\pi i}\int_{4M_\pi^2}^\infty \mathrm{disc}_x\left[f_1(x)\right]\mathrm{D}_t^n x, \\
\mathcal{F}_t^s(t) &= \tilde{P}_{n-1}^s(t) + \frac{1}{2\pi i}\int_{4M_\pi^2}^\infty \mathrm{disc}_x\left[f_1(x)\right]\mathrm{D}_s^n x \\
&\quad + \frac{1}{2\pi i}\int_{4M_\pi^2}^\infty \mathrm{disc}_x\left[f_1(x)\right]\mathrm{D}_u^n x \\
&\quad + \frac{1}{2\pi i}\int_{4M_\pi^2}^\infty \mathrm{disc}_x\left[f_1(x)\right]\mathrm{D}_t^n x.
\end{aligned} \tag{7.49}$$

Inside D, these three functions need to be equal. Equating Eq. (7.48) and Eq. (7.49) yields

$$\tilde{P}_{n-1}^t(s) = \tilde{P}_{n-1}^u(s) = \tilde{P}_{n-1}^s(t). \tag{7.50}$$

Hence, $P_{n-1}(s,t,u) \coloneqq \tilde{P}_{n-1}^t(s)$ is inside D a polynomial in s, t (and u).[3] As a side result, this implies that the (non-entire part of the) t-dependence of the coefficients in the polynomial P_{n-1}^t cancels the t-dependence of the integral in Eq. (7.47), such that $\tilde{P}_{n-1}^t$ is not only a polynomial in s, but also one in t. Stated differently, this means that the apparently missing integral along the t-channel discontinuity is contained in the fixed-t dispersion relation from the beginning, namely in the coefficients in the subtraction polynomial (similar statements hold for the other two dispersion relations). Obviously, this can only work if the required number of subtractions is sufficiently high. As a counterexample, consider the hypothetical scenario in which no subtractions are required. Then the previous argument does not apply, for there is no subtraction polynomial in the fixed-a dispersion relation that could contain the a-channel integral. Increasing the number of subtractions artificially does not solve the problem, since the coefficients in the subtraction polynomial generated in this way are fixed by sum rules.

Assuming that the required number of subtractions is high enough (i.e., for the scenario at hand at least one), the analytic continuation of one of the dispersive representations (7.48) and (7.49) out of D is trivial: the only dependence of the Mandelstam variables is contained in the polynomial and the Cauchy kernels. It yields the following expression for the amplitude:

$$\begin{aligned}
\mathcal{F}(s,t,u) &= P_{n-1}(s,t,u) + \frac{1}{2\pi i}\int_{4M_\pi^2}^\infty \mathrm{disc}_x\left[f_1(x)\right]\mathrm{D}_s^n x \\
&\quad + \frac{1}{2\pi i}\int_{4M_\pi^2}^\infty \mathrm{disc}_x\left[f_1(x)\right]\mathrm{D}_u^n x \\
&\quad + \frac{1}{2\pi i}\int_{4M_\pi^2}^\infty \mathrm{disc}_x\left[f_1(x)\right]\mathrm{D}_t^n x.
\end{aligned} \tag{7.51}$$

This representation is holomorphic in s, t, and u. Moreover, it possesses the correct branch cuts.

[3] It is this part of the derivation that goes through only if D is non-empty.

According to Eq. (7.51), the symmetry of $\mathcal{F}$ implies that P_{n-1} is totally symmetric, too. As long as $n < 3$ this implies via $s+t+u = R$ that P_{n-1} is in fact independent of the MANDELSTAM variables, i.e., $P_{n-1}(s,t,u) = C_n \in \mathbb{R}$, $n \in \{1,2\}$. Thus, we can decompose Eq. (7.51) into

$$\mathcal{F}_{q^2}(s,t,u) = \mathcal{B}\left(s,q^2\right) + \mathcal{B}\left(t,q^2\right) + \mathcal{B}\left(u,q^2\right), \tag{7.52}$$

where we made the dependence on q^2 explicit again and

$$\mathcal{B}\left(a,q^2\right) \coloneqq \frac{C_1\left(q^2\right)}{3} + \frac{1}{2\pi i}\int_{4M_\pi^2}^{\infty} \mathrm{disc}_x\left[f_1\left(x,q^2\right)\right] \mathrm{D}_a^1 x \tag{7.53}$$

if $n = 1$ as well as

$$\mathcal{B}\left(a,q^2\right) \coloneqq \frac{C_2^{(0)}\left(q^2\right)}{3} + \frac{C_2^{(1)}\left(q^2\right)}{3}a + \frac{1}{2\pi i}\int_{4M_\pi^2}^{\infty} \mathrm{disc}_x\left[f_1\left(x,q^2\right)\right] \mathrm{D}_a^2 x, \tag{7.54}$$

with

$$C_2^{(0)}\left(q^2\right) + C_2^{(1)}\left(q^2\right)\frac{R}{3} = C_2\left(q^2\right), \tag{7.55}$$

if $n = 2$. Equation (7.52) is precisely the reconstruction theorem of $\gamma^{(*)}\pi \to \pi\pi$ in its final form [66, 195].

7.2.2 Inhomogeneous OMNÈS problem

By expressing the discontinuity in Eq. (7.53) and Eq. (7.54) via the unitarity relation (7.31) the function $\mathcal{B}$ can be expressed as the solution to an inhomogeneous OMNÈS problem, as discussed pedagogically in detail, e.g., in Ref. [109]. The result reads [51, 66, 109, 196]

$$\begin{aligned}
\mathcal{B}\left(s,q^2\right) &= \sum_{k=0}^{n-1} c_k\left(q^2\right)\mathcal{B}_k\left(s,q^2\right), \\
\mathcal{B}_k\left(s,q^2\right) &\coloneqq \Omega(s)\left[s^k + \frac{s^n}{\pi}\int_{4M_\pi^2}^{\infty} \frac{\widehat{\mathcal{B}}_k\left(x,q^2\right)}{x^n(x-s)}\frac{\sin\left[\delta(x)\right]}{|\Omega(x)|}\mathrm{d}x\right].
\end{aligned} \tag{7.56}$$

Here

$$\widehat{\mathcal{B}}_k\left(s,q^2\right) \coloneqq \frac{3}{2}\int_{-1}^{1}\left(1-z^{\star 2}\right)\mathcal{B}_k\left(t\left(s,z^\star,q^2\right),q^2\right)\mathrm{d}z^\star \tag{7.57}$$

are the hat functions, $n \in \mathbb{N}$ is the number of subtractions that are employed in the dispersive integrals, c_k are the subtraction functions, the mappings $\mathcal{B}_k$ are known as basis functions, the OMNÈS function is given as [197]

$$\Omega(s) \coloneqq \exp\left[\frac{s}{\pi}\int_{4M_\pi^2}^{\infty}\frac{\delta(x)}{x(x-s)}\mathrm{d}x\right], \tag{7.58}$$

and

$$\begin{aligned} t\left(s, z^{\star}, q^2\right) &= a\left(s, q^2\right) + z^{\star} b\left(s, q^2\right), \\ a\left(s, q^2\right) &\coloneqq \frac{3M_\pi^2 + q^2 - s}{2}, \\ b\left(s, q^2\right) &\coloneqq \frac{\sigma(s)}{2}\sqrt{\lambda\left(s, q^2, M_\pi^2\right)}, \end{aligned} \tag{7.59}$$

is the Mandelstam variable t expressed in terms of the other kinematic variables via the Källén function $\lambda(y, v, w) \coloneqq (y - v - w)^2 - 4vw$.[4] Equation (7.56) and Eq. (7.57) are a special case of KT equations [110] that are discussed in greater detail in Part IV.

The basis functions subsume $\pi\pi$ rescattering and are fixed as soon as the $\pi\pi$ phase δ is known. While the Omnès function describes $\pi\pi$ scattering in one channel, the integral in Eq. (7.56) incorporates mixed rescattering, where pions rescatter pairwise, e.g., first in the s and subsequently in the t channel. That is, the replacement $\mathscr{B}_k(s, q^2) \mapsto s^k \Omega(s)$ amounts to taking into account only $\pi\pi$ rescattering in the individual channels. This is explored in more depth in Ch. 10.

In the form of Eq. (7.56) the KT equations are valid only if $q^2 < (3M_\pi)^2$, i.e., as long as the photon cannot decay. By deformation of either one of the integration contours the equations can be analytically continued towards $q^2 > (3M_\pi)^2$ [198, 199] as discussed in Ch. 11, however, this is not needed for the lattice data of interest. This analytic continuation reveals that the basis functions indeed possess a three-particle cut in q^2 that is associated with pairwise $\pi\pi$ rescattering, but they do not contain any q^2-dependence arising from genuine three-pion interactions [200]. Such interactions are to be described by the subtraction functions c_k, which are not fixed by the KT approach. Thus, to arrive at a complete representation of $\gamma^{(*)}\pi \to \pi\pi$, we need both a representation of δ as well as a parameterization of the subtraction functions.

We describe the phase shift δ via the NLO[5] IAM as introduced in Sec. 4.2, which depends on the low energy constant $l^r \coloneqq l_2^r - 2l_1^r$ and the pion decay constant in the chiral limit F. Since F_π has not been computed on the lattice ensembles of interest, we set F to its literature value, see Sec. 6.4.3. We compute the basis functions numerically via the method described in Sec. 11.3. In particular, the phase of the NLO IAM does not approach π, instead, $\lim_{s\to\infty} T(s) = -[96\pi l^r + i + 2/(3\pi)]^{-1}$, which yields $\lim_{s\to\infty} \delta(s) < \pi$ for all reasonable values of l^r, and so we guide δ smoothly to π at energies far above the resonance region as described ibidem. With this choice of δ, $\Omega(s) = O(1/s)$ holds. Since the integral in Eq. (7.56) is cut off as soon as δ reaches π, the asymptotic behavior of the Omnès function implies

$$\mathscr{B}_k\left(s, q^2\right) = O\left(s^{n-2}\right). \tag{7.60}$$

7.2.3 Subtraction functions

The subtraction functions need to be holomorphic in the complex q^2 plane except for a cut along $[9M_\pi^2, \infty)$ that is associated with $\gamma^* \to \pi\pi\pi$. Hence, we can write down an m-times subtracted dispersion relation of the form

$$c_k\left(q^2\right) = \sum_{j=0}^{m-1} b_{kj}\left(q^2\right)^j + \frac{\left(q^2\right)^m}{2\pi i} \int_{9M_\pi^2}^{\infty} \frac{\mathrm{disc}_x\left[c_k(x)\right]}{x^m\left(x - q^2\right)} \mathrm{d}x, \tag{7.61}$$

[4] Equation (7.59) is a special case of Eq. (11.13).

[5] As discussed in Ch. 8, there are only two datasets by two different collaborations available, both at pion masses exceeding 300 MeV. A fit of the NNLO IAM to these data is stable only with strong constraints on the LECs, and thus we opt for an NLO fit instead.

where $\mathrm{disc}_x[c_k(x)]$ denotes the discontinuity along the branch cut as defined in Eq. (7.39). As long as $q^2 < 9M_\pi^2$, the SCHWARZ reflection principle dictates $b_{kj} \in \mathbb{R}$ and $\mathrm{disc}[c_k] = 2i\,\mathrm{Im}[c_k]$, compare Eq. (2.7). In the energy region that contributes most to the dispersive integral in Eq. (7.61) the three-pion physics is dominated by the $\omega(782)$ and $\phi(1020)$ resonances [9], both of which are narrow and (at the physical point) far away from the three-pion threshold. Thus, $\mathrm{disc}[c_k]$ inside the integral can be reasonably well described by a sum of two BREIT–WIGNER functions, yielding a dispersively improved variant of a BREIT–WIGNER parameterization that ensures the correct analytic properties [117, 201]. In practice, the lattice data we are going to analyze are obtained at $M_\pi > 300\,\mathrm{MeV}$, at which mass the ω becomes a bound state [151]. Accordingly, instead of being incorporated into the dispersive integral, it appears as a pole at $q^2 = M_\omega^2$. This can be taken into account by writing down a dispersion relation in the form of Eq. (7.61) for $c_k(q^2)/\mathcal{P}(q^2)$ with $\mathcal{P}(q^2) = (1 - q^2/M_\omega^2)^{-1}$ and multiplying the result by the pole factor $\mathcal{P}$.

Since the lattice data are obtained at virtualities significantly below the 3π threshold, Eq. (7.61) can be expanded as a TAYLOR series; keeping the first m terms yields

$$c_k\left(q^2\right) = \sum_{j=0}^{m-1} b_{kj}\left(q^2\right)^j. \tag{7.62}$$

However, the convergence of the TAYLOR series is poor as soon as $\left|q^2\right|$ gets close to the 3π threshold, this drawback goes hand in hand with a wrong asymptotic behavior for large $\left|q^2\right|$, i.e., the expression diverges. To improve on Eq. (7.62), a conformal polynomial can be used instead [202, 203]. That is, Eq. (7.61) is approximated by

$$c_k\left(q^2\right) = \sum_{j=0}^{m-1} b_{kj} w\left(q^2\right)^j, \tag{7.63}$$

where the conformal variable w reads

$$w\left(q^2\right) \coloneqq \frac{\sqrt{9M_\pi^2 - q^2} - 3M_\pi}{\sqrt{9M_\pi^2 - q^2} + 3M_\pi}. \tag{7.64}$$

In this way, the cut along $[9M_\pi^2, \infty)$ is retained. Moreover, the asymptotic behavior is improved, as w is bounded.

At the 3π threshold, $\mathrm{Im}[c_k]$ should scale like $(q^2 - 9M_\pi^2)^4$ to be in accordance with the three-particle phase space [204]. This is impossible to obtain with Eq. (7.63), because for q^2 below threshold the SCHWARZ reflection principle needs to be fulfilled, so that $b_{kj} \in \mathbb{R}$. Expanding w in powers of $x \coloneqq \sqrt{9M_\pi^2 - q^2}$ makes it clear that only odd powers of x contribute to $\mathrm{Im}[c_k]$. This problem is fundamental to the method, for the RIEMANN mapping theorem implies that each biholomorphic map from the cut complex plane to the interior of the unit disk is of conformal form. It is, however, easily possible to remove the leading square-root-like scaling via fixing [183]

$$b_{k1} = -\sum_{j=2}^{m-1} j b_{kj}. \tag{7.65}$$

Altogether we have six different parameterizations of the subtraction functions: a polynomial, a conformal polynomial, and a conformal polynomial with modified threshold behavior, each either with or without the pole factor $\mathcal{P}$ in front. Lastly, the number m of terms needs to be fixed. We use $N - k$ terms with a single global value of N for the k-th subtraction function c_k, since it multiplies s^k

	Eq. (7.62)	Eq. (7.63)	Eq. (7.63) and Eq. (7.65)
without $\mathcal{P}$	I	II	III
with $\mathcal{P}$	I$\mathcal{P}$	II$\mathcal{P}$	III$\mathcal{P}$

Table 7.1: The naming scheme of the different parameterizations of the subtraction functions. For example, strategy II$\mathcal{P}$ amounts to $c_k(q^2) = \mathcal{P}(q^2)\sum_{j=0}^{N-k} b_{kj} w(q^2)^j$.

in Eq. (7.56), such that with our choice in the simple polynomial representation (7.62) the highest combined power of MANDELSTAM s and q^2 has mass dimension $2N$. An overview of the different strategies is given in Table 7.1.

7.2.4 Partial wave via kernel method

In the analysis of lattice-QCD data we are chiefly interested in the partial wave f_1, which is related to the basis functions (7.56) and hat functions (7.57) via Eq. (7.11), Eq. (7.12), and the reconstruction theorem (7.52). Specifically,

$$f_1\left(s,q^2\right) = \sum_{k=0}^{n-1} c_k\left(q^2\right)\left[\mathscr{B}_k\left(s,q^2\right) + \widehat{\mathscr{B}}_k\left(s,q^2\right)\right] \tag{7.66}$$

holds. For the time being, we do not allow for decays, i.e., the constraint $q^2 < 9M_\pi^2$ applies. If, furthermore, we focus on the scattering domain, i.e., $s \geq 4M_\pi^2$, where the lattice data are obtained, in principle the computation of the partial wave f_1 is straightforward, for the MANDELSTAM variable t in Eq. (7.57) does not interfere with the cut of $\mathscr{B}_k$, since its real part stays below the $\pi\pi$ threshold. However, as soon as $q^2 > M_\pi^2$, the variable t develops a non-vanishing imaginary part. This does not pose a problem as long as one wishes to evaluate $\widehat{\mathscr{B}}_k$ only at a couple of (s,q^2) values, e.g., at the values corresponding to the lattice data or at the relatively few values needed in the numerical solution of the KT equations, see Sec. 11.3. But if one seeks to compute $\widehat{\mathscr{B}}_k$ at a large number of s and q^2 values, effectively the imaginary part of t enforces the evaluation of $\mathscr{B}_k$ on a two-dimensional subset of the $(s,z^\star)$ plane, which is numerically demanding. While this issue can in principle be avoided by deforming the path of integration in the angular integral [51], in practice this method suffers from removable singularities, whose proper numerical treatment is slightly cumbersome. The situation gets worse if one wants to evaluate $\widehat{\mathscr{B}}_k$ at complex values of s (as needed in a search for resonance poles), for care needs to be taken to avoid interference of MANDELSTAM t with the cut of $\mathscr{B}_k$.[6]

Fortunately, the well established kernel method [66, 97, 193] provides an elegant solution to both issues. In the following we derive this method, the first part of this derivation resembles the discussion in Ref. [205]; however, here we allow for $q^2 \neq 0$ and in the second part discuss carefully certain properties of the eponymous kernel that become relevant due to the possibility of a non-vanishing virtuality.

[6]The results of Sec. 11.1.2, in particular Fig. 11.1, show that the branch point of $\mathscr{B}_k$ is not hit in the naive computation of $\mathscr{B}_k$ via Eq. (7.57), however, one would still be concerned with the possibility of t crossing the cut.

The starting point is the following simple dispersive representation of $\mathscr{B}_k$:

$$\mathscr{B}_k\left(s,q^2\right) = P_k(s) + \frac{s^d}{\pi}\int\limits_{4M_\pi^2}^{\infty} \frac{\operatorname{Im}\left[\mathscr{B}_k\left(x,q^2\right)\right]}{(x-s)\,x^d}\mathrm{d}x. \tag{7.67}$$

Here d is the number of subtractions, $P_k(s) = \sum_{j=0}^{d-1} h_{kj}s^j$ the subtraction polynomial with coefficients $h_{kj} \in \mathbb{R}$, which can be determined via matching to Eq. (7.56). For instance, given $\mathscr{B}_k(s,q^2) = O(s^{n-2})$ for $n = 2$ it is more than sufficient to use $d = 2$. Equating the Taylor expansions around $s = 0$ of both Eq. (7.67) and the definition of $\mathscr{B}_k$ in Eq. (7.56) we obtain

$$h_{00} = 1, \quad h_{01} = \frac{\mathrm{d}\Omega}{\mathrm{d}s}(0), \quad h_{10} = 0, \quad h_{11} = 1, \tag{7.68}$$

where we used $\Omega(0) = 1$.

Coming back to the general case, inserting Eq. (7.67) into Eq. (7.57) yields

$$\widehat{\mathscr{B}}_k\left(s,q^2\right) = \sum_{j=0}^{d-1} h_{kj}G_j\left(s,q^2\right) + \frac{1}{\pi}\int\limits_{4M_\pi^2}^{\infty} W_d\left(s,q^2,x\right)\operatorname{Im}\left[\mathscr{B}_k\left(x,q^2\right)\right]\mathrm{d}x, \tag{7.69}$$

with

$$\begin{aligned} G_j\left(s,q^2\right) &\coloneqq \frac{3}{2}\int\limits_{-1}^{1}\left(1-z^{\star 2}\right)t\left(s,z^\star,q^2\right)^j\mathrm{d}z^\star, \\ W_d\left(s,q^2,x\right) &\coloneqq \frac{3}{2}\int\limits_{-1}^{1}\frac{\left(1-z^{\star 2}\right)t\left(s,z^\star,q^2\right)^d}{\left(x-t\left(s,z^\star,q^2\right)\right)x^d}\mathrm{d}z^\star. \end{aligned} \tag{7.70}$$

Decomposing Mandelstam t as in Eq. (7.59) we obtain

$$\begin{aligned} G_j\left(s,q^2\right) &= \frac{3}{2}\int\limits_{-1}^{1}\left(1-z^{\star 2}\right)\left[a\left(s,q^2\right)+z^\star b\left(s,q^2\right)\right]^j\mathrm{d}z^\star \\ &= \frac{3}{2}\sum_{r=0}^{j}\binom{j}{r}a\left(s,q^2\right)^{j-r}b\left(s,q^2\right)^r\int\limits_{-1}^{1}\left(1-z^{\star 2}\right)z^{\star r}\mathrm{d}z^\star \\ &= 6\sum_{r=0}^{\lfloor j/2\rfloor}\binom{j}{2r}\frac{a\left(s,q^2\right)^{j-2r}b\left(s,q^2\right)^{2r}}{(2r+1)(2r+3)}. \end{aligned} \tag{7.71}$$

As special cases we obtain

$$G_0\left(s,q^2\right) = 2, \qquad G_1\left(s,q^2\right) = 2a\left(s,q^2\right). \tag{7.72}$$

We manipulate the Kernel W_d accordingly,

$$W_d\left(s,q^2,x\right) = \frac{3}{2}\frac{1}{x^d}\sum_{k=0}^{d}\binom{d}{k}a\left(s,q^2\right)^{d-k}b\left(s,q^2\right)^{k-1}\left[\mathscr{I}_k\left(\xi\left(s,q^2,x\right)\right)-\mathscr{I}_{k+2}\left(\xi\left(s,q^2,x\right)\right)\right], \tag{7.73}$$

with

$$\mathscr{I}_k(\xi) \coloneqq \int_{-1}^{1} \frac{z^k}{\xi - z} \mathrm{d}z \tag{7.74}$$

and

$$\xi\left(s, q^2, x\right) \coloneqq \frac{x - a\left(s, q^2\right)}{b\left(s, q^2\right)}. \tag{7.75}$$

To compute the integrals $\mathscr{I}_k$, we use

$$\frac{z^k}{\xi - z} = \frac{\xi^k}{\xi - z} - \sum_{j=0}^{k-1} \xi^{k-j-1} z^j, \tag{7.76}$$

which holds for arbitrary $\xi, z \in \mathbb{C}$ and $k \in \mathbb{N}_0$ as can be proven by induction. This allows for rewriting $\mathscr{I}_k$ in terms of $\mathscr{I}_0$ via

$$\mathscr{I}_k(\xi) = \xi^k \mathscr{I}_0(\xi) - 2 \sum_{j=0}^{\left\lfloor \frac{k-1}{2} \right\rfloor} \frac{\xi^{k-2j-1}}{2j+1}. \tag{7.77}$$

Finally, we note that $\mathscr{I}_0 = 2Q_0$, with

$$Q_0(\xi) = \frac{1}{2} \int_{-1}^{1} \frac{1}{\xi - y} \mathrm{d}y \tag{7.78}$$

the lowest Legendre function of the second kind. Again, as special cases we obtain [97, 193]

$$W_1\left(s, q^2, x\right) = \mathscr{W}\left(s, q^2, x\right) - \frac{2}{x}, \qquad W_2\left(s, q^2, x\right) = W_1\left(s, q^2, x\right) - \frac{2a\left(s, q^2\right)}{x^2}, \tag{7.79}$$

with

$$\mathscr{W}\left(s, q^2, x\right) \coloneqq \frac{3}{b\left(s, q^2\right)} \left[\left(1 - \xi\left(s, q^2, x\right)^2\right) Q_0\left(\xi\left(s, q^2, x\right)\right) + \xi\left(s, q^2, x\right) \right]. \tag{7.80}$$

As a next step, let us study the kernel $\mathscr{W}$ in more detail. Computing the integral in Eq. (7.78) yields

$$Q_0(\xi) = \frac{1}{2} \left[\ln\left(\frac{1+\xi}{1-\xi}\right) - i\pi \operatorname{sign}\left(\operatorname{Im}(\xi)\right) \right], \tag{7.81}$$

with

$$\operatorname{sign}(x) \coloneqq \begin{cases} 1, & x > 0, \\ 0, & x = 0, \\ -1, & x < 0, \end{cases} \tag{7.82}$$

being the sign function, the principal value of the logarithm cut along the negative real axis, and $Q_0(\xi) \coloneqq \lim_{\epsilon \searrow 0} Q_0(\xi + i\epsilon)$ if $\xi \in \mathbb{R}$. Together with this prescription Eq. (7.81) is valid in the entire complex plane, has a branch cut along $\xi \in [-1, 1]$, and satisfies the Schwarz reflection principle.

If $x \to \infty$ or $b(s, q^2) \to 0$, ξ approaches infinity. In the domain of interest, $b(s, q^2) = 0$ holds if $s = 4M_\pi^2$ or $s = (\sqrt{q^2} + M_\pi)^2$, the latter happens only if $q^2 \geq 0$. Hence, it is advisable to study the

asymptotic behavior of the kernel. That is, we study $\mathscr{W}$ as a function of $\xi = 1/\zeta$ in the limit $\zeta \to 0$. Using the well known expansion $\ln(1+x) = \sum_{k=1}^{\infty}(-1)^{k+1}x^k/k$, we derive

$$\mathscr{W}\left(s,q^2,x\right) = \frac{6}{x - a\left(s,q^2\right)} \sum_{j=0}^{\infty} \frac{1}{(2j+1)(2j+3)} \left(\frac{1}{\xi\left(s,q^2,x\right)}\right)^{2j}. \tag{7.83}$$

According to the ratio test, Eq. (7.83) converges absolutely as long as $|\xi| > 1$. In particular, we see that $\lim_{\xi\to\infty} \mathscr{W}$ is manifestly finite. Thus, Eq. (7.83) provides an elegant way to treat the removable singularities at $b(s,q^2) = 0$. As a cross check, note that in the scattering region, i.e., $s \geq 4M_\pi^2$, $b(s,q^2) \in \mathbb{R} \cup i\mathbb{R}$ holds. Thus, ξ is either purely real or purely imaginary. In either case, Eq. (7.83) is purely real, as is Eq. (7.71), since only even powers of b appear. Via Eq. (7.69) this implies that $\widehat{\mathscr{B}}_k$ is real, and therefore according to the Schwarz reflection principle the hat function does not have a right-hand cut, as it needs to be the case. In passing, we note that the terms subtracted from $\mathscr{W}$ in Eq. (7.79) precisely cancel out the leading terms in Eq. (7.83) such that $W_d(s,q^2,x) = O(x^{d+1})$, as it needs to be the case to ensure convergence of the integral in Eq. (7.69).

Applying Eq. (7.69) in the case of interest, i.e., $n = d = 2$, we obtain

$$\widehat{\mathscr{B}}_k\left(s,q^2\right) = 2h_{k0} + 2a\left(s,q^2\right)h_{k1} + \frac{1}{\pi}\int_{4M_\pi^2}^{\infty} W_2\left(s,q^2,x\right)\mathrm{Im}\left[\mathscr{B}_k\left(x,q^2\right)\right]\mathrm{d}x, \tag{7.84}$$

with the coefficients h_{kj} given in Eq. (7.68) and W_2 to be computed via Eqs. (7.79), (7.80), and (7.83). Clearly, Eq. (7.84) allows for evaluation of the hat function at arbitrary complex values of s requiring the imaginary part of $\mathscr{B}_k$ along the physical scattering region only. This both speeds up the evaluation as a function of s drastically and allows for a trivial continuation into the complex plane, thereby solving the issues of Eq. (7.57). Because the high-energy region in the integral in Eq. (7.84) is strongly suppressed by the asymptotic behavior of W_2, the integral can be cut off at high energies.

Lastly, let us remark that the representation of the hat function in terms of a kernel provides the basis for a solution method of the KT equations that is an alternative to the approach presented in Ch. 11 [68, 206].

7.3 Pion-mass dependence and anomaly

To control the pion-mass dependence of the partial wave (7.66), we need to understand at which places the pion mass enters this expression. First and foremost, there is the IAM phase δ, whose pion-mass dependence has been discussed in detail in Part II. Notably, the fit paremter l^r is independent of the pion mass, as is F; the sole pion-mass dependence stemming from the ChPT expressions. Second, the pion mass appears explicitly in the KT equations, see Eqs. (7.56)–(7.59), which can be taken care of by merely adjusting the numerical value. Lastly, the subtraction functions c_k depend on the pion mass in several ways. The parametrizations including a pole factor $\mathcal{P}$ contain the ω mass M_ω. To take into account its pion-mass dependence, we use the result of the analysis in Ref. [151], namely

$$M_\omega\left(M_\pi^2\right) = 0.7686(20)\,\mathrm{GeV} + 0.719(9)\,\mathrm{GeV}^{-1}M_\pi^2. \tag{7.85}$$

What remains besides the trivial pion-mass dependence of the conformal variable (7.64) is the one of the variables b_{kj} appearing in Eq. (7.62) or Eq. (7.63). Since there are only lattice data sets at two

different pion masses available, only very simple parameterizations of the pion-mass dependence of each b_{kj} can presently be constrained. For that reason, we opt for the simplest ansatz

$$b_{kj}\left(M_\pi^2\right) = \alpha_{kj} + \beta_{kj} M_\pi^2, \qquad \alpha_{kj}, \beta_{kj} \in \mathbb{R}. \tag{7.86}$$

Here the fact that the variables are linear in M_π^2 instead of M_π is motivated by ChPT, for otherwise the b_{kj} would possess branch points in the quark mass. As soon as more data sets at different pion masses become available, it will be possible to test more refined prescriptions.

With the subtraction functions extrapolated to the physical point, defined as before by the PDG value of the mass of the charged pion [9], the anomaly (7.30) can be determined via matching the dispersive representation to ChPT. For $n = 2$ subtractions the matching yields [66]

$$eF_{3\pi}(1+G) = 3\left\{c_0(0)\left[1 + \frac{\mathrm{d}\Omega}{\mathrm{d}s}(0)\, M_\pi^2\right] + c_1(0)\, M_\pi^2\right\}, \tag{7.87}$$

with

$$G = \frac{3}{2}\frac{M_\pi^2}{M_\rho^2} - \frac{1}{32\pi^2}\frac{M_\pi^2}{F^2}\left[1 + \ln\left(\frac{M_\pi^2}{M_\rho^2}\right)\right] \tag{7.88}$$

determined via one-loop ChPT and a new LEC has been fixed via resonance saturation [207]. We stress that, as soon as $c_0(0)$ and $c_1(0)$ are known, Eq. (7.87) can be used to determine $F_{3\pi}$ without using the prediction (7.30). The value extracted in this way can then be compared with the prediction (7.30) to test the latter.

Chapter 8

Lattice data

In the following, we describe the translation of the finite-volume lattice data into the continuum. As alluded to in Sec. 3.2.8, lattice-QCD computations of $\gamma^{(*)}\pi \to \pi\pi$ rely on knowledge of $\pi\pi \to \pi\pi$. To be precise, the Lellouch–Lüscher formula (3.112) applied to $\gamma^{(*)}\pi \to \pi\pi$ and assuming dominance of the P wave boils down to [40, 191]

$$\left|\mathscr{A}\left(s, q^2\right)\right|^2 = \pounds\left(s\right)\left|\mathscr{A}_{\mathrm{FV}}\left(s, q^2\right)\right|^2, \tag{8.1}$$

with $\mathscr{A}$ as introduced in Eq. (7.26) and $\mathscr{A}_{\mathrm{FV}}$ the finite-volume analogue of $\mathscr{A}$, i.e., the amplitude that appears when the finite-volume matrix element in Eq. (3.112) is decomposed in the same way as the infinite-volume one is in Eq. (7.26). Here the Lellouch–Lüscher factors $\pounds$ read

$$\pounds\left(s\right) = \frac{4\pi}{q^\star}\frac{\partial}{\partial\sqrt{s}}\left[\delta\left(\sqrt{s}\right) - \mathcal{Z}\left(\sqrt{s}\right)\right], \tag{8.2}$$

with $\mathcal{Z}$ as defined in Eq. (6.1) and $q^\star = |\boldsymbol{k}^\star|$ as defined in Sec. 3.2.1. The factors are uniquely defined only on the energies that are solutions of Eq. (6.1), that is, they are not defined as functions of arbitrary values of s [208, App. A4]. We stress that these factors yield the $\gamma^{(*)}\pi^+ \to \pi^+\pi^0$ amplitude, i.e., the experimentally observable amplitude that we are interested in. If instead one wishes to compute the isospin-projected $\gamma^{(*)}\pi \to \pi\pi(I = 1)$ amplitude, the replacement $\pounds \mapsto 2\pounds$ needs to be performed, for

$$\left|\pi^\pm\pi^0\right\rangle = \frac{1}{\sqrt{2}}\left(\mp\left|2, \pm1\right\rangle - \left|1, \pm1\right\rangle\right), \tag{8.3}$$

and only the $I = 1$ component contributes to the process. That is, the $\gamma^{(*)}\pi \to \pi\pi(I = 1)$ amplitude is enhanced by a factor $\sqrt{2}$ compared to the $\gamma^{(*)}\pi^+ \to \pi^+\pi^0$ one [40].

The explicit form of the Lellouch–Lüscher factors (8.2) makes it evident that the $\pi\pi \to \pi\pi$ P-wave phase δ is needed in the translation of the finite-volume data to the continuum. Hence, any complete computation of the $\gamma^{(*)}\pi \to \pi\pi$ P wave on the lattice includes both the $\pi\pi$ energy levels needed to fix δ, as well as the finite-volume amplitude $\mathscr{A}_{\mathrm{FV}}$. As of this writing, the results of only two such computations have been published. The first was performed by HadSpec at $M_\pi \approx 391\,\mathrm{MeV}$, consisting of the $\pi\pi \to \pi\pi$ computation presented in Ref. [165] (precisely the 840_20 data set introduced in Table 5.1) and the $\gamma^{(*)}\pi \to \pi\pi$ data analyzed in Refs. [107, 191]. We call these data M391. The second was carried out at $M_\pi \approx 317\,\mathrm{MeV}$, consisting of the $\pi\pi \to \pi\pi$ analysis of Ref. [86] and the $\gamma^{(*)}\pi \to \pi\pi$ data described in Ref. [108]. These data we denote as M317.

It is worth noting that the quantization condition used in Ref. [86] (and also in Ref. [108]) uses the boost vector $\mathfrak{P} = (0, 1, 1)$ instead of $\mathfrak{P} = (1, 1, 0)$, and thus it takes on a different form than

Refs. [86, 108]	this work
E	E2
T_1	T1
A_2	A1
B_1	A1
B_2	B1
B_3	B2

Table 8.1: Mapping of irreps: the irreps in the left column correspond to those in the right after rotating $\mathfrak{P} = (0, 1, 1)$ to $\mathfrak{P} = (1, 1, 0)$.

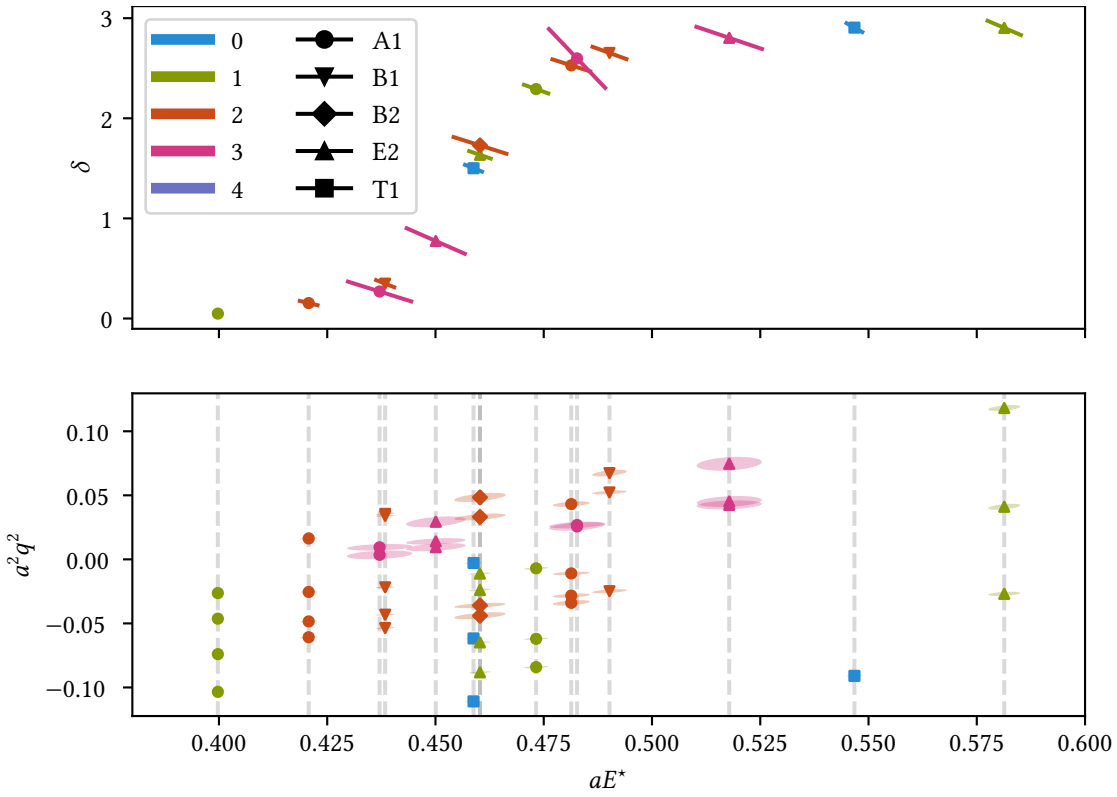

Figure 8.1: The M317 data. While the top plot depicts the $\pi\pi$ P-wave phase shift, with the irrep and $|\mathfrak{P}|^2$ encoded as in Fig. 6.1, the bottom plot shows the location of the computed values of $\mathscr{A}_{\mathrm{FV}}$ in the energy-virtuality plane. Each vertical dashed line marks the position of a $\pi\pi$ energy level (the difference between the B2 level and the E2 one at $aE^\star \approx 0.460$ cannot be resolved at the scale of the plot). The error ellipses show the correlation between the virtualities and the energies.

Eq. (5.5). However, by transforming the former boost vector into the latter via an appropriate rotation, the quantization condition can be rendered into the same form. The corresponding mapping of irreps is shown in Table 8.1.

In the following, we take a closer look at M317, M391 being very similar in its structure. There are 15 different $\pi\pi$ energy levels $aE_k^{\star\mathrm{lat}}$, $k = 1, \ldots, 15$. At each such energy there are one ore more

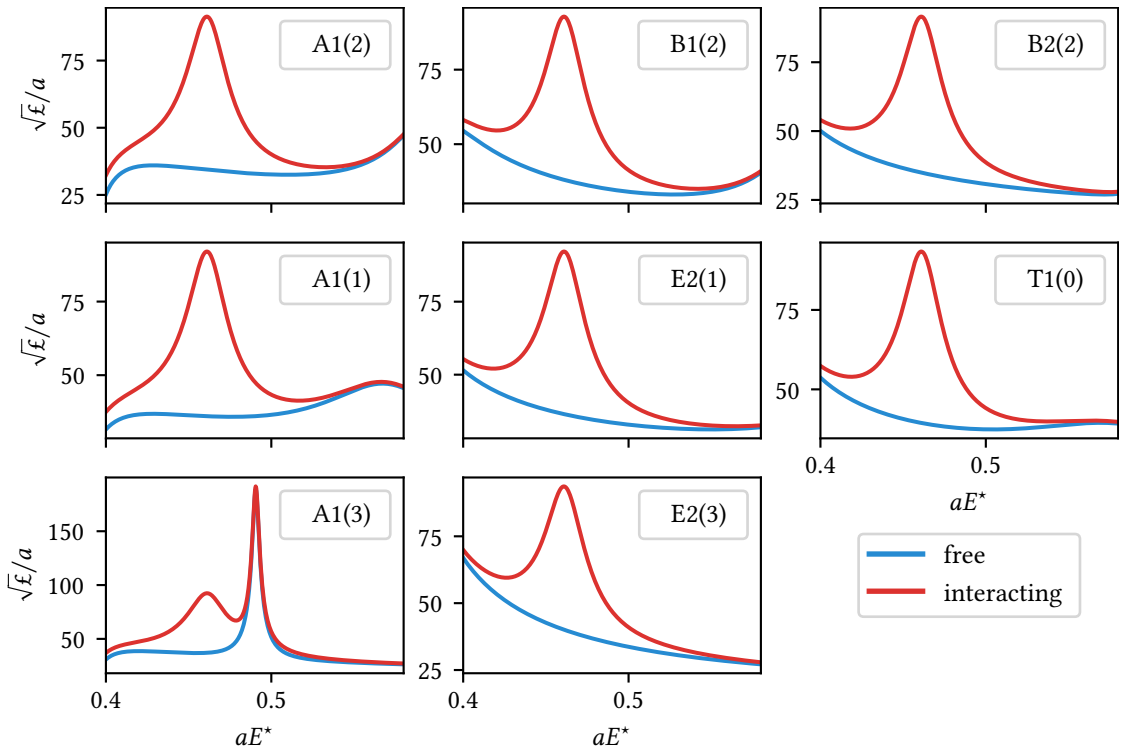

Figure 8.2: The Lellouch–Lüscher factors associated with the M317 data at $M_\pi \approx 317\,\mathrm{MeV}$ for all relevant combinations of irrep and boost vector, given in the legends as irrep($|\mathfrak{P}|^2$). Shown are both the free factors, i.e., the ones with $\delta = 0$, and the interacting ones, that is, the ones with $\delta = \delta^{\mathrm{IAM}}$. These plots might be compared with Fig. 3 in Ref. [108], which depicts the (differently scaled) factors for Breit–Wigner parametrizations of the $\pi\pi$ phase shift.

values of $\mathscr{A}_{\mathrm{FV}}(a^2 s_k^{\mathrm{lat}}, a^2 q^{2\,\mathrm{lat}})/a$, each corresponding to a different virtuality $a^2 q_j^{2\,\mathrm{lat}}$, $j = 1, \ldots, 48$. Altogether, the finite-volume amplitude has been determined at 48 different kinematical points. Here we introduced the abbreviation $s_k^{\mathrm{lat}} := (E_k^{\star\mathrm{lat}})^2$. All quantities carry an error stemming mainly from the statistical nature of the lattice computation, with the energies and virtualities significantly correlated, as is illustrated in Fig. 8.1. Clearly, the majority of the data points is located in the ρ-resonance region.

Since the Lellouch–Lüscher factor (8.2) depends on the derivative of the phase δ and the $\pi\pi$ data points as shown in Fig. 8.1 are not dense enough to allow for a reliable interpolation, a parametrization of δ is needed. We use the NLO IAM to parametrize δ, in accordance with our choice of δ in the KT equations, see Sec. 7.2.2. That is, we first fit the $\pi\pi$ data to fix the NLO IAM, use the latter subsequently as input to compute the Lellouch–Lüscher factors, which in turn enable us to compute $|\mathscr{A}|$ via Eq. (8.1), finally yielding $|f_1|$ via Eq. (7.25):

$$\left|f_1^{\mathrm{lat}}\left(s_k^{\mathrm{lat}}, q_j^{2\,\mathrm{lat}}\right)\right| = \frac{2e\sqrt{3}}{M_\pi q_k^\star}\sqrt{£\left(s_k^{\mathrm{IAM}}\right)}\left|\mathscr{A}_{\mathrm{FV}}\left(s_k^{\mathrm{lat}}, q_j^{2\,\mathrm{lat}}\right)\right|. \tag{8.4}$$

Here $s_k^{\mathrm{IAM}} := (aE_k^{\star\mathrm{IAM}})^2$ is the squared energy obtained in the fit that is associated with s_k^{lat}, see Eq. (6.7). As mentioned below Eq. (8.2), the Lellouch–Lüscher factors need to be evaluated at these energies, for otherwise they are not uniquely defined. The difference $\left|E_k^{\star\mathrm{IAM}} - E_k^{\star\mathrm{lat}}\right|$ is small, but the IAM energies do not agree perfectly with the lattice ones. While at a first sight the appear-

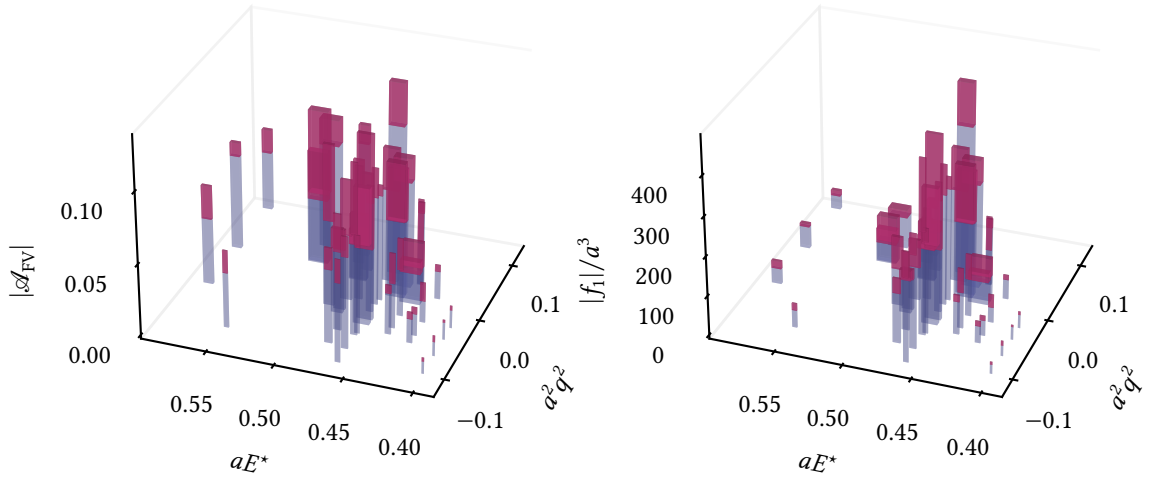

Figure 8.3: All 48 values of the M317 data of both the finite-volume amplitude (left) and the partial wave (right) in the virtuality-energy plane. The width of the bars gives the 1σ error in $aE^\star$, the depth the one in a^2q^2, while the height of the magenta segments corresponds to the 1σ error of $|\mathscr{A}_{\mathrm{FV}}|$ and $|f_1|/a^3$, respectively.

ance of two different energies in Eq. (8.4) might seem problematic, at the current level of precision of the data it is irrelevant. Note that $\arg(\mathscr{A}) = \arg(f_1)$ is fixed via Watson's thereom (7.32).

The fit is described in detail in Ch. 9, using its result we obtain the Lellouch–Lüscher factors as depicted in Fig. 8.2. For comparison the factors obtained with $\delta = 0$ are shown, too. Clearly, the inclusion of the correct P-wave phase shift is crucial, for it yields the peak associated with the ρ resonance, with $\partial\mathcal{Z}/\partial\sqrt{s}$ providing—in the relevant energy range—a background that depends only modestly on the energy, the sole exception being the irrep A1 with $\mathfrak{P} = (1, 1, 1)$.

Lastly, in Fig. 8.3 we show the absolute value of both the finite-volume amplitude and the partial wave (computed via Eq. (8.4)) at the data points of the M317 data. In accordance with the foregoing discussion, the ρ peak becomes prominent only after the inclusion of the Lellouch–Lüscher factors. Moreover, the data seem to hint at an increase of $|f_1|$ with growing q^2, which will be investigated in more detail in Ch. 9. Notably, the errors of $|\mathscr{A}_{\mathrm{FV}}|$ are sizable, translating into huge errors of $|f_1|$, thereby limiting the precision of our analysis.

Chapter 9

Fit and results

We fit the formalism introduced in Ch. 7 to the lattice data described in Ch. 8. Before discussing the results in Sec. 9.2, the fitting method is outlined in Sec. 9.1.

9.1 Fitting procedure

As already stressed, currently there are only two $\gamma\pi$ data sets available, M317 and M391. Hence, to fix the pion-mass dependence, we need to analyze these two data sets simultaneously.

The fit to the $\pi\pi$ energy levels including the error estimation proceeds exactly as described in Ch. 6. Since F_π is not included in the M317 data, we use the literature value of F as described in Sec. 6.4.3. Moreover, since we aim for a combined fit, we use the literature value of F also in the analysis of the M391 $\pi\pi$ data, to ensure that there is one unique value of F involved in the analysis. Since the two $\pi\pi$ data sets were independently generated, the χ^2 is the sum of two terms in the form of Eq. (6.8), one for each data set.

With the parameter l^r of the NLO IAM fixed, we use δ^{IAM} to compute $|f_1^{\mathrm{lat}}|$ via Eq. (8.4). The KT P wave (7.66) is subsequently fit to $|f_1^{\mathrm{lat}}|$. To take into account the errors of the energies and virtualities, we follow the standard approach and introduce an auxiliary fit parameter for each kinematic variable, see, e.g., Refs. [86, 167]. Accordingly, we define

$$\chi^2_{\gamma\pi} := \left(v^{\mathrm{lat}} - v^{\mathrm{KT}}\right) C^{-1}_{\gamma\pi} \left(v^{\mathrm{lat}} - v^{\mathrm{KT}}\right)^T, \tag{9.1}$$

with

$$v^{\mathrm{lat}} := \begin{pmatrix} \frac{\left|f_1^{\mathrm{lat}}\left(a^2 s_1^{\mathrm{lat}}, a^2 q_1^{2\,\mathrm{lat}}\right)\right|}{a^3} \\ \vdots \\ \frac{\left|f_1^{\mathrm{lat}}\left(a^2 s_{N_{\pi\pi}}^{\mathrm{lat}}, a^2 q_{N_{\gamma\pi}}^{2\,\mathrm{lat}}\right)\right|}{a^3} \\ a^2 q_1^{2\,\mathrm{lat}} \\ \vdots \\ a^2 q_{N_{\gamma\pi}}^{2\,\mathrm{lat}} \\ a E_1^{\star\,\mathrm{lat}} \\ \vdots \\ a E_{N_{\pi\pi}}^{\star\,\mathrm{lat}} \end{pmatrix}, \qquad v^{\mathrm{KT}} := \begin{pmatrix} \frac{\left|f_1\left(a^2 s_1, a^2 q_1^2\right)\right|}{a^3} \\ \vdots \\ \frac{\left|f_1\left(a^2 s_{N_{\pi\pi}}, a^2 q_{N_{\gamma\pi}}^2\right)\right|}{a^3} \\ a^2 q_1^2 \\ \vdots \\ a^2 q_{N_{\gamma\pi}}^2 \\ a E_1^\star \\ \vdots \\ a E_{N_{\pi\pi}}^\star \end{pmatrix}, \tag{9.2}$$

$N_{\pi\pi} \in \mathbb{N}$ the number of $\pi\pi$ energy levels, $N_{\gamma\pi} \in \mathbb{N}$ the number of $\gamma\pi$ data points, the auxiliary fit parameters $q_1^2, \ldots, q_{N_{\gamma\pi}}^2$, $E_1^\star, \ldots, E_{N_{\pi\pi}}^\star$, as well as $s_k := (E_k^\star)^2$, and covariance matrix $C_{\gamma\pi}$. Here we made

	fit	Ref. [162]	FLAG [47]	Ref. [182]
χ^2/dof	$31.7/(27-1) = 1.22$			
p value	0.20			
$l^r \times 10^3$	12.79(11)(10)(12)	9.9(1.3)	19(17)	
M_ρ/MeV	747.2(2.7)(2.8)(1.0)			$763.7^{+1.7}_{-1.5}$
Γ_ρ/MeV	145.0(1.9)(1.9)(1.0)			$146.4^{+2.0}_{-2.2}$
$\text{Re}(g_{\rho\pi\pi})$	5.960(22)(21)(25)			$5.98^{+0.04}_{-0.07}$
$-\text{Im}(g_{\rho\pi\pi})$	0.7175(82)(79)(94)			$0.56^{+0.07}_{-0.10}$

Table 9.1: The outcomes of the IAM fit to the $\pi\pi$ data. The first error arises due to the statistical error of the $\pi\pi$ data, the second due to the error of the lattice spacings, and the third due to the error of the literature value of F. The third and fourth column contain reference values for the LEC from ChPT and lattice QCD [47, 173–177], respectively, while the fifth column lists the ρ properties as determined via Roy-like equations.

the fact explicit that everything is computed in lattice units. The error of the IAM phase leads to an error of the Lellouch–Lüscher factors. The corresponding covariance matrix is added to the appropriate entries of $C_{\gamma\pi}$. Equation (9.1) is minimized with respect to the auxiliary fit parameters and the variables b_{kj} appearing in the parameterization of the subtraction functions. To that end, we employ the combination of the differential-evolution algorithm and Powell's method described in Sec. 6.2. Since only the absolute value of the partial wave is fit and f_1 is linear in the fit parameters b_{kj}, the latter are fixed by the fit only up to a global phase ± 1. To fix this, we impose the upper case of Eq. (7.32), i.e., $\arg[f_1(s, q^2)] = \delta(s)$.

Since the two data sets are uncorrelated and the pion-mass dependence of each fit parameter b_{kj} is described by two free parameters, compare Eq. (7.86), we can perform the fits to the two $\gamma\pi$ data sets independently, the fit parameters being the values of b_{kj} at the two different pion masses. That is, for both $M317$ and $M391$ we minimize a χ^2 of the form (9.1), each time working in the lattice units of the given data set.

To assess the statistical error of the fit to the $\gamma\pi$ data, we simply use the Hessian $H_{\chi^2_{\gamma\pi}}$. That is, the covariance $\text{Cov}[\kappa_i, \kappa_j]$ of two fit parameters κ_i and κ_j is estimated via [9, 209]

$$\text{Cov}\left[\kappa_i, \kappa_j\right] = 2\left[H^{-1}_{\chi^2_{\gamma\pi}}\right]_{ij}, \qquad \left[H_{\chi^2_{\gamma\pi}}\right]_{ij} := \frac{\partial^2 \chi^2_{\gamma\pi}}{\partial\kappa_i \partial\kappa_j}, \tag{9.3}$$

where the derivatives are evaluated at the values of the fit parameters corresponding to the minimum of $\chi^2_{\gamma\pi}$. On top of this, in principle the error of the IAM needs to be taken into account not only in the covariance matrix $C_{\gamma\pi}$ but also in the KT equations and directly in the Lellouch–Lüscher factors. That is, for each jackknife (or bootstrap) run of the IAM fit a slightly different phase δ^{IAM} is obtained, which in turn could be plugged into both the Lellouch–Lüscher factors and the KT equations, subsequently repeating the $\gamma\pi$ fit for each different phase to estimate the associated error. However, it becomes clear in Sec. 9.2 that the error of the $\pi\pi$ fit is negligible compared to the statistical one of the $\gamma\pi$ fit arising from the large errors of $|\mathscr{A}_{\text{FV}}|$, and thus there is no need for such an elaborate error computation.

Although Eq. (9.2) is phrased in lattice units, the lattice spacing a still enters if the parametrizations of the subtraction functions involve an ω pole, see Table 7.1, because Eq. (7.85) needs to be

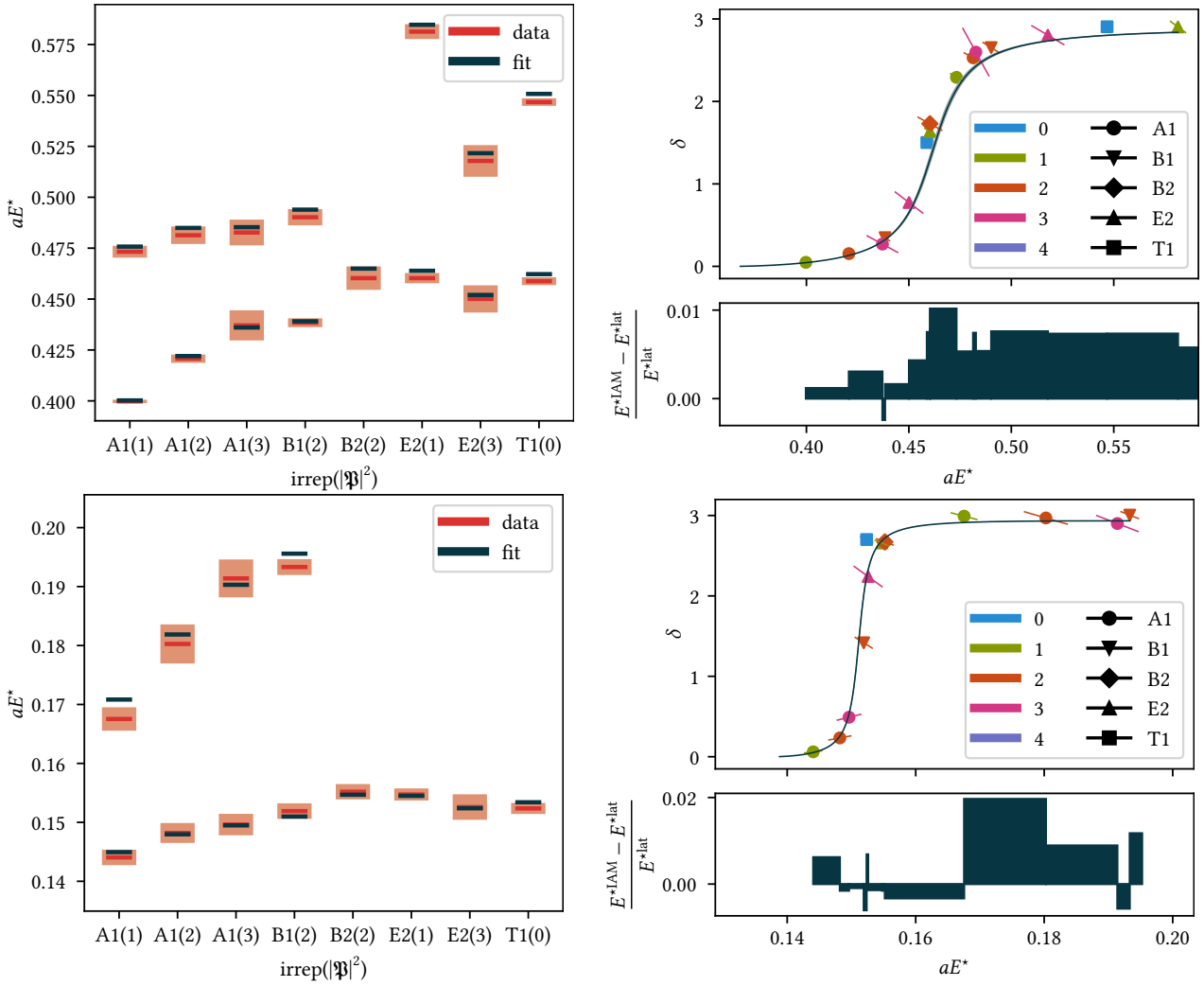

Figure 9.1: The fit IAM in comparison to the 2π lattice data in complete analogy to Fig. 6.1. The top (bottom) plots correspond to the M317 (M391) data.

translated into lattice units. However, while the fits are sensitive to the presence of the pole as observed in Sec. 9.2, the precise value of this pole does not matter at all at the current level of precision of the data; thus this error can be safely ignored, too.

Nevertheless, the error of the lattice spacing cannot be entirely ignored. Namely, as soon as we want to combine both $\gamma\pi$ fits to allow for an extrapolation to the physical point, as performed in Sec. 9.2.3, the obtained values of b_{kj} at the two different pion masses need to be translated into a common set of units, so that the two lattice spacings enter the picture. Since the scale of the two data sets is set in different ways (in case of M317 via the $\Upsilon(1S)$–$\Upsilon(2S)$ splitting and in case of M391 via the Ω baryon mass, see Sec. 6.4.2), an additional systematic error arises, which is difficult to quantify (this also applies to the simultaneous fit of the two $\pi\pi$ data sets). However, compared to the sizable statistical uncertainty of the data and the systematic error of the chiral extrapolation to be discussed in Sec. 9.2.4, the systematic error associated with the scale setting is likely irrelevant at present. Therefore, the uncertainty associated with the lattice spacing given in the remainder

of this work will always refer to its statistical error only. There is also a systematic error from the continuum extrapolation, since the calculation in Ref. [108] was performed at a single lattice spacing of $a \approx 0.11\,\text{fm}$, while the one in Ref. [191] was performed on an anisotropic lattice with temporal spacing $a \approx 0.03\,\text{fm}$ and spatial spacing $a_s \approx 0.12\,\text{fm}$. Without several data sets at different lattice spacings determined via the same scale setting, this error cannot be reliably estimated.

9.2 Results

9.2.1 Fits to $\pi\pi$ data

The result of a simultaneous fit of the NLO IAM to the M317 $\pi\pi$ data and the M391 one is compared with this data in Fig. 9.1, while the goodness of the fit is shown in Table 9.1 together with the obtained value of l^r, the resulting p value of 20 % being reasonable. There is a 2σ tension with the ChPT value of l^r; however, this deviation comes at no surprise, given the unitarization via the IAM, as discussed in Sec. 6.5.1. With l^r fixed, we continue the $\pi\pi$ P wave to the second RIEMANN sheet—as in Sec. 6.5.1—to determine the ρ characteristics at the physical point as listed in Table 9.1. Comparing with the literature values given ibidem, we note a 4σ discrepancy in M_ρ and a 2σ tension in $\text{Im}(g_{\rho\pi\pi})$, while both the width and the real part of the coupling agree well. This is explained by the fact that the NLO IAM has only a single free parameter, leading to a trade-off between the different ρ properties. To improve on this, the NNLO IAM can be employed, see again Sec. 6.5.1, however, with data at only two different pion masses both exceeding 300 MeV, we find that stable fits are not feasible.

9.2.2 Fits to $\gamma\pi$ data

Next, we fit the $\gamma\pi$ data. We use $n = 2$ subtractions in Eq. (7.66), for once-subtracted KT equations fail to describe the energy dependence of the data correctly, and thus do not allow for statistically acceptable fits. Note that increasing the number of subtractions to $n = 3$ does not provide additional flexibility, since the reconstruction theorem (7.52) is invariant under the shift $\mathscr{B}(s,q^2) \mapsto \mathscr{B}(s,q^2) + \lambda(q^2)(3s - 3M_\pi^2 - q^2)$, with λ an arbitrary function, and thus one subtraction function can be eliminated. According to Eq. (7.60) this shift is forbidden for $n = 2$ due to the high-energy behavior of $\mathscr{B}$, but becomes possible for $n = 3$. In addition, we pick $N = 2$, that is, we have three fit parameters b_{kj} in c_0 and two in c_1, see Sec. 7.2.3. If instead $N = 1$ is used, the fit quality becomes poor, while at $N = 3$ the fit stability deteriorates. The exception are the strategies III and III$\mathcal{P}$, where we pick $N = 3$, which again amounts to five fit parameters due to Eq. (7.65).

To obtain statistically acceptable fits to the M391 data, we need to exclude the six data points at the highest energy, $E^{\star\text{lat}} \approx 1096\,\text{MeV}$. These points lie far above the resonance region, for although at this pion mass the ρ is heavy, i.e., $M_\rho = 846.1(3.1)(3.2)(0.1)\,\text{MeV}$ (errors as in Table 9.1), its width $\Gamma_\rho = 10.8(8)(9)(1)\,\text{MeV}$ is tiny. Moreover, several of the data points with the smallest absolute errors of $|\mathscr{A}_{\text{FV}}|$ are located at this energy. Hence, the six excluded data points provide rather strong constraints on the asymptotic high-energy behavior of the KT equations instead of the resonance physics in which we are primarily interested.

We carry out fits for each strategy enumerated in Table 7.1, with an overview of the fit qualities given in Table 9.2. While the goodness of the fit at the lower pion mass is rather insensitive to the parameterization of the subtraction functions, the data at the higher pion mass are more selective, because the relative error of $|\mathscr{A}_{\text{FV}}|$ at the higher pion mass is smaller than the error at lower mass.

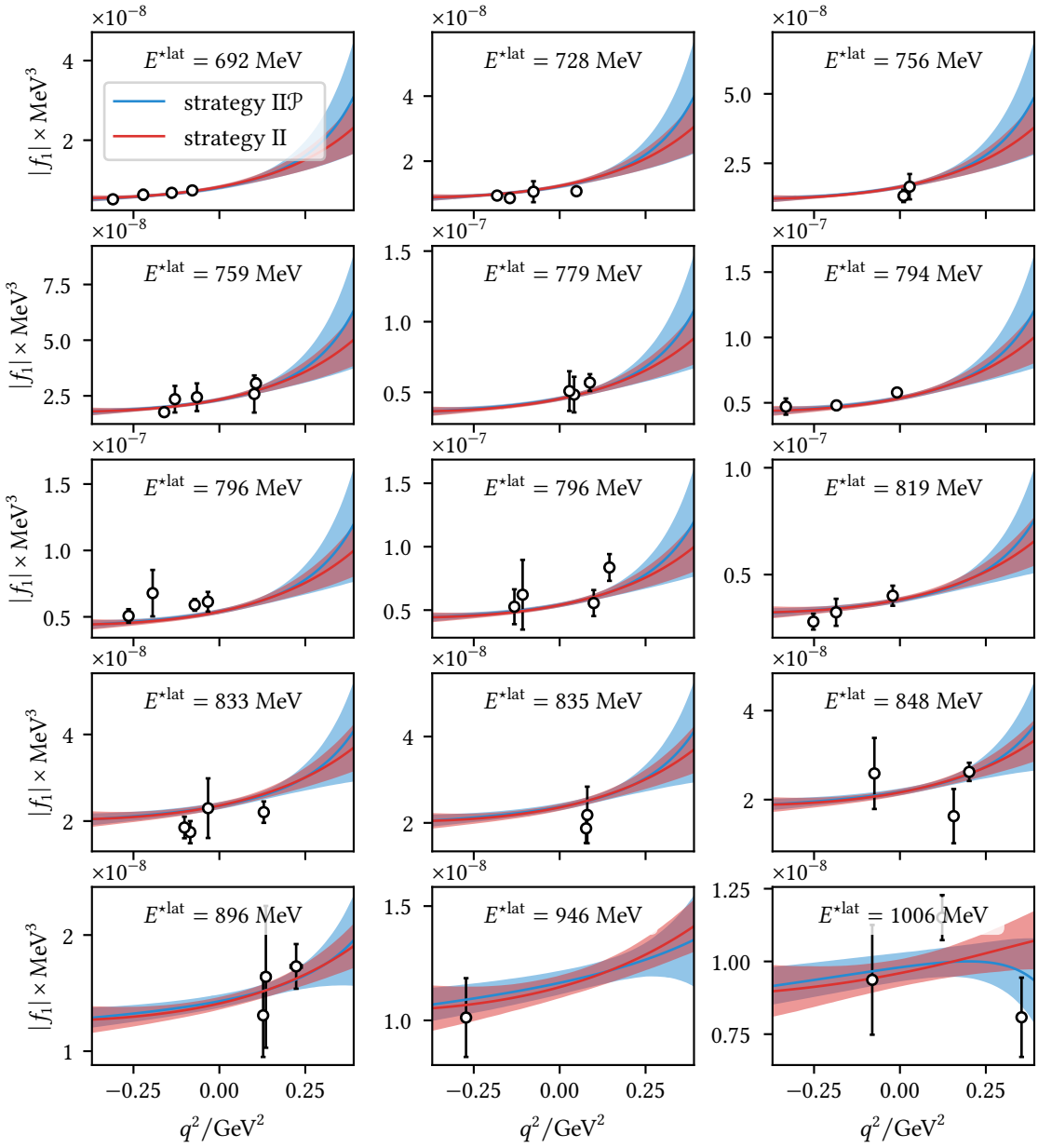

Figure 9.2: The results of two fit strategies in comparison with the $M317$ $\gamma\pi$ data. Shown are slices of constant energy. For convenience, the results are displayed in physical units, but the fit is carried out in lattice units, so that the error bands are associated with the statistical error of the data only.

Notably, we observe improvement when including a pole factor, which is true for all strategies, with the overall p value improving by at least an order of magnitude in each case, and even by two orders of magnitude when going from strategy I to I$\mathcal{P}$. As soon as a pole factor is included, it does not matter much if the remaining q^2 dependence is parameterized by a plain polynomial, a conformal one, or a conformal one with modified threshold behavior, the overall p values of strategy I$\mathcal{P}$, II$\mathcal{P}$, and III$\mathcal{P}$ are similar, with a slight improvement when using conformal parameterizations. Hence, in the following we group the results of the three parameterizations including a pole together. If no pole is used, at higher pion mass the fit clearly disfavors a plain polynomial and instead prefers a

		M317	M391	combined
I	$\frac{\chi^2_{\gamma\pi}}{\text{dof}}$	$\frac{57.8}{48-5} = 1.34$	$\frac{67.0}{37-5} = 2.09$	$\frac{57.8+67.0}{85-10} = 1.66$
	p value	6.54×10^{-2}	2.81×10^{-4}	2.70×10^{-4}
I$\mathcal{P}$	$\frac{\chi^2_{\gamma\pi}}{\text{dof}}$	$\frac{61.1}{48-5} = 1.42$	$\frac{44.0}{37-5} = 1.37$	$\frac{61.1+44.0}{85-10} = 1.40$
	p value	3.61×10^{-2}	7.70×10^{-2}	1.26×10^{-2}
II	$\frac{\chi^2_{\gamma\pi}}{\text{dof}}$	$\frac{59.2}{48-5} = 1.38$	$\frac{53.9}{37-5} = 1.69$	$\frac{59.2+53.9}{85-10} = 1.51$
	p value	5.13×10^{-2}	8.99×10^{-3}	2.96×10^{-3}
II$\mathcal{P}$	$\frac{\chi^2_{\gamma\pi}}{\text{dof}}$	$\frac{57.9}{48-5} = 1.35$	$\frac{43.6}{37-5} = 1.36$	$\frac{57.9+43.6}{85-10} = 1.35$
	p value	6.43×10^{-2}	8.31×10^{-2}	2.26×10^{-2}
III	$\frac{\chi^2_{\gamma\pi}}{\text{dof}}$	$\frac{59.5}{48-5} = 1.38$	$\frac{51.9}{37-5} = 1.62$	$\frac{59.5+51.9}{85-10} = 1.49$
	p value	4.83×10^{-2}	1.44×10^{-2}	4.04×10^{-3}
III$\mathcal{P}$	$\frac{\chi^2_{\gamma\pi}}{\text{dof}}$	$\frac{57.2}{48-5} = 1.33$	$\frac{43.6}{37-5} = 1.36$	$\frac{57.2+43.6}{85-10} = 1.34$
	p value	7.20×10^{-2}	8.32×10^{-2}	2.51×10^{-2}

Table 9.2: The quality of the fit to the $\gamma\pi$ data for the different parameterizations of the subtraction functions.

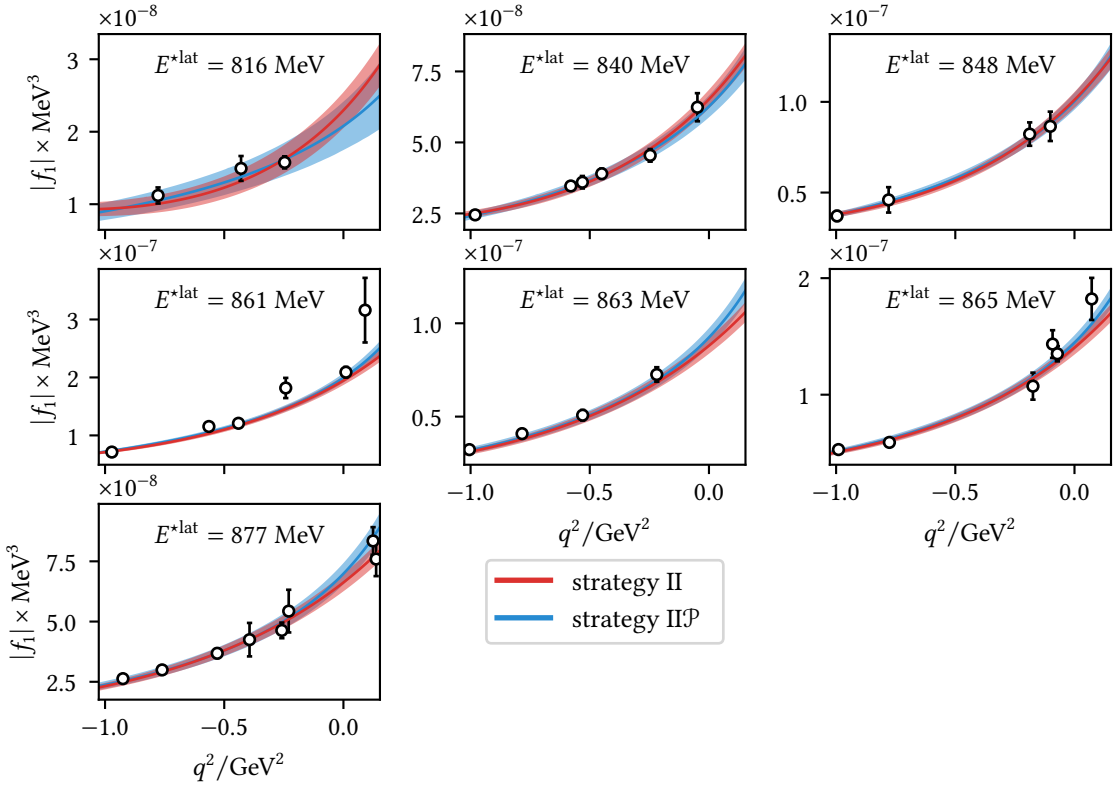

Figure 9.3: As Fig. 9.2, but for the M391 data.

conformal one, with only a very slight further improvement when modifying the threshold scaling. Thus, we exclude strategy I and combine strategies II and III. As representatives of each group, we pick strategies II and II$\mathcal{P}$. The corresponding partial waves are compared with the two lattice data sets in Fig. 9.2 and Fig. 9.3. As can be observed, independently of the presence of a pole factor, the magnitude of f_1 increases with growing q^2, in accordance with phenomenology [117].

To check if we are sensitive to the mixed rescattering effects included in the KT equations, we re-perform the fits with the replacement $\mathscr{B}_k(s,q^2) \mapsto s^k\Omega(s)$. At $M_\pi \approx 317\,\text{MeV}$ we obtain a p value of 4.97×10^{-2} with strategy II and 6.26×10^{-2} with strategy II$\mathcal{P}$, while at $M_\pi \approx 391\,\text{MeV}$ we obtain 8.77×10^{-3} and 8.49×10^{-2}, respectively. Comparing with the corresponding entries of Table 9.2, the observed difference is insignificant, and thus we conclude that mixed rescattering does not need to be taken into account to describe the data at the present level of precision.

9.2.3 Chiral extrapolation

Equipped with the KT fit results, we can determine the pion-mass dependence of the fit parameters via Eq. (7.86). To that end, we need to translate the fit parameters associated with the two different data sets to a common set of units; hence the errors of the lattice spacings enter the picture.

The pion-mass dependence of the fit parameters is depicted in Fig. 9.4. While the leading parameters in the series expansion (7.63), b_{00} and b_{10}, are constrained more strongly by the data at lower pion mass than the one at higher pion mass, the opposite is true for the highest-order term associated with b_{02}. The latter comes at no surprise, for the data at higher mass contain much larger virtualities in the spacelike region, exceeding in absolute value the timelike virtualities of both data sets significantly, giving thus more weight to the b_{02} term. With decreasing pion mass, the ω pole moves from the real axis below the 3π threshold on the first Riemann sheet into the complex plane on the second sheet. Since the pole factor $\mathcal{P}$ that is present in strategies I$\mathcal{P}$, II$\mathcal{P}$, and III$\mathcal{P}$ describes a bound state, naturally the question arises if the change in the nature of the pole needs to be reflected in the extrapolation in the pion mass for these strategies. A resonant ω could be implemented via a dispersively improved Breit–Wigner parameterization as alluded to below Eq. (7.61), which, in practice, is almost indistinguishable from a pole ansatz unless very close to the singularities. Given the large uncertainties of b_{jk} at the physical point, this change is thus immaterial, especially, since for the extraction of the observables the subtraction functions need to be evaluated at vanishing virtuality only, and for every strategy $c_k(0) = b_{k0}$ holds.

Taking care of the pion-mass dependence of the fit parameters, the IAM, and the KT equations, we can extrapolate the partial wave to the physical point. Computing the cross section via Eq. (7.29) yields the line shape shown in Fig. 9.5 exhibiting the characteristic resonance peak. In both fit strategies, the error increases when moving beyond the resonance, which reflects the fact that most data points lie around the resonance region. In principle, the omitted data points at the highest energy could provide further constraints, but since no acceptable fits could be found when including these points, we conclude that with the currently available lattice data the asymptotic form of the cross section remains largely unconstrained. In this regard, we remark that the KT basis functions with $n = 2$ subtractions increase too fast asymptotically compared to expectations from the Froissart bound [210], so that a proper high-energy completion needs to be imposed. However, these considerations become relevant only well beyond 1 GeV, and thus do not affect the current fit, for which the $n = 2$ subtraction scheme provides the adequate number of free parameters to be able to describe both the chiral anomaly and the ρ-meson properties [97].

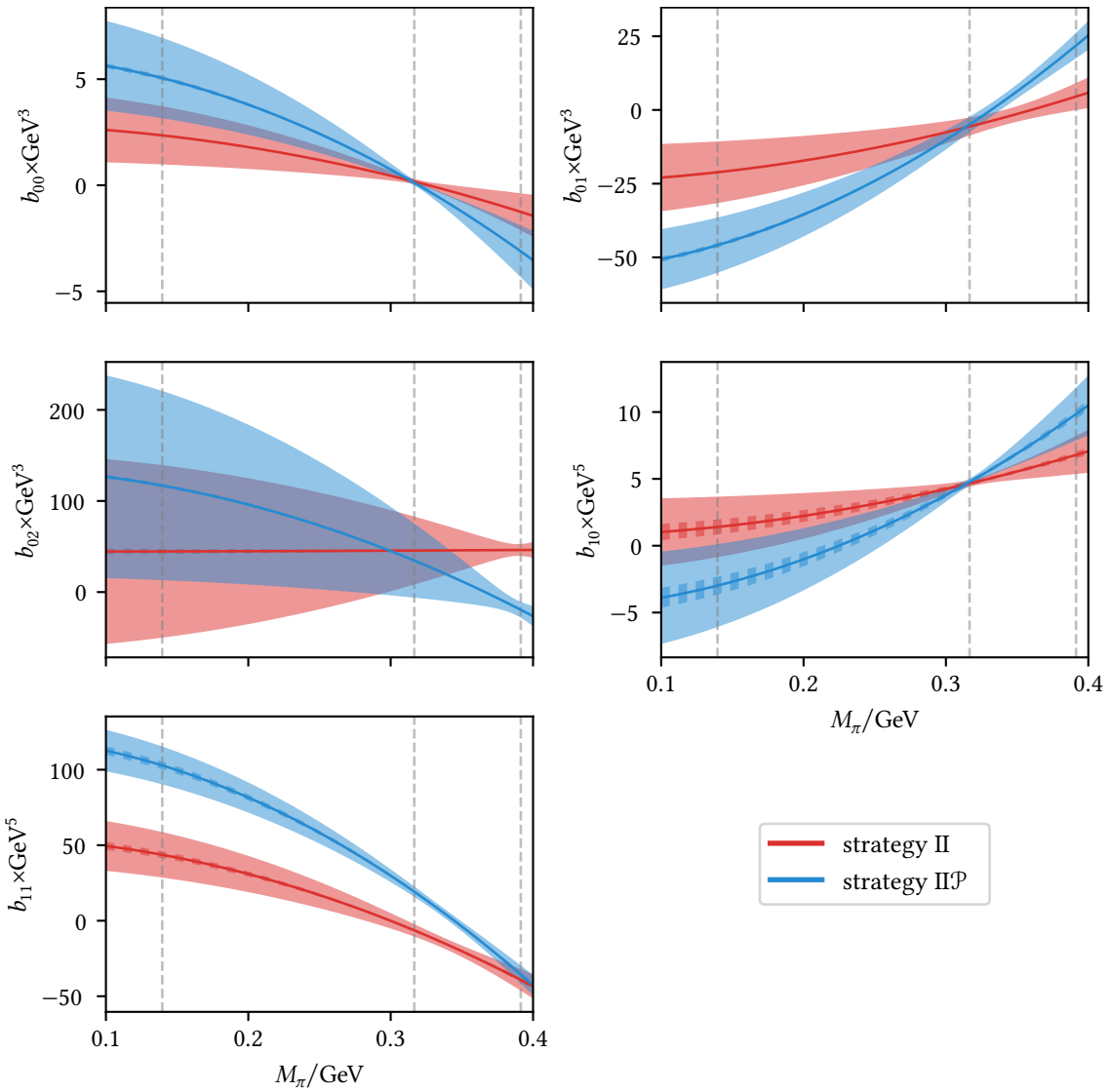

Figure 9.4: The pion-mass dependence of the fit parameters for two different fit strategies. The dashed gray lines mark the physical pion mass and the ones of the two lattice data sets, the dashed error bands correspond to the error of the lattice spacings, while the filled ones are associated with the statistical error of the data.

9.2.4 Chiral anomaly and radiative coupling

Finally, we can determine the anomaly $F_{3\pi}$ and the radiative coupling at the physical point via Eq. (7.87) and Eq. (7.34), respectively. The values are listed for the different fit strategies in Table 9.3. Since the outcomes of the different fit variants are highly correlated with only minor differences in fit quality and very similar statistical errors, we do not compute weighted averages, but instead only perform plain averages to determine the central values. Doing so for the acceptable fits without a

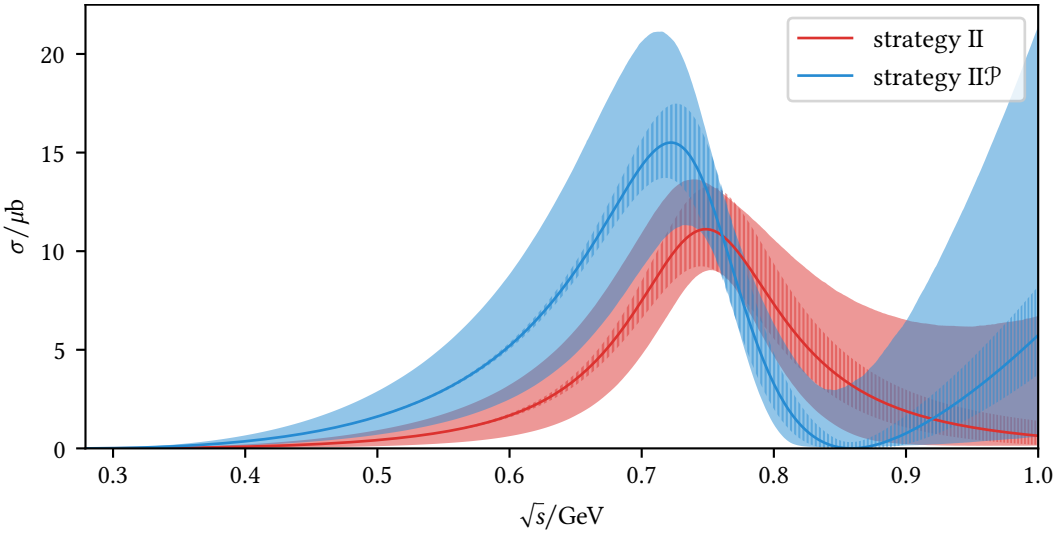

Figure 9.5: The cross section at the physical point for two different fit strategies. The error bands are as in Fig. 9.4.

pole factor, i.e., averaging over strategy II and III, results in

$$\begin{aligned} F_{3\pi} &= 24(13)(1)\,\text{GeV}^{-3}, \\ g_{\rho\gamma\pi} &= [0.51(6)(4) + i0.03(13)(2)]\ \text{GeV}^{-1}, \\ |g_{\rho\gamma\pi}| &= 0.51^{+0.08}_{-0.05}(4)\,\text{GeV}^{-1}, \end{aligned} \tag{9.4}$$

with errors as in Table 9.3, while the strategies including an ω pole, i.e., I$\mathcal{P}$, II$\mathcal{P}$, and III$\mathcal{P}$, yield

$$\begin{aligned} F_{3\pi} &= 47(18)(1)\,\text{GeV}^{-3}, \\ g_{\rho\gamma\pi} &= [0.60(8)(4) + i0.26(18)(3)]\ \text{GeV}^{-1}, \\ |g_{\rho\gamma\pi}| &= 0.66^{+0.15}_{-0.12}(3)\,\text{GeV}^{-1}. \end{aligned} \tag{9.5}$$

Both values of $F_{3\pi}$ are compatible with the prediction (7.30), albeit only due to their large errors. Fits including the pole ansatz do display a better fit quality, but not at a level that would conclusively demonstrate the necessity of the pole. Since, further, both fit variants agree within statistical uncertainties, we conclude that the current lattice data cannot discriminate between Eq. (9.4) and Eq. (9.5) and quote the resulting spread as an additional systematic error. This error also arises due to the absence of lattice data at several different pion masses by one collaboration, forcing us to fit our representation to two data sets by two different collaborations at only two different pion masses, which makes it impossible to fix the pion-mass dependence of the subtraction functions beyond the simple ansatz (7.86). Averaging over all fit results except for strategy I, we finally quote

$$\begin{aligned} F_{3\pi} &= 38(16)(1)(11)\,\text{GeV}^{-3}, \\ g_{\rho\gamma\pi} &= [0.57(7)(4)(4) + i0.17(16)(3)(12)]\ \text{GeV}^{-1}, \\ |g_{\rho\gamma\pi}| &= 0.60^{+0.12}_{-0.09}(3)(7)\,\text{GeV}^{-1}, \end{aligned} \tag{9.6}$$

where the last error is our estimate of the systematic uncertainty associated with the parameterization of the subtraction functions.

	$F_{3\pi} \times \mathrm{GeV}^3$	$\mathrm{Re}(g_{\rho\gamma\pi}) \times \mathrm{GeV}$	$\mathrm{Im}(g_{\rho\gamma\pi}) \times \mathrm{GeV}$
I	13(11)(0)	0.50(6)(4)	0.09(11)(2)
I$\mathcal{P}$	46(18)(1)	0.59(8)(4)	0.26(18)(3)
II	23(13)(1)	0.51(6)(4)	0.02(13)(2)
II$\mathcal{P}$	48(18)(1)	0.61(8)(4)	0.27(18)(3)
III	26(13)(1)	0.52(6)(4)	0.05(13)(2)
III$\mathcal{P}$	48(18)(1)	0.61(8)(4)	0.27(18)(3)

Table 9.3: The anomaly and the radiative coupling at the physical point. The fit uncertainty gives the first error, the second error corresponds to the error of the lattice spacings.

The resulting value of $F_{3\pi}$ is perfectly consistent with the chiral prediction (7.30), but carries a large uncertainty. This is the first extraction of this low-energy parameter from lattice-QCD calculations, and will improve accordingly once better data become available. The residue $g_{\rho\gamma\pi}$ is currently not known better than from an $SU(3)$ VMD estimate [211], which suggests $|g_{\rho\gamma\pi}| = 0.79(8)\mathrm{GeV}^{-1}$ [97], again compatible with Eq. (9.6) (within 1.2σ).[1] The difference to the VMD estimate increases to 2.3σ for Eq. (9.4), while there is full agreement with Eq. (9.5). This provides a-posteriori evidence for the presence of an ω pole in the subtraction functions, as does the final result for the cross section shown in Fig. 9.5 when compared to the expected peak cross section around 20 μb [106]. The radiative coupling has also been extracted in Ref. [108] under the assumption that the pion-mass dependence of $|G_{\rho\gamma\pi}| = |g_{\rho\gamma\pi}|M_\pi/2$ is weak, leading to $|g_{\rho\gamma\pi}|_{[108]} = 1.15(5)(3)\,\mathrm{GeV}^{-1}$. This value differs from the VMD estimate by 3.6σ, a discrepancy that went unnoticed in Ref. [108] because it is mitigated by a missing factor 2 in Eq. (17) for $\Gamma(\rho \to \pi\gamma)$ therein [217]. Moreover, our analysis shows that the uncertainties especially from the chiral extrapolations are substantially larger. In particular, a pion-mass independent $|G_{\rho\gamma\pi}|$ renders the residue divergent in the chiral limit, while at $M_\pi = 317\,\mathrm{MeV}$ one has $|g_{\rho\gamma\pi}|_{[108]}^{M_\pi=317\,\mathrm{MeV}} = 0.507(20)(13)\,\mathrm{GeV}^{-1}$ as well as $|g_{\rho\gamma\pi}|^{M_\pi=317\,\mathrm{MeV}} = 0.552(18)(18)(0)$, the latter being the average (9.6) at this pion mass. We conclude that $|g_{\rho\gamma\pi}|$ instead of $|G_{\rho\gamma\pi}|$ is approximately pion-mass independent, thus avoiding the divergence in the chiral limit.

[1] The branching fractions cited in Ref. [9] imply $|g_{\rho\gamma\pi}| = 0.72(4)\,\mathrm{GeV}^{-1}$ for the charged channel and $|g_{\rho\gamma\pi}| = 0.73(6)\,\mathrm{GeV}^{-1}$ for the neutral one. However, these values derive from high-energy Primakoff measurements [212–214] and VMD fits to $e^+e^- \to \pi^0\gamma$ data [215, 216], respectively, and thus involve a substantial model dependence.

Part IV

Rescattering effects in 3π decays

Chapter 10

Rescattering of pions

We have already encountered rescattering of pions in several places. In Sec. 4.2 we mentioned that the unitarization procedure via the IAM accounts, in fact, for rescattering of pions in the s channel. Furthermore, the basis functions of the KT equations encode rescattering, too, as stated in Sec. 7.2.2. It is now the time to make this notion of rescattering more precise, in particular, to distinguish more carefully between different kinds of rescattering. We stress that in this chapter we care mainly about qualitative insights into the nature of rescattering, so contrarily to the rest of this thesis we are not too concerned with correct bookkeeping and instead focus on the key concepts only.

10.1 Rescattering and unitarity

Consider T_s, the part of the $\pi\pi \to \pi\pi$ amplitude that contains all s-channel loops as depicted in Fig. 10.1. This sum of iterated loops is precisely what we mean by s-channel rescattering of pions. For simplicity, we work in the CM frame. Denoting the vertex by V and the loop by L, formally we can write

$$\begin{aligned} T_s &= V + VLV + VLVLV + \dots \\ &= V \sum_{k=0}^{\infty} (LV)^k \\ &= \frac{V}{1 - LV} \\ &= \frac{1}{\frac{1}{V} - L}, \end{aligned} \tag{10.1}$$

where we used the geometric series. The loop L is a special case of $I_{\mathrm{IV}}(P)$ as defined in Eq. (3.24), with $P = (s, \mathbf{0})$ and $f(k) = -i$.[1,2] Its discontinuity as defined in Eq. (7.39) can be straightforwardly

[1] The factor -1 arises from two powers of i stemming from the numerators of the propagators, while the factor i corresponds to the global factor $i\mathscr{M}$ in the definition of the scattering amplitude $\mathscr{M}$, see Eq. (2.1), and needs to be included if we want to use the Cutkosky rules in the form of Eq. (10.2).

[2] Of course, the propagators are to be replaced by the full 1PI contribution. However, the only aspect that matters here is the imaginary part of the loop L, which is computed by setting the propagators on-shell, see Eq. (10.2). Picking the renormalization conditions (3.59), the argument remains unaffected by this subtlety.

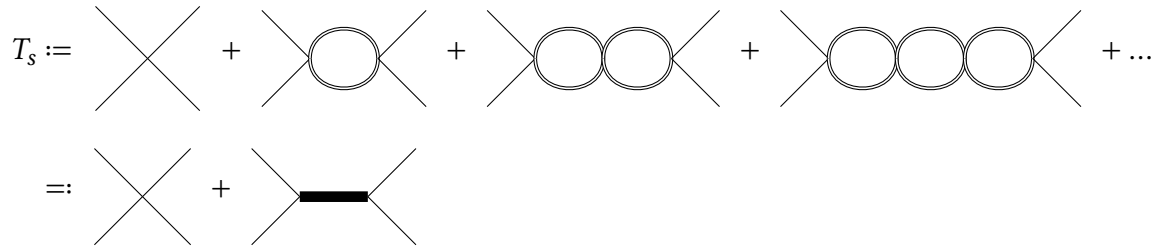

Figure 10.1: Pion–pion rescattering in the s channel. Double lines denotes the full pion propagator Δ as defined in Fig. 3.1, while the thick line denotes the two-pion propagator that is defined as the sum of all iterated pion loops.

computed via the Cutkosky rules [189, 218], i.e., by performing the replacements

$$\begin{aligned} \frac{1}{k^2 - M_\pi^2 + i\epsilon} &\to -2\pi i\, \Theta\left(k^0\right) \delta\left(k^2 - M_\pi^2\right), \\ \frac{1}{(P-k)^2 - M_\pi^2 + i\epsilon} &\to -2\pi i\, \Theta\left((P-k)^0\right) \delta\left((P-k)^2 - M_\pi^2\right), \end{aligned} \tag{10.2}$$

in Eq. (3.24), with Θ defined in Eq. (3.83). Since the loop obeys the Schwarz reflection principle (2.7), $\mathrm{disc}_s[L(s)] = 2i\,\mathrm{Im}[L(s)]$ holds. Altogether, this results in

$$\mathrm{Im}\left[L\left(s\right)\right] = \frac{\sigma(s)}{16\pi}, \tag{10.3}$$

with σ being the phase space as introduced in Eq. (2.29). By inserting Eq. (10.3) into Eq. (10.1) we finally obtain

$$T_s = \frac{1}{\frac{1}{V} - \mathrm{Re}\left[L\right] - \frac{i}{16\pi}\sigma}. \tag{10.4}$$

Note that the vertex V is real, for the Hamiltonian needs to be Hermitian, and thus the couplings in the underlying Lagrangian must be real.

The comparison of Eq. (10.4) with the single-channel K-matrix representation (2.17) shows a remarkable similarity. In fact, the factor $1/(16\pi)$ that spoils perfect agreement is an artifact of our sloppy bookkeeping, which ignored the partial-wave projection, see Eq. (2.3) and Eq. (2.5). Thus, Eq. (10.4) is a special case of the K-matrix representation, with

$$K \sim \frac{1}{V} - \mathrm{Re}\left[L\right]. \tag{10.5}$$

Recalling that elastic unitarity (2.16) is equivalent to the amplitude taking on the form of a K-matrix representation as shown in Sec. 2.1, we conclude that s-channel rescattering generates an amplitude that fulfills elastic unitarity. By inverting the line of thought, we see that each K-matrix representation at least correctly accounts for the imaginary part generated by s-channel rescattering, although of course to obtain the corresponding real part the correct K matrix needs to be picked. It is this argument that makes us identify pion rescattering in the s channel with elastic unitarity in the very same channel.

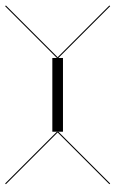

Figure 10.2: The two-pion propagator in the t channel.

Accordingly—keeping in mind its derivation in Sec. 4.2—the IAM accounts for pion rescattering in the s channel, where the K matrix has been approximated by ChPT truncated at either NLO or NNLO. In this regard, the unitarization can be interpreted as an approximated resummation of the perturbative expansion.

It is instructive to take a look at the crossed version of the two-pion propagator, see Fig. 10.2 for the t-channel one. This equals the Bethe–Salpeter kernel B introduced in Sec. 3.2.5, if contributions to the latter of the u channel and of higher-energetic intermediate states are ignored. If we replace the vertex V by the kernel B in Eq. (10.1), we will obtain the exact representation of the scattering amplitude $i\mathscr{M}$ as depicted in Fig. 3.2. The derivation of Eq. (10.4) still works out, in particular, B is real inside the elastic s-channel scattering region, but the real part, and thus the K matrix, becomes much more convoluted, because it describes more physics.

10.2 Rescattering and Khuri–Treiman equations

We are now ready for a better understanding of the rescattering encoded in KT equations. For simplicity, we will focus on the process $\gamma^{(*)}\pi \to \pi\pi$, whose KT equations have been described in Sec. 7.2, but as alluded to ibidem, the KT framework is by no means restricted to this process. All the observations made here carry easily over to other processes in its application domain. The discussion in Sec. 7.2 makes it clear that the KT equations (7.56) are obtained by using elastic unitarity in all three kinematic channels, i.e., the s, t, and u channel. Following the line of thought of Sec. 10.1, this amounts to taking into account $\pi\pi$ rescattering in all three channels.[3] Accordingly, the KT equations amount to expanding the scattering amplitude in terms of the two-pion propagator as depicted in Fig. 10.3. Note that certain box-like topologies, e.g., the one shown in Fig. 10.4, are not included in KT equations, because here we encounter four-pion intermediate states, but the employed unitarity relation (7.31) incorporates only two-pion states.

The KT equations can be analytically continued into the decay region, i.e., we can make explicit use of crossing symmetry. How to do so is discussed in detail in Ch. 11, qualitatively, the implications of this continuation can be completely understood on a diagrammatic basis by simply performing the crossing in all diagrams of Fig. 10.3, obtaining the outcome visualized in Fig. 10.5. Remarkably, there emerge contributions with three intermediate pions, as indicated by the dashed line in Fig. 10.5. That is, the basis functions $\mathscr{B}_k$ of the KT equations in the decay region partly encode three-pion rescattering, where one pion always spectates the other two pions interacting tightly [190]. This description of three-pion rescattering is incomplete, since contributions where all three pions interact simultaneously as depicted in Fig. 10.6 are not accounted for. These are to

[3]Contrarily to the IAM, the approximation being made is not the truncation of ChPT but the truncation of the partial-wave expansion, see Eq. (7.44).

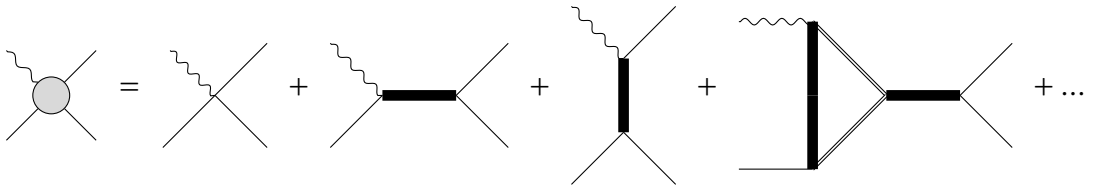

Figure 10.3: A diagrammatic representation of the contributions to $\gamma^{(*)}\pi \to \pi\pi$ that are included in the KT equations. For ease of visualization, we do not depict the u-channel contributions.

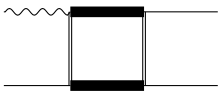

Figure 10.4: A box-like topology that is not included in the KT equations.

be parametrized by the subtraction functions c_k.

As two-pion rescattering and two-body unitary are linked, so are three-pion rescattering and three-body unitarity, i.e., the unitarity relation of $\pi\pi\pi \to \pi\pi\pi$ that is obtained by restricting the attention to $\pi\pi\pi$ intermediate states. Due to the connectedness structure of the S matrix [11, Ch. 4.3] this unitarity relation contains contributions where two pions interact and the other is an observer as well as contributions where all three pions interact closely [23, Ch. 4.2]. We have seen that the former are encoded in the KT basis functions. Hence, the basis functions on their own satisfy three-body unitarity partly, if properly continued into the decay region [200]. The incorporation of full three-body unitarity into KT equations remains a subject of research [219]. For a general overview about the subject, we refer the reader to Ref. [220] and mention in passing that three-body unitarity is also a useful tool in the discussion of three-particle scattering on the lattice [221].

Now let us turn our attention towards the relation between the KT basis functions (7.56) and the Omnès function (7.58). The latter satisfies the elastic unitarity condition of the pion vector form factor (see, e.g., Ref. [190] for a pedagogical derivation), and so it describes the rescattering of two pions in a P wave. Thus, if we replace $\mathscr{B}_k$ by $s^k\Omega(s)$, that is, ignore the contributions of the hat function $\widehat{\mathscr{B}}_k$ in the KT equations (7.56), we effectively ignore the last diagram in Fig. 10.3 (and Fig. 10.5) and all similar contributions. These are precisely the contributions called mixed rescat-

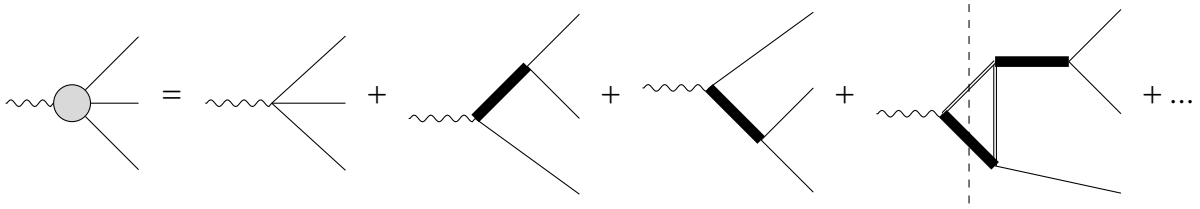

Figure 10.5: The KT equations in the decay region. Each diagram is obtained by crossing the corresponding one in Fig. 10.3. See also Fig. 2.2 in Ref. [190].

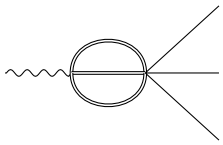

Figure 10.6: Genuine three-pion scattering that is not described by the KT basis functions.

tering in Sec. 7.2.2. That is, as claimed ibidem, ignoring the hat function amounts to focusing on $\pi\pi$ rescattering in individual kinematic channels only. Naturally, the question arises how important the mixed rescattering is, i.e., if its effects are visible in scattering or decay data. The results of Part III show that this is not the case for the $\gamma^{(*)}\pi \to \pi\pi$ lattice data, which comes at no surprise given the large error of the data. Moreover, as discussed in Ch. 1, depending on the process and dataset, mixed rescattering becomes visible in experiments or remains unseen. Hence, we aim to develop a method to assess the size of mixed rescattering in a given decay channel. Before doing so, we discuss the KT framework in greater detail.

Chapter 11

Gasser–Rusetsky method for Khuri–Treiman equations

In this chapter, we tie up loose ends. Namely, we finally discuss the analytic continuation of KT equations into the decay region. Moreover, we explain how to solve the KT equations numerically, which needs to be done, e.g., in the analysis described in Part III. To that end, we discuss a modified form of the method presented in Ref. [199]. This method performs the analytic continuation via a deformation of the contour of integration associated with Mandelstam *s*. There is an alternative approach [198], which deforms the contour of integration of the $z^\star$ integral; however, this approach is more cumbersome. Nevertheless, it has been applied frequently with great success, e.g., in Refs. [51, 70, 222].

11.1 General Khuri–Treiman problem

In the following, scattering of the form $\mathscr{P}_1(p_1) + \mathscr{P}_2(p_2) \to \mathscr{P}_3(p_3) + \mathscr{P}_4(p_4)$ as well as decays $\mathscr{P}_1(p_1) \to \mathscr{P}_2(p_2) + \mathscr{P}_3(p_3) + \mathscr{P}_4(p_4)$ are investigated; both processes are related via crossing symmetry. Here, as in Ch. 2, $\mathscr{P}_i$ labels a particle and p_i its four-momentum. The squared momenta $p_i^2 =: m_i^2$ are in general independent free variables and might be space-, time-, or lightlike. Hence, almost all equations given in the following depend also on m_i^2; however, this dependence is often not displayed explicitly. If one of the particles is heavy enough to decay into the other three, without loss of generality this will always be $\mathscr{P}_1$.

The KT approach starts with the derivation of the reconstruction theorem for the scattering process at hand, like it has been done for $\gamma^{(*)}\pi \to \pi\pi$ in Sec. 7.2.1. Even if one is interested merely in the decay, the investigation starts with the scattering. As a result of the reconstruction theorem, one obtains a set $\{\mathscr{B}_\mathscr{J}\}_{\mathscr{J}\in\mathbb{I}}$. Here the index set $\mathbb{I}$ labels the different single-variable functions $\mathscr{B}_\mathscr{J}$ that are determined by the following set of potentially coupled integral equations, each in the form of an inhomogeneous Omnès problem:

$$\begin{aligned}
\mathscr{B}_\mathscr{J}(s) &= \Omega_\mathscr{J}(s)\left[P_\mathscr{J}(s) + \frac{s^{n_\mathscr{J}}}{\pi}\int\limits_{s_\mathscr{J}^{\text{thr}}}^{\infty} \frac{\widehat{\mathscr{B}}_\mathscr{J}(x)\sin\left[\delta_\mathscr{J}(x)\right]}{\left|\Omega_\mathscr{J}(x)\right|(x-s)\,x^{n_\mathscr{J}}}\mathrm{d}x\right], \\
\widehat{\mathscr{B}}_\mathscr{J}(x) &\coloneqq \sum_{\mathscr{J}\in\mathbb{I}}\sum_{m\in\mathbb{N}_0} C^m_{\mathscr{J}\mathscr{J}}(x)\left\langle z^{\star m}\mathscr{B}_\mathscr{J}\right\rangle(x).
\end{aligned} \tag{11.1}$$

The $C^m_{\mathcal{J}\mathcal{J}}$ are known analytic functions (that typically contain a combination of rational functions and square roots),

$$\left\langle z^{\star m}\mathscr{B}_{\mathcal{J}}\right\rangle(x) \coloneqq \frac{1}{2}\int_{-1}^{1} z^{\star m}\overline{\mathscr{B}}_{\mathcal{J}}(x,z^\star)\,\mathrm{d}z^\star, \tag{11.2}$$

and depending on the index $\mathcal{J}$ and the problem at hand either

$$\overline{\mathscr{B}}_{\mathcal{J}}(x,z^\star) \coloneqq \mathscr{B}_{\mathcal{J}}(t(x,z^\star)) \tag{11.3}$$

or

$$\overline{\mathscr{B}}_{\mathcal{J}}(x,z^\star) \coloneqq \frac{1}{2}\left[\mathscr{B}_{\mathcal{J}}(s(x,z^\star)) + \mathscr{B}_{\mathcal{J}}(u(x,z^\star))\right] \tag{11.4}$$

or something similar. In addition,

$$\Omega_{\mathcal{J}}(s) \coloneqq \exp\left[\frac{s}{\pi}\int_{s^{\mathrm{thr}}_{\mathcal{J}}}^{\infty}\frac{\delta_{\mathcal{J}}(x)}{x(x-s)}\mathrm{d}x\right] \tag{11.5}$$

is the Omnès function, see Eq. (7.58), and $P_{\mathcal{J}}(s)$ a polynomial of degree $n_{\mathcal{J}}-1$. In case of $\gamma^{(*)}\pi\to\pi\pi$, there is only a single function $\mathscr{B}$, which is why we omitted the index in its discussion. Due to the linearity of the equations the problem reduces to compute the basis functions

$$\mathscr{B}^k_{\mathcal{J}}(s) = \Omega_{\mathcal{J}}(s)\left[s^k + \frac{s^{n_{\mathcal{J}}}}{\pi}\int_{s^{\mathrm{thr}}_{\mathcal{J}}}^{\infty}\frac{\widehat{\mathscr{B}}^k_{\mathcal{J}}(x)\sin\left[\delta_{\mathcal{J}}(x)\right]}{\left|\Omega_{\mathcal{J}}(x)\right|(x-s)\,x^{n_{\mathcal{J}}}}\mathrm{d}x\right] \tag{11.6}$$

for all $\mathcal{J}\in\mathbb{I}$ and all non-negative integers $k<n_{\mathcal{J}}$. Since Eq. (11.6) is just a special case of Eq. (11.1), in the following the latter is discussed.

Clearly,

$$\frac{\widehat{\mathscr{B}}_{\mathcal{J}}(x)\sin\left[\delta_{\mathcal{J}}(x)\right]}{\left|\Omega_{\mathcal{J}}(x)\right|} = \frac{\widehat{\mathscr{B}}_{\mathcal{J}}(x)\sin\left[\delta_{\mathcal{J}}(x)\right]\sigma_{\mathcal{J}}(x)e^{i\delta_{\mathcal{J}}(x)}}{\left|\Omega_{\mathcal{J}}(x)\right|\sigma_{\mathcal{J}}(x)e^{i\delta_{\mathcal{J}}(x)}} = \sigma_{\mathcal{J}}(x)\,\widehat{\mathscr{B}}_{\mathcal{J}}(x)\,\frac{T_{\mathcal{J}}(x)}{\Omega_{\mathcal{J}}(x)}, \tag{11.7}$$

with

$$T_{\mathcal{J}}(x) = \frac{\sin\left[\delta_{\mathcal{J}}(x)\right]e^{i\delta_{\mathcal{J}}(x)}}{\sigma_{\mathcal{J}}(x)} \tag{11.8}$$

the partial wave for the process at hand and $\sigma_{\mathcal{J}}$ the corresponding two-body phase space, see Eq. (2.19). Inserting this into Eq. (11.1) results in

$$\mathscr{B}_{\mathcal{J}}(s) = \Omega_{\mathcal{J}}(s)\,P_{\mathcal{J}}(s) + \sum_{\mathcal{J}\in\mathbb{I}}\int_{s^{\mathrm{thr}}_{\mathcal{J}}}^{\infty}\int_{-1}^{1} K_{\mathcal{J}\mathcal{J}}(s,x,z^\star)\,\overline{\mathscr{B}}_{\mathcal{J}}(x,z^\star)\,\mathrm{d}z^\star\mathrm{d}x \tag{11.9}$$

with the kernel

$$K_{\mathcal{J}\mathcal{J}}(s,x,z^\star) \coloneqq \Omega_{\mathcal{J}}(s)\left(\frac{s}{x}\right)^{n_{\mathcal{J}}}\frac{1}{x-s}\frac{T_{\mathcal{J}}(x)}{\Omega_{\mathcal{J}}(x)}\sigma_{\mathcal{J}}(x)\sum_m\frac{z^{\star m}}{2}C^m_{\mathcal{J}\mathcal{J}}(x)\,. \tag{11.10}$$

It is worth noting that $T_{\mathcal{J}}/\Omega_{\mathcal{J}}$ does not have a right-hand cut, since for values of x along this cut

$$\begin{aligned}\operatorname{disc}_x\left[\frac{T_{\mathcal{J}}(x)}{\Omega_{\mathcal{J}}(x)}\right] &= 2i\,\mathrm{Im}\left[\frac{T_{\mathcal{J}}(x_+)}{\Omega_{\mathcal{J}}(x_+)}\right] \\ &= 2i\,\mathrm{Im}\left[\frac{T_{\mathcal{J}}(x_+)\,\Omega_{\mathcal{J}}(x_+)^*}{\Omega_{\mathcal{J}}(x_+)\,\Omega_{\mathcal{J}}(x_+)^*}\right] \\ &= \frac{2i}{\left|\Omega_{\mathcal{J}}(x_+)\right|^2}\mathrm{Im}\left[\left|T_{\mathcal{J}}(x_+)\right| e^{i\delta_{\mathcal{J}}(x)}\left|\Omega_{\mathcal{J}}(x_+)\right| e^{-i\delta_{\mathcal{J}}(x)}\right] \\ &= 0\end{aligned} \tag{11.11}$$

holds.

Eq. (11.9) is well-defined only inside a particular kinematic region defined by certain values of m_i^2. To evaluate it, e.g., for $m_1 > m_2+m_3+m_4$, i.e., when a decay is possible, it needs to be analytically continued via deformation of the contours of integration. To that end, the analytic structure of the integrand in Eq. (11.9) parametrized by the external masses needs to be understood. The kernel Eq. (11.10) inherits a left-hand cut in x from $T_{\mathcal{J}}(x)$ and a right-hand cut in s from $\Omega_{\mathcal{J}}(s)$. Apart from that its non-trivial analytic structure in x and s is determined by known analytic expressions (i.e. the Cauchy kernel, the phase space, and $C^m_{\mathcal{J}\mathcal{J}}$). In addition, it is a polynomial in $z^\star$.

Apart from the kernel, singularities also arise if in the computation of $\overline{\mathscr{B}}_{\mathcal{J}}$ the function $\mathscr{B}_{\mathcal{J}}$ is evaluated at its branch point located at $s^{\mathrm{thr}}_{\mathcal{J}}$. That is, if

$$t(x, z^\star) = s^{\mathrm{thr}}_{\mathcal{J}} \tag{11.12}$$

(or a similar relation for $s(x, z^\star)$ and/or $u(x, z^\star)$) holds. The explicit expressions relating the Mandelstam variables read

$$t = \frac{R-s}{2} - \frac{\left(m_1^2-m_2^2\right)\left(m_3^2-m_4^2\right)}{2s} + \frac{\sqrt{\lambda\left(s,m_1^2,m_2^2\right)\lambda\left(s,m_3^2,m_4^2\right)}}{2s}z^\star \tag{11.13}$$

and

$$u = \frac{R-s}{2} + \frac{\left(m_1^2-m_2^2\right)\left(m_3^2-m_4^2\right)}{2s} - \frac{\sqrt{\lambda\left(s,m_1^2,m_2^2\right)\lambda\left(s,m_3^2,m_4^2\right)}}{2s}z^\star. \tag{11.14}$$

Here, as before, $z^\star = \cos(\theta^\star)$, with $\theta^\star = \sphericalangle(\boldsymbol{p}_1^\star, \boldsymbol{p}_3^\star)$ the scattering angle in the s channel, $R = \sum_i m_i^2$, and λ is the Källén function. So u can be obtained from t by replacing $z^\star$ by $-z^\star$ and interchanging m_1^2 and m_2^2 (or alternatively m_3^2 and m_4^2).

Inserting Eq. (11.13) into Eq. (11.12) results in

$$\sum_{i=0}^{4} c_i\left(z^{\star\,2}\right)x^i = 0, \tag{11.15}$$

with

$$
\begin{aligned}
c_0\left(z^{\star\,2}\right) &\coloneqq \left(z^{\star\,2}-1\right)\left(m_1^2-m_2^2\right)^2\left(m_3^2-m_4^2\right)^2,\\
c_1\left(z^{\star\,2}\right) &\coloneqq 2\left(m_1^2-m_2^2\right)\left(m_3^2-m_4^2\right)\left(R-2s_{\mathcal{J}}^{\mathrm{thr}}\right)\\
&\quad -2z^{\star\,2}\left(\left(m_1^2+m_2^2\right)\left(m_3^2-m_4^2\right)^2+\left(m_1^2-m_2^2\right)^2\left(m_3^2+m_4^2\right)\right),\\
c_2\left(z^{\star\,2}\right) &\coloneqq z^{\star\,2}\left(\left(m_1^2-m_2^2\right)^2+\left(m_3^2-m_4^2\right)^2+4\left(m_1^2+m_2^2\right)\left(m_3^2+m_4^2\right)\right)\\
&\quad -R^2+4s_{\mathcal{J}}^{\mathrm{thr}}\left(R-s_{\mathcal{J}}^{\mathrm{thr}}\right)-2\left(m_1^2-m_2^2\right)\left(m_3^2-m_4^2\right),\\
c_3\left(z^{\star\,2}\right) &\coloneqq 2R\left(1-z^{\star\,2}\right)-4s_{\mathcal{J}}^{\mathrm{thr}},\\
c_4\left(z^{\star\,2}\right) &\coloneqq z^{\star\,2}-1.
\end{aligned}
\tag{11.16}
$$

Since the coefficients c_i depend on $z^{\star\,2}$ and not $z^\star$, the corresponding equations for $u(x,z^\star)=s_{\mathcal{J}}^{\mathrm{thr}}$ or $s(x,z^\star)=s_{\mathcal{J}}^{\mathrm{thr}}$ can be obtained by interchanging the appropriate pair of masses (e.g., $m_3^2\leftrightarrow m_4^2$ to obtain the coefficients for $u(x,z^\star)=s_{\mathcal{J}}^{\mathrm{thr}}$). Eq. (11.15) is a quadratic equation in $z^\star$, and thus the singularities in the complex $z^\star$ plane as a function of x can be obtained in closed analytic form by solving Eq. (11.15) for $z^\star$. Alternatively, Eq. (11.15) can be solved in closed analytic form to obtain the singularities in the complex x plane as a function of $z^\star$, since the equation is quartic in x and solutions to quartic equations can still be given in closed analytic form.

It is worth noting that Eq. (11.16) simplifies considerably as soon as either $m_1^2=m_2^2$ or $m_3^2=m_4^2$. Since the general solution is lengthy, we discuss separately two simpler, but highly relevant, cases.

11.1.1 Special case: four particles of equal mass

First consider the simple case $m_1=m_2=m_3=m_4=:m$ and $s_{\mathcal{J}}^{\mathrm{thr}}=4m^2$ to understand the general procedure. This case corresponds, e.g., to the scattering process $\pi\pi\to\pi\pi$, if only $\pi\pi$ intermediate states are taken into account, with the corresponding KT equations being discussed in Ref. [223]. The singularities $z_{\mathrm{sing}}^\star$ in $z^\star$ are determined by

$$
z_{\mathrm{sing}}^{\star\,2}=\left(\frac{x+4m^2}{x-4m^2}\right)^2. \tag{11.17}
$$

Hence, if the contour of integration in x remains unchanged, i.e. $x\in[4m^2,\infty)$, the singular values of $z^\star$ are $z_{\mathrm{sing}}^\star\in(-\infty,-1)\cup(1,\infty)$. Thus, the original contour of integration in $z^\star$, namely $z^\star\in[-1,1]$, does not interfere with the singular region in the $z^\star$ plane, so that no deformation of contours is necessary. The same result can be obtained by solving for x instead of $z^\star$. If $z^{\star\,2}=1$, the singularity in x is at $x_{\mathrm{sing}}=0$, otherwise it is determined by

$$
x_{\mathrm{sing}}=4m^2\left[\pm\sqrt{f\left(z^{\star\,2}\right)^2-1}-f\left(z^{\star\,2}\right)\right],\qquad f\left(z^{\star\,2}\right)=\frac{1+z^{\star\,2}}{1-z^{\star\,2}}. \tag{11.18}
$$

Hence, $x_{\mathrm{sing}}\in(-\infty,0]$ for $z^\star\in[-1,1]$, that is, the original contours of integration are fine as expected.

11.1.2 Special case: identical masses in the final state of the decay

Consider now the special case with $m_1 \equiv M$ and $m_2 = m_3 = m_4 =: m$ as well as $s_{\mathcal{J}}^{\text{thr}} = 4m^2$. That is, the aim is to develop an understanding of the singularities in the decay of one particle into three particles of equal mass, where the intermediate two-particle states consist of particles of the same species as the ones in the decay product. In this case, Eq. (11.15) and Eq. (11.16) simplify to

$$\begin{aligned} 0 =& x^3\left[z^{\star 2}-1\right] + 2x^2\left[\left(M^2-5m^2\right) - z^{\star 2}R\right] \\ &+ x\left[z^{\star 2}R^2 - \left(M^2-5m^2\right)^2\right] - 4z^{\star 2}m^2\left(M^2-m^2\right)^2 . \end{aligned} \tag{11.19}$$

Solving for $z^{\star 2}$ yields

$$z_{\text{sing}}^{\star 2} = \frac{x\left(5m^2-M^2+x\right)^2}{\left(x-4m^2\right)\left[x^2-2x\left(M^2+m^2\right)+\left(M^2-m^2\right)^2\right]}. \tag{11.20}$$

The original path of integration in the $z^\star$ plane extends from -1 to 1, i.e. it covers the interval $[0,1]$ on the real axis in the $z^{\star 2}$ plane. Solving Eq. (11.19) for x with $z_{\text{sing}}^{\star 2} \in \{0,1\}$ fixed results in[1]

$$\begin{aligned} z_{\text{sing}}^{\star 2} = 0 \quad &\Leftrightarrow \quad x_{\text{sing}} \in \left\{0, M^2-5m^2\right\}, \\ z_{\text{sing}}^{\star 2} = 1 \quad &\Leftrightarrow \quad x_{\text{sing}} = \frac{M^2-m^2}{2}. \end{aligned} \tag{11.21}$$

Moreover,

$$\lim_{x\to\infty} z_{\text{sing}}^{\star 2} = 1. \tag{11.22}$$

Again, the original path of integration in the x plane extends along $[4m^2,\infty)$. As long as $M^2 < 9m^2$, that is as long as the decay is kinematically forbidden, the singularities Eq. (11.21) stay below $4m^2$, and thus they do not interfere with the original path of integration. However, as soon as $M^2 \geq 9m^2$, both $M^2-5m^2 \geq 4m^2$ and $(M^2-m^2)/2 \geq 4m^2$. That is, the original path of integration fails to work inside the decay region. Another special point at which significant simplifications arise is $M^2 = 9m^2$, that is the boundary of the decay region (in M^2). In this case Eq. (11.19) boils down to

$$0 = \left(x-4m^2\right)^2\left[x\left(z^{\star 2}-1\right) - 16m^2 z^{\star 2}\right], \tag{11.23}$$

which is solved by

$$x_{\text{sing}} \in \left\{4m^2, -16m^2\frac{z^{\star 2}}{1-z^{\star 2}}\right\}. \tag{11.24}$$

The second solution is non-positive for $z^{\star 2} \in [0,1)$, but the first one interferes directly with the lower limit of integration in x, pointing again to the fact that the original contours of integration fail to work as soon as the decay is kinematically allowed.

The correct way to circumvent this problem is to analytically continue Eq. (11.9) as a function of M^2 via a deformation of the contours of integration. There are different ways to perform this continuation, since there are two integrals, both of which can be deformed. Here, the choice is made to keep the contour of integration in $z^\star$, i.e. $z^\star \in [-1,1]$, while distorting the contour of

[1] Note that in both cases Eq. (11.19) boils down to a quadratic equation in x.

integration in x. Hence, in the following the singularities in the x plane as a function of $z^{\star 2} \in [0,1]$ are studied.

The endpoints $x_{\text{sing}}(z^{\star 2} = 0)$ and $x_{\text{sing}}(z^{\star 2} = 1)$ are given by Eq. (11.21). In addition, the singularities $x_{\text{sing}}(z^{\star 2})$ for $z^{\star 2} \in (0,1)$ are obtained by solving the in this case cubic Eq. (11.19). This can be done, e.g., using CARDANO's formula.

To be precise, denote an n-th root of unity by

$$\xi_n := \exp\left[\frac{2\pi i}{n}\right], \qquad \xi_n^n = 1. \tag{11.25}$$

Furthermore, for arbitrary $\zeta \in \mathbb{C}$, define the principal value of the n-th root as

$$\zeta^{1/n} := \exp\left[\frac{1}{n}\ln(\zeta)\right]. \tag{11.26}$$

Here $\ln(\zeta) = \ln(|\zeta|) + i\arg(\zeta)$ denotes the principal branch of the logarithm, with a cut along $(-\infty, 0]$. The value of the n-th root on its other $n-1$ RIEMANN sheets is accordingly given as

$$\exp\left[\frac{1}{n}(\ln(\zeta) + r2\pi i)\right] = \exp\left[\frac{1}{n}\ln(\zeta)\right]\exp\left[\frac{r2\pi i}{n}\right] = \zeta^{1/n}\xi_n^r, \tag{11.27}$$

with $r \in 1, \ldots, n-1$. In the special case of a cube root,

$$\xi_3 = \frac{-1 + i\sqrt{3}}{2}, \qquad \xi_3^2 = \xi_3^* \tag{11.28}$$

hold.

Now consider the equation

$$\sum_{i=0}^{3} c_i x^i = 0, \tag{11.29}$$

where the coefficients c_i in the case of interest are fixed via comparision with Eq. (11.19). The solutions of Eq. (11.29) read [224, 225]

$$x_{\text{sing},k} = -\frac{1}{3c_3}\left[c_2 + \xi_3^k\Delta_\pm + \frac{\Delta_0}{\xi_3^k\Delta_\pm}\right], \qquad k \in \{0,1,2\}. \tag{11.30}$$

Here

$$\begin{aligned} \Delta_0 &:= c_2^2 - 3c_3c_1, \\ \Delta_1 &:= 2c_2^3 - 9c_3c_2c_1 + 27c_3^2c_0, \\ \Delta_\pm &:= \left(\frac{\Delta_1 \pm \sqrt{\Delta_1^2 - 4\Delta_0^3}}{2}\right)^{1/3}, \end{aligned} \tag{11.31}$$

where the choice of the sign in $\Delta_\pm$ is arbitrary—according to Eq. (11.27) it merely corresponds to a change of the sheet of the square root—as long as $\Delta_\pm \neq 0$. However, if it equals 0 for one choice of the sign, the other one is to be picked. Note that due to Eq. (11.27) the different solutions correspond to different choices of the RIEMANN sheet of the cube root in $\Delta_\pm$.

In the following, consider arbitrary $M^2, m \in \mathbb{R}$ and $z^{\star 2} \in (0,1)$. Thus, in the case of interest $c_i, \Delta_0, \Delta_1 \in \mathbb{R}$. Moreover, $\xi_3\Delta_\pm$ is real for $M^2 > 9m^2$. Hence, $x_{\text{sing},1} \in \mathbb{R}$, moreover, $x_{\text{sing},0} = x_{\text{sing},2}^*$ due to Eq. (11.28):

$$\Delta_\pm = \xi_3^3\Delta_\pm = \xi_3^2\xi_3\Delta_\pm = \xi_3^*\xi_3\Delta_\pm = (\xi_3\xi_3\Delta_\pm)^*. \tag{11.32}$$

The singularities $x_{\text{sing},k}$ for $k = 0, 1, 2$ are plotted in the x plane for all values of $z^{\star 2} \in [0, 1]$ and for different values of M^2 in Fig. 11.1. Independently of the value of M^2, the negative real axis is always singular. Moreover, it is the only singular region as long as M^2 is non-positive. As soon as $M^2 > 0$, a structure symmetric around the real axis starts to form, which in the beginning is connected to the negative real axis. A further increase in M^2 results in a detachment of this structure from the negative real axis, it moves steadily towards the branch point at $4m^2$. To be precise, as soon as it detaches from the negative real axis at $M^2 = 5m^2$ the structure is given as

$$\mathbb{S} := \left\{ x_{\text{sing},k} \,:\, k \in \{0, 2\} \text{ and } z^{\star 2} \in (0, 1) \right\} \cup \left\{ M^2 - 5m^2, \frac{M^2 - m^2}{2} \right\}. \tag{11.33}$$

Here the two elements given at the end correspond to Eq. (11.21). When M^2 reaches the decay threshold, i.e. $M^2 = 9m^2$, $\mathbb{S}$ collapses to a single point at exactly the branch point $4m^2$. For $M^2 > 9m^2$, $\mathbb{S}$ emerges again; it moves along the real axis to the right and increases in size with increasing M^2. Moreover,

$$\begin{aligned} \max\{\mathrm{Re}\,(y) \,:\, y \in \mathbb{S}\} &= \begin{cases} \frac{M^2-m^2}{2}, & M^2 < 9m^2, \\ M^2 - 5m^2, & M^2 > 9m^2, \end{cases} \\ \min\{\mathrm{Re}\,(y) \,:\, y \in \mathbb{S}\} &= \begin{cases} M^2 - 5m^2, & M^2 < 9m^2, \\ \frac{M^2-m^2}{2}, & M^2 > 9m^2 \end{cases} \end{aligned} \tag{11.34}$$

holds.

The problem is not only that for $M^2 > 9m^2$ the singularities interfere with the original path of integration, but also that at $M^2 = 9m^2$ they hit the branch point, which marks the beginning of the path of integration. Since the endpoints of an integration contour are fixed, this is a serious obstacle for any analytic continuation.

The way out is to equip M^2 with a small, positive imaginary part, that is, to perform the replacement $M^2 \mapsto M^2 + i\epsilon$ with $\epsilon > 0$, and consider the limit $\epsilon \searrow 0$ in the end. This does not alter the singularities depicted in Fig. 11.1 in any significant[2] way except for the location of $\mathbb{S}$ at $M^2 = 9m^2$: instead of $\mathbb{S}|_{M^2=9m^2} = \{4m^2\}$ now $\mathbb{S}|_{M^2=9m^2+i\epsilon} = \{4m^2 + i\epsilon\}$ holds. That is, the singularities do not hit the branch point.

To understand how the contour of integration in the x plane needs to be deformed, start with Eq. (11.9) for $M^2 < 9m^2$, where the original contour $[4m^2, \infty)$ is fine. Now increase M^2 continuously, while sticking to the $+i\epsilon$ prescription. At $M^2 = 9m^2$ the singularity structure $\mathbb{S}$ passes by the start of the integration contour above the real axis, for larger values of M^2 the structure $\mathbb{S}$ grows in size. Hence, to avoid any collision of the contour with $\mathbb{S}$, the contour needs to be deformed into the lower half plane. This is illustrated in Fig. 11.2 for $M^2 = 12m^2$. Note that the depicted choice of the deformed path, denoted $\mathcal{C}$, is just one possible choice out of many. Any path that starts at $4m^2$, extends towards infinity, and avoids the singularities via bending into the lower half plane is legitimate.

[2]For $M^2 \neq 9m^2$ there is no change in $\mathbb{S}$, since the limit $\epsilon \searrow 0$ can be performed without running into any problems. However, for $\epsilon \neq 0$ the parts of $\mathbb{S}$ that are traced out by $x_{\text{sing},0}$ and $x_{\text{sing},2}$ are partly interchanged, due to the branch cuts of the roots appearing in Eq. (11.31).

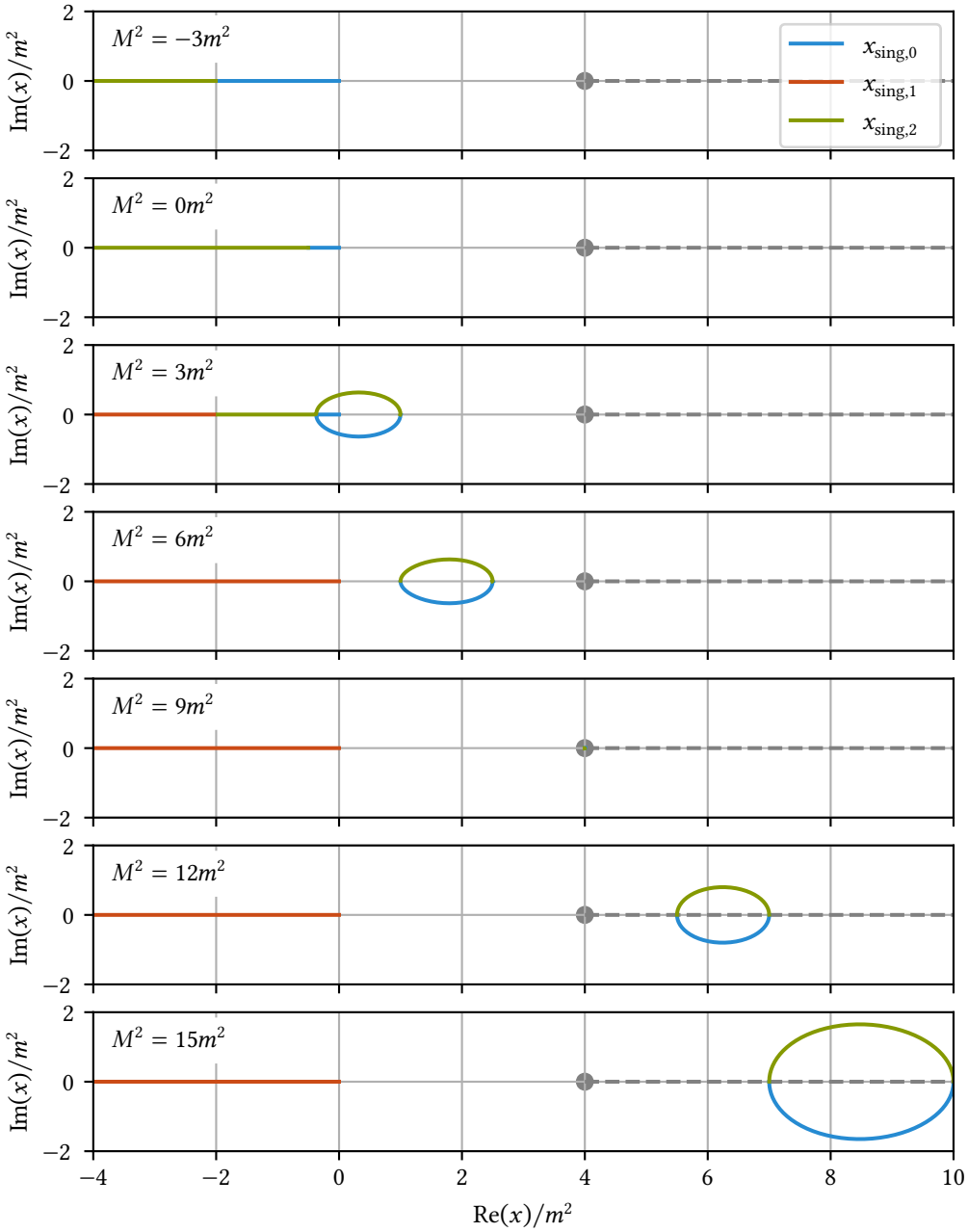

Figure 11.1: The singularities for different values of M^2. The gray blob denotes the branch point at $4m^2$, while the original path of integration is represented by the dotted gray line. At $M^2 = 9m^2$ the singularities $x_{\text{sing},0}$ and $x_{\text{sing},2}$ shrink down to a point located exactly at the branch point $4m^2$.

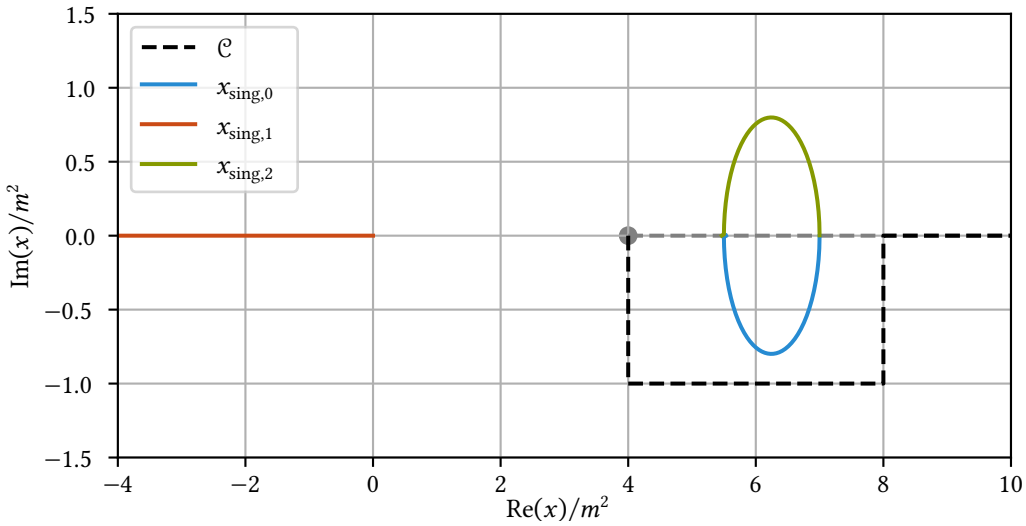

Figure 11.2: The singularities for $M^2 = 12m^2$ as well as the deformed contour of integration, denoted by $\mathcal{C}$. As before the gray blob represents the branch point at $4m^2$, while the original path of integration is depicted as a dotted gray line.

11.2 Final form of the Khuri–Treiman equations

The KT equations in their final form arise if the outer path of integration in Eq. (11.9) is deformed as discussed leading to

$$\mathcal{B}_{\mathcal{J}}(s) = \Omega_{\mathcal{J}}(s)\, P_{\mathcal{J}}(s) + \sum_{\mathcal{J}\in\mathbb{I}} \int_{\mathcal{C}_{\mathcal{J}}} \int_{-1}^{1} K_{\mathcal{J}\mathcal{J}}(s,\zeta,z^\star)\, \overline{\mathcal{B}}_{\mathcal{J}}(\zeta,z^\star)\, \mathrm{d}z^\star \mathrm{d}\zeta, \tag{11.35}$$

with $\mathcal{C}_{\mathcal{J}}$ the appropriately deformed contour of integration of the $\mathcal{J}$-th single-variable function. The branch cut of the $\mathcal{J}$-th integral in Eq. (11.35) is generated by the Cauchy kernel $1/(x-s)$ in Eq. (11.10), and thus it runs along $\mathcal{C}_{\mathcal{J}}$. To avoid having multiple inconsistent cuts in Eq. (11.35), it is necessary to choose overlapping contours of integration for all $\mathcal{J} \in \mathbb{I}$ that contribute to a given $\mathcal{B}_{\mathcal{J}}$, i.e., there must exist a path $\mathcal{G}_{\mathcal{J}}$, such that $\mathcal{C}_{\mathcal{J}} \subseteq \mathcal{G}_{\mathcal{J}}$ for all $\mathcal{J} \in \mathbb{I}$ that yield $K_{\mathcal{J}\mathcal{J}} \neq 0$. For notational simplicity, we make a global choice, i.e., $\mathcal{C}_{\mathcal{J}} = \mathcal{C}$ for all $\mathcal{J} \in \mathbb{I}$.[3] Clearly, this $\mathcal{C}$ needs to be chosen such that it avoids the singularities in all the $|\mathbb{I}|$ integrals. Furthermore, note that the Omnès function as given in Eq. (11.5) has a branch cut along $[s_{\mathcal{J}}^{\text{thr}}, \infty)$. Both the first term in Eq. (11.35) as well as the kernel $K_{\mathcal{J}\mathcal{J}}$ inherit this cut, which is undesirable for the cut arising from the integration in the second term runs along $\mathcal{C}$, again leading to inconsistent cuts. To avoid these troubles, we continue the Omnès function analytically to its second Riemann sheet. Proceeding

[3] In certain cases where the thresholds $s_{\mathcal{J}}^{\text{thr}}$ differ, a single global choice does not work. This is not an issue, merely enforces the replacement of $\mathcal{C}$ by $\mathcal{C}_{\mathcal{J}}$ in the following equations.

along the lines of the discussion in Sec. 2.2 and borrowing the notation used ibidem we obtain

$$\begin{aligned}\Omega_{\mathcal{J}}(s_+) - \Omega_{\mathcal{J}}(s_-) &= |\Omega_{\mathcal{J}}(s)| \left(e^{i\delta_{\mathcal{J}}(s)} - e^{-i\delta_{\mathcal{J}}(s)}\right) \\ &= 2i\,|\Omega_{\mathcal{J}}(s)| \sin\left[\delta_{\mathcal{J}}(s)\right] \\ &= 2i\Omega_{\mathcal{J}}(s_-)\,\sigma_{\mathcal{J}}(s_+)\,T_{\mathcal{J}}(s_+)\,,\end{aligned} \tag{11.36}$$

where we used $\arg[\Omega_{\mathcal{J}}(s_\pm)] = \pm\delta(s)$ as well as Eq. (11.8). From this we deduce that the Omnès function on its second Riemann sheet reads

$$\Omega^{\mathrm{II}}_{\mathcal{J}}(s) = \frac{\Omega_{\mathcal{J}}(s)}{1 + 2i\sigma_{\mathcal{J}}(s)\,T_{\mathcal{J}}(s)}. \tag{11.37}$$

We denote by $\tilde{\Omega}_{\mathcal{J}}$ the appropriate combination of $\Omega_{\mathcal{J}}$ and $\Omega^{\mathrm{II}}_{\mathcal{J}}$ that has a cut along $\mathcal{C}$. For example, in case of the scenario discussed in Sec. 11.1.1, $\tilde{\Omega}_{\mathcal{J}} = \Omega_{\mathcal{J}}$, while in the scenario outlined in Sec. 11.1.2, more specifically, the one depicted in Fig. 11.2,

$$\tilde{\Omega}_{\mathcal{J}}(s) \coloneqq \begin{cases}\Omega^{\mathrm{II}}_{\mathcal{J}}(s)\,, & \mathrm{Re}\,(s) \in [4m^2, 8m^2] \wedge \mathrm{Im}\,(s) \in \left[-m^2, 0\right], \\ \Omega_{\mathcal{J}}(s)\,, & \text{else.}\end{cases} \tag{11.38}$$

This choice is enforced by the analytic continuation in M^2 as shown in Fig. 11.1: for $M^2 < 9m^2$ the path of integration $\mathcal{C}_{\text{initial}}$ runs along $[4m^2, \infty)$, while for $M^2 > 9m^2$ it gets deformed into the contour $\mathcal{C}$, so clearly the part of the complex plain enclosed by $\mathcal{C} \cup \mathcal{C}_{\text{initial}}$ is associated with what was known previously as the second sheet. Accordingly, we replace $\Omega_{\mathcal{J}}(s)$ in the first term in Eq. (11.35) as well as in Eq. (11.10) by $\tilde{\Omega}_{\mathcal{J}}$. Note that we do not replace $\Omega_{\mathcal{J}}(x)$ in Eq. (11.10), for as discussed in Eq. (11.11) its cut is of no relevance. In this way all $\mathscr{B}_I$ have a single cut running along $\mathcal{C}$.

11.3 Numerical solution

To solve the KT equations (11.35), we rewrite them solely in terms of $\overline{\mathscr{B}}_{\mathcal{J}}$. If $\overline{\mathscr{B}}_{\mathcal{J}}$ is given as in Eq. (11.3), we merely evaluate Eq. (11.35) at $s \mapsto t(x', z^{\star\prime})$. If instead Eq. (11.4) applies, we evaluate Eq. (11.35) once at $s \mapsto s(x', z^{\star\prime})$ and once at $s \mapsto u(x', z^{\star\prime})$ and add the results. In this way we obtain

$$\overline{\mathscr{B}}_{\mathcal{J}}(x', z^{\star\prime}) = \overline{G}_{\mathcal{J}}(x', z^{\star\prime}) + \sum_{\mathcal{J}\in\mathbb{I}} \int_{\mathcal{C}} \int_{-1}^{1} \overline{K}_{\mathcal{J}\mathcal{J}}(x', z^{\star\prime}, \zeta, z^{\star})\, \overline{\mathscr{B}}_{\mathcal{J}}(\zeta, z^{\star})\, \mathrm{d}z^{\star} \mathrm{d}\zeta, \tag{11.39}$$

with $G_{\mathcal{J}}(s) \coloneqq \tilde{\Omega}_{\mathcal{J}}(s) P_{\mathcal{J}}(s)$ and the relation between $\overline{G}_{\mathcal{J}}$ and $G_{\mathcal{J}}$ (as well as the one between $\overline{K}_{\mathcal{J}\mathcal{J}}$ and $K_{\mathcal{J}\mathcal{J}}$) mimicking the one between $\overline{\mathscr{B}}_{\mathcal{J}}$ and $\mathscr{B}_{\mathcal{J}}$.

A priori, the path $\mathcal{C}$ extends towards infinity. However, in practice the scattering amplitudes $T_{\mathcal{J}}$ and the phases $\delta_{\mathcal{J}}$ are only known up to a certain energy $\sqrt{\lambda_{\mathcal{J}}}$, in addition, the contributions of the high-energy region to the integral are suppressed due to the powers of x in the denominator of Eq. (11.10). Moreover, while we need a holomorphic expression for $T_{\mathcal{J}}$ in the low-energy region (where the amplitudes are evaluated along segments of $\mathcal{C}$ that reach into the complex plane, see Fig. 11.2), in the high-energy region $T_{\mathcal{J}}$ is needed only along the real axis, that is, it is sufficient

to specify $\delta_{\mathcal{J}}$ along the real axis. If we let $\delta_{\mathcal{J}}$ approach an integer multiple of π at an energy $\sqrt{\Lambda_{\mathcal{J}}} > \sqrt{\lambda_{\mathcal{J}}}$, according to Eq. (11.8) the scattering amplitude vanishes for $s > \Lambda_{\mathcal{J}}$, and thus the integral along $\mathcal{C}$ is cut off at $\Lambda_{\mathcal{J}}$. Denote the phase in the low-energy region as before by $\delta_{\mathcal{J}}$. Our goal is to construct a phase $\Delta_{\mathcal{J}}^{(n)}$ that equals $\delta_{\mathcal{J}}$ in the low-energy region and equals $n\pi$, $n \in \mathbb{Z}$, for all $s \geq \Lambda_{\mathcal{J}}$. In addition, $\Delta_{\mathcal{J}}^{(n)}$ shall be one time continuously differentiable. This can be easily achieved via a polynomial $p_{\mathcal{J}}$ of degree three, i.e.,

$$\Delta_{\mathcal{J}}^{(n)}(s) \coloneqq \begin{cases} \delta_{\mathcal{J}}, & s \leq \lambda_{\mathcal{J}}, \\ p_{\mathcal{J}}(s), & \lambda_{\mathcal{J}} < s \leq \Lambda_{\mathcal{J}}, \\ n\pi, & \Lambda_{\mathcal{J}} < s, \end{cases} \tag{11.40}$$

with $p_{\mathcal{J}}(\lambda_{\mathcal{J}}) = \delta_{\mathcal{J}}(\lambda_{\mathcal{J}})$, $p_{\mathcal{J}}(\Lambda_{\mathcal{J}}) = n\pi$, $p'_{\mathcal{J}}(\lambda_{\mathcal{J}}) = \delta'_{\mathcal{J}}(\lambda_{\mathcal{J}})$, and $p'_{\mathcal{J}}(\Lambda_{\mathcal{J}}) = 0$. Recasting these conditions into a matrix equation for the coefficients of $p_{\mathcal{J}}$ results in

$$p_{\mathcal{J}}(s) = \begin{pmatrix} 1 & s & s^2 & s^3 \end{pmatrix} \begin{pmatrix} 1 & \lambda_{\mathcal{J}} & \lambda_{\mathcal{J}}^2 & \lambda_{\mathcal{J}}^3 \\ 1 & \Lambda_{\mathcal{J}} & \Lambda_{\mathcal{J}}^2 & \Lambda_{\mathcal{J}}^3 \\ 0 & 1 & 2\lambda_{\mathcal{J}} & 3\lambda_{\mathcal{J}}^2 \\ 0 & 1 & 2\Lambda_{\mathcal{J}} & 3\Lambda_{\mathcal{J}}^2 \end{pmatrix}^{-1} \begin{pmatrix} \delta_{\mathcal{J}}(\lambda_{\mathcal{J}}) \\ n\pi \\ \delta'_{\mathcal{J}}(\lambda_{\mathcal{J}}) \\ 0 \end{pmatrix}. \tag{11.41}$$

We stress that this is only one possibility to treat the phase at high energies that is particularly convenient, for it provides a natural cut-off at $\Lambda_{\mathcal{J}}$, with the drawback that depending on the behavior of $\delta_{\mathcal{J}}$ close to $\lambda_{\mathcal{J}}$ the polynomial might lead to undesired oscillations. Other choices are possible and feasible.

We compute the integral via Gauß–Legendre quadrature [169],

$$\overline{\mathcal{B}}_{\mathcal{J}}(x', z^{\star\prime}) = \overline{G}_{\mathcal{J}}(x', z^{\star\prime}) + \sum_{\mathcal{J}\in\mathbb{I}} \sum_{j,k} \overline{K}_{\mathcal{J}\mathcal{J}}\left(x', z^{\star\prime}, \mathcal{C}\left(x_j\right), z_k^\star\right) \overline{\mathcal{B}}_{\mathcal{J}}\left(\mathcal{C}\left(x_j\right), z_k^\star\right) \mathcal{C}'\left(x_j\right) w_j^x w_k^z, \tag{11.42}$$

where x_j, $z_k^\star$ are the sites of the quadrature, w_j^x the weights associated with the integration along $\mathcal{C}$ with curve parameter x, and w_j^z the weights associated with the integration over $z^\star$. At this stage, it becomes useful to introduce the shorthand notation

$$\begin{aligned} \mathbb{B}_{\mathcal{J}}^{jk} &\coloneqq \overline{\mathcal{B}}_{\mathcal{J}}\left(\mathcal{C}\left(x_j\right), z_k^\star\right), \\ \mathbb{G}_{\mathcal{J}}^{jk} &\coloneqq \overline{G}_{\mathcal{J}}\left(\mathcal{C}\left(x_j\right), z_k^\star\right), \\ \mathbb{K}_{\mathcal{J}\mathcal{J}}^{ab;jk} &\coloneqq \overline{K}_{\mathcal{J}\mathcal{J}}\left(\mathcal{C}\left(x_a\right), z_b^\star, \mathcal{C}\left(x_j\right), z_k^\star\right) \mathcal{C}'\left(x_j\right) w_j^x w_k^z. \end{aligned} \tag{11.43}$$

Equipped with these abbreviations, Eq. (11.42) evaluated at $x' = \mathcal{C}(x_a)$ and $z^{\star\prime} = z_b^\star$ can be written as

$$\mathbb{B}_{\mathcal{J}}^{ab} = \mathbb{G}_{\mathcal{J}}^{ab} + \sum_{\mathcal{J}\in\mathbb{I}} \sum_{j,k} \mathbb{K}_{\mathcal{J}\mathcal{J}}^{ab;jk} \mathbb{B}_{\mathcal{J}}^{jk}, \tag{11.44}$$

or, treating $(a, b, \mathcal{J})$ as a label of a component of a vector,

$$\mathbb{B} = \mathbb{G} + \mathbb{K}\mathbb{B}. \tag{11.45}$$

Solving Eq. (11.45) for $\mathbb{B}$ results in

$$\mathbb{B} = (1 - \mathbb{K})^{-1} \mathbb{G}. \tag{11.46}$$

If the spectral radius ρ of the matrix $\mathbb{K}$, i.e., $\rho(\mathbb{K}) \coloneqq \max\{|\kappa| : \kappa \text{ eigenvalue of } \mathbb{K}\}$, fulfills $\rho(\mathbb{K}) < 1$, the inverse of $1 - \mathbb{K}$ can be expressed as a geometric series,

$$(1 - \mathbb{K})^{-1} = \sum_{n=0}^{\infty} \mathbb{K}^n. \tag{11.47}$$

Truncating this series amounts to an iterative solution of Eq. (11.45). That is, start with a randomly chosen vector $\mathbb{A}$ as an initial guess for $\mathbb{B}$. Applying Eq. (11.45) N times yields

$$\mathbb{B} \approx \sum_{r=0}^{N-1} \mathbb{K}^r \mathbb{G} + \mathbb{K}^N \mathbb{A}, \tag{11.48}$$

which becomes Eq. (11.46) in the limit $N \to \infty$, for $\lim_{N\to\infty} \mathbb{K}^N = 0$ if $\rho(\mathbb{K}) < 1$, such that the term proportional to $\mathbb{A}$ vanishes. This also shows explicitly that if the iterative approach converges, its solution is independent of the initial guess. It should be stressed that Eq. (11.46) works even if the iterative solution (11.48) does not converge. Indeed, the iterative solution does not converge, e.g., in certain KT equations for the decay of a charged D meson [68]. The benefit of the iterative approach is that it needs less computational time, for the matrix inversion is replaced by a few matrix multiplications. With our eye already on efficiency, it is worth noting that the computation of the kernel $\mathbb{K}$ is not a daunting task even if the number of components of $\mathbb{B}$ is quite large, for the rows and columns of the matrix $\mathbb{K}$ are only weakly coupled. To make this explicit, focus for notational simplicity on the case (11.3). Inserting Eq. (11.10) into Eq. (11.43) shows that $\mathbb{K}$ can be decomposed into a product of three matrices

$$\begin{aligned}
\mathbb{K} &= \mathbb{O}\mathfrak{c}\mathbb{T}, \\
\mathbb{O}^{ab;jk}_{\mathcal{J}\mathcal{J}} &\coloneqq \Omega_{\mathcal{J}}(\mathcal{C}(x_a))\, \mathcal{C}(x_a)^{n_{\mathcal{J}}}\, \delta_{\mathcal{J}\mathcal{J}} \delta_{aj} \delta_{bk}, \\
\mathfrak{c}^{ab;jk}_{\mathcal{J}\mathcal{J}} &\coloneqq \frac{1}{\mathcal{C}(x_j) - \mathcal{C}(x_a)} \delta_{\mathcal{J}\mathcal{J}} \delta_{bk}, \\
\mathbb{T}^{ab;jk}_{\mathcal{J}\mathcal{J}} &\coloneqq \frac{T_{\mathcal{J}}(\zeta)}{\Omega_{\mathcal{J}}(\zeta)} \frac{\sigma_{\mathcal{J}}(\zeta)}{\zeta^{n_{\mathcal{J}}}} \sum_m \frac{z_k^m}{2} C^m_{\mathcal{J}\mathcal{J}}(\zeta)\Big|_{\zeta=\mathcal{C}(x_j)} \delta_{aj}\, \delta_{bk}.
\end{aligned} \tag{11.49}$$

In particular, note that by construction the quantities whose computation is time consuming, namely $\Omega_{\mathcal{J}}$ and $T_{\mathcal{J}}$, are needed only for all values of $\mathcal{C}(x_a)$. Hence the time needed for the construction of $\mathbb{K}$ scales roughly linearly in the number of x sites and not like a square.

As another remark, note that there might be square-root-like singularities at threshold, for the kernel $K_{\mathcal{J}\mathcal{J}}$ contains a term $\sigma_{\mathcal{J}}(x)/(x-s)$. If, e.g., $s^{\text{thr}}_{\mathcal{J}} = 4M_\pi^2$ and the phase space $\sigma_{\mathcal{J}}$ is given as in Eq. (2.29), for s approaching threshold we have

$$\frac{\sigma_{\mathcal{J}}(x)}{x-s} \sim \frac{1}{\sqrt{x - 4M_\pi^2}}. \tag{11.50}$$

Square-root-like singularities like this one are integrable and can be taken care of by an appropriate parametrization of the contour of integration. For example, via the change of variables $x(y) = 4M_\pi^2 + y^2$ we obtain

$$\frac{1}{\sqrt{x - 4M_\pi^2}} \mathrm{d}x = 2\mathrm{d}y, \tag{11.51}$$

thereby explicitly removing the ostensible singularity.

Equipped with $\mathbb{B}$ we can plug it into Eq. (11.35) to compute $\mathscr{B}_{\mathscr{J}}(s)$ for arbitrary values of s. The only subtlety arises if we want to evaluate $\mathscr{B}_{\mathscr{J}}$ at a value of s that lies on top of the curve $\mathcal{C}$. In that case a naive numerical computation of the integral fails due to the presence of the Cauchy kernel in $K_{\mathscr{J}\mathscr{J}}$. To illustrate the treatment of this case, consider for the time being the integral

$$I(s) \coloneqq \int_a^b \frac{f(x)}{x-s}\mathrm{d}x, \tag{11.52}$$

with f a holomorphic function and $a < b$ the finite real-valued boundaries of the integral. First, let $s \notin [a,b]$, such that the Cauchy kernel $1/(x-s)$ does not pose any problem. By adding zero we obtain

$$\begin{aligned} I(s) &= \int_a^b \frac{f(x)-f(s)}{x-s}\mathrm{d}x + f(s)\int_a^b \frac{1}{x-s}\mathrm{d}x \\ &= \int_a^b \frac{f(x)-f(s)}{x-s}\mathrm{d}x + f(s)\ln\left(\frac{b-s}{a-s}\right). \end{aligned} \tag{11.53}$$

Now we continue the expression analytically into the region $s \in (a,b)$. Since

$$\lim_{x\to s}\frac{f(x)-f(s)}{x-s} = \frac{\mathrm{d}f(s)}{\mathrm{d}s}, \tag{11.54}$$

the integrand remains well defined. The treatment of the logarithm requires only a little more care. With $s_\pm \coloneqq s \pm i\epsilon$ and the limit $\epsilon \searrow 0$ implicit we have

$$\begin{aligned} \ln\left(\frac{b-s_\pm}{a-s_\pm}\right) &= \ln\left(\frac{b-s}{a-s} \pm i\epsilon\frac{b-s}{(a-s)^2} + O\left(\epsilon^2\right)\right) \\ &= \ln\left(\frac{b-s}{a-s}\right) \pm i\pi, \end{aligned} \tag{11.55}$$

where we used the definition of the principal value of the logarithm, $\ln(\zeta) = \ln(|\zeta|) + i\arg(\zeta)$, as well as $(b-s)/(a-s) < 0$ and $(b-s)/(a-s)^2 > 0$ for $s \in (a,b)$. Thus, we arrive at

$$I(s_\pm) = \int_a^b \frac{f(x)-f(s)}{x-s}\mathrm{d}x + f(s)\ln\left(\frac{b-s}{a-s}\right) \pm i\pi f(s)\,, \tag{11.56}$$

an expression whose numeric evaluation is straightforward. The general case, namely the integration along the curve $\mathcal{C}$ instead of a segment of the real axis, can be treated in the same fashion by approximating $\mathcal{C}$ in the neighborhood of s by a straight line.[4]

11.4 Kernels for specific cases

The KT equations take on a particularly simple form if the particle $\mathscr{P}_1$ carries the quantum numbers $I(J^{PC}) = 0(1^{--})$, all other particles are pions, and we drop terms beyond P waves in the reconstruction theorem. For instance, $\mathscr{P}_1$ might be the $\omega(782)$, the $\phi(1020)$, or a photon of arbitrary virtuality.

[4]Note that we can always choose $\mathcal{C}$ to be piecewise linear, so in our case this is not an approximation.

In this scenario, there is only one single-variable function, i.e., the set $\mathbb{I} = \{1\}$ is a singleton, and therefore the corresponding index is often dropped. The associated amplitude T is the $\pi\pi \to \pi\pi$ P wave. Furthermore, Eq. (11.3) applies and $C^m_{\mathcal{J}\mathcal{J}}$ in Eq. (11.10) is given as

$$C^m_{\mathcal{J}\mathcal{J}} = 3\delta_{\mathcal{J}1}\delta_{\mathcal{J}1}\left(\delta_{m0} - \delta_{m2}\right). \tag{11.57}$$

Indeed, by plugging in this expression into the KT equations we re-obtain Eq. (7.56) and Eq. (7.57). As a matter of fact, the KT equations need to be adapted only slightly if $\mathscr{P}_1$ has the quantum numbers $I(J^{PC}) = 1(1^{-+})$ instead, such as the $\pi_1(1400)$ or $\pi_1(1600)$, both candidates for non-$\bar{q}q$ mesons [9, 226]. More specifically, Eq. (11.57) is to be replaced by

$$C^m_{\mathcal{J}\mathcal{J}} = -\frac{3}{2}\delta_{\mathcal{J}1}\delta_{\mathcal{J}1}\left(\delta_{m0} - \delta_{m2}\right). \tag{11.58}$$

In addition, the reconstruction theorem needs to be adapted, too, that is, Eq. (7.52) is replaced by [227]

$$\mathfrak{f}_{q^2}(s,t,u) = \mathscr{B}\left(t, q^2\right) - \mathscr{B}\left(u, q^2\right). \tag{11.59}$$

Chapter 12

Assessing the strength of mixed rescattering

Now that we have a good understanding of KT equations, we can try to assess the strength of the mixed rescattering as defined in Sec. 10.2. That is, we want to compare KT equations with plain Omnès functions quantitatively. We will focus on decays of one particle of mass $M > 3M_\pi$ into three pions, i.e., KT equations as specified in Sec. 11.1.2. One might be tempted to perform the comparison on the level of the constituents of the reconstruction theorems, i.e., by comparing the Omnès function (11.5) with the KT solution (11.35). However, this is problematic due to the ambiguities of reconstruction theorems. As discussed in Sec. 9.2.2, the function $\mathscr{B}$ appearing in the reconstruction theorem of $\gamma^* \to \pi\pi\pi$ is not unique, instead, it can be freely shifted by a certain polynomial. Similar ambiguities appear in most reconstruction theorems. Hence, it is a priori not settled which function $\mathscr{B}$ is the one that should be compared with the Omnès function. To avoid this complication, we opt to work directly with the squared total amplitude, which has the additional benefit that is has a clear interpretation as a probability distribution.

As the two free kinematic variables, we pick Mandelstam s and Mandelstam t. The decay is kinematically allowed inside a subset D of the plane spanned by the two Mandelstam variables, namely

$$D \coloneqq \left\{(s,t) \in \mathbb{R}^2 \,:\, s \in \left[4M_\pi^2, (M-M_\pi)^2\right], z^\star \in [-1,1]\right\}. \tag{12.1}$$

At the boundaries of the decay region D the Kibble cubic [228]

$$\mathscr{K}(s,t) \coloneqq stu - M_\pi^2\left(M^2 - M_\pi^2\right)^2 \tag{12.2}$$

vanishes. Explicitly, solving $\mathscr{K}(s,t) = 0$ for t yields two solutions $t_\pm(s)$, which upon inspection indeed fulfill $t_\pm(s) = t(s,\pm 1, M^2)$, with t as in Eq. (7.59), i.e.,

$$\mathscr{K}(s,t) = s\left[t\left(s,1,M^2\right) - t\right]\left[t - t\left(s,-1,M^2\right)\right]. \tag{12.3}$$

Accordingly, the boundary of the scattering region in the s channel is given as $\mathscr{K}(s,t) = 0$ for $s \geq (M_\pi + M)^2$.

A useful tool in the experimental study of a decay into three particles is a Dalitz plot [229], where N events of a given decay process are measured and their distribution over the decay region D is analyzed. This can be done by binning, i.e., by devising a partition of the set D, counting the number of events falling into each element of this partition, and plotting these as a histogram

over D. Alternatively, one can conduct an analysis without binning by making direct use of the likelihood function. Here, we follow the latter approach.

The idea is to interpret the outcome of the KT equations as a truth and examine to which extent plain Omnès functions are capable of reproducing this truth. Denote the absolute value squared of the decay amplitude (spin-averaged as appropriate) in terms of KT equations as $\mathcal{S}^{\mathrm{KT}}$ and its counterpart in terms of Omnès functions as $\mathcal{S}^{\text{Omnès}}$. The KT solution defines a probability density function (PDF)

$$\begin{aligned} f^{\mathrm{KT}} &: D \to \mathbb{R}, \\ (s,t) &\mapsto f^{\mathrm{KT}}(s,t) \coloneqq \frac{\mathcal{S}^{\mathrm{KT}}(s,t)}{\int\limits_D \mathcal{S}^{\mathrm{KT}}(s,t)\,\mathrm{d}s\mathrm{d}t}. \end{aligned} \tag{12.4}$$

So does its Omnès counterpart: $f^{\text{Omnès}}$ is obtained by replacing $\mathcal{S}^{\mathrm{KT}}$ by $\mathcal{S}^{\text{Omnès}}$ in Eq. (12.4). Note that in general these distributions are well defined only because the domain is restricted to D. Now we can generate data $\mathbb{D}$ via drawing $N \in \mathbb{N}$ samples (s_j, t_j) from f^{KT}:

$$\mathbb{D} \coloneqq \left\{ \left(s_j, t_j\right) \,:\, j = 1, \ldots, N \right\}. \tag{12.5}$$

The likelihood function L of a given PDF f with respect to the data $\mathbb{D}$ is defined as

$$L(\mathbb{D}; f) \coloneqq \prod_{j=1}^{N} f\left(s_j, t_j\right). \tag{12.6}$$

To assess if the Omnès model is favored over the KT equations by the data, we take a look at the likelihood ratio

$$\Delta L(\mathbb{D}) \coloneqq \frac{L\left(\mathbb{D}; f^{\text{Omnès}}\right)}{L\left(\mathbb{D}; f^{\mathrm{KT}}\right)}. \tag{12.7}$$

Clearly, if $\Delta L > 1$, the likelihood of the Omnès model exceeds the one of the KT equations, the situation is reversed if $\Delta L < 1$. Note that $\Delta L > 1$ is possible despite the data being drawn from f^{KT}, because N is finite. This is precisely the reasoning behind our approach: from a theoretical point of view, it is clear that the KT equations are an improvement over plain Omnès functions, for the former incorporate more physical effects. Hence, the KT equations should be closer to reality than a plain Omnès model, nevertheless, due to finite statistics, i.e., finite N, an experiment might still conclude the opposite (or be inconclusive). It is this question that we want to address: how large does N need to be for an experiment to likely favor KT equations?

For the ease of computations it is beneficial to work with the log likelihood

$$\mathscr{L}(\mathbb{D}; f) \coloneqq \ln\left[L(\mathbb{D}; f)\right] = \sum_{j=1}^{N} \ln\left[f\left(s_j, t_j\right)\right]. \tag{12.8}$$

That is, we investigate the log-likelihood difference

$$\Delta\mathscr{L}(\mathbb{D}) \coloneqq \ln\left[\Delta L(\mathbb{D})\right] = \mathscr{L}\left(\mathbb{D}; f^{\text{Omnès}}\right) - \mathscr{L}\left(\mathbb{D}; f^{\mathrm{KT}}\right). \tag{12.9}$$

Since $\Delta L > 1$ is equivalent to $\Delta\mathscr{L} > 0$, a positive log-likelihood difference indicates the superiority of the Omnès model.

We now perform $B \in \mathbb{N}$ runs. That is, we generate B datasets $\mathbb{D}_b$, $b = 1, \dots, B$, of size N. On each dataset we compute $\Delta\mathscr{L}$ to assess its probabilistic distribution. Combining Eq. (12.8) and Eq. (12.9) we obtain

$$\frac{1}{N}\Delta\mathscr{L}(\mathbb{D}) = \frac{1}{N}\sum_{j=1}^{N} \ln\left[\frac{f^{\text{Omnès}}\left(s_j, t_j\right)}{f^{\text{KT}}\left(s_j, t_j\right)}\right]. \tag{12.10}$$

Since the data are sampled from f^{KT}, Eq. (12.10) is a Monte-Carlo estimator of the Kullback–Leibler divergence [230]

$$d_{\text{KL}} \coloneqq \int_D f^{\text{KT}}(s,t) \ln\left[\frac{f^{\text{KT}}(s,t)}{f^{\text{Omnès}}(s,t)}\right] \mathrm{d}s\mathrm{d}t, \tag{12.11}$$

which is also known as the relative entropy from $f^{\text{Omnès}}$ to f^{KT}. Explicitly,

$$E\left[\frac{1}{N}\Delta\mathscr{L}(\mathbb{D})\right] = -d_{\text{KL}} \tag{12.12}$$

holds, where E denotes the expectation value (with respect to repeated runs). Furthermore, since the N samples are drawn independently, we have

$$\mathrm{Var}\left[\Delta\mathscr{L}\right] = \sum_{j=1}^{N} \mathrm{Var}\left[\ln\left(\frac{f^{\text{Omnès}}}{f^{\text{KT}}}\right)\right] = N\mathrm{Var}\left[\ln\left(\frac{f^{\text{Omnès}}}{f^{\text{KT}}}\right)\right] = N v_{\text{KL}}, \tag{12.13}$$

with Var denoting the variance as in Sec. 6.4.1, and

$$v_{\text{KL}} \coloneqq \int_D f^{\text{KT}}(s,t) \ln\left[\frac{f^{\text{KT}}(s,t)}{f^{\text{Omnès}}(s,t)}\right]^2 \mathrm{d}s\mathrm{d}t - d_{\text{KL}}^2 \tag{12.14}$$

the variance with respect to f^{KT}, because the j samples are drawn from that very PDF. Accordingly, if the B runs yield normally distributed values of $\Delta\mathscr{L}$, their distribution will be described by the cumulative distribution function (CDF)

$$\mathscr{N}(x; \mu(N), \sigma(N)) \coloneqq \frac{1}{2}\left[1 + \mathrm{erf}\left(\frac{x - \mu(N)}{\sqrt{2}\,\sigma(N)}\right)\right], \tag{12.15}$$

with

$$\mu(N) = -N d_{\text{KL}}, \qquad \sigma(N) = \sqrt{N v_{\text{KL}}}, \tag{12.16}$$

and erf the error function. The probability q that the data favor the Omnès model over the KT one, i.e., $\Delta\mathscr{L} > 0$, reads then

$$q = 1 - \mathscr{N}(0; \mu(N), \sigma(N)). \tag{12.17}$$

Plugging in Eq. (12.15) and Eq. (12.16) results in

$$N(q) = \left\lceil 2 v_{\text{KL}} \left[\frac{\mathrm{erf}^{-1}(1-2q)}{d_{\text{KL}}}\right]^2 \right\rceil, \tag{12.18}$$

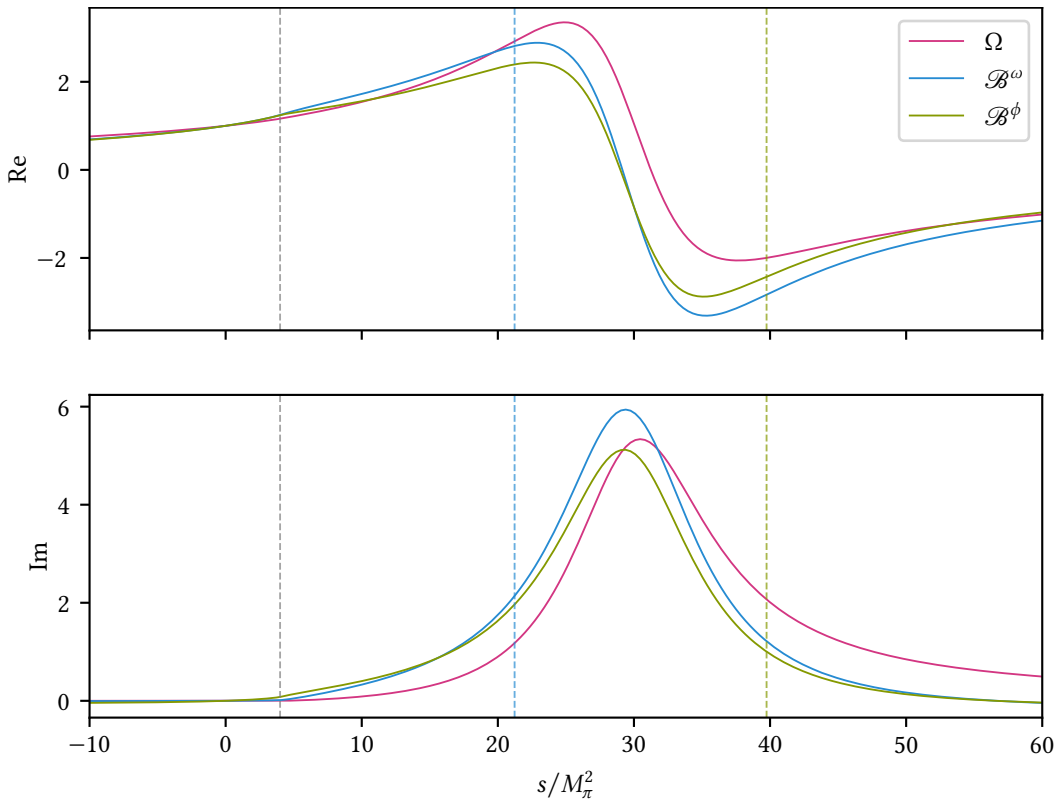

Figure 12.1: The KT solution compared to the Omnès function at the masses of the ω and ϕ meson. The leftmost dashed line at $s = 4M_\pi^2$ indicates the lower end of the decay region, the middle (rightmost) one the upper end of the decay region of $\omega \to \pi\pi\pi$ ($\phi \to \pi\pi\pi$).

where erf^{-1} denotes the inverse of the error function and the ceiling is used to obtain an integer. Equation (12.18) allows for computing the number N of events that is needed to operate at a desired value of q. Since the error functions increases monotonically, N grows with decreasing q, as expected: a larger number of events is needed to exclude the Omnès model with higher probability. Since the log-likelihood difference is the sum of N identically distributed independent random variables, see Eq. (12.10), for $N \to \infty$ its distribution is indeed normal as a consequence of the central limit theorem.

To illustrate the approach, we focus again on the $I(J^{PC}) = 0(1^{--})$ channel, see Sec. 11.4, with a single subtraction. In this case the sole subtraction constant[1] acts as a global pre-factor, and thus it drops out of the PDF (12.4). Therefore, its value is of no relevance; we set it to unity. According to Eq. (11.35) and Eq. (11.57), the sole basis function reads

$$\mathscr{B}(s) = \Omega(s)\left[1 + \frac{3s}{2}\int_{\mathcal{C}}\int_{-1}^{1} \frac{\sigma(x)}{x(x-s)}\frac{T(x)}{\Omega(x)}\left(1 - z^{\star 2}\right)\mathscr{B}\left(t(x,z^\star)\right)\mathrm{d}z^\star\mathrm{d}x\right], \tag{12.19}$$

compare Eq. (7.56) and Eq. (7.57). Since we set the subtraction constant to unity, we can directly identify this basis function with the function appearing in the reconstruction theorem (7.52).

[1] If one is interested in the decay of a particle with fixed mass, the subtraction functions discussed in Sec. 7.2.3 need to be evaluated at a single fixed virtuality only. Hence, they act as constants, and thus are called subtraction constants in this context.

	ω		ϕ	
N	q	$\hat{q}$	q	$\hat{q}$
100	47 %	47 %	37 %	36 %
1000	41 %	41 %	15 %	15 %
10000	24 %	25 %	0.47 ‰	0.56 ‰

Table 12.1: The q values corresponding to Fig. 12.2.

Hence,

$$\begin{aligned} \mathcal{S}^{\mathrm{KT}} &= \frac{1}{4}\mathscr{K}(s,t)\left|\mathscr{B}(s)+\mathscr{B}(t)+\mathscr{B}(u)\right|^2, \\ \mathcal{S}^{\text{Omnès}} &= \frac{1}{4}\mathscr{K}(s,t)\left|\Omega(s)+\Omega(t)+\Omega(u)\right|^2, \end{aligned} \tag{12.20}$$

where the three-particle phase space $\mathscr{K}/4$ arises as the helicity-averaged squared absolute value of the Lorentz structure in Eq. (7.9) and Eq. (7.10). Again, we describe the $\pi\pi$ P wave T via the NLO IAM, setting $48\pi^2(l_2^r - 2l_1^r) = 5.73$ [151]. We employ the prescription (11.40) with $\lambda = 600M_\pi^2$ and $\Lambda = 700M_\pi^2$ to guide the IAM phase smoothly to π at high energies. There are several resonances in the channel of interest, here we focus on the ones with lowest mass, i.e., the $\omega(782)$ and $\phi(1020)$ [9]. We compare the KT function $\mathscr{B}$ at the masses of both resonances with the plain Omnès function in Fig. 12.1.

Although in the limit $N \to \infty$ the log-likelihood difference follows a normal distribution, this does not need to be the case if N is small. To check for a given N if the description in terms of a normal distribution is valid, we proceed as follows. Via a simple accept-reject approach[2] we draw 10^7 samples from f^{KT}. From these samples, which constitute an empirical probability distribution approximating f^{KT}, we draw uniformly with replacement $B = 10^6$ bootstrap samples $\mathbb{D}_b$, $b = 1, \ldots, B$, each of size N. A bootstrap sample corresponds to one experimental run. On each bootstrap sample we compute $\Delta\mathscr{L}(\mathbb{D}_b)$, the resulting histogram is compared with the PDF of the normal distribution (12.15). The results for $N \in \{10^2, 10^3, 10^4\}$ are shown for both the ω and the ϕ in Fig. 12.2. Clearly, the distribution of $\Delta\mathscr{L}$ is nicely described by the normal distribution (12.15) in every case, as is confirmed by a Q-Q plot. Furthermore, the bootstrap bias is tiny.

We can not only compute q via Eq. (12.17), but also estimate it via determining the fraction of bootstrap samples with $\Delta\mathscr{L} > 0$; this estimator is denoted by $\hat{q}$. Both values are shown in Table 12.1 for the two different masses and three values of N. Again, the agreement between a normal distribution and the empirical one is clearly visible. The only notable difference arises for $N = 10^4$ at the mass of the ϕ meson, where q is at the sub-per-mille level. Hence, we are probing the tails of the distribution, where the PDF takes on small values. It is expected that a very high number of bootstrap samples is needed to describe the tail correctly, and thus the deviation comes at no surprise. In addition, we observe that the q values of the ω meson are significantly larger than the ones of the ϕ, in agreement with the histograms of the former being closer to zero in Fig. 12.2.

To investigate this more thoroughly, we use Eq. (12.18) to compute N for q values corresponding to the typical confidence levels defined via

$$1 - q = \mathcal{N}(n_\sigma; 0, 1) - \mathcal{N}(-n_\sigma; 0, 1), \qquad n_\sigma \in \mathbb{N}. \tag{12.21}$$

[2] We draw tuples (a, b, c) uniformly from $[4M_\pi^2, (M - M_\pi)^2] \times [4M_\pi^2, (M - M_\pi)^2] \times [0, \max_{(s,t)\in D} f^{\mathrm{KT}}(s,t)]$ and accept them if $(a, b, c) \in D \times [0, f^{\mathrm{KT}}(a, b)]$.

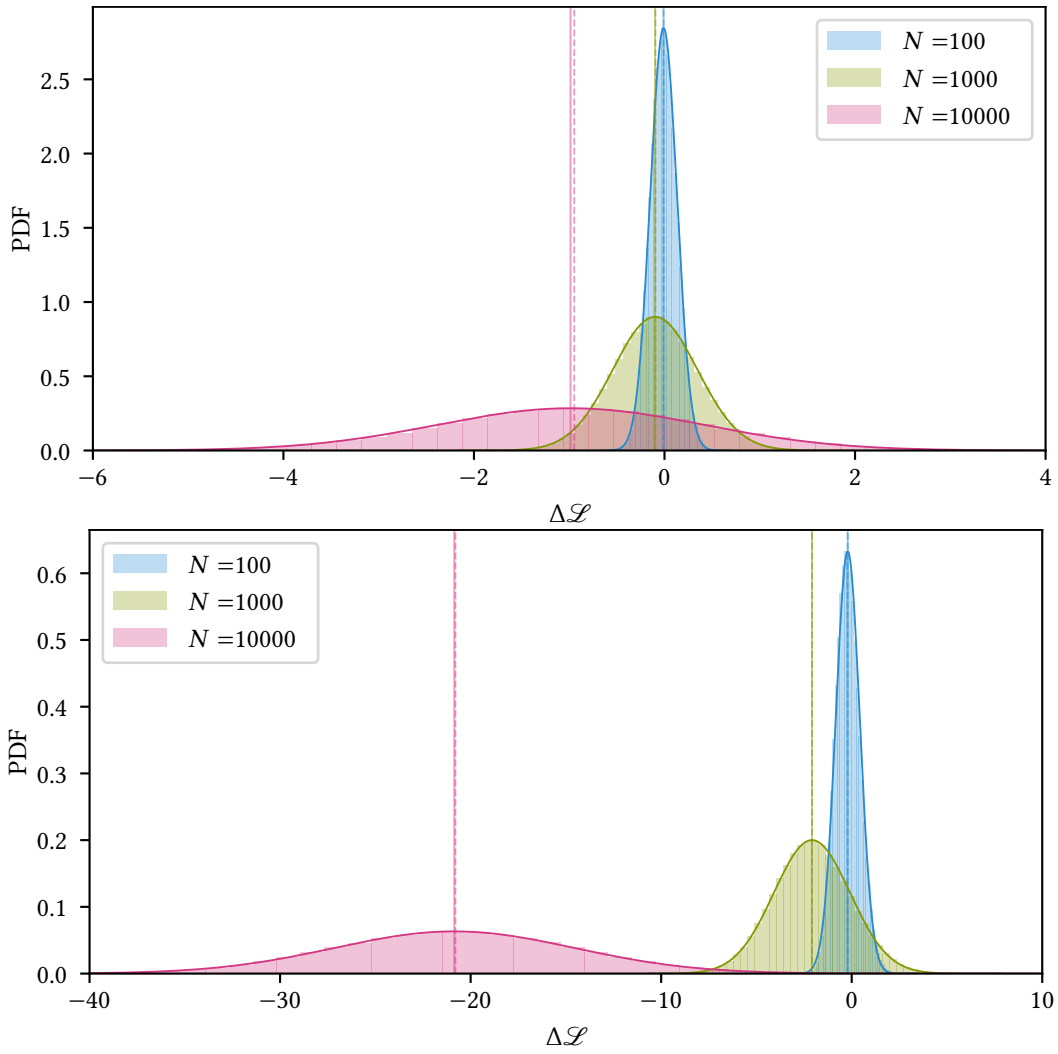

Figure 12.2: The distribution of $\Delta\mathscr{L}$ for $\omega \to \pi\pi\pi$ (top) and $\phi \to \pi\pi\pi$ (bottom). For each given N the bootstrap samples are shown as a histogram (normalized to unity) together with the PDF of the normal distribution (12.15). The solid vertical lines mark the value of d_{KL}, the dashed line the average of the bootstrap samples. The difference between these lines is the bootstrap bias.

n_σ	q	N^ω	N^ϕ
1	3.17×10^{-1}	4559	207
2	4.55×10^{-2}	57659	2612
3	2.70×10^{-3}	156239	7077
4	6.33×10^{-5}	296521	13431
5	5.73×10^{-7}	477664	21635

Table 12.2: The needed number of events N^ω (N^ϕ) for $\omega \to \pi\pi\pi$ ($\phi \to \pi\pi\pi$) to reach a confidence level corresponding to n_σ standard deviations of the normal distribution.

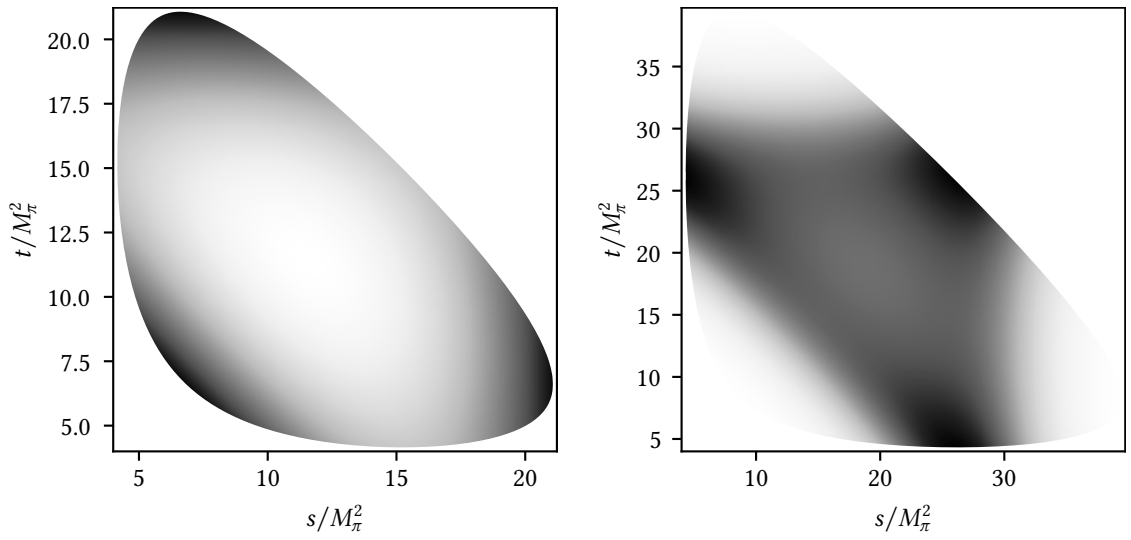

Figure 12.3: $4\mathcal{S}^{\mathrm{KT}}/\mathscr{K}$ (see Eq. (12.20)) for $\omega \to \pi\pi\pi$ (left) and $\phi \to \pi\pi\pi$ (right). The units are arbitrary, the darker a region, the higher the value. The plot on the right-hand side clearly shows three resonance bands at $s = M_\rho$ (vertical), $t = M_\rho$ (horizontal), and $u = M_\rho$ (diagonal). To be compared with Fig. 5 in Ref. [51].

The results are given in Table 12.2. According to Eq. (12.18),

$$\frac{N^\omega(q)}{N^\phi(q)} = \frac{\nu_{\mathrm{KL}}^\omega}{\nu_{\mathrm{KL}}^\phi}\left(\frac{d_{\mathrm{KL}}^\phi}{d_{\mathrm{KL}}^\omega}\right)^2 \approx 22. \tag{12.22}$$

So indeed the decay of the ω meson is not nearly as sensitive to mixed rescattering as the decay of the ϕ meson. Qualitatively, this is not so much a result of a change of the KT solution $\mathscr{B}$, see Fig. 12.1, but of the increase of size of the decay region D with growing decay mass, see the dashed lines ibidem. While the ρ appears in $\omega \to \pi\pi\pi$ only at the boundary of the decay region, for a decaying ϕ the resonance bands are well contained in the decay region as illustrated in Fig. 12.3 [51]. In Ref. [129] the authors performed an analysis of $\omega \to \pi\pi\pi$ based on $2.6{\times}10^5$ events, corresponding to $q = 1.66{\times}10^{-4}$ according to Eq. (12.17). Accordingly, in our formalism their finding—that the data is not sensitive to mixed rescattering—is unlikely, lying between $n_\sigma = 3$ and $n_\sigma = 4$, see Table 12.2. Contrarily, the analysis of 2×10^6 events in $\phi \to \pi\pi\pi$ in Ref. [51] strongly favored the KT solution over an Omnès approach, in full alignment with Table 12.2.

The approach at hand can be carried over to other channels via substituting the appropriate KT equations and reconstruction theorem, see, e.g., Sec. 11.4 for $I(J^{PC}) = 1(1^{-+})$. Moreover, one can allow for additional parameters in the Omnès model, i.e., for multiplying the Omnès function by a polynomial. In this case, $\hat{q}$ values can be obtained by fitting $f^{\text{Omnès}}$ to the data drawn from f^{KT}. However, clearly f^{KT} needs to be fixed in our approach, that is, all subtraction constants appearing in the KT equations need to be determined beforehand.

Part V

Epilogue

Chapter 13

Conclusions

The improvements of lattice-QCD computations of simple hadronic scattering processes make an analysis of lattice data with refined models both possible and necessary. Possible, because good models tend to have quite a few fit parameters, in particular if they are based on higher-order ChPT. Hence, to fix these parameters, the errors of the data points have to be small. Moreover, to control pion-mass dependent terms, data at different pion masses need to be available. Necessary, for simple models come with sizable systematic errors. If such models are applied to precise data, the systematic errors will dominate the error budget, so that predictions might not be as precise as possible.

Ideally, models of scattering amplitudes should obey the fundamental principles of scattering theory, that is, they should respect the unitarity of the S matrix and be holomorphic in the kinematic variables, with all branch points and poles corresponding to physical states. Moreover, if possible the models should be symmetric under crossing. Only models fulfilling in particular the second condition allow for universally sound extractions of resonance properties. A potent model in this context is the IAM, although it does violate crossing symmetry; for it can be derived from ChPT and unitarity alone, has the correct analytic structure for a pole search, and is particularly at NLO sufficiently simple to use. By performing the partial-wave projection at NNLO analytically, we were able to obtain compact ChPT expressions; in this way carrying the simplicity partly over to NNLO.

Equipped with these expressions, we have shown that state-of-the-art lattice results of the $\pi\pi \to \pi\pi$ P wave at unphysically high pion masses allow for stable fits of the NNLO IAM without imposing phenomenological knowledge on the fit parameters, the sole exception being the LEC l_3^r, which describes physics beyond the reach of the analyzed data. By comparing fits at NLO with NNLO ones, we were able to estimate the systematic error that is associated with the truncation of ChPT. Indeed, at NLO the systematic error dominated, while it reduced significantly at NNLO. We then extracted the properties of the ρ resonance from its pole position, studied their pion-mass dependence, and extrapolated them to the physical point. To obtain reliable estimates of the total errors of the ρ characteristics, we took into account both the statistical error of the $\pi\pi$ data and the one of the lattice spacings via resampling techniques. In case of the HadSpec data, the reduction of the systematic error with increasing order led to the ρ properties at NNLO being more precise than at NLO, albeit less accurate. In case of the fits to the CLS data, the increased statistical error at higher order compensated for the reduction of the systematic one at the physical point, but at higher pion masses the NNLO results become more precise, too. Our analysis of the systematic error hints at a breakdown scale of the theory at roughly the ρ mass, in agreement with naive expectations from ChPT and in contrast to previous work [94].

The observed discrepancies between fit results and literature values, especially of the LEC l_4^r in the CLS fits, seemed worrisome. While at NLO a good agreement in all observables cannot be expected, since there is only one free parameter in the P wave, the NNLO IAM does not suffer from this limitation. Indeed, our analysis indicates that the NNLO IAM is, in fact, flexible enough to be sensitive to lattice artifacts. To be precise, our fit results point towards a tension between the CLS $\pi\pi$ data and the F_π one that cannot be resolved completely by scale-setting issues. It seems likely that future attempts to analyze lattice data via the NNLO IAM need to incorporate a precise modeling of lattice artifacts. Such attempts are not limited to the P wave. In fact, we provide all needed analytic expressions for $(I, J) \in \{(0,0), (2,0), (1,1), (0,2), (2,2)\}$ in Ref. [149], thereby facilitating applications of the IAM in particular to future $\pi\pi \to \pi\pi$ lattice data in the S wave, where the $f_0(500)$ resonance appears. Note that a proper treatment of the D waves via the IAM requires knowledge of the NNNLO ChPT expressions [231].

Coming back to the introductory remarks of this chapter, our analysis of $\gamma^{(*)}\pi \to \pi\pi$ data illustrated clearly the limitations one encounters if the data are neither of high precision nor cover sufficiently many values of the pion mass. Namely, our fits were not able to discriminate between a simple model phrased in terms of an Omnès function and the more refined KT approach. Moreover, with data at only two different pion masses available, the pion-mass dependence of the subtraction functions was necessarily modeled in a simplistic manner.

Despite these limitations, our analysis clearly demonstrated the possibility to analyze lattice data with dispersive frameworks that exceed the simple IAM in complexity. Most importantly, we were able to determine the cross section, the radiative coupling of the ρ resonance, and the anomaly $F_{3\pi}$ at the physical point, although the data are obtained at pion masses exceeding 300 MeV. The results of the latter two agree with phenomenological expectations and the theoretical prediction, respectively, albeit within large uncertainties. As soon as the analysis of the already obtained experimental data is finished [106], our computation of the cross section could also be falsified. If future lattice computations yield results covering more pion masses with improved precision, both the statistical and the systematic uncertainty of the observables at the physical point will reduce significantly.

These results show convincingly that the application domain of KT equations is no longer restricted to experimental data, but extends towards the lattice. The analytic continuation of KT equations to the decay region builds a bridge towards possible future applications of dispersive frameworks in the analysis of three-to-three scattering data obtained on the lattice. Whether and when the mixed rescattering effects encoded in KT equations will become visible on the lattice, remains to be seen. We developed a method to determine the impact of such rescattering effects in experiments a priori, which is currently restricted to simple but interesting scenarios. Future work is needed to refine this approach and extend it to more complicated processes.

Appendix

Appendix A

Chiral-perturbation-theory expressions

Here we give the explicit expressions completing the ChPT $\pi\pi$ P wave described in Sec. 4.1. While the coefficients appearing at NLO, i.e., in Eq. (4.3) are rather compact, namely

$$\begin{aligned}
b_0^{11}(s) &:= -\frac{120M_\pi^6 - 197M_\pi^4 s + 61M_\pi^2 s^2 - 2s^3}{27648\pi^3\left(s-4M_\pi^2\right)},\\
b_1^{11}(s) &:= -\frac{64M_\pi^8 - 55M_\pi^6 s + 6M_\pi^4 s^2}{2304\pi^3 s\sigma(s)\left(s-4M_\pi^2\right)},\\
b_2^{11}(s) &:= -\frac{M_\pi^4\left(6M_\pi^4 + 13M_\pi^2 s - 3s^2\right)}{1536\pi^3\left(s-4M_\pi^2\right)^2},\\
b_{l_1^r}^{11}(s) &:= -2b_{l_2^r}^{11}(s) = \frac{s\left(4M_\pi^2 - s\right)}{48\pi},\\
b_{l_3^r}^{11}(s) &:= 0,
\end{aligned} \tag{A.1}$$

the NNLO coefficients of Eq. (4.5) are more lengthy. The ones multiplying the powers of logarithms read

$$\begin{aligned}
c_0^{11}(s) :=& \frac{1}{6370099200\pi^5 s\left(s-4M_\pi^2\right)}\Bigg[7372800\pi^2 M_\pi^{10} + 704\left(178753 - 17280\pi^2\right)M_\pi^8 s\\
&+ 128\left(3765\pi^2 - 825499\right)M_\pi^6 s^2 + 4\left(7303133 + 246120\pi^2\right)M_\pi^4 s^3\\
&- 12\left(572531 + 28840\pi^2\right)M_\pi^2 s^4 + \left(654787 + 38880\pi^2\right)s^5\\
&- 120s\ln\left(\frac{M_\pi^2}{\mu^2}\right)\Bigg(714048M_\pi^8 - 518888M_\pi^6 s + 229588M_\pi^4 s^2 - 65468M_\pi^2 s^3\\
&+ 6633s^4 - 300\left(s-4M_\pi^2\right)^2\left(29M_\pi^4 - 10M_\pi^2 s + 9s^2\right)\ln\left(\frac{M_\pi^2}{\mu^2}\right)\Bigg)\Bigg],
\end{aligned} \tag{A.2}$$

$$
\begin{aligned}
c_1^{11}(s) :=& \frac{1}{53084160\pi^5 s\sigma(s)\left(s-4M_\pi^2\right)}\Bigg[3840\left(20+3\pi^2\right)M_\pi^{10}+80\left(1356\pi^2-8977\right)M_\pi^8 s \\
&+20\left(52063-1032\pi^2\right)M_\pi^6 s^2+2\left(360\pi^2-186289\right)M_\pi^4 s^3+78734M_\pi^2 s^4-6633s^5 \\
&+600s\left(348M_\pi^8-710M_\pi^6 s+393M_\pi^4 s^2-100M_\pi^2 s^3+9s^4\right)\ln\left(\frac{M_\pi^2}{\mu^2}\right)\Bigg], \\
c_2^{11}(s) :=& \frac{1}{884736\pi^5 s\left(s-4M_\pi^2\right)^2}\Bigg[4096M_\pi^{12}-108\left(137+4\pi^2\right)M_\pi^{10}s+\left(10159-300\pi^2\right)M_\pi^8 s^2 \\
&+60\left(\pi^2-133\right)M_\pi^6 s^3+2995M_\pi^4 s^4-590M_\pi^2 s^5+45s^6+120M_\pi^8 s\left(29M_\pi^2-s\right)\ln\left(\frac{M_\pi^2}{\mu^2}\right)\Bigg], \\
c_3^{11}(s) :=& \frac{M_\pi^6\left(95M_\pi^2-16s\right)}{36864\pi^5\left(s-4M_\pi^2\right)}-\frac{M_\pi^4\left(24M_\pi^6-314M_\pi^4 s+11M_\pi^2 s^2+6s^3\right)}{221184\pi^5 s\sigma(s)\left(s-4M_\pi^2\right)}, \\
c_4^{11}(s) :=& -\frac{M_\pi^6\left(36M_\pi^4+25M_\pi^2 s-5s^2\right)}{147456\pi^5\left(s-4M_\pi^2\right)^2},
\end{aligned}
$$

the LECs scale with

$$
\begin{aligned}
c_{l_1^r}^{11}(s) :=& -\frac{M_\pi^6\left(116M_\pi^4-11M_\pi^2 s+4s^2\right)}{768\pi^3\left(s-4M_\pi^2\right)^2}\left[L(s)\right]^2 \\
&-\frac{1840M_\pi^8-8780M_\pi^6 s+5498M_\pi^4 s^2-1594M_\pi^2 s^3+153s^4}{46080\pi^3\sigma(s)\left(s-4M_\pi^2\right)}L(s) \\
&-\frac{\left(s-4M_\pi^2\right)\left(628M_\pi^4-64M_\pi^2 s+153s^2\right)\ln\left(\frac{M_\pi^2}{\mu^2}\right)}{46080\pi^3} \\
&+\frac{1213056M_\pi^8-1003536M_\pi^6 s+426916M_\pi^4 s^2-112736M_\pi^2 s^3+10531s^4}{2764800\pi^3\left(s-4M_\pi^2\right)}, \\
c_{l_2^r}^{11}(s) :=& \frac{M_\pi^6\left(8M_\pi^2+s\right)\left(4s-33M_\pi^2\right)}{1536\pi^3\left(s-4M_\pi^2\right)^2}\left[L(s)\right]^2 \\
&-\frac{20960M_\pi^8-31220M_\pi^6 s+14602M_\pi^4 s^2-3406M_\pi^2 s^3+297s^4}{92160\pi^3\sigma(s)\left(s-4M_\pi^2\right)}L(s) \\
&-\frac{\left(s-4M_\pi^2\right)\left(1272M_\pi^4-436M_\pi^2 s+297s^2\right)\ln\left(\frac{M_\pi^2}{\mu^2}\right)}{92160\pi^3} \\
&+\frac{2694144M_\pi^8-2309664M_\pi^6 s+984284M_\pi^4 s^2-240964M_\pi^2 s^3+21419s^4}{5529600\pi^3\left(s-4M_\pi^2\right)}, \\
c_{l_3^r}^{11}(s) :=& -\frac{5M_\pi^{10}}{64\pi^3\left(s-4M_\pi^2\right)^2}\left[L(s)\right]^2-\frac{5M_\pi^4\left(12M_\pi^4-10M_\pi^2 s+s^2\right)}{768\pi^3\sigma(s)\left(s-4M_\pi^2\right)}L(s) \\
&+\frac{M_\pi^4\left(496M_\pi^4-218M_\pi^2 s+s^2\right)}{4608\pi^3\left(s-4M_\pi^2\right)}-\frac{5M_\pi^4\left(s-4M_\pi^2\right)\ln\left(\frac{M_\pi^2}{\mu^2}\right)}{768\pi^3}, \\
c_{l_3^r l_4^r}^{11}(s) :=& 0,
\end{aligned}
\tag{A.3}
$$

and the higher polylogarithms are to be multiplied by

$$d^{11}(s) \coloneqq \frac{M_\pi^6 \left(16s - 95M_\pi^2\right)}{9216\pi^5 \left(s - 4M_\pi^2\right)}. \tag{A.4}$$

The expressions for the other partial waves are given in Ref. [149].

Glossary

1PI one-particle-irreducible

2PI two-particle-irreducible

BIC Bayesian information criterion

CDF cumulative distribution function

ChPT chiral perturbation theory

CLS Coordinated Lattice Simulations

CM center-of-mass

EFT effective field theory

FLAG Flavour Lattice Averaging Group

HadSpec Hadron Spectrum

IAM inverse-amplitude method

irrep irreducible representation

KSFR Kawarabayashi–Suzuki–Fayyazuddin–Riazuddin

KT Khuri–Treiman

LEC low-energy constant

LO leading order

NLO next-to-leading order

NNLO next-to-next-to-leading order

NNNLO next-to-next-to-next-to-leading order

PDG Particle Data Group

PDF probability density function

QCD quantum chromodynamics

QFT quantum field theory

SM standard model

VMD vector meson dominance

Bibliography

[1] H. Fritzsch, M. Gell-Mann, and H. Leutwyler, Phys. Lett. B **47**, 365 (1973).

[2] K. West, *Good Morning*, Graduation, Roc-A-Fella Records & Def Jam Recordings, 2007, track 1.

[3] S. L. Glashow, Nucl. Phys. **22**, 579 (1961).

[4] F. Englert and R. Brout, Phys. Rev. Lett. **13**, 321 (1964).

[5] P. W. Higgs, Phys. Rev. Lett. **13**, 508 (1964).

[6] A. Salam and J. C. Ward, Phys. Lett. **13**, 168 (1964).

[7] S. Weinberg, Phys. Rev. Lett. **19**, 1264 (1967).

[8] S. Weinberg, *The Quantum Theory of Fields, Volume 2, Modern Applications*, 2nd ed. (Cambridge University Press, Cambridge, United Kingdom, 2005).

[9] P. A. Zyla et al. (Particle Data Group), PTEP **2020**, 083C01 (2020).

[10] C. W. Misner, K. S. Thorne, and J. A. Wheeler, *Gravitation*, 1st Princeton University Press ed., original ed. published in 1973 by W. H. Freeman and Company (Princeton University Press, Princeton, New Jersey, USA, 2017).

[11] S. Weinberg, *The Quantum Theory of Fields, Volume 1, Foundations*, 2nd ed. (Cambridge University Press, Cambridge, United Kingdom, 2005).

[12] R. Percacci, *An Introduction to Covariant Quantum Gravity and Asymptotic Safety* (World Scientific, Singapore, 2017).

[13] C. Rovelli and F. Vidotto, *Covariant Loop Quantum Gravity, An Elementary Introduction to Quantum Gravity and Spinfoam Theory* (Cambridge University Press, Cambridge, United Kingdom, 2014).

[14] A. Jaffe and E. Witten, *Quantum Yang-Mills Theory*, Clay Mathematics Institute, http://www.claymath.org/sites/default/files/yangmills.pdf (visited on 12/01/2021).

[15] N. Brambilla et al., Eur. Phys. J. C **74**, 2981 (2014), arXiv:1404.3723 [hep-ph].

[16] K. G. Wilson, Phys. Rev. D **10**, 2445 (1974).

[17] I. Montvay and G. Münster, *Quantum Fields on a Lattice* (Cambridge University Press, Cambridge, United Kingdom, 1994).

[18] C. Gattringer and C. B. Lang, *Quantum Chromodynamics on the Lattice, An Introductory Presentation* (Springer, Berlin and Heidelberg, Germany, 2010).

[19] J. Gasser and H. Leutwyler, Nucl. Phys. B **250**, 465 (1985).

[20] S. Weinberg, Physica A **96**, 327 (1979).

[21] J. Gasser and H. Leutwyler, Annals Phys. **158**, 142 (1984).

[22] S. Scherer and M. R. Schindler, *A Primer for Chiral Perturbation Theory* (Springer, Berlin and Heidelberg, Germany, 2012).

[23] R. J. Eden et al., *The Analytic S-Matrix* (Cambridge University Press, Cambridge, United Kingdom, 1966).

[24] R. Omnès, *Introduction to Particle Physics* (Wiley-Interscience – a division of John Wiley & Sons Ltd., London, United Kingdom, 1970).

[25] I. T. Todorov, *Analytic Properties of Feynman Diagrams in Quantum Field Theory* (Pergamon Press, Oxford, United Kingdom, 1971).

[26] H. M. Nussenzveig, *Causality and Dispersion Relations* (Academic Press, New York, New York, USA, 1972).

[27] D. Iagolnitzer, *Scattering in Quantum Field Theories, The Axiomatic and Constructive Approaches* (Princeton University Press, Princeton, New Jersey, USA, 1993).

[28] S. Dyatlov and M. Zworski, *Mathematical Theory of Scattering Resonances* (American Mathematical Society, Providence, Rhode Island, USA, 2019).

[29] R. G. Edwards and B. Joó, Nucl. Phys. B Proc. Suppl. **140**, 832 (2005), arXiv:hep-lat/0409003.

[30] K. Jansen and C. Urbach, Comput. Phys. Commun. **180**, 2717 (2009), arXiv:0905.3331 [hep-lat].

[31] M. A. Clark et al., Comput. Phys. Commun. **181**, 1517 (2010), arXiv:0911.3191 [hep-lat].

[32] R. A. Soltz et al., Ann. Rev. Nucl. Part. Sci. **65**, 379 (2015), arXiv:1502.02296 [hep-lat].

[33] S. Borsanyi et al. (Budapest–Marseille–Wuppertal), Phys. Rev. Lett. **121**, 022002 (2018), arXiv:1711.04980 [hep-lat].

[34] M. Fischer et al. (Extended Twisted Mass), Phys. Lett. B **819**, 136449 (2021), arXiv:2006.13805 [hep-lat].

[35] M. Fischer et al. (Extended Twisted Mass), Eur. Phys. J. C **81**, 436 (2021), arXiv:2008.03035 [hep-lat].

[36] C. Andersen et al., Nucl. Phys. B **939**, 145 (2019), arXiv:1808.05007 [hep-lat].

[37] M. T. Hansen et al. (Hadron Spectrum), Phys. Rev. Lett. **126**, 012001 (2021), arXiv:2009.04931 [hep-lat].

[38] L. Maiani and M. Testa, Phys. Lett. B **245**, 585 (1990).

[39] R. A. Briceño, J. J. Dudek, and R. D. Young, Rev. Mod. Phys. **90**, 025001 (2018), arXiv:1706.06223 [hep-lat].

[40] R. A. Briceño, M. T. Hansen, and A. Walker-Loud, Phys. Rev. D **91**, 034501 (2015), arXiv:1406.5965 [hep-lat].

[41] J. Bulava and M. T. Hansen, Phys. Rev. D **100**, 034521 (2019), arXiv:1903.11735 [hep-lat].

[42] S. Aoki and T. Doi, Front. in Phys. **8**, 307 (2020), arXiv:2003.10730 [hep-lat].

[43] J. Bijnens, G. Colangelo, and G. Ecker, JHEP **02**, 020 (1999), arXiv:hep-ph/9902437.

[44] J. Bijnens, N. Hermansson-Truedsson, and S. Wang, JHEP **01**, 102 (2019), arXiv:1810.06834 [hep-ph].

[45] T. Ebertshäuser, H. W. Fearing, and S. Scherer, Phys. Rev. D **65**, 054033 (2002), arXiv:hep-ph/0110261.

[46] J. Bijnens, L. Girlanda, and P. Talavera, Eur. Phys. J. C **23**, 539 (2002), arXiv:hep-ph/0110400.

[47] S. Aoki et al. (FLAG), Eur. Phys. J. C **80**, 113 (2020), arXiv:1902.08191 [hep-lat].

[48] V. Bernard and U.-G. Meißner, Ann. Rev. Nucl. Part. Sci. **57**, 33 (2007), arXiv:hep-ph/0611231.

[49] O. Bär, *Chiral Perturbation Theory for Lattice QCD*, Habilitationsschrift (Humboldt University, Berlin, 2010).

[50] R. García-Martín et al., Phys. Rev. D **83**, 074004 (2011), arXiv:1102.2183 [hep-ph].

[51] F. Niecknig, B. Kubis, and S. P. Schneider, Eur. Phys. J. C **72**, 2014 (2012), arXiv:1203.2501 [hep-ph].

[52] G. Colangelo et al., Eur. Phys. J. C **78**, 947 (2018), arXiv:1807.11937 [hep-ph].

[53] T. Aoyama et al., Phys. Rept. **887**, 1 (2020), arXiv:2006.04822 [hep-ph].

[54] J. R. Peláez and A. Rodas, *Dispersive $\pi K \to \pi K$ and $\pi\pi \to K\bar{K}$ amplitudes from scattering data, threshold parameters and the lightest strange resonance κ or $K_0^*(700)$* (2020), arXiv:2010.11222 [hep-ph].

[55] T. N. Truong, Phys. Rev. Lett. **61**, 2526 (1988).

[56] A. Dobado, M. J. Herrero, and T. N. Truong, Phys. Lett. B **235**, 134 (1990).

[57] T. N. Truong, Phys. Rev. Lett. **67**, 2260 (1991).

[58] A. Dobado and J. R. Peláez, Phys. Rev. D **47**, 4883 (1993), arXiv:hep-ph/9301276.

[59] D. R. Bolton, R. A. Briceño, and D. J. Wilson, Phys. Lett. B **757**, 50 (2016), arXiv:1507.07928 [hep-ph].

[60] S. Weinberg, *What is quantum field theory, and what did we think it was?*, in T. Y. Cao, *Conceptual Foundations of Quantum Field Theory* (Cambridge University Press, Cambridge, United Kingdom, Mar. 1999), pp. 241–251, arXiv:hep-th/9702027.

[61] S. M. Roy, Phys. Lett. B **36**, 353 (1971).

[62] G. Sommer, Fortsch. Phys. **18**, 577 (1970).

[63] M. Hoferichter et al., Phys. Rept. **625**, 1 (2016), arXiv:1510.06039 [hep-ph].

[64] J. Bijnens et al., Phys. Lett. B **374**, 210 (1996), arXiv:hep-ph/9511397.

[65] J. Bijnens et al., Nucl. Phys. B **508**, 263 (1997), arXiv:hep-ph/9707291 [hep-ph]; Erratum: Nucl. Phys. B **517**, 639 (1998).

[66] M. Hoferichter, B. Kubis, and D. Sakkas, Phys. Rev. D **86**, 116009 (2012), arXiv:1210.6793 [hep-ph].

[67] J. T. Daub, C. Hanhart, and B. Kubis, JHEP **02**, 009 (2016), arXiv:1508.06841 [hep-ph].

[68] F. Niecknig and B. Kubis, JHEP **10**, 142 (2015), arXiv:1509.03188 [hep-ph].

[69] G. Colangelo, E. Passemar, and P. Stoffer, Eur. Phys. J. C **75**, 172 (2015), arXiv:1501.05627 [hep-ph].

[70] T. Isken et al., Eur. Phys. J. C **77**, 489 (2017), arXiv:1705.04339 [hep-ph].

[71] F. Niecknig and B. Kubis, Phys. Lett. B **780**, 471 (2018), arXiv:1708.00446 [hep-ph].

[72] M. Hoferichter and P. Stoffer, JHEP **07**, 073 (2019), arXiv:1905.13198 [hep-ph].

[73] J. R. Peláez, Phys. Rept. **658**, 1 (2016), arXiv:1510.00653 [hep-ph].

[74] D. Schildknecht, Acta Phys. Polon. B **37**, 595 (2006), arXiv:hep-ph/0511090.

[75] S. Aoki et al. (CP-PACS), Phys. Rev. D **76**, 094506 (2007), arXiv:0708.3705 [hep-lat].

[76] M. Göckeler et al. (QCDSF), PoS **LATTICE2008**, 136 (2008), arXiv:0810.5337 [hep-lat].

[77] X. Feng, K. Jansen, and D. B. Renner (ETMC), Phys. Rev. D **83**, 094505 (2011), arXiv:1011.5288 [hep-lat].

[78] C. B. Lang et al., Phys. Rev. D **84**, 054503 (2011), arXiv:1105.5636 [hep-lat]; Erratum: Phys. Rev. D **89**, 059903 (2014).

[79] C. Pelissier and A. Alexandru, Phys. Rev. D **87**, 014503 (2013), arXiv:1211.0092 [hep-lat].

[80] T. Metivet (Budapest–Marseille–Wuppertal), PoS **LATTICE2014**, 079 (2015), arXiv:1410.8447 [hep-lat].

[81] X. Feng et al., Phys. Rev. D **91**, 054504 (2015), arXiv:1412.6319 [hep-lat].

[82] D. J. Wilson et al., Phys. Rev. D **92**, 094502 (2015), arXiv:1507.02599 [hep-ph].

[83] G. S. Bali et al. (RQCD), Phys. Rev. D **93**, 054509 (2016), arXiv:1512.08678 [hep-lat].

[84] D. Guo et al., Phys. Rev. D **94**, 034501 (2016), arXiv:1605.03993 [hep-lat].

[85] Z. Fu and L. Wang, Phys. Rev. D **94**, 034505 (2016), arXiv:1608.07478 [hep-lat].

[86] C. Alexandrou et al., Phys. Rev. D **96**, 034525 (2017), arXiv:1704.05439 [hep-lat].

[87] M. Werner et al., Eur. Phys. J. A **56**, 61 (2020), arXiv:1907.01237 [hep-lat].

[88] F. Erben et al., Phys. Rev. D **101**, 054504 (2020), arXiv:1910.01083 [hep-lat].

[89] C. Hanhart, J. R. Peláez, and G. Ríos, Phys. Rev. Lett. **100**, 152001 (2008), arXiv:0801.2871 [hep-ph].

[90] B. Hu et al., Phys. Rev. Lett. **117**, 122001 (2016), arXiv:1605.04823 [hep-lat].

[91] M. Döring, B. Hu, and M. Mai, Phys. Lett. B **782**, 785 (2018), arXiv:1610.10070 [hep-lat].

[92] B. Hu et al., Phys. Rev. **D96**, 034520 (2017), arXiv:1704.06248 [hep-lat].

[93] R. Molina and J. Ruiz de Elvira, JHEP **11**, 017 (2020), arXiv:2005.13584 [hep-lat].

[94] J. R. Peláez and G. Ríos, Phys. Rev. D **82**, 114002 (2010), arXiv:1010.6008 [hep-ph].

[95] J. Nebreda, J. R. Peláez, and G. Ríos, Phys. Rev. D **83**, 094011 (2011), arXiv:1101.2171 [hep-ph].

[96] Y. Akahoshi, S. Aoki, and T. Doi, Phys. Rev. D **104**, 054510 (2021), arXiv:2106.08175 [hep-lat].

[97] M. Hoferichter, B. Kubis, and M. Zanke, Phys. Rev. D **96**, 114016 (2017), arXiv:1710.00824 [hep-ph].

[98] J. Wess and B. Zumino, Phys. Lett. B **37**, 95 (1971).

[99] E. Witten, Nucl. Phys. B **223**, 422 (1983).

[100] S. L. Adler et al., Phys. Rev. D **4**, 3497 (1971).

[101] M. V. Terent'ev, Phys. Lett. B **38**, 419 (1972).

[102] R. Aviv and A. Zee, Phys. Rev. D **5**, 2372 (1972).

[103] I. Larin et al. (PrimEx-II), Science **368**, 506 (2020).

[104] Y. M. Antipov et al., Phys. Rev. D **36**, 21 (1987).

[105] I. Giller et al., Eur. Phys. J. A **25**, 229 (2005), arXiv:hep-ph/0503207.

[106] J. A. Seyfried, *Determination of the Chiral Anomaly and Studies on the Pion Polarizability in Pion-Nickel Reactions from COMPASS at CERN*, Master's thesis (TU Munich, 2017).

[107] R. A. Briceño et al. (Hadron Spectrum), Phys. Rev. Lett. **115**, 242001 (2015), arXiv:1507.06622 [hep-ph].

[108] C. Alexandrou et al., Phys. Rev. D **98**, 074502 (2018), arXiv:1807.08357 [hep-lat]; Erratum: Phys. Rev. D **105**, 019902 (2022).

[109] M. Niehus, *Quark mass dependence of $\gamma\pi \to \pi\pi$*, Master's thesis (Bonn University, 2017).

[110] N. N. Khuri and S. B. Treiman, Phys. Rev. **119**, 1115 (1960).

[111] L. Lellouch and M. Lüscher, Commun. Math. Phys. **219**, 31 (2001), arXiv:hep-lat/0003023.

[112] A. Rusetsky, PoS **LATTICE2019**, 281 (2019), arXiv:1911.01253 [hep-lat].

[113] M. T. Hansen and S. R. Sharpe, Ann. Rev. Nucl. Part. Sci. **69**, 65 (2019), arXiv:1901.00483 [hep-lat].

[114] M. Mai, M. Döring, and A. Rusetsky, Eur. Phys. J. ST **230**, 1623 (2021), arXiv:2103.00577 [hep-lat].

[115] T. D. Blanton, F. Romero-López, and S. R. Sharpe, Phys. Rev. Lett. **124**, 032001 (2020), arXiv:1909.02973 [hep-lat].

[116] M. T. Hansen, F. Romero-López, and S. R. Sharpe, JHEP **04**, 113 (2021), arXiv:2101.10246 [hep-lat].

[117] M. Hoferichter et al., Eur. Phys. J. C **74**, 3180 (2014), arXiv:1410.4691 [hep-ph].

[118] M. Hoferichter et al., JHEP **10**, 141 (2018), arXiv:1808.04823 [hep-ph].

[119] G. Colangelo et al., Phys. Lett. B **738**, 6 (2014), arXiv:1408.2517 [hep-ph].

[120] F. Jegerlehner and A. Nyffeler, Phys. Rept. **477**, 1 (2009), arXiv:0902.3360 [hep-ph].

[121] J. P. Miller et al., Ann. Rev. Nucl. Part. Sci. **62**, 237 (2012).

[122] B. Abi et al. (Muon $g-2$), Phys. Rev. Lett. **126**, 141801 (2021), arXiv:2104.03281 [hep-ex].

[123] S. Borsanyi et al., Nature **593**, 51 (2021), arXiv:2002.12347 [hep-lat].

[124] G. Colangelo, M. Hoferichter, and P. Stoffer, Phys. Lett. B **814**, 136073 (2021), arXiv:2010.07943 [hep-ph].

[125] P. Athron et al., JHEP **09**, 080 (2021), arXiv:2104.03691 [hep-ph].

[126] L. D. Landau and E. M. Lifshitz, *Mechanics, Volume 1 of Course of Theoretical Physics*, 3rd ed. (Butterworth–Heinemann, Oxford, United Kingdom, 1976).

[127] T. R. Kuphaldt, *Lessons In Electric Circuits*, ibiblio, http://www.ibiblio.org/kuphaldt/electricCircuits/index.htm (visited on 12/13/2021).

[128] A. Aloisio et al. (KLOE), Phys. Lett. B **561**, 55 (2003), arXiv:hep-ex/0303016; Erratum: Phys. Lett. B **609**, 449 (2005).

[129] M. Ablikim et al. (BESIII), Phys. Rev. D **98**, 112007 (2018), arXiv:1811.03817 [hep-ex].

[130] M. Albaladejo et al. (JPAC), Eur. Phys. J. C **80**, 1107 (2020), arXiv:2006.01058 [hep-ph].

[131] S. Weinberg, *Lectures on Quantum Mechanics*, 2nd ed. (Cambridge University Press, Cambridge, United Kingdom, 2015).

[132] M. Jacob and G. C. Wick, Annals Phys. **7**, 404 (1959).

[133] J. A. Oller, E. Oset, and J. R. Peláez, Phys. Rev. D **59**, 074001 (1999), arXiv:hep-ph/9804209 [hep-ph]; Errata: Phys. Rev. D **60**, 099906 (1999); Phys. Rev. D **75**, 099903 (2007).

[134] G. F. Chew and S. Mandelstam, Phys. Rev. **119**, 467 (1960).

[135] R. J. Eden and P. V. Landshoff, Phys. Rev. **136**, B1817 (1964).

[136] B. Efron and R. J. Tibshirani, *An Introduction to the Bootstrap* (Chapman & Hall/CRC, Boca Raton, Florida, USA, 1993).

[137] M. Lüscher, Commun. Math. Phys. **104**, 177 (1986).

[138] M. Lüscher, Commun. Math. Phys. **105**, 153 (1986).

[139] M. Lüscher, Nucl. Phys. B **354**, 531 (1991).

[140] C. h. Kim, C. T. Sachrajda, and S. R. Sharpe, Nucl. Phys. B **727**, 218 (2005), arXiv:hep-lat/0507006.

[141] M. T. Hansen and S. R. Sharpe, Phys. Rev. D **86**, 016007 (2012), arXiv:1204.0826 [hep-lat].

[142] M. T. Hansen and S. R. Sharpe, Phys. Rev. D **90**, 116003 (2014), arXiv:1408.5933 [hep-lat].

[143] E. W. Weisstein, *Poisson Sum Formula*, MathWorld – A Wolfram Web Resource, https://mathworld.wolfram.com/PoissonSumFormula.html (visited on 11/02/2020).

[144] D. M. Brink and G. R. Satchler, *Angular Momentum*, 2nd ed. (Clarendon Press, Oxford, United Kingdom, 1968).

[145] M. Gell-Mann, R. J. Oakes, and B. Renner, Phys. Rev. **175**, 2195 (1968).

[146] S. Ropertz, C. Hanhart, and B. Kubis, Eur. Phys. J. C **78**, 1000 (2018), arXiv:1809.06867 [hep-ph].

[147] M. A. O. Werner, *Hadron-Hadron Interactions from $N_f = 2+1+1$ Lattice QCD, The ρ-resonance*, PhD thesis (Bonn University, 2020).

[148] M. Göckeler et al., Phys. Rev. D **86**, 094513 (2012), arXiv:1206.4141 [hep-lat].

[149] M. Niehus et al., Phys. Rev. Lett. **126**, 102002 (2021), arXiv:2009.04479 [hep-ph].

[150] S. Weinberg, Phys. Rev. Lett. **17**, 616 (1966).

[151] M. Dax, T. Isken, and B. Kubis, Eur. Phys. J. C **78**, 859 (2018), arXiv:1808.08957 [hep-ph].

[152] J. Bijnens, G. Colangelo, and G. Ecker, Annals Phys. **280**, 100 (2000), arXiv:hep-ph/9907333.

[153] J. Bijnens, G. Colangelo, and P. Talavera, JHEP **05**, 014 (1998), arXiv:hep-ph/9805389.

[154] A. Dobado and J. R. Peláez, Phys. Rev. D **56**, 3057 (1997), arXiv:hep-ph/9604416.

[155] J. Nieves, M. Pavón Valderrama, and E. Ruiz Arriola, Phys. Rev. D **65**, 036002 (2002), arXiv:hep-ph/0109077.

[156] S. L. Adler, Phys. Rev. **139**, B1638 (1965).

[157] A. Gómez Nicola, J. R. Peláez, and G. Ríos, Phys. Rev. D **77**, 056006 (2008), arXiv:0712.2763 [hep-ph].

[158] P. C. Bruns and M. Mai, Phys. Lett. B **778**, 43 (2018), arXiv:1707.08983 [hep-lat].

[159] D. Djukanovic et al., Phys. Lett. B **680**, 235 (2009), arXiv:0902.4347 [hep-ph].

[160] J. Gasser et al., Phys. Lett. B **652**, 21 (2007), arXiv:0706.0955 [hep-ph].

[161] J. Gasser et al., Phys. Lett. B **675**, 49 (2009), arXiv:0903.0801 [hep-ph].

[162] J. Bijnens and G. Ecker, Ann. Rev. Nucl. Part. Sci. **64**, 149 (2014), arXiv:1405.6488 [hep-ph].

[163] R. J. Dowdall et al. (HPQCD), Phys. Rev. D **88**, 074504 (2013), arXiv:1303.1670 [hep-lat].

[164] K. Rummukainen and S. Gottlieb, Nucl. Phys. B **450**, 397 (1995), arXiv:hep-lat/9503028 [hep-lat].

[165] J. J. Dudek, R. G. Edwards, and C. E. Thomas (Hadron Spectrum), Phys. Rev. D **87**, 034505 (2013), arXiv:1212.0830 [hep-ph]; Erratum: Phys. Rev. D **90**, 099902 (2014).

[166] M. Bruno, T. Korzec, and S. Schaefer, Phys. Rev. D **95**, 074504 (2017), arXiv:1608.08900 [hep-lat].

[167] M. Petschlies and C. Urbach, *Computational Physics*, lecture script (Bonn University, 2017).

[168] R. Storn and K. Price, Journal of Global Optimization **11**, 341 (1997).

[169] W. H. Press et al., *Numerical Recipes, The Art of Scientific Computing*, 3rd ed. (Cambridge University Press, Cambridge, United Kingdom, 2007).

[170] P. Virtanen et al., Nature Methods **17**, 261 (2020).

[171] M. Lüscher, JHEP **08**, 071 (2010), arXiv:1006.4518 [hep-lat]; Erratum: JHEP **03**, 092 (2014).

[172] R. G. Edwards et al., Phys. Rev. D **84**, 074508 (2011), arXiv:1104.5152 [hep-ph].

[173] A. Bazavov et al. (MILC), PoS **LATTICE2010**, 074 (2011), arXiv:1012.0868 [hep-lat].

[174] S. R. Beane et al. (NPLQCD), Phys. Rev. D **86**, 094509 (2012), arXiv:1108.1380 [hep-lat].

[175] S. Borsányi et al., Phys. Rev. D **88**, 014513 (2013), arXiv:1205.0788 [hep-lat].

[176] S. Dürr et al. (Budapest–Marseille–Wuppertal), Phys. Rev. D **90**, 114504 (2014), arXiv:1310.3626 [hep-lat].

[177] P. A. Boyle et al., Phys. Rev. D **93**, 054502 (2016), arXiv:1511.01950 [hep-lat].

[178] E. Epelbaum, H. Krebs, and U.-G. Meißner, Eur. Phys. J. A **51**, 53 (2015), arXiv:1412.0142 [nucl-th].

[179] F. Guerrero and J. A. Oller, Nucl. Phys. B **537**, 459 (1999), arXiv:hep-ph/9805334; Erratum: Nucl. Phys. B **602**, 641 (2001).

[180] A. Gómez Nicola and J. R. Peláez, Phys. Rev. D **65**, 054009 (2002), arXiv:hep-ph/0109056.

[181] R. E. Kass and A. E. Raftery, J. Am. Statist. Assoc. **90**, 773 (1995).

[182] R. García-Martín et al., Phys. Rev. Lett. **107**, 072001 (2011), arXiv:1107.1635 [hep-ph].

[183] G. Colangelo, M. Hoferichter, and P. Stoffer, JHEP **02**, 006 (2019), arXiv:1810.00007 [hep-ph].

[184] K. Kawarabayashi and M. Suzuki, Phys. Rev. Lett. **16**, 255 (1966).

[185] Riazuddin and Fayyazuddin, Phys. Rev. **147**, 1071 (1966).

[186] M. C. Birse, Z. Phys. A **355**, 231 (1996), arXiv:hep-ph/9603251.

[187] J. Ruiz de Elvira et al., Eur. Phys. J. C **77**, 659 (2017), arXiv:1706.09015 [hep-lat].

[188] M. Niehus, M. Hoferichter, and B. Kubis, JHEP **12**, 038 (2021), arXiv:2110.11372 [hep-ph].

[189] M. E. Peskin and D. V. Schroeder, *An Introduction to Quantum Field Theory* (Perseus Books, Reading, Massachusetts, USA, 1995).

[190] F. Niecknig, *Dispersive analysis of charmed meson decays*, PhD thesis (Bonn University, 2016).

[191] R. A. Briceño et al., Phys. Rev. D **93**, 114508 (2016), arXiv:1604.03530 [hep-ph].

[192] K. M. Watson, Phys. Rev. **95**, 228 (1954).

[193] M. Dax, D. Stamen, and B. Kubis, Eur. Phys. J. C **81**, 221 (2021), arXiv:2012.04655 [hep-ph].

[194] G. Höhler, *Pion Nucleon Scattering, Part 2: Methods and Results of Phenomenological Analyses*, edited by H. Schopper, in: Landolt–Börnstein, *Numerical Data and Functional Relationships in Science and Technology*, Group I: *Nuclear and Particle Physics*, **9b** (Springer, Berlin and Heidelberg, Germany, 1983).

[195] T. Hannah, Nucl. Phys. B **593**, 577 (2001), arXiv:hep-ph/0102213.

[196] D. Sakkas, *Dispersion Analysis of the $\gamma\pi \to \pi\pi$ Anomalous Process*, Master's thesis (Bonn University, 2011).

[197] R. Omnès, Nuovo Cim. **8**, 316 (1958).

[198] J. B. Bronzan and C. Kacser, Phys. Rev. **132**, 2703 (1963).

[199] J. Gasser and A. Rusetsky, Eur. Phys. J. C **78**, 906 (2018), arXiv:1809.06399 [hep-ph].

[200] I. J. R. Aitchison and R. Pasquier, Phys. Rev. **152**, 1274 (1966).

[201] B. Moussallam, Eur. Phys. J. C **73**, 2539 (2013), arXiv:1305.3143 [hep-ph].

[202] W. R. Frazer, Phys. Rev. **123**, 2180 (1961).

[203] F. J. Ynduráin, *Low Energy Pion Physics* (2002), arXiv:hep-ph/0212282.

[204] H. Leutwyler, *Electromagnetic form factor of the pion*, in K. A. Olive, M. A. Shifman, and M. B. Voloshin, *Continuous Advances in QCD 2002, Arkadyfest, Honoring the 60th Birthday of Arkady Vainshtein* (World Scientific, Singapore, 2002), arXiv:hep-ph/0212324.

[205] D. Stamen, *Dispersive Analysis of the Primakoff Reaction $\gamma K \to K\pi$: Khuri–Treiman Solution and Matching*, Master's thesis (Bonn University, 2020).

[206] S. Descotes-Genon and B. Moussallam, Eur. Phys. J. C **74**, 2946 (2014), arXiv:1404.0251 [hep-ph].

[207] J. Bijnens, A. Bramon, and F. Cornet, Phys. Lett. B **237**, 488 (1990).

[208] R. A. Briceño, J. J. Dudek, and L. Leskovec, Phys. Rev. D **104**, 054509 (2021), arXiv:2105.02017 [hep-lat].

[209] R. J. Barlow, *Statistics, A Guide to the Use of Statistical Methods in the Physical Sciences* (John Wiley & Sons, Chichester, United Kingdom, 1989).

[210] M. Froissart, Phys. Rev. **123**, 1053 (1961).

[211] F. Klingl, N. Kaiser, and W. Weise, Z. Phys. A **356**, 193 (1996), arXiv:hep-ph/9607431.

[212] T. Jensen et al., Phys. Rev. D **27**, 26 (1983).

[213] J. Huston et al., Phys. Rev. D **33**, 3199 (1986).

[214] L. Capraro et al., Nucl. Phys. B **288**, 659 (1987).

[215] R. R. Akhmetshin et al. (CMD-2), Phys. Lett. B **605**, 26 (2005), arXiv:hep-ex/0409030.

[216] M. N. Achasov et al. (SND), Phys. Rev. D **93**, 092001 (2016), arXiv:1601.08061 [hep-ex].

[217] C. Alexandrou et al., Phys. Rev. D **105**, 019902 (2022).

[218] R. E. Cutkosky, J. Math. Phys. **1**, 429 (1960).

[219] M. Mikhasenko et al., JHEP **08**, 080 (2019), arXiv:1904.11894 [hep-ph].

[220] I. J. R. Aitchison, *Unitarity, Analyticity and Crossing Symmetry in Two- and Three-hadron Final State Interactions* (2015), arXiv:1507.02697 [hep-ph].

[221] M. Mai and M. Döring, Eur. Phys. J. A **53**, 240 (2017), arXiv:1709.08222 [hep-lat].

[222] H. Akdag, T. Isken, and B. Kubis, (2021), arXiv:2111.02417 [hep-ph].

[223] M. Albaladejo et al. (JPAC), Eur. Phys. J. C **78**, 574 (2018), arXiv:1803.06027 [hep-ph].

[224] E. W. Weisstein, *Cubic Formula*, MathWorld – A Wolfram Web Resource, http://mathworld.wolfram.com/CubicFormula.html (visited on 03/06/2020).

[225] Wikipedia contributors, *Cubic equation*, Wikipedia, The Free Encyclopedia, https://en.wikipedia.org/w/index.php?title=Cubic_equation&oldid=942158077 (visited on 03/06/2020).

[226] A. Rodas et al. (JPAC), Phys. Rev. Lett. **122**, 042002 (2019), arXiv:1810.04171 [hep-ph].

[227] T. Isken, *private communication*, 2019.

[228] T. W. B. Kibble, Phys. Rev. **117**, 1159 (1960).

[229] R. H. Dalitz, Phil. Mag. Ser. 7 **44**, 1068 (1953).

[230] K. P. Burnham and D. R. Anderson, *Model Selection and Multimodel Inference, A Practical Information-Theoretic Approach*, 2nd ed. (Springer, Berlin and Heidelberg, Germany, 2002).

[231] A. Dobado and J. R. Peláez, Phys. Rev. D **65**, 077502 (2002), arXiv:hep-ph/0111140.

Acknowledgements

First and foremost, I thank Bastian Kubis for his continuous support, not only concerning scientific questions, but perhaps even more importantly, his incentive to participate in specific conferences, his support in obtaining a scholarship, and the creation of a communicative and pleasant atmosphere in the group that makes working there a joy. I would like to thank Carsten Urbach for being my second supervisor and for answering many questions concerning lattice-related issues. In addition, I thank Bernhard Ketzer and Barbara Niethammer for being third and fourth referee, respectively.

I am indebted to Martin Hoferichter, who not only suggested the analysis of the $\gamma^{(*)}\pi \to \pi\pi$ lattice data, but also provided key input to the lattice-related projects. Without him, none of the publications would have been possible. In this context, I express my gratitude towards Jacobo Ruiz de Elvira, who was of great help in the IAM analysis. The joint work on projects was always a pleasure, as were the times spent together at conferences. Writing of conferences, I owe thanks to Barbara Kraus for assisting in many organizational issues, e.g., related to travels to conference venues.

Members of the HadSpec collaboration, in particular Raúl Briceño, were of great help in the analysis of their lattice data and always open for questions, thanks a lot. Also, I thank Marcus Petschlies for discussions concerning $\gamma^{(*)}\pi \to \pi\pi$ and Peter Bruns for triggering the analysis in Sec. 4.2.1. In addition, I thank Mikhail Mikhasenko for lively debates on three-hadron physics; in particular, his ideas concerning the comparison presented in Ch. 12.

If there had not been so many great people around, working at the HISKP would not have been as delightful as it turned out to be. First, I thank Tobias Isken for great times at several conferences abroad and interesting discussions of both physics-related topics and less scientific ones. Next, I thank Martin Ueding for keeping the level of irony and sarcasm high during lunch time, and for setting up the SLURM cluster at the HISKP, which greatly facilitated several computations. His help on certain software-design-related issues is also highly appreciated. I give thanks to Dominik Stamen and Hakan Akdag for working together on KT-related questions. In addition, I thank the entire group (both current and former members), among others, Christoph Hanhart, Bai-Long Hoid, Kevin Olschewsky, Janak Prabhu, Stefan Ropertz, Markus Werner, and Marvin Zanke, for the great atmosphere, interesting debates, and fun.

Moreover, I thank Lorenz Mayer and Urmi Ninad for the joyful hours we spent studying QFT.

Furthermore, I would like to thank Bernard Metsch for inspiring lectures on theoretical electrodynamics and general relativity in the bachelor's, which greatly motivated me to delve into the realm of theoretical physics.

I wish to thank Dominik, Lorenz, Marvin, and Tobias for proof-reading this thesis.

Financial support by the Bonn–Cologne Graduate School of Physics and Astronomy (BCGS) and the DFG (CRC 110, "Symmetries and the Emergence of Structure in QCD") is gratefully acknowledged.